



# University of HUDDERSFIELD

## University of Huddersfield Repository

Jaber, Adel Ali

Absolute calibration of radiometric partial discharge sensors for insulation condition monitoring in electrical substations

### Original Citation

Jaber, Adel Ali (2017) Absolute calibration of radiometric partial discharge sensors for insulation condition monitoring in electrical substations. Doctoral thesis, University of Huddersfield.

This version is available at <http://eprints.hud.ac.uk/id/eprint/34189/>

The University Repository is a digital collection of the research output of the University, available on Open Access. Copyright and Moral Rights for the items on this site are retained by the individual author and/or other copyright owners. Users may access full items free of charge; copies of full text items generally can be reproduced, displayed or performed and given to third parties in any format or medium for personal research or study, educational or not-for-profit purposes without prior permission or charge, provided:

- The authors, title and full bibliographic details is credited in any copy;
- A hyperlink and/or URL is included for the original metadata page; and
- The content is not changed in any way.

For more information, including our policy and submission procedure, please contact the Repository Team at: [E.mailbox@hud.ac.uk](mailto:E.mailbox@hud.ac.uk).

<http://eprints.hud.ac.uk/>

**ABSOLUTE CALIBRATION OF RADIOMETRIC PARTIAL  
DISCHARGE SENSORS FOR INSULATION CONDITION  
MONITORING IN ELECTRICAL SUBSTATIONS**

by

**ADEL ALI JABER**

A thesis submitted to the Department of Computing and Engineering  
In conformity with the requirements for  
the degree of Doctor of Philosophy

University of Huddersfield  
(March 2017)

## ABSTRACT

Measurement of partial discharge (PD) is an important tool in the monitoring of insulation integrity in high voltage (HV) equipment. Partial discharge is measured traditionally using galvanic contact techniques based on IEC 60270 standard or near field coupling [1]. Free-space radiometric (FSR) detection of PD is a relatively new technique. This work advances calibration method for FSR measurements and proposer a methodology for FSR measurement of absolute PD intensity. Until now, it has been believed that absolute measurement of partial discharge intensity using radiometric method is not possible. In this thesis it is demonstrated that such measurement is possible and the first ever such absolute measurements are presented. Partial discharge sources have been specially constructed. These included a floating electrode PD emulator, an acrylic cylinder internal PD emulator and an epoxy dielectric internal PD emulator. Radiated signals are captured using a wideband biconical antenna [1]. Free-space radiometric and galvanic contact measurement techniques are compared. Discharge pulse shape and PD characteristics under high voltage DC and AC conditions are obtained. A comparison shows greater similarity between the two measurements than was expected. It is inferred that the dominant mechanism in shaping the spectrum is the band-limiting effect of the radiating structure rather than band limiting by the receiving antenna. The cumulative energies of PD pulses in both time and frequency domains are also considered [2]. The frequency spectrum is obtained by FFT analysis of time-domain pulses. The relative spectral densities in the frequency bands 50 MHz – 290 MHz, 290 MHz – 470 MHz and 470 MHz – 800 MHz are determined. The calibration of the PD sources for used in the development of Wireless Sensor Network (WSN) is presented. A method of estimating absolute PD activity level from a radiometric measurement by relating effective radiated power (ERP) to PD intensity using a PD calibration device is proposed and demonstrated. The PD sources have been simulated using CST Microwave Studio. The simulations are used to establish a relationship between radiated PD signals and PD intensity as defined by apparent charge transfer. To this end, the radiated fields predicted in the simulations are compared with measurements. There is sufficient agreement between simulations and measurements to suggest the simulations

could be used to investigate the relationship between PD intensity and the field strength of radiated signals [3].

## **ACKNOWLEDGEMENTS**

I would like to take this opportunity to express my sincere gratitude to many people who have helped me and supported during this studying of PhD. Firstly, I would like to thank Allah for his guidance for completion of this work. Secondly, I would like to express my appreciation to my supervisors, Dr. Pavlos Lazaridis and Prof. Ian Glover for their guidance and encouragement during my pursuit of PhD study. My thanks and appreciations go to our colleagues who are working in the partial discharge project. Many thanks to all members of the School of Computing and Engineering. A lot of thanks to my parents and special thanks to my wife and children for their countless help.

## **STATEMENT OF ORIGINALITY**

I hereby certify that all of the work described within this thesis is the original work of the author. Any published (or unpublished) ideas and/or techniques from the work of others are fully acknowledged in accordance with the standard referencing practices.

(Adel Ali Jaber)

(March 2017)

## LIST OF PUBLICATIONS

- I. **A. Jaber**, P. Lazaridis, Zaharias D. Zaharis, Mohamed Moradzadeh, M. F. Q. Vieira, M Judd, and I. A. Glover, Calibration of Free-Space Radiometric Partial Discharge Measurements - Submitted to I EEE dielectrics and electrical insulation. Accepted 20 June 2017.
- II. **A. Jaber**, P. Lazaridis, B. Saeed, P. Mather, M. F. Q. Vieira, R. Atkinson, C. Tachtatzis, E. Iorkyase, M. Judd, and I. A. Glover, Diagnostic Potential of Free-Space Radiometric Partial Discharge Measurements - <sup>32</sup>nd URSI of Radio Scientists General Assembly and Scientific Symposium, Montreal, Canada, 19-26 August 2017.
- III. **A. Jaber**, P. Lazaridis, B. Saeed, U. Khan, Y. Zhang, D. Upton, H. Ahmed, P. Mather, M. F. Q. Vieira, R. Atkinson, M. Judd, and I. A. Glover, " Free-Space Radiometric Estimation of Apparent Charge in Partial Discharge Processes for the Monitoring of Insulation Integrity in High Voltage Systems," in 2016 URSI UK Festival of Radio Science Conference, York, UK, 2016, pp. 1-1.
- IV. **A. Jaber**, P. Lazaridis, B. Saeed, Y. Zhang, U. Khan, D. Upton, H. Ahmed, P. Mather, M. F. Q. Vieira, R. Atkinson, M. Judd, and I. A. Glover, "Validation of Partial Discharge Emulators Simulation using Free-Space Radiometric Measurements," in Students on Applied Engineering (ISCAE), International Conference, Newcastle, United Kingdom, 2016, pp. 475-478. Best paper award.
- V. **A. Jaber**, P. Lazaridis, B. Saeed, Y. Zhang, U. Khan, D. Upton, H. Ahmed, P. Mather, M. F. Q. Vieira, R. Atkinson, M. Judd, and I. A. Glover, "Assessment of Effective Radiated Power of the Partial Discharge Emulator Source" in International Conference on Wireless and Satellite Systems (pp. 108-115). Springer, Cham, Cardiff, Great Britain (2016, September).
- VI. **A. Jaber**, P. Lazaridis, B. Saeed, Y. Zhang, U. Khan, D. Upton, H. Ahmed, P. Mather, M. F. Q. Vieira, R. Atkinson, M. Judd, and I. A. Glover, "Comparative study of Partial

- Discharge Emulators for the Calibration of Free-Space Radiometric Measurements," in Automation and Computing (ICAC), 2016 22nd International Conference on, Colchester, UK, 2016, pp. 313-316.
- VII. **A. Jaber**, P. Lazaridis, Y. Zhang, B. Saeed, U. Khan, D. Upton, H. Ahmed, P. Mather, M. F. Q. Vieira, R. Atkinson, M. Judd, and I. A. Glover, "Assessment of absolute partial discharge intensity from a free-space radiometric measurement," in URSI Asia-Pacific Radio Science Conference (URSI AP-RASC), Seoul, Korea, 2016, pp. 1011-1014.
- VIII. **A. Jaber**, P. Lazaridis, B. Saeed, Y. Zhang, U. Khan, D. Upton, H. Ahmed, P. Mather, M. F. Q. Vieira, R. Atkinson, M. Judd, and I. A. Glover "Frequency Spectrum Analysis of Radiated Partial Discharge Signals," in IET EUROEM 2016 conference (European Electromagnetics Symposium), London, UK, 2016, pp. 1-2.
- IX. **A. Jaber**, P. Lazaridis, B. Saeed, Y. Zhang, U. Khan, D. Upton, H. Ahmed, P. Mather, M. F. Q. Vieira, R. Atkinson, M. Judd, and I. A. Glover, "PD Source Calibration and Comparison of Free-Space Radiated and Galvanic Contact PD Spectra," in 2015 URSI UK Festival of Radio Science Conference, Manchester, UK, 2015, pp. 1-1.
- X. **A. Jaber**, P. Lazaridis, Y. Zhang, D. Upton, H. Ahmed, U. Khan, B. Saeed, P. Mather, M. F. Q. Vieira, R. Atkinson, M. Judd, and I. A. Glover, "Comparison of contact measurement and free-space radiation measurement of partial discharge signals," in Automation and Computing (ICAC), 21st International Conference on, Glasgow, UK, 2015, pp. 1-4.

**The Author has also Contributed to the Following Papers:**

- I. Y. Zhang, D. Upton, **A. Jaber**, H. Ahmed, B. Saeed, P. Mather, P. Lazaridis, A. Mopty, C. Tachtatzis, R. Atkinson, M. Judd, M. F. Q. Vieira, and I. A. Glover, "Radiometric wireless sensor network monitoring of partial discharge sources in electrical substations," International Journal of Distributed Sensor Networks, vol. 2015, p. 179.
- II. Y. Zhang, J. M. Neto, D. Upton, **A. Jaber**, U. Khan, B. Saeed, H. Ahmed, P. Mather, R. Atkinson, J.S. Neto, M.F. Q. Vieira, P. Lazaridis and I.A. Glover, "Radiometer

- monitoring system for artrial discharge detection in substation," in Radio Science Conference (URSI AT-RASC), 1st URSI Atlantic Gran Canaria, Spain, 2015, pp. 1-1.
- III. Y. Zhang, D. Upton, **A. Jaber**, H. Ahmed, U. Khan, B. Saeed, P. Mather, P. Lazaridis, R. Atkinson, M.F. Q Vieira, I.A. Glover, "Multiple source localization for partial discharge monitoring in electrical substation," in Antennas & Propagation Conference (LAPC), Loughborough, UK, 2015, pp. 1-4.
- IV. Y. Zhang, D. Upton, **A. Jaber**, U. Khan, B. Saeed, H. Ahmed, P. Mather, R. Atkinson, P. Lazaridis, M.F. Q Vieira and I.A. Glover, "An Ultrawideband Patch Antenna for UHF Detection of Partial Discharge," in Radio Science Conference (URSI AT-RASC), 2015 1st URSI Atlantic, Gran Canaria, Spain, 2015, pp. 1-1.
- V. J. M. Neto, Y. Zhang, **A. Jaber**, M. Zhu, M. Judd, R. Atkinson, J. Soraghan, J.S. Neto, M.F. Q Vieira, and I A Glover, "Radiometric location of partial discharge sources for the future smart grid," in General Assembly and Scientific Symposium (URSI GASS), Beijing, 2014, pp. 1-4.
- VI. D W Upton, P J Mather, Y Zhang, **A Jaber**, H Ahmed, U Khan, B Saeed, M F Q Vieira, R Atkinson and I A Glover, "Signal Conditioning Electronics for UHF Partial Discharge Detection and Location System" in 2014 URSI UK Festival of Radio Science Conference, Manchester, UK, 2014, pp. 1-1.

# LIST OF CONTENTS

<b>ABSTRACT</b> .....	<b>ii</b>
<b>ACKNOWLEDGEMENTS</b> .....	<b>iv</b>
<b>STATEMENT OF ORIGINALITY</b> .....	<b>v</b>
<b>LIST OF PUBLICATIONS</b> .....	<b>vi</b>
<b>LIST OF CONTENTS</b> .....	<b>ix</b>
<b>LIST OF FIGURES</b> .....	<b>xiii</b>
<b>LIST OF TABLES</b> .....	<b>xix</b>
<b>LIST OF ABBREVIATIONS</b> .....	<b>xxi</b>
<b>LIST OF SYMBOLS</b> .....	<b>xxii</b>
<b>CHAPTER 1 INTRODUCTION</b> .....	<b>1</b>
1.1 Background .....	2
1.2 Motivation .....	10
1.3 Objectives.....	10
1.4 Methodology .....	11
1.5 Novelty and Research Contribution .....	12
1.6 Thesis Structure.....	12
<b>CHAPTER 2 LITERATURE REVIEW</b> .....	<b>14</b>
2.1 Introduction .....	15
2.2 Basic Concepts of Partial Discharge Test Circuit .....	15
2.3 Partial Discharge Types .....	20
2.3.1 Internal discharges .....	21
2.3.2 Surface discharges .....	23
2.3.3 Corona discharges.....	23
2.4 Partial Discharge Detection.....	24
2.4.1 Electromagnetic methods.....	26
2.4.1.1 Electrical methods - according to the IEC60270 .....	26
2.4.1.2 Free-space radiometric methods.....	27
2.4.1.3 High frequency current transformer methods .....	27
2.4.1.4 Transient earth voltage methods (TEV) .....	28

2.4.2	Ultra-high frequency PD methods .....	28
2.4.3	Acoustic and ultrasonic methods .....	29
2.4.4	Optical methods .....	30
2.4.5	Chemical methods.....	30
2.4.6	Light and ultraviolet.....	31
2.4.7	Thermal methods .....	32
2.5	Comparison of Methods .....	32
2.6	Previous Work.....	34
2.6.1	Free-space radiometric measurements system.....	35
2.6.2	Galvanic contact measurements system.....	37
2.6.3	Comparison between free-space radiometric and galvanic contact measurements system .....	38
2.6.4	Calibration of partial discharge measurements.....	40
2.6.5	Modeling of UHF PD radiation .....	41
2.7	Partial Discharge Radiation.....	43
2.8	Summary .....	48
<b>CHAPTER 3 MEASUREMENT APPARATUS .....</b>		<b>49</b>
3.1	Introduction .....	50
3.2	Measuring Circuit.....	50
3.3	Antenna .....	51
3.4	Floating Electrode PD Emulator .....	53
3.4.1	Theory.....	54
3.4.2	Equivalent circuit .....	56
3.5	An Acrylic Tube Internal PD Emulator .....	58
3.6	Epoxy Dielectric Internal PD Emulator .....	58
3.7	HVPD pC Calibrator .....	59
3.8	Data Capture.....	60
<b>CHAPTER 4 SPECTRUM MEASUREMENTS.....</b>		<b>61</b>
4.1	Introduction .....	62
4.2	Time Series Events.....	62

4.3	Correlation of FSR and Galvanic Contact Measurement of PD Events .....	67
4.4	Frequency Spectra of FSR and Galvanic Contact Measurements.....	69
4.4.1	Frequency spectrum energy analysis .....	74
4.5	Cumulative Distribution of Energy .....	79
4.6	Summary .....	80
<b>CHAPTER 5 AN ABSOLUTE RADIOMETRIC PARTIAL DISCHARGE INTENSITY MEASUREMENT.....</b>		<b>82</b>
5.1	Introduction .....	83
5.2	PD Calibration.....	84
5.2.1	Calibration of floating-electrode PD emulator .....	86
5.2.2	Calibration an acrylic tube internal PD emulator .....	95
5.2.3	Calibration an epoxy dielectric internal PD emulator.....	105
5.2.4	Relationship between calculated charge and effective radiated power for different PD emulators.....	112
5.3	Summary .....	114
<b>CHAPTER 6 VALIDATION OF PARTIAL DISCHARGE EMULATORS SIMULATION USING FREE-SPACE RADIOMETRIC MEASUREMENTS.....</b>		<b>115</b>
6.1	Introduction .....	116
6.2	FSR PD Measurements and Simulations .....	118
6.3	Summary .....	124
<b>CHAPTER 7 PARTIAL DISCHARGE ACTIVITY UNDER AC AND DC VOLTAGES..</b>		<b>125</b>
7.1	Introduction .....	126
7.1	Influence of Emulator Geometry on PD Intensity under AC Applied Voltages	126
7.1.1	FSR measurement .....	127
7.1.2	Galvanic contact measurements.....	131
7.1.3	Influence of gap length between the HV ground plate electrode and the floating electrode .....	135
7.2	FSR Measurement at Different Locations of Receiving Antenna .....	138
7.3	Influence of Emulator Geometry on PD Intensity for various DC Applied High Voltages.....	142

7.4	Summary .....	144
<b>CHAPTER 8 CONCLUSIONS AND FUTURE WORK.....</b>		<b>145</b>
8.1	Conclusions .....	146
8.2	Recommendations for Future Work.....	148
<b>REFERENCES.....</b>		<b>150</b>
<b>APPENDICES.....</b>		<b>168</b>

## LIST OF FIGURES

Figure 1-1 Proportion of failures due to insulation breakdown in different categories of HV plant. (Compiled from [11-17] ).	3
Figure 1-2 Origin of PD in an insulator.	4
Figure 1-3 IEC 60270 PD measurement setup.	8
Figure 1-4 PD measurement calibration circuit.	9
Figure 1-5 Free-space radiometric PD measurement and setup.	9
Figure 2-1 PD test object (a) Insulation cavity (b) Equivalent circuit.	16
Figure 2-2 PD test circuit within test object.	16
Figure 2-3 Cavity breakdown sequence under alternating voltage.	18
Figure 2-4 Low sensitivity measurement of PD current circuit.	18
Figure 2-5 Internal discharge (void, metal discharge and treeing) of PD [63].	21
Figure 2-6 Electrical trees of PD [47, 48] (a) Branch-like electrical tree (b) Bush-like electrical tree.	22
Figure 2-7 Surface discharge of PD [63].	23
Figure 2-8 Corona discharge [69].	24
Figure 2-9 Lichtenberg's dust figures [70].	24
Figure 2-10 PD detection methods.	25
Figure 2-11 Typical UHF PD monitoring system.	29
Figure 2-12 Electric and magnetic fields of a moving charge particle $Q$ .	44
Figure 2-13 Radiation during the acceleration of charge.	45
Figure 2-14 Pulse shape of the radiation at point $M - N$ and $L - J$ .	45
Figure 2-15 The electric field at angle $\theta$ caused by charge $q$ accelerated from point $A$ to $B$ then moving with constant speed until reaching point $C$ .	46
Figure 3-1 PD measurement apparatus.	51
Figure 3-2 Biconical antenna used in the FSR measurements.	52
Figure 3-3 Biconical antenna (a) antenna gain (b) antenna factor.	52
Figure 3-4 Diagram showing the gap arrangement containing a floating electrode and the electric fields.	54

Figure 3-5 Floating – electrode PD emulator (dimensions in mm). .....	56
Figure 3-6 Equivalent circuit of floating electrode PD emulator and detector. ....	57
Figure 3-7 Waveform of the discharge source model. ....	57
Figure 3-8 Acrylic tube internal PD emulator (dimensions in mm). ....	58
Figure 3-9 Epoxy dielectric internal PD emulator (dimensions in mm). ....	59
Figure 3-10 HVPD pC calibrator [165]. ....	60
Figure 4-1 FSR and galvanic contact measurement of PD event using a floating electrode PD emulator. ....	63
Figure 4-2 FSR and galvanic contact measurement of PD event using an acrylic tube internal PD emulator. ....	64
Figure 4-3 FSR and galvanic contact measurement of PD event using an acrylic tube internal PD emulator filled with transformer oil. ....	65
Figure 4-4 FSR and galvanic contact measurement of PD event using an epoxy dielectric internal PD emulator. ....	66
Figure 4-5 Comparison of normalized measurements of PD signals using four types of PD emulators. ....	68
Figure 4-6 Frequency spectra of FSR and galvanic contact measurements using a floating electrode PD emulator. ....	70
Figure 4-7 Frequency spectra of FSR and galvanic contact measurements using an acrylic tube internal PD emulator. ....	71
Figure 4-8 Frequency spectra of FSR and galvanic contact measurements using an acrylic tube internal PD emulator filled with transformer oil. ....	72
Figure 4-9 Frequency spectra of FSR and galvanic contact measurements using an epoxy dielectric internal PD emulator. ....	73
Figure 4-10 Frequency spectrum divided into bands for the FSR measurement method. ....	74
Figure 4-11 Sub-band spectra and energy proportions for FSR measurement. ....	75
Figure 4-12 Sub-band spectra energy contained in the two frequency bands for FSR measurement. ....	75
Figure 4-13 Frequency bands energy content for the galvanic contact measurement method. ....	77

Figure 4-14 Sub-band spectra and energy proportions for the galvanic contact measurement. ....	78
Figure 4-15 Sub-band spectra energy contained in the two frequency bands for the galvanic contact measurement method.....	78
Figure 4-16 (a) Time-cumulative distribution of FSR energy. (b) Time-cumulative distribution of the galvanic contact energy. ....	79
Figure 5-1 Injection of a known calibration pulse into a DSO.....	84
Figure 5-2 Example of current waveform for an injected charge into a DSO (1 nC.).....	85
Figure 5-3 Integral of measured current pulse (calculated charge) versus calibration device injected charge. ....	86
Figure 5-4 Injected charge across the terminals of floating-electrode PD source. ....	87
Figure 5-5 Resulting of calculated charge versus injected charge of floating-electrode PD emulator. ....	88
Figure 5-6 Measurement circuit for emulator calibration.....	89
Figure 5-7 Measured waveform for an injected charge of 1 nC. ....	89
Figure 5-8 Calculate charge versus specified charge of charge injection device. ....	90
Figure 5-9 Floating-electrode PD emulator signal (a) a galvanic contact measurement pulse and (b) Frequency spectrum of galvanic contact measurement.....	91
Figure 5-10 Floating-electrode PD source signal FSR measurement pulse. ....	92
Figure 5-11 Average frequency spectrum of FSR measurements at 15 kV measurements for four locations of receiving antenna from floating-electrode PD emulator.....	92
Figure 5-12 (a) Received peak voltage, (b) Electric field strength and (c) ERP as a function of (floating-electrode PD emulator) – antenna distance from emulator. ....	95
Figure 5-13 Injected charge across the terminals of an acrylic tube internal PD emulator. ....	96
Figure 5-14 Graph of calculated charge versus injected charge of an acrylic tube internal PD emulator (a) without oil filling and (b) with oil filling. ....	96
Figure 5-15 Experimental measurement circuit calibration of acrylic tube internal PD emulator. ....	98

Figure 5-16 Graph of calculated charge versus injected charge of acrylic tube internal PD emulator (a) without oil filling and (b) with oil filling. ....	99
Figure 5-17 Measurement apparatus using an acrylic tube internal PD emulator. ....	99
Figure 5-18 An acrylic tube internal PD emulator without oil filling FSR measurement pulse. ....	100
Figure 5-19 Averaged frequency spectra of FSR measurements at 20 kV for four locations of the receiving antenna from an acrylic tube internal PD emulator without oil filling. ....	100
Figure 5-20 A galvanic contact measurement signal and average frequency spectrum of an acrylic tube internal PD emulator without oil filling. ....	101
Figure 5-21 A galvanic contact measurement signal and frequency spectrum of acrylic tube internal PD emulator with oil filling. ....	101
Figure 5-22 FSR measurement pulse of an acrylic tube internal PD emulator with oil filling. ....	102
Figure 5-23 Averaged frequency spectra of FSR measurements at 20 kV for four locations of the receiving antenna from an acrylic tube internal PD emulator with oil filling. ....	102
Figure 5-24 (a) Received peak voltage, (b) Electric field strength and (c) ERP as a function of (emulator without oil filling) – antenna distance from emulator ....	104
Figure 5-25 (a) Received peak voltage, (b) Electric field strength and (c) ERP as a function of (emulator with oil filling) – antenna distance from emulator. ....	105
Figure 5-26 Injected charge across the terminals of an epoxy dielectric internal PD emulator. ....	106
Figure 5-27 Calculated charge versus injected charge. ....	106
Figure 5-28 Measurement circuit for the calibration of an epoxy dielectric internal PD emulator. ....	107
Figure 5-29 Calculated charge versus specified charge from the charge injection device. ....	108
Figure 5-30 Measurement system using an epoxy dielectric internal PD emulator. ....	109
Figure 5-31 Epoxy dielectric internal PD emulator (a) Galvanic contact measurement pulse (b) Frequency spectra. ....	109
Figure 5-32 FSR measured pulse from an epoxy dielectric internal PD emulator. ....	110

Figure 5-33 Averaged frequency spectra of FSR measurement at 18 kV for four locations of the receiving antenna from of an epoxy dielectric internal PD emulator. ....	110
Figure 5-34 (a) Received peak voltage, (b) Electric field strength and (c) ERP as a function of epoxy dielectric internal PD emulator – antenna range.....	112
Figure 5-35 Determined ERP for different types of PD sources versus calculated charge. ....	113
Figure 6-1 PD emulator types: (a) floating-electrode (b) acrylic tube internal and (c) epoxy dielectric internal. ....	117
Figure 6-2 PD measurement circuit with an epoxy dielectric internal PD emulator. ....	118
Figure 6-3 PD FSR measurement signal (a) floating-electrode (b) acrylic tube internal and (c) epoxy dielectric internal. ....	119
Figure 6-4 Excitation current signal (a) floating-electrode (b) Acrylic tube internal and (c) Epoxy dielectric internal. ....	120
Figure 6-5 Simulated PD electrical fields (a) floating-electrode (b) Acrylic tube internal and (c) Epoxy dielectric internal.....	121
Figure 6-6 Comparison of measured and simulated PD electrical field amplitudes.....	122
Figure 6-7 Simulated transient behavior of the signals propagating of different distances from the floating electrode PD emulator model. ....	123
Figure 6-8 Simulated transient behavior of the signals propagating of different distances from an acrylic tube internal PD model.....	124
Figure 7-1 Time series events of FSR PD signal for various gaps. ....	129
Figure 7-2 Peak voltage amplitude of FSR measurements for each gap as a function of the applied HV value. ....	130
Figure 7-3 Mean average spectra of FSR measurements as a function of the inter-electrode gap length between electrodes of PD emulator with different applied voltage. ....	131
Figure 7-4 Time series events of galvanic contact measurement PD signal.....	132
Figure 7-5 Peak voltage amplitude of galvanic contact measurements for each gap. ....	133
Figure 7-6 Mean average spectra of a galvanic contact measurements for various gap distances and different applied voltages. ....	134
Figure 7-7 Voltage amplitude of FSR measurements signal under AC applied voltage.	136

Figure 7-8 Peak voltage amplitude of FSR measurements for various gap lengths. ....	137
Figure 7-9 Mean averaged spectra of FSR measurements.....	137
Figure 7-10 Measurement space plan and measurement space. ....	139
Figure 7-11 FSR measurements at different locations from the receiving antenna.....	139
Figure 7-12 Mean averaged spectra at different distances from the receiving antenna..	140
Figure 7-13 (a) Received peak voltage (b) Electric field strength and (c) ERP as a function of PD source – antenna distance from emulator. ....	141
Figure 7-14 Relationship between FSR and galvanic contact measurement signals under DC applied voltage for each inter-electrode of gap length. ....	143

## LIST OF TABLES

Table 2-1 Comparative table including the main features between detection methods. ..	33
Table 4-1 Correlation of FSR and galvanic contact measurements signals.....	67
Table 4-2 Energy of FSR measurement frequency bands for each emulator type. ....	76
Table 4-3 Energy of a galvanic contact measurement frequency bands for each emulator type.....	80
Table 5-1 Relationship between injected charge and calculated charge.....	85
Table 5-2 Relationship between injected charge and calculated charge of floating-electrode PD emulator. ....	87
Table 5-3 Relationship between injected charge and calculated charge across measured circuit. ....	90
Table 5-4 Concurrent measurements of FSR and galvanic measurements using the floating-electrode PD emulator.....	94
Table 5-5 Relationship between injected charge and calculated charge across the terminals of an acrylic tube internal PD emulator. ....	97
Table 5-6 Relationship between injected charge and calculated charge across the terminals of a measurement circuit with an acrylic tube internal PD emulator.....	98
Table 5-7 Concurrent measurements of FSR and galvanic measurements using the acrylic tube internal PD emulator with and without oil filling. ....	103
Table 5-8 Relationship between injected charge and calculated charge across the terminals of an epoxy dielectric internal PD emulator. ....	107
Table 5-9 Relationship between injected charge and calculated charge for an epoxy dielectric internal PD emulator. ....	108
Table 5-10 Simultaneous measurements of FSR and galvanic pulses using the epoxy dielectric internal PD emulator. ....	111
Table 5-11 Relationship between calculated charge and peak effective radiated power of PD emulators.....	113
Table 6-1 Correlation of measured PD signal and simulated signal.....	123

Table 7-1 Peak voltage of FSR pulse amplitude under AC and DC applied voltage at different distances between PD source and the biconical receiving antenna.....	126
Table 7-2 Peak voltage amplitude of FSR measurements depending on gap length between floating electrodes of PD emulator under AC applied voltage. ....	128
Table 7-3 Peak voltage of a galvanic contact measurement depending on inter-electrode gap length.....	135
Table 7-4 Peak voltage of FSR measurement depending on inter-electrode gap length.	136
Table 7-5 Received peak voltage at various distances.....	140
Table 7-6 Peak voltage amplitude of galvanic contact measurement and FSR depending on inter-electrode gap length for DC applied voltage.....	142

## LIST OF ABBREVIATIONS

<b>Abbreviations</b>	<b>Description</b>
AC	Alternating current
CM	Condition monitoring
CC	Correlation coefficient
CST	Computer simulation technology
DC	Direct current
DSO	Digital sampling oscilloscope
ERP	Effective radiated power
EM	Electromagnetic
FDTD	Finite-difference time-domain
FE	Floating electrode
FFT	Fast Fourier transform
FSR	Free-space radiometry
GIS	Gas insulation system
HF	High frequency
HFCT	High frequency current transducer
HVPD pC	High voltage partial discharge (picocoulomb)
HV	High voltage
IEC	International electrotechnical commission
PD	Partial discharge
RF	Radio frequency
RMSE	Root Mean Squared Error
RSS	Received signal strength
TEV	Transient earth voltage
UHF	Ultra-high frequency
UWB	Ultra-wideband
VHF	Very High Frequency
WSN	Wireless sensor network

## LIST OF SYMBOLS

<b>Symbols</b>	<b>Description</b>
$C_a$	Test object
$CD$	Coupling device
$CC$	Coaxial cable
$C_k$	Coupling capacitor
$d$	Distance
$E_c$	Breakdown strength of the cavity material
KCL	Kirchhoff's current law
$q_0$	Known charge
$i(t)$	Current pulse
MI	Measuring instrument
pC	Pico-coulombs
$Q$	Charge
$T_{ref}$	Reference time
$Z_{mi}$	Input impedance of measuring system
$R$	Resistor
$I_0$	Peak current
$\sigma$	Pulse width
V	Voltage
$V_a$	Applied voltage
$\epsilon_r$	Permittivity of dielectric
$\phi_i$	Phase angle

## CHAPTER 1

### INTRODUCTION

---

*This chapter gives the background of condition monitoring (CM) in power systems and various partial discharge (PD) measurement techniques, focusing on the Free-space radiometric (FSR) technique and a galvanic contact PD measurement technique based on (international electrotechnical commission) IEC 60270 standard. The motivation, research aims and objectives, key novelty and research contribution are presented. The thesis outline is also drawn in order to give the reader an overview of the work.*

---

## 1.1 Background

Condition monitoring (CM) in power systems and the progress of new CM systems have become one of the main significant topics for most energy companies since the beginning of 1990s. Energy companies have to find an approach to avoid sudden breakdown, minimize downtime, reduce maintenance cost, extend the period of equipment, enhance the reliability of operation and provide better service to customers and improve power supply [4]. Many electricity supply organizations around the world are facing growing energy demand and an ageing transmission and distribution infrastructure [2]. Furthermore, the health and safety operations needs of electrical apparatus in power systems are so significant that unexpected faults and shutdowns may result in an accident and a high penalty in lost output cost.

The cost of replacing infrastructure is high and as such careful management of the existing infrastructure is required to maximize its use whilst minimizing the risk of failures with consequent large costs [5]. To facilitate efficient and reliable operation continuous CM of the electrical machines within substations is necessary [2]. Predictive maintenance systems are capable of evaluating the condition of apparatus by executing continuous monitoring. This helps utility operators to execute maintenance only when required, making the maintenance activity more cost effective. However, this poses the risk of apparatus loss due to catastrophic failure. There are several general references [6-9] that are very useful, with information on CM of electrical equipment in power stations.

A major problem in high voltage (HV) power systems is degradation and breakdown of insulation. Statistics indicate that most HV equipment failures occur due to insulation breakdown [10]. Figure 1-1 shows the percentage of failures caused by insulation breakdown for a range of equipment categories [11-17]. Therefore, if partial discharge (PD) could be monitored continuously throughout the power system then, (i) a compromised item of power substations could be de-rated to avoid disastrous failure by rerouting network energy flows, (ii) planned maintenance could be replaced with

condition- or risk-based maintenance [18, 19], and (iii) replacement or de-rating of aging equipment in power station could be postponed until demonstrably necessary.

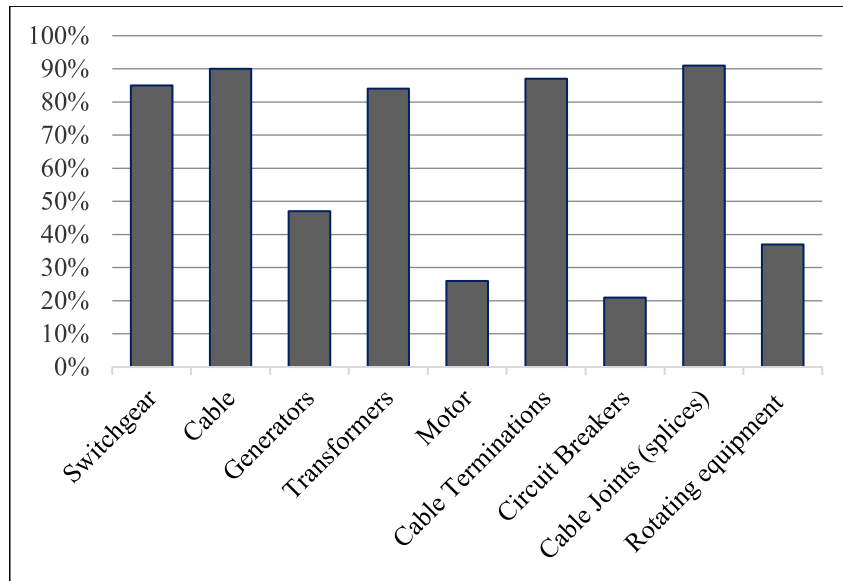


Figure 1-1 Proportion of failures due to insulation breakdown in different categories of HV plant. (Compiled from [11-17] ).

Partial discharge refers to a discharge that does not completely span the electrodes producing it. Figure1-2 illustrates the origin of PD in an insulator containing a void subjected to a high voltage. Since the void has lower electrical permittivity than the surrounding insulation ( $\epsilon_v < \epsilon_d$ ) the electric field strength within the void is greater than that in the surrounding insulation. Furthermore, the insulation strength of the void is less than that of the insulation. Both these factors mean that the electric field may exceed the breakdown value inside the void without exceeding the breakdown value in the insulation resulting in a discharge in the void but not in the surrounding dielectric. When such a discharge occurs, the electric field within the void collapses and so the discharge is extinguished. Assuming the potential difference across the electrodes persists, the electric field across the void then rises again initiating a subsequent discharge. Partial discharge is therefore characterized by a series of discrete current pulses. These current pulses propagate away from discharge in all (or both) directions. The duration of these current pulses for dielectrics typically used as insulation in power systems equipment is measured

on a timescale of nanoseconds to microseconds. Further, current pulses flowing in system impedance generates voltage pulse. The spectrum of PD can therefore extend into the Gigahertz region although most of the energy usually resides below a few hundred Megahertz [2, 20].

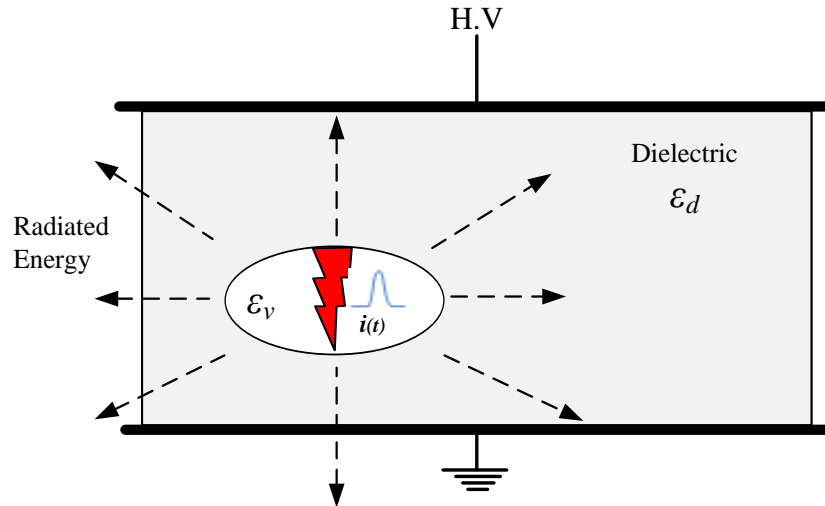


Figure 1-2 Origin of PD in an insulator.

Measurement of PD is a useful tool in the identification of incipient insulation faults. It allows the progress of insulation degradation to be monitored resulting in informed decisions about when intervention is necessary. Partial discharge measurement has already been used to diagnose substation insulation faults, and predict imminent equipment failure, with consequent reduction of system outage [21]. Partial discharge can be monitored using optical, chemical, acoustic or electrical methods [22-27]. High voltage substations in the UK for example, are usually surveyed for PD radiation every two years [28]. These surveys are carried out by trained engineers to detect PD source using a wideband 10MHz – 900MHz radio receiver. The engineer detects the occurrence of insulation faults by inferring signal intensity, using headphones or a received signal strength (RSS) indicator as the receiver frequency band and receive antenna position are varied.

Traditional electrical PD measurement methods have been developed for precise detection. Most of them are focused on wideband measurements. Common methods for PD detection include the electrical arrangements provided in the IEC 60270 standard [29], transient earth

voltage (TEV) sensors, high frequency current transformers (HFCT) sensors, ultra-high frequency (UHF) measurements [30], acoustic emission-based methods, and radiometric methods [31]. The former is usually used in an off-load test environment (often for acceptance testing of equipment) and the latter are usually used in an on-load (operational) environment. Galvanic contact measurement, performed in accordance with the (international electrotechnical commission) IEC 60270 standard, is generally accepted to provide the most accurate method of PD measurement and is often, therefore, used as a reference. The HFCTs and TEV sensors used to collect PD pulses [32-36] depend on coupling, near field inductive, surface-wave and therefore these methods involve the physical attachment of a sensor to a particular item of plant. The close coupling between the PD source and the wideband sensor (especially in the case of HFCTs) means that much of the information in, and character of, the PD signal is preserved; in particular, its apparent charge and signal spectrum. Valuable diagnostic content about the nature of the PD process resides in these characteristics. The energy spectrum, for example, can distinguish less damaging corona from more damaging internal PD due to insulation voids. The apparent charge, which is a measure of PD absolute intensity, can indicate the degree to which a PD process has advanced. This in turn may allow an early, incipient, insulation fault that does not require immediate attention to be distinguished from late-stage, severe, PD indicative of imminent plant failure. The measurement methods provided in acoustic measurements depend on the detection of the acoustic wave, which propagates inside the insulation each time a PD signal occurs. The UHF PD method has been applied in [30, 37, 38] to locate insulation defects in transformers. In terms of this technique, the sensor is situated inside the transformer tank. Ultra-high frequency methods have also been deployed as free-space radiometric (FSR), i.e. systems with external antennas to cover all the items in an electrical substation, which receive radiated energy from the PD origin. The radio frequency (RF) technique has achieved an over the past twenty years from its application the detection of discharge and discharge location finding in HV equipment especially in gas-insulated switchgear (GIS) [39-42] and more recently in power transformers [30, 43-45]. While not the most widely used technique sensing of PD for diagnosis, it is a well-established technique for diagnosing insulation defects. However, the presence of noise disturbances

when wireless PD measurements are executed represent a challenge due to the sensitivity loss, particularly when PD signals with low energy are present in the HV installation. An additional challenge of PD wireless measurements appears when more than one location of PD source signals is present in the measured electric substation [32]. In this state, the non-conventional method with appropriate sensors and the implementation of effective signal processing tools are necessary to improve assessment of the insulation condition. Automated RF detection and location of PD has recently become possible using a technology based on measurements of time-difference-of-arrival (TDOA) at spatially separated receivers. Moore, Portugues and Glover developed this technology in 2003. They [46] describe research conducted in conjunction with a company on smart grids and the Radio Communication Agency. They provided a novel non-contact method for the radiometric PD source detection. The apparatus uses a wideband sensor (an antenna) and reference voltage inputs, which are directly sampled. The characterization of the recorded impulses is preformed based on analysis of pulse count distributions and the pulse spectra. Results show that the PD produced by electrical insulation breakdown can be located by radiometry using a directly sampled antenna system.

Radiometric PD detection for insulation CM using a radio receive has been proposed as a particularly convenient technique for PD source location and monitoring, at least in part, because it requires no physical connection to the plant [28, 47, 48]. The lack of requirement for physical connection to power substations equipment is an important feature when applied to energized equipment. This does not only remove the need to take HV equipment out of service for installation of a monitoring system but it can also afford area coverage over hundreds of square metres from a single sensor. This sensor is also easier to reconfigure and install than the other systems. In addition, the measurements are executed during the operation of the HV system. An additional feature of free space radiometric (FSR) measurements is that PD activity can be gained under various load situations in permanent monitoring or temporal monitoring applications that is a suitable for the identification of certain kinds of faults and permits the analysis evolution of the faults over time [21]. The practical benefits of employing radiometric PD method for detecting PD in HV equipment have led to efforts being concentrated on the detection of electrical plants

using FSR methods. The development of monitoring FSR measurement methods has made it possible to execute CM more effectively on an electrical substation. It is predicted that FSR CM techniques will be made more cheaper and reliable, so that, they can be generally employed in smart grid [49].

The (more recent) FSR method of PD measurement uses an antenna to receive signals radiated by the transient PD pulses. The precise relationship between the FSR signal at the receive antenna terminals and the PD current pulse may be complicated. If the antenna employed is a broadband variation on an electric dipole, for example, the received RF signal might be expected to be proportional to the time derivative of the incident PD field [50]. The radiation process may also differentiate the PD signal, double differentiate the PD signal or process the signal in some intermediate way, depending on the balance of magnetic and electric coupling between guided and free-space waves. There is, in addition, the possibility of further spectral distortion due to the frequency response of the radio propagation channel.

In our currently research, PD is measured concurrently using FSR and a galvanic contact PD measurement techniques. Using this combined measurement techniques, PD events have been captured and recorded concurrently in terms of apparent charge and radiated energy. The utility of the galvanic contact technique is to calibrate the FSR measurement. The relationship between these two measures can yield significant information regarding the shape of the underlying PD pulse. It is suggested that it can be used to link FSR measurement PD data to absolute PD intensity. Traditionally, it has been the temporal evolution of FSR-derived data that has been used to flag PD of immediate engineering concern since the absolute PD intensity (in pC) has been thought impractical to assess. The successful study and analysis of PD intensity as a detection method for CM in electricity substation. The benefits to detect insulation faults and diagnose the severity (to void potentially catastrophic damage), in real-time in entire substation. In addition, if absolute PD measurements using FSR methods is shown to be possible, it could lead directly to more convenient and cheaper and continuous CM of HV insulation in electrical substation.

The classical galvanic contact method of monitoring PD activity uses a HV capacitor to decouple the test equipment from the HV supply. Figure 1-3 shows a PD measurement circuit that is specified in the IEC 60270 standard. This measurement does not comply rigorously with the IEC60270 standard but the configuration of the measurement is similar. It comprises a coupling capacitor  $C_k$ , a test object  $C_a$ , a coupling device  $CD$  with input impedance  $Z_{mi}$ , a coaxial cable  $CC$  and a measuring instrument  $MI$  [29].

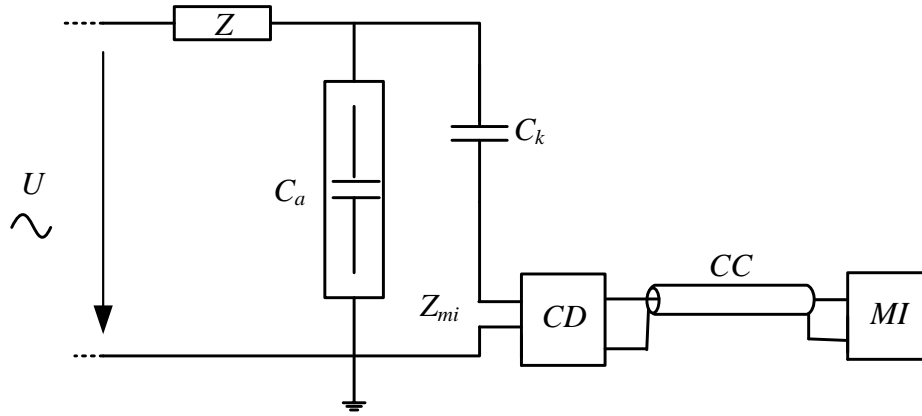


Figure 1-3 IEC 60270 PD measurement setup.

The circuit measures the PD current pulse flowing over the test object. When a discharge occurs, the voltage across the test object decreases momentarily due to the voltage drop across the HV source impedance ( $Z$  in Figure 1-3) and this is compensated by charge flowing into the test object from  $C_k$ . A current pulse  $i(t)$  with small time duration (typically nanoseconds) flows in the measurement circuit and a voltage pulse  $v_0(t)$  is created across the  $CD$  which is detected by the measuring instrument. The charge represented by the integral of  $i(t)$  is the apparent charge referred to above and typically of the order of picocoulombs. It is related to, but not exactly the same as, the charge transferred by the PD event inside the test object, [29].

The apparent charge is assessed using the galvanic contact measurement illustrated in Figure 1-4. A short-duration current pulse representing a known charge  $q_0$  is injected into the test object. The response of the measuring instrument can then be related to this known charge. The calibrator comprises a generator  $G$  generating step voltage pulses of amplitude

$V_0$  in series with a high accuracy capacitor  $C_0$ . If the voltage  $V_0$  is precisely known, repeatable pulses with a charge of  $Q_{cal} = V_0 \times C_0$  are injected into the test device [51].

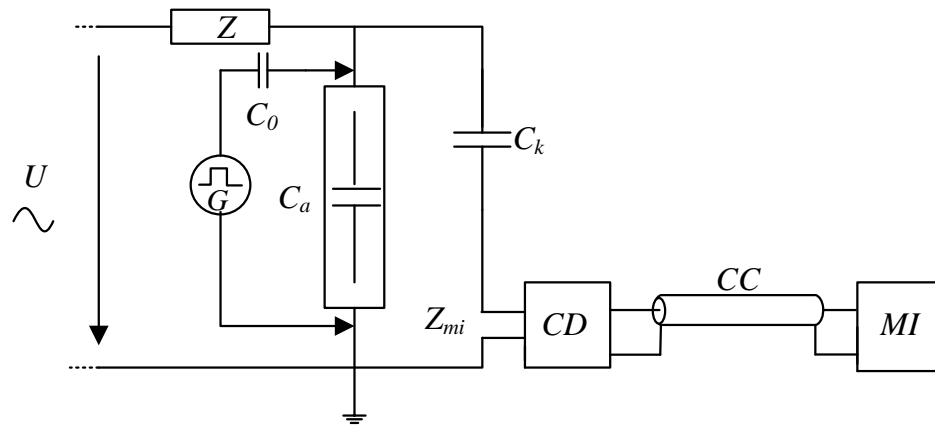


Figure 1-4 PD measurement calibration circuit.

The FSR measurement is illustrated in Figure 1-5. The antenna is a broadband biconical dipole and the digital sampling scope has an analogue measurement bandwidth of 4 GHz. A biconical antenna receives the RF energy radiated by the PD source.

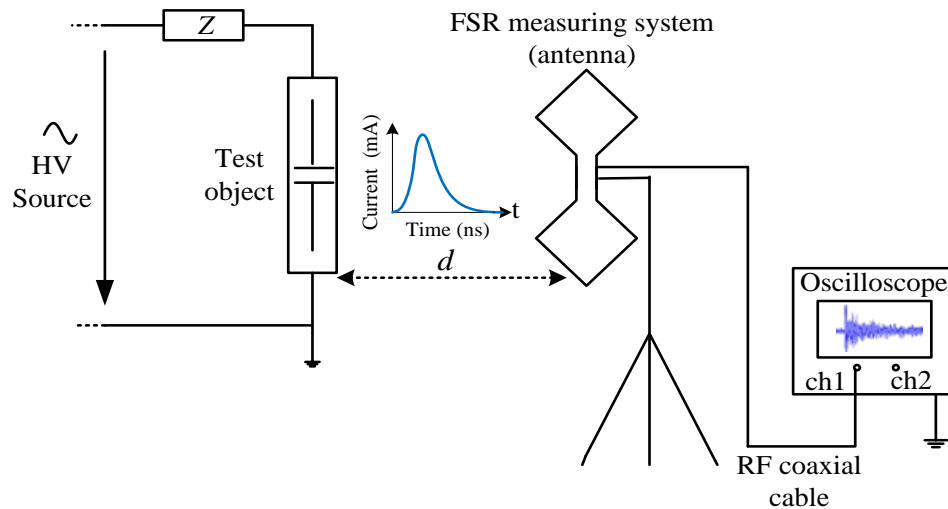


Figure 1-5 Free-space radiometric PD measurement and setup.

The PD sources used to compare the FSR and galvanic contact signals are a floating electrode emulator, an acrylic tube internal emulator without transformer oil filling, an

acrylic tube internal emulator filled with transformer oil, and an epoxy dielectric internal emulator. The measurements were carried out in a laboratory environment.

## 1.2 Motivation

Replacing ageing power systems is financially expensive and this motivates cost-effective asset management in order to maximize plant lifetime whilst minimizing the risk of failure with consequent large costs. To facilitate efficient and reliable operation, continuous CM of the electrical equipment within substations is required [2]. Measurement of PD activity can be used to diagnose substation insulation faults and predict catastrophic failure of HV equipment. The severity of PD is normally characterized by its intensity measured in picocoulombs (pC) of apparent charge. Such measurements can be made using galvanic contact and reactive near-field coupling techniques. Free-space radiometric measurements make absolute PD intensity difficult if not impossible. This is because the received signal amplitude depends on several factors, which are unknown to a greater or lesser extent and in at least one case might be argued to be practically unknowable. In order of increasing difficulty to establish, these unknown factors include: (i) the path loss between the radiating structure and the receiving antenna, (ii) the polarization of the radiated field in the direction of the receiving antenna, (iii) the gain of the radiating structure in the direction of the receiving antenna and (iv) the radiated power [2].

The primary motivation for this work is to challenge the assertion that FSR measurement cannot provide absolute PD intensity measurements. If absolute PD measurements using FSR methods is shown to be possible it could lead directly to more convenient and cheaper, continuous CM of HV insulation in electrical substation.

## 1.3 Objectives

The objectives of the thesis are (i) to address the calibration of PD emulators required for the development of a PD WSN such that absolute PD intensity (pC) might be inferred from radiometric measurements, and (ii) the investigation of the use radiometric measurements to estimate the absolute intensity of PD in HV insulation integrity monitoring applications.

## 1.4 Methodology

The methodology to achieve these objectives is as follows:

- (i) A literature survey of existing partial discharge measurement and partial discharge calibration schemes will be undertaken.
- (ii) A suitable measurement technology for the radiometric measurement of partial discharge will be selected and design and implement an experiment to measure partial discharge using the radiometric technique and the electrical galvanic contact method will be made.
- (iii) The relationship between a radiometric measured signal and a galvanic contact measured signal using a variety of partial discharge sources will be explored. The frequency spectrum of radiated PD signals with the spectrum measured using the electrical galvanic contact method will be compared. The author regards the latter as the measurement method most likely to preserve diagnostic information.
- (iv) A calibrate a classical partial discharge apparent charge measurement circuit will be designed and the calculation of apparent charge from a galvanic contact measurement will be demonstrate. The plausibility of estimate absolute PD activity level from a radiometric measurement by relating effective radiated power to partial discharge intensity will be established. If absolute PD measurements using FSR methods is shown to be possible, it could lead directly to more convenient and cheaper and continuous condition monitoring of HV insulation in electrical substation.
- (v) The simulation models which are used for the calibration of radiometric measurements will be validated by measuring the radiated fields, comparing them with the fields predicted from simulation. The validated simulations will be used to investigate the relationship between FSR PD measurements and absolute PD intensity.
- (vi) Partial discharge FSR and galvanic contact measurements activity under AC and DC applied voltages at different distances between a PD source and antenna will be investigated.

## 1.5 Novelty and Research Contribution

A novel method of estimating absolute partial discharge activity level from a radiometric measurement is proposed and (partially) demonstrated. Several aspects of PD emulator calibration have been advanced incrementally. A completely novel proposal of the estimation of absolute PD intensity from a radiometric measurement has been made. Such a measurement has been presented.

## 1.6 Thesis Structure

The thesis is divided into eight chapters as follows:

**Chapter 1** provides the background of the research. Motivation, research aims and objectives, novelty and research contribution, and the structure of the thesis are defined.

**Chapter 2** provides a general overview of the PD concept theory and describes the different types of definitions used for PD phenomena. A basic explanation starting with a background in electrical insulation that is essential for a suitable understanding of the causes that trigger PDs and a general description of the main types of PD and detection is provided. Relevant previous research work for the correlation between FSR and galvanic contact measurements, the calibration of PD sources and the effects of the UHF electromagnetic wave propagation of PD using CST software is presented. There is also a detailed explanation of the origin of EM radiation from PD events.

**Chapter 3** describes the experimental measurement systems and lists the main equipment and instruments that are used for PD measurement and PD calibration emulators. The structures and electrical circuit for the floating electrode PD emulator are explained. Two types of PD internal emulators (an acrylic tube internal PD source and epoxy dielectric internal PD emulator) are also described.

**Chapter 4** presents the measurement results of simultaneously using FSR technique and a galvanic contact technique based on the IEC 60270 standard. The frequency spectrum of radiated PD energy is compared with the spectrum measured using the electrical contact

method in order to establish the plausibility of estimating effective radiated power (ERP) as an alternative measure of absolute PD intensity to apparent charge. The PD sources used for the comparison are floating electrode PD emulator, an acrylic tube internal PD emulator, an acrylic tube internal PD emulator filled with transformer oil and epoxy dielectric internal PD emulator. An example of frequency domains energies and cumulative energies of the floating electrode PD emulator are also considered.

**Chapter 5** addresses the calibration of several types of PD emulators, which are specially constructed: a floating electrode PD emulator, an acrylic tube internal PD emulator, an acrylic tube internal PD emulator filled with transformer oil and epoxy dielectric internal PD emulator required for the development of a PD WSN. A method of estimating absolute PD activity level from a radiometric measurement by relating effective radiated power to PD intensity using a PD calibration device is presented.

**Chapter 6** presents the simulation of three models and measurement of FSR PD signals from real PD sources. The simulation results obtained from the CST Microwave Studio (CST MWS), which are validated by FSR PD measurements are also presented and analysed.

**Chapter 7** discusses the results obtained from PD measurement activity under AC and DC applied voltage at different distances between a floating-electrode PD emulator and a wideband receiving biconical antenna. In this chapter, it is also investigated how the relationship between FSR signal measurement and a galvanic contact signal measurement changes with changing the applied AC voltage and gap length between the floating inter-electrodes of PD emulator. The outdoors FSR PD measurement at different locations of the receiving antenna from PD emulator is measured.

**Chapter 8** summarises the main conclusions from the research activity and recommendations for future work.

## CHAPTER 2

### LITERATURE REVIEW

---

*A literature survey of existing PD measurement and PD calibration schemes will be undertaken in this chapter. It starts with the definition of PD and studies the theoretical aspects of the PD concept. Based on theory, it then describes the different types of definitions used for PD phenomena. It also describes three of the most prevalent types of PD (internal (treeing), surface and corona. Several common detection techniques (electromagnetic, UHF, acoustic and ultrasonic, optical, chemical, light and ultraviolet, and thermal) are presented. This chapter also reviews previous work on FSR and galvanic contact measurements and then offers comparisons between these two measurement techniques, the calibration of PD FSR technique and modelling of UHF PD radiation. Furthermore, the basic theory of electromagnetic pulses emitted by PD events is also described.*

---

## 2.1 Introduction

Designers in HV systems are aware of the problems related to PD for the HV equipment. When it comes to HV systems, PD monitoring is more economic. Identifying how PD can be detected and measured quickly and what measuring device to use have become an important task.

Electrical discharge signals are found in HV equipment and they are usually early signs of failure. Partial discharge is “*a localized electrical discharge that only partially bridges the insulation between conductors and which may occur adjacent to a conductor*” [29]. Therefore, continuous CM of the HV equipment in the power systems is essential in detecting the discharge before it grows into complete breakdown of insulation and causes unexpected power failure. Many types of CM system detect PD. Some of the CM systems require a section of the network under test to be isolated from the rest of the grid before testing can be performed. This is called the offline CM system and it is regularly used to perform condition assessment of equipment such as power transformers and underground cables. With the recent developments in sensing technology, CM systems that are able to continuously monitor PD for faults while the system is online in HV electricity substations are feasible. Once the monitoring system has been installed, information such as the PD activity and the location of the fault are determined. Several discharge kinds have their own discharge features, which can be used to identify them. The harmfulness of PD and time needed to cause a complete breakdown depend on discharge type.

## 2.2 Basic Concepts of Partial Discharge Test Circuit

Figure 2-1 (a) shows a gas-filled cavity between two electrodes on either side of a solid or liquid dielectric material [52]. Discharge ‘short circuits’  $C_c$  increasing capacitance. Supply voltage falls momentarily ( $V = Q/C$ ). Current pulse,  $i_c(t)$ , flows into  $C_b'$  and  $C_b''$  charging the additional capacitance and applied voltage returns to normal value. The electric field distribution within this test object is simulated by partial capacitance.  $C_c$  represents the electric field lines within the cavity,  $C_b'$  and  $C_b''$  within the solid dielectric [53].  $C_a = C_a' + C_a''$  represented the external field of the cavity. Due to the geometric dimensions and as

$C_b = C_{b'} \times C_{b''} / (C_{b'} + C_{b''})$ , the magnitude of the capacitance can satisfy the inequality [53]:

$$C_a > C_c > C_b$$

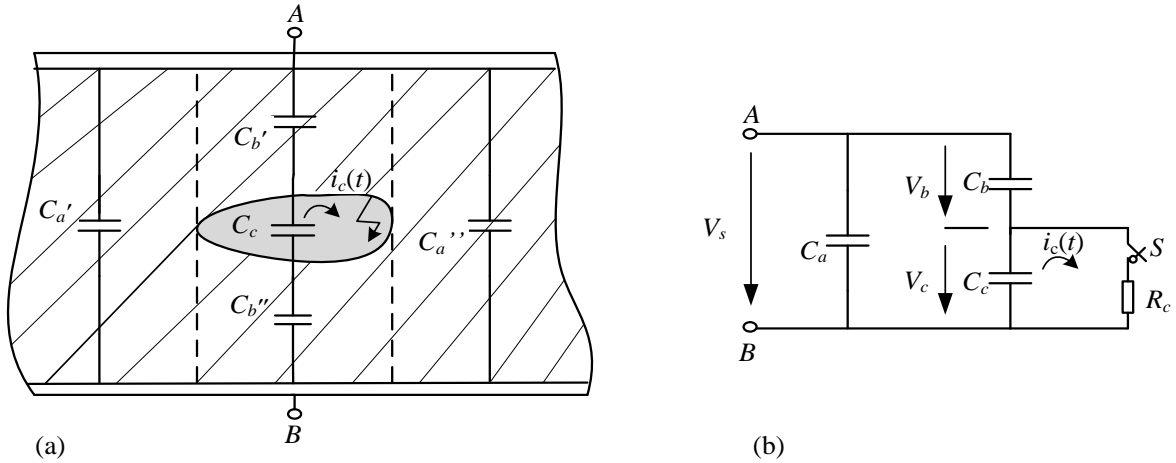


Figure 2-1 PD test object (a) Insulation cavity (b) Equivalent circuit.

When HV is applied, the void will cause PD. The field in the void is increased due to the shape of the cavity and the difference in permittivity. The equivalent test circuit is shown in Figure 2-1(b). Here, the voltage  $V_c$  is controlled by the switch  $S$  in parallel across the void capacitance  $C_c$ . The switch  $S$  is closed for a short time period, during that time current  $i_c(t)$  flows. This discharge current cannot be directly measured due to its short duration of a few nanoseconds. The test object in Figure 2-1(a) is connected to AC HV source. The detection circuits can be derived from a complete circuit as illustrated in Figure 2-2.  $C_k$  acts as a storage capacitor or a steady voltage source throughout PD duration [53].

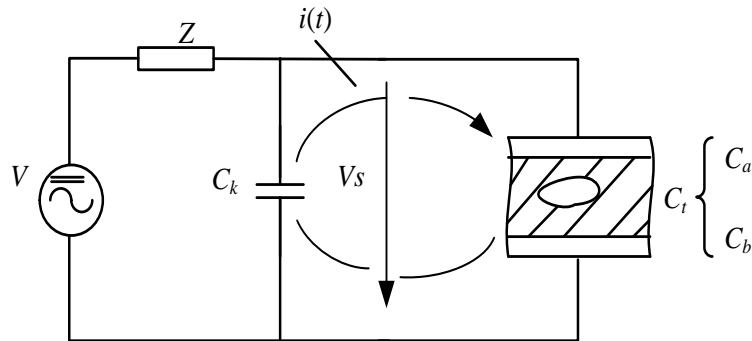


Figure 2-2 PD test circuit within test object.

The charging current  $i(t)$  between  $C_t$  and  $C_k$  and tries to stop the voltage drop  $\delta V_a$  across  $C_t$  where  $C_t \approx (C_a + C_b)$ . When  $C_t \ll C_k$ , then  $\delta V_a$  is compensated and the charge transfer providing by the current pulse  $i(t)$  is:

$$q = \int i(t) = \delta V_a (C_a + C_b) \quad (2-1)$$

therefore, if  $C_a \gg C_b$

$$q = C_b \delta V_c \quad (2-2)$$

Hence, it is referred to as the “apparent charge” that is the quantity measure of the PD. The apparent charge word was presented because this charge is unequal to the quantity of charge locally flowing across cavity  $C_c$ . This amount of PD is actual than  $\delta V_a$  in equation 2-2, as the  $C_a$  has no effect on it.

- **The recurrence of discharge (discharge sequence)**

In the Figure 2-1,  $C_c$  corresponds to the cavity,  $C_b$  corresponds to the capacitance of the dielectric, and  $C_a$  is the capacitance of the rest of the dielectric. If the cavity is filled with gas, the field strength across  $C_c$  is:

$$E_c = \varepsilon_r E_a \quad (2-3)$$

where  $\varepsilon_r$  is relative permittivity of dielectric.

In practice, the shape of a cavity is often approximately spherical in a material, and the internal field strength for these cases is [53, 54]:

$$E_c = \frac{3\varepsilon_r E}{\varepsilon_{rc} + 2\varepsilon_r} = \frac{3E}{2} \quad (2-4)$$

Here, under an applied voltage  $V_a$ , the average stress in the dielectric is  $E$ . When  $V_c$  reaches breakdown  $V^+$  in the gap, discharge occurs. Figure 2-3 shown the structure of breakdown for a sinusoidal voltage. The voltage, which appears across the cavity, if it does not break down, is shown as dashed curve. As voltage  $V_c$  reaches  $V^+$ , a discharge occurs and  $V_c$  is

collapses. The  $V$  across the cavity then rises once more until it reaches  $V^+$  and a new discharge takes place. Therefore, numerous discharges may occur. When the applied  $V$  is reduced, the cavity is discharged as the voltage across cavity will reaches  $V^-$ .

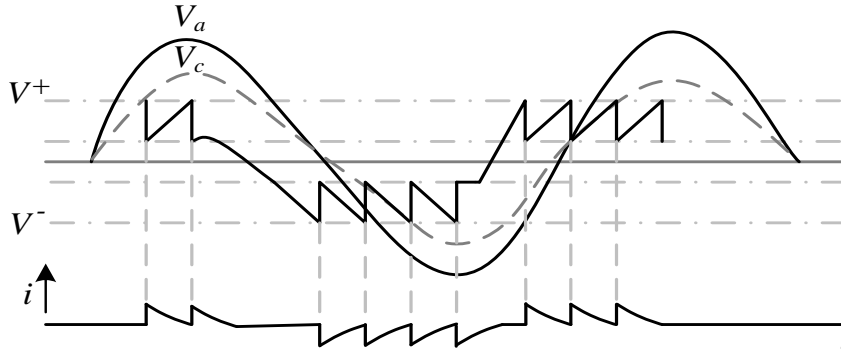


Figure 2-3 Cavity breakdown sequence under alternating voltage.

- **Partial discharge currents**

The difficulty in measuring PD currents is described in [53]. If  $V$  is AC, the currents flowing within branches  $C_t$  and  $C_k$  as shown in Figure 2-4 are approximately in phase.  $i(t)$  could be similar in both branches, if there is no stray capacitance parallel to  $C_k$ , with differing polarity. A shunt resistor with coaxial cable matched is presented for accurate measurements in the circuit below in Figure 2-4 [54].

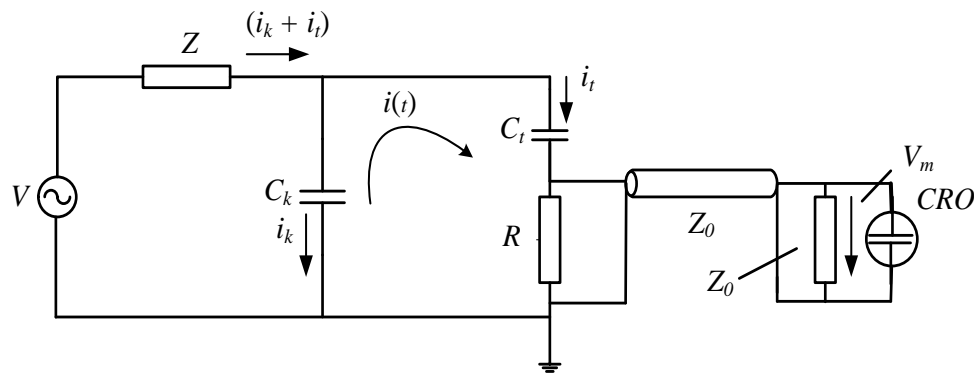


Figure 2-4 Low sensitivity measurement of PD current circuit.

The input voltage across the measuring device (oscilloscope) is given by:

$$V_m(t) = \frac{(i_t + i_k)Z_0R}{(R + Z_0)} \quad (2-5)$$

The measuring data has some effect on current pulse shapes. This can be summarized by the following statements [53]:

- PD current pulses created in voids within liquids and solids are short, less than a few nanoseconds in duration.
- In air, the current discharge pulses are less than 100 nanoseconds in duration. Longer current pulses for PD in solid materials or fluids without pronounced voids have been measured [53].
- **Various PD quantities**

In any test object for PD under a given condition could be considered by measurement quantity like integrated quantities, charge and repetition rate [53, 55, 56].

- Apparent charge

The apparent charge of a PD is that injected charge into terminals of the test object will change the voltage between the terminals by the same quantity as the PD. It is expressed in pC. The apparent charge is unequal to the quantity of charge locally [57].

- Repetition rate

Repetition rate is the average of PD pulse numbers per second measured over a certain time. Only pulses within an identified range of magnitudes or above a specified magnitude can be considered in practice.

- PD inception voltage

The lowest voltage, which results in detected PD as voltage rise from zero.

- PD extinction voltage

The lowest voltage at which PD is observed when the voltage is steadily reduced from a higher voltage to a lower voltage.

- PD test voltage

An identified voltage provided in a test process below which the test object must not exhibit PDs exceeding a specified magnitude.

- Average current discharge

The summation of the absolute values of the apparent charges  $q_i$  in a reference time  $T_{ref}$ , divided by this time interval:

$$I = \frac{1}{T_{ref}} (|q_{i1}| + |q_{i2}| + \dots + |q_i|) \quad (2-6)$$

- Discharge power

Discharge power is the average PD power. It can be calculated from apparent charges and voltage using:

$$P = \frac{1}{T_{ref}} (q_1 u_1 + q_2 u_2 + \dots + q_i u_i) \quad (2-7)$$

where the instantaneous voltage is  $u$ ,

- PD phase angle

Phase angle  $\phi_i$  and time  $t_i$  is the incidence of a PD pulse is:

$$\phi_i = 360^\circ \left( \frac{t_i}{T} \right) \quad (2-8)$$

where the period of the test voltage is  $T$ .

### 2.3 Partial Discharge Types

There are different types of definitions used for PD phenomena in [58, 59]. Partial discharge is classified into three types in this thesis: internal discharges, surface discharges and corona. Damaging PD depends on the discharge type and location. Several discharge kinds can be recognised because they all have their own features. Internal discharges

deteriorated insulation directly and consequently are very damaging. The last stage of internal discharge is electrical treeing which causes dielectric breakdown and has the highest influence on insulation deterioration. Surface discharges are generated by dirt and moisture. Surface tracking is also very damaging which lead to erosion of the insulation surface and defect of insulation over time [60]. Corona discharges are not damaging in cables [61].

### 2.3.1 Internal discharges

This type of discharge occurs inside the insulation (cavities), near insulation interfaces as shown in Figure 2-5. Inside a cavity, the strength of the electric field is determined by the shape and size of the cavity, gas content of the cavity, voltage across the insulation and the difference between the dielectric around the cavity and the permittivity of the gas inside the cavity. In a cavity, when an electrical breakdown takes place the voltage strain in the cavity surpasses the breakdown voltage. The pressure and composition of gas inside a cavity, static charges from the previous discharges and the cavity wall conditions, which all have impact on breakdown voltage level in the cavity. Furthermore, the strength of the gas breakdown is generally less than solid insulation. This is why PD occurs in cavities with less voltage than the breakdown voltage of the concrete insulation. This fact also clarifies the random nature of PDs. Internal discharges might also ignite contaminants, e.g. small metal particles. [61, 62].

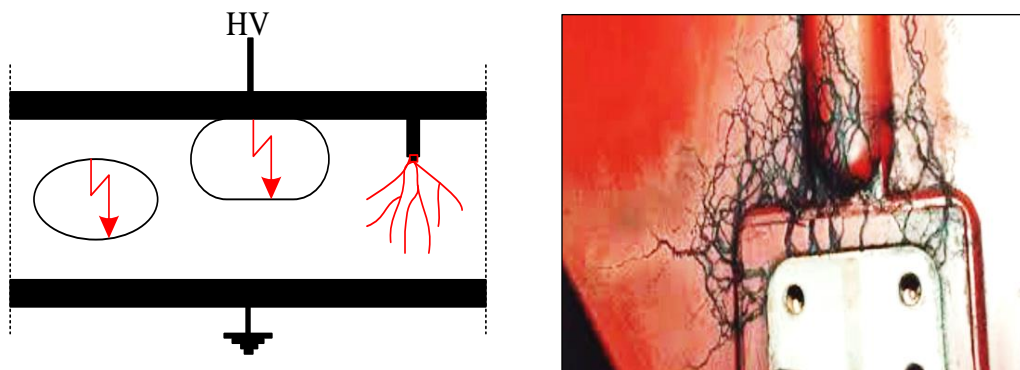


Figure 2-5 Internal discharge (void, metal discharge and treeing) of PD [63].

- **Electrical treeing**

Electrical trees are a special internal discharge type, which are formed inside the insulation, and occur one-step prior to a catastrophic breakdown of the insulation. As the name suggests, during electrical treeing, tree-like structures are formed inside the insulation, produced by the multiple micro-scale internal discharges [52]. Electrical trees can be described in three phases. These are, tree initiation, where degradation leads to the formation of the first channel, tree growth, where the channels extend, and finally, breakdown occurs when the channels have bridged the electrodes [61, 64, 65].

There are two basic figures of the electrical trees, branch and bush-like form which depends on the HV stress. If the mean HV is  $< 5$  kV/mm, then a branch-like tree shape will be formed. Whereas, when the voltage stress is  $> 5$  kV/mm, bush-like will typically be shaped. The transition among branch and bush-like trees is not sharp. In addition, the pattern starts off as bush-like and then changes to branch-like when the voltages are medium [65, 66]. Figures 2-6 (a) and (b) presented two examples of electrical trees.

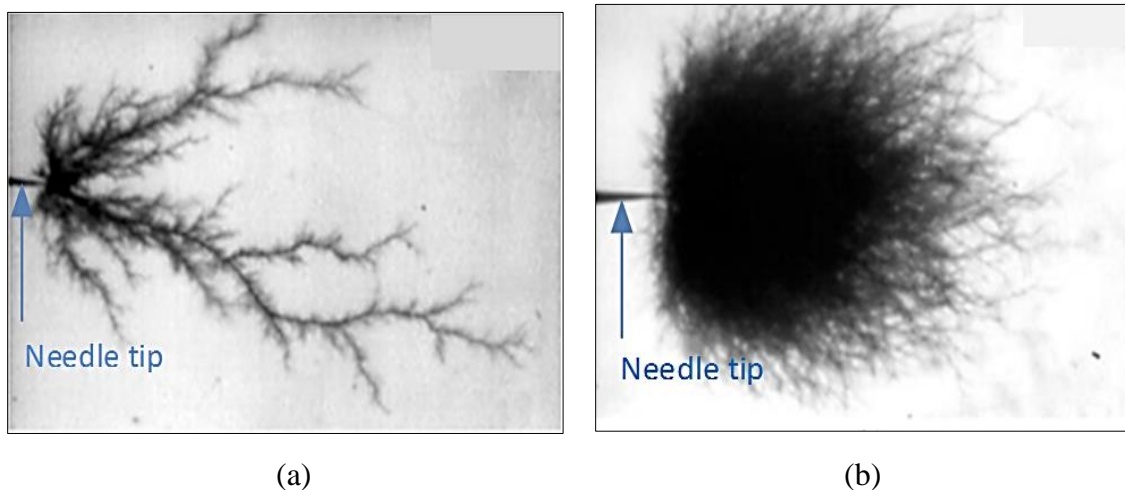


Figure 2-6 Electrical trees of PD [47, 48] (a) Branch-like electrical tree (b) Bush-like electrical tree.

Generally, it evolves from no discharge to catastrophic flashover in a few hours [61, 65, 66]. Transient overvoltages are high magnitude voltages peaks with fast rising edges, short-duration, commonly referred to as surges from a lightning strike. Lightning strikes are the

most common source of extreme transient overvoltages. If a voltage surge from a lightning strike, has sufficient energy; the electrical tree growth during the insulation may cause breakdown.

### 2.3.2 Surface discharges

Surface discharges occur between two dielectric materials or along the surface of dielectric material. This type of discharge may occur as shown in Figure 2-7 in places where external layers of the material are corrupted. It generates surface tracking where carbonized conductive tracks are shaped. Strong electric fields are produced at irregular pathways where some PD occurs in the area. Surface contamination and moisture generate a leakage current to the earth. This leakage generates heat due to ohmic loss that evaporates the moisture, leading to the generation of small voids. Most of the voltage drops across these voids, which may result in an arcing. PD in a form of arcing burns the insulation producing permanent carbonized paths [65, 67]. When the moisture has been completely evaporated, the gaps between carbonised paths may then be-come the source of new PD.

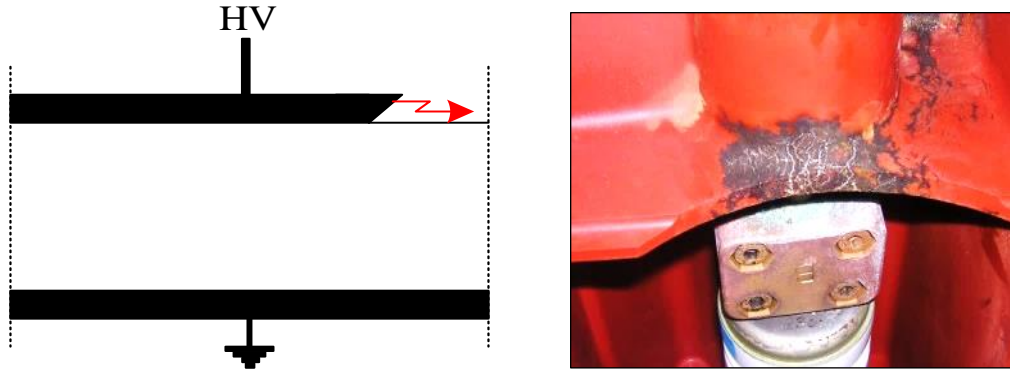


Figure 2-7 Surface discharge of PD [63].

### 2.3.3 Corona discharges

Corona discharges occur around sharp edges in the interface between metal and air as shown in Figure 2-8. There are different types of corona discharges, however they are not presented in this thesis. This type of discharges generates ozone that could be damaging to the insulator materials due to the chemical reactions that originate in insulators. The current

signals produced by the corona may be similar in some characteristics to those from other type of PDs and thus they confuse measurement interpretation [68]. Corona discharges have some other characteristics that can be used to distinguish them from discharges occurring in solid dielectrics [65]. This type of discharges typically occur near the positive and/or negative voltage [61].

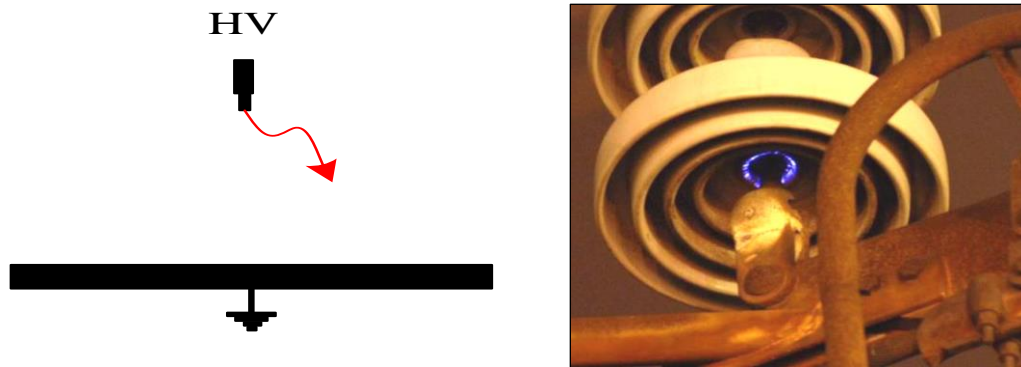


Figure 2-8 Corona discharge [69].

## 2.4 Partial Discharge Detection

The history of PD detection is generally considered to stretch as far back as the eighteenth century to a publication by the experimental physicist, astronomer and mathematician Georg Christoph Lichtenberg who discovered what are now called ‘Lichtenberg figures’ in 1777 [70]. An example of such a pattern is shown in Figure 2-9. These are radial patterns, formed when a sharp electrode at a high potential is placed near an insulating surface.

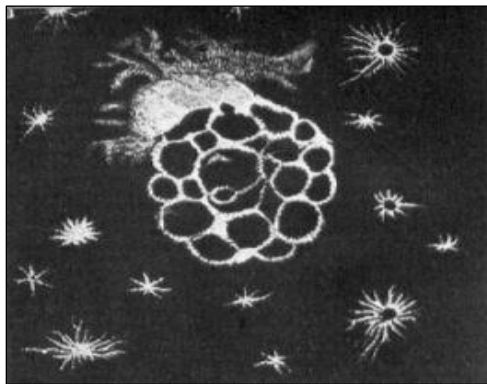


Figure 2-9 Lichtenberg’s dust figures [70].

Most of the insulation degradation in HV electrical equipment is caused by PD [10]. Much work has been done to find reliable PD detection techniques, understand PD mechanisms and locate PD sources. The reliability of HV equipment depends on their insulation condition. The insulation condition of electrical equipment can be monitored and analysed using PD detection systems. Partial discharge activities can generate electrical pulses and other effects such as chemical reactions in insulating materials, acoustic waves and electromagnetic waves. Specific types of PD detection methods can detect these signals. Recently, unconventional techniques have been developed for the detection of PD in HV equipment. Several methods, for example, physical detection techniques (including electromagnetic, optical, UHF, acoustic and ultrasonic, light and ultraviolet, and thermal) and chemical phenomena (gas ionization) have been introduced for the localization and the detection of PD sources in HV equipment in electrical power substations. Two of the most common methods in use are electromagnetic and acoustic PD detection [71]. These techniques do not conform to the IEC 60270 standard because they have different PD quantities from apparent charges as set out in IEC 60270 standard. A variety of unconventional PD detection methods are explained in the following sections. These sections review the PD detection techniques for power equipment in HV systems. Although all the techniques can be used to detect insulation defects, some have practical advantages over others. Several methods are used for the detection and localization of PD as presented in Figure 2-10.

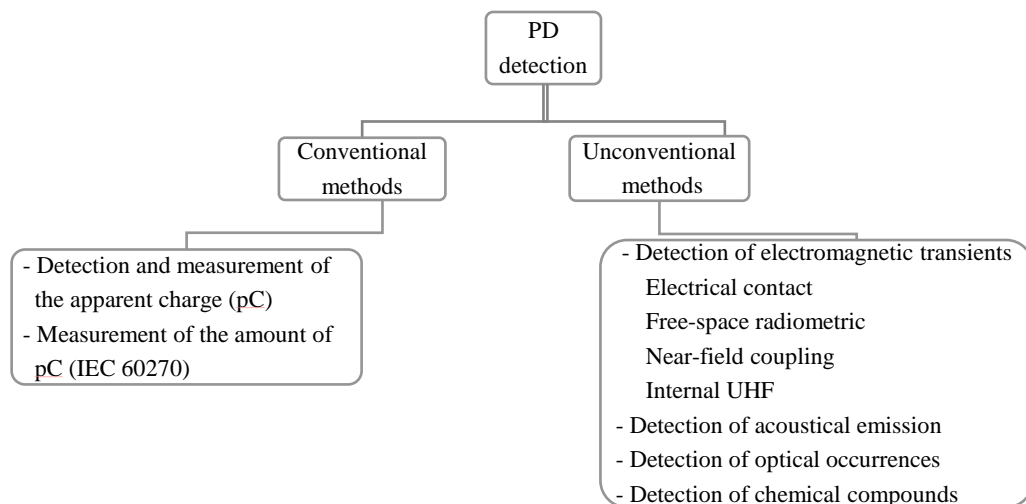


Figure 2-10 PD detection methods.

### 2.4.1 Electromagnetic methods

The electromagnetic measurements are classified into four types, traditional detection, direct probing measurement based on standard IEC60270, free-space radiometric methods, High Frequency Current Transformer (HFCT) sensor and Transient Earth Voltage (TEV) sensor. The direct probing technique requires a coupling capacitor to be connected to the circuit and to the test object. The measurement is made by using a sensor that acts as an antenna in the area of the test objects. The HFCT sensors are usually used to measure PD in power cables and in a remotely connected HV plant. The TEV sensor is a capacitive probe designed to detect local, HF PD pulses in cables, switchgear, transformers, machine cable boxes, and other plant. These techniques create online PD electrical detection and provide real time monitoring of electrical HV equipment; however, it they have disadvantages and the main one is susceptibility to noise. On HV electrical substation environment, there are high levels of noise, broadband and narrowband. In some stages, due to the short PD pulse duration, it is difficult to distinguish between PD and noise. This issue is the main challenges to detect PD online techniques. Offline testing equipment can be used in electrical substations in order to eradicate the noise with as a consequence large costs per day in loss of income for the electrical company [72].

#### 2.4.1.1 Electrical methods - according to the IEC60270

There are many guidelines, which can be followed to design reliable PD detection systems. For example, the IEC60270 [56] standard sets out the test methodologies required for measuring the apparent charge released during a PD pulse. This particular guideline gives the designer with the definitions and descriptions related to the instrumentation requirements, ranging from measurement circuits, calibration methods and test procedures.

To this day, PD detection systems operate based on the measurement of the apparent charge as a fundamentally PD quantity. Note that the term apparent is used here to refer to the accumulated charge as this metric does not refer to the local charge present at the site of discharge, but rather the quantity of charge that if injected at the terminals of a particular test object, could yield the same reading in both measurement system [57]. The standard

approach to measuring the PD is based on the detection of a current pulse at the terminals of the test object. Figure 1-3 presents a typical circuit used for the measurement of PD, as defined in the IEC60270. As shown, the test object can be a simple dielectric specimen to a HV apparatus being imposed to a PD test. In this research work, the test object of interest is a floating electrode PD emulator, an acrylic tube internal PD emulator and an epoxy dielectric internal PD emulator that will generate the required PD.

#### 2.4.1.2 Free-space radiometric methods

The nature of PD pulse short (nanosecond) duration signals results in RF components comprised of radiated electromagnetic energy from conductors leading away from the site or from the discharge site directly. This generates a radiometric detection method at distances used suitable broadband radio receiver [31]. The PD radiometric method of utilizing a sensor (antenna) to capture RF signal is shown in Figure 1-5. Free-space radiometric measurement is particularly convenient technique for PD source location and monitoring, at least in part because it requires no physical connection to plant. An additional advantage is that positioning information is available by using remotely located antennas to receive the RF signal radiated by the transient PD pulses at various locations. This information determines the PD source and the severity of insulation defects. A description of radiometric detection is specified by Moore, Portugues and Glover in [46]. They confirmed that radiometric methods have been successfully deployed in detecting and locating PD in gas-insulated switchgear (GIS). FSR techniques require a time domain measuring apparatus, i.e. digital oscilloscope, to capture the radiated PD signal. The PD is then determined using several processing techniques. These techniques attractive because they provide real time monitoring of the HV system possible.

#### 2.4.1.3 High frequency current transformer methods

HFCT are called inductive sensors. The HFCT methods have a wide frequency response between 50 MHz – 100 MHz with high sensitivity. It is typically made of a toroid or a coil. They couple the magnetic component of the field. Therefore, the rate of change of the current change passing through the coil is proportional to the voltage that is induced in the

coil. The magnetic coupling relies on the number of turns, the magnetic field strength, frequency, and distance to the test object. The sensor coil can have a ferrite core that can provide more sensitivity, however it is no longer linear that is unwanted from the calibration point of view.

#### 2.4.1.4 Transient earth voltage methods (TEV)

The TEV sensor is a small RF antenna, which can detect the HF PD pulses, which propagate from a local discharge within the HV equipment such as bushings and switchgear etc. The TEV sensors are magnetically fixed on the outside of the HV apparatus in the plant. In this way, they work as an external capacitive coupler to detect PD pulses on the outer surface of the switchgear. Hence, the TEV is sometimes referred to as the capacitive coupler [73]. The frequency response of the TEV sensors is usually between 4 MHz - 100 MHz [74].

#### 2.4.2 Ultra-high frequency PD methods

One of the online PD detection methods in HV systems is the ultra-high frequency (UHF) detection technique. Electromagnetic signals have different frequency spectra depending on the type of the PD source and medium of the surrounding defects [75, 76]. For example, protrusion defects can generate PD pulses with a very fast rise time, up to  $\sim 0.9$  ns in oil. The fastest rise time for bad contact defects measured by [77] was  $\sim 17$  ns. These PD pulses have frequency spectra in the range of 30 MHz – 300 MHz and 300 MHz – 3 GHz [78]. This is known as the UHF frequency range. Thus, this method of detection of PD signals is known as the UHF PD detection method [22, 38, 76]. Figure 2-11 illustrates the diagram of the UHF PD detection method. The essential device to detect the PD signal is an antenna that acts as a sensor that picks up electromagnetic signals emitted by the PD sources. The sensor is connected to a measurement unit to show and record the PD signals. In cases where the PD signal is too small, an amplifier can be installed between the sensor and the measurement unit. Using an amplifier that has a specific operational frequency, the PD signals can be magnified whilst blocking interference signals. In the UHF range, interference mainly broadcasting comes from known sources of communication such as

mobile phones or digital TV signals. Thus using a specific amplifier that eliminates the interference frequencies, the measurement unit can display and record clear PD signal. The PD signals can be recorded in two different modes of measurement, i.e. time domain and frequency domain.

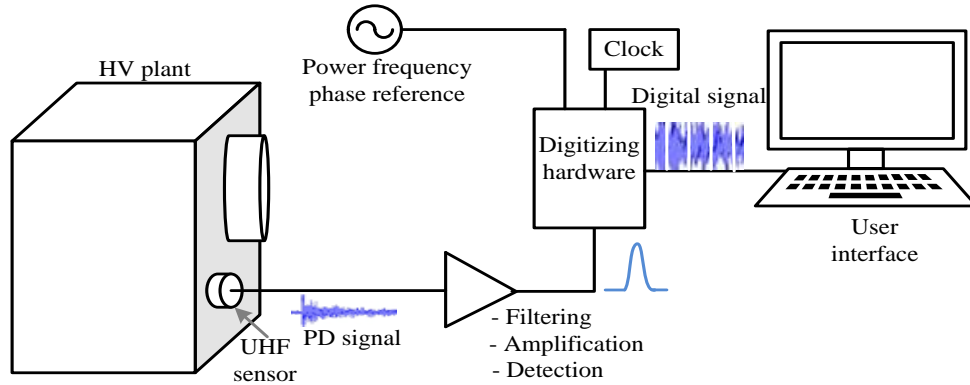


Figure 2-11 Typical UHF PD monitoring system.

### 2.4.3 Acoustic and ultrasonic methods

Acoustic and Airborne ultrasonic sensors are an alternative for online PD detection in power equipment in a substation. The sensors should be located in a safe way for the detection the acoustic emission of PD [79]. Sound-resonance sensors and condenser microphones can typically detect mechanical vibration of acoustic signals from PD using a frequency band of 10 kHz - 300 kHz. Fiber optic acoustic sensors, accelerometers, piezoelectric transducers and airborne acoustics can be used as part of an on-line monitoring method and contact acoustic sensors. These methods have been effectively used to localise the PD [77]. The main issue with this method is the complicated nature of the acoustic propagation pathways. An additional problem with these methods is the sensitivity required. Typically, due various attenuation mechanisms, the received acoustic signal intensity is low. In order to detect a PD, the sensors should be responsive to small changes in the amplitude of the signal [72, 80].

#### 2.4.4 Optical methods

Optical sensors can detect the optical emission from a PD source. Different factors depend on optical signals such as PD intensity, temperature, pressure and insulation material. Two types of optical PD detection methods with different types of recombination processes, excitation and ionization through the discharge: detect changes of an optical beam and direct detection of optical PD signal. Oliveira, et al. [81] presented an overhead transmission line (OHTL) of PD optical detection that uses sensors in the fiber with light emitting diodes (LEDs). The essential features of using this technique are high sensitivity compared to conventional methods especially for on-site measurement and immunity from electromagnetic interferences [77]. However, optical PD sensing methods depend on the medium within which the PD is expected to occur. The insulation medium is also required to be optically transparent. As most solid dielectrics are not transparent, the optical PD method is appropriate to gas insulators and liquid [82]. Furthermore, in comparison with the conventional measuring, the optical detection of PD cannot be calibrated [83].

#### 2.4.5 Chemical methods

It is also possible to detect PD signals through the monitoring of the chemical changes in the composition of the insulating materials in HV equipment, e.g. in the materials used in transformers and gas-insulated switchgear (GIS). Often, the chemical detection of PDs involves the utilisation of dissolve gas analysis (DGA) and/or high performance liquid chromatography (HPLC) methods [84]. During the DGA procedure, the oil samples from the tank of an oil-cooled transformer [85] or an insulation material from the GIS is taken and analysed, in order to quantify the composition levels of different gases. In case of a transformer, the HPLC test provides a measurement for by-products of insulation breakdown. A common drawback related to DGA and HPLC tests is suffering from uncertainty issues, which is due to lack of a known standard relation among the amount of glucose that is discharged through the breakdown of insulation, and the type and severity level of the HV transformer defect condition. Furthermore, this method is not capable of locating the source, which can be disadvantageous in certain applications.

Chemical detection can also be used in other critical HV equipment. For example in GIS, sulfur hexafluoride (SF<sub>6</sub>) insulated used as an insulating gas, is a chemically stable molecule under normal operations but chemical reactions associated with SF<sub>6</sub> may take place if the temperature of the equipment exceeds 200°C (arcing or PD conditions) [86]. Moreover, other components (e.g. air, moisture and metallic) may be found. The sensitivity of a detector is dependent on an extent of any gases gathered and the proximity of the detector to the PD site.

The limitations of chemical testing are that these methods do not provide any information about the location of the PD and/or insulation damage. The chemical technique cannot be used for online monitoring [27]. An interesting development in this field is currently being conducted by adding certain chemical tags to specific portions of the insulation. These tags are released in the oil when the insulation breaks down and can be detected. The problem with this method is that it has a fair amount of uncertainty regarding the severity of the PD activity, also that this method does not provide instantaneous information about the state of the component being evaluated [87].

#### **2.4.6 Light and ultraviolet**

It is possible to detect the light created by the corona during a PD event and/or surface PDs, which can allow a direct inference to be made between the detected light and the physical condition of the insulation. The light created during a PD event is in the ultraviolet (UV) spectrum. In the presence of solar UV light (i.e. in sunshine), it is incredibly difficult to detect any PDs with the naked eye. However, there is equipment such as daylight corona cameras, which are fitted with special filters to prevent background solar UV from interfering with the electrical UV of interest; thus, PD detection in the daylight is now a possible practice. The particular PD detection technique is mainly suitable for outdoor power systems, e.g. distribution and transmission lines. Surface PD detection is of particular interest in switchgear applications, as described in [88].

### **2.4.7 Thermal methods**

Partial discharge is often accompanied by hot spots due to dielectric breakdown, inadequate cooling and abnormally high current densities. When an electrode is subjected to high currents, thermal runaway occurs as a result of ohmic heating (caused by ohmic losses), which is an accelerated-ageing factor. For proper implementation of thermal PD detection methods, temperature measurements are usually taken indirectly. A common way to detect the presence of hot spots is through the measurement of the load current and the oil temperature of the device. Other thermal methods include the use of thermal imaging cameras. However, this method has its own limitations, as the heat generated by a PD is relatively low and the thermal impedances likely to be encountered on the path between the camera and the PD can significantly affect the quality of the measurement. Thermal imaging cameras are occasionally used to detect PD events on overhead power lines [82].

## **2.5 Comparison of Methods**

Comparison components that are used between PD detection techniques are reported in section 2.4. The comparison presented that the electromagnetic detection address many of the acoustic and ultrasonic, optical, chemical, light and ultraviolet and thermal methods and as well specified that FSR and galvanic contact measurement based on the IEC 60270 standard are more appropriate to compare the FSR measurements with galvanic contact measurements. Table 2-1 illustrates the main features between detection methods.

Free space radiometric is chosen, as it is a particularly convenient technique for PD detection. The advantage of FSR detection over other methods is reported in section 1.1 which positioning information is available by using remotely located antennas to receive the RF signal radiated by the transient PD pulses at multiple positions. This location information can help to determine the PD source and the severity of dielectric defects. The galvanic contact measurement based on the IEC 60270 standard is chosen to calculate the absolute PD intensity.

Table 2-1 Comparative table including the main features between detection methods.

	Electrical	RF / UHF /EMI	Acoustic and Ultrasonic	Optical	Chemical	Light and Ultraviolet	Thermal Methods
<b>Description</b>	<ul style="list-style-type: none"> <li>• Electrical circuit that picks up current pulse produced by charge transfer during PD.</li> </ul>	<ul style="list-style-type: none"> <li>• Measures radio frequency interference and/or electromagnetic wave generated by partial discharge.</li> </ul>	<ul style="list-style-type: none"> <li>• Measures the acoustic emissions produced by a PD.</li> </ul>	<ul style="list-style-type: none"> <li>• Measures light emission from PDs.</li> </ul>	<ul style="list-style-type: none"> <li>• Chemical changes in the composition of insulating materials.</li> </ul>	<ul style="list-style-type: none"> <li>• Light and ultraviolet detected by using daylight corona cameras.</li> </ul>	<ul style="list-style-type: none"> <li>• Thermal is caused by high ohmic losses, which produce heat, leading to accelerated ageing.</li> </ul>
<b>Advantage</b>	<ul style="list-style-type: none"> <li>• Good sensitivity and standard for all HVEquipment.</li> <li>• High precision measurements.</li> <li>• Very low signal attenuation.</li> </ul>	<ul style="list-style-type: none"> <li>• Non-contact, applicable for all voltage types.</li> <li>• Allows testing of equipment in real conditions.</li> <li>• Locate of PD is possible using sensors at multiple location.</li> <li>• PD can be calibrated.</li> </ul>	<ul style="list-style-type: none"> <li>• Non-contact, applicable for all voltage types.</li> <li>• Allows testing of equipment of real conditions.</li> <li>• Location information of PD is possible using sensors at multiple positions.</li> </ul>	<ul style="list-style-type: none"> <li>• Non-contact, applicable for all voltage types.</li> <li>• Immunity from electromagnetic interference.</li> </ul>	<ul style="list-style-type: none"> <li>• Very well established, immune against noises and relatively easy to measure.</li> <li>• Good recording of PD signals in the laboratory environment.</li> <li>• High sensitivity.</li> </ul>	<ul style="list-style-type: none"> <li>• Ideal for outdoor power system, distribution lines and transmission lines.</li> </ul>	<ul style="list-style-type: none"> <li>• PD activity on overhead lines or exposed busbars,</li> </ul>
<b>Disadvantage</b>	<ul style="list-style-type: none"> <li>• Sensitive to electrical noise.</li> <li>• Very difficult to apply on site.</li> <li>• Cannot test circuit in operating condition in most cases.</li> <li>• Influenced by electromagnetic interference.</li> </ul>	<ul style="list-style-type: none"> <li>• Depending on equipment being tested, EM emissions can prevent detection of PD.</li> <li>• Interference of signals by environmental noise.</li> </ul>	<ul style="list-style-type: none"> <li>• Sensitive to other acoustic emissions.</li> <li>• Signals cannot always propagate through insulation.</li> <li>• Interference of signals by environmental noise.</li> </ul>	<ul style="list-style-type: none"> <li>• Insensitive to any form of internal PD.</li> <li>• Needs to be optically transparent.</li> <li>• Sensitive to light and highly directional.</li> <li>• optical detection of PD cannot be calibrated</li> </ul>	<ul style="list-style-type: none"> <li>• Location and intensity of PD.</li> <li>• Not provide any information about the position or extent of the PD and/or insulation damage.</li> <li>• Level of dissolved gas has no correlation with the specific type of fault.</li> <li>• Creates uncertainty</li> </ul>	<ul style="list-style-type: none"> <li>• Quantify PD.</li> </ul>	<ul style="list-style-type: none"> <li>• Quantify PD.</li> </ul>
<b>Possible sensors</b>	<ul style="list-style-type: none"> <li>• Capacitive.</li> <li>• Inductive.</li> </ul>	<ul style="list-style-type: none"> <li>• RF sensors.</li> <li>• Antennas.</li> <li>• FSR (wide area detection of RFI)</li> <li>• HFCT (cables).</li> <li>•TEV (local items, e.g. switchgear).</li> <li>• UHF sensors.</li> </ul>	<ul style="list-style-type: none"> <li>• Acoustic sensor</li> <li>• Ultrasonic/RF</li> <li>• Ultrasonic free space LOS sensor</li> <li>• Ultrasonic fixed sensor</li> <li>• Fiber optic acoustic sensors</li> <li>• piezoelectric sensors</li> <li>• Airborne acoustic sensor</li> </ul>	<ul style="list-style-type: none"> <li>• Fiber optical UVsensors.</li> </ul>	<ul style="list-style-type: none"> <li>• DGA and/or HPLC.</li> </ul>	<ul style="list-style-type: none"> <li>• UV/visible imager.</li> </ul>	<ul style="list-style-type: none"> <li>• Thermal imaging camera.</li> </ul>
<b>Main application area</b>	<ul style="list-style-type: none"> <li>• All high voltage equipment.</li> </ul>	<ul style="list-style-type: none"> <li>• All high voltage equipment.</li> </ul>	<ul style="list-style-type: none"> <li>• Switchgear.</li> <li>• Power transformer.</li> </ul>	<ul style="list-style-type: none"> <li>• Power transformer.</li> <li>• GIS and cable</li> </ul>	<ul style="list-style-type: none"> <li>• Power transformers.</li> <li>• GIS (SF6 – insulated).</li> </ul>	<ul style="list-style-type: none"> <li>• Transmission lines and distribution lines (corona type).</li> </ul>	<ul style="list-style-type: none"> <li>• Cable. terminations and switchgear.</li> </ul>

## 2.6 Previous Work

Free-space radiometric and galvanic contact methods are quite different; they may be expected to have significantly different responses to the same PD event. Furthermore, whilst the FSR methods can provide information about the location of PD it cannot easily quantify apparent charge. The galvanic contact measurement technique gives information about apparent charge and may also provide information about the nature of an insulation fault based on the measured PD spectrum [2, 89]. The main focus of this chapter is to evaluate previous work in FSR and galvanic contact measurements techniques, the calibration of PD FSR measurement, and the modeling of UHF PD radiation.

Paoletti and Golubev [90] presented the theory of PD phenomena, furthermore, various measurements and implementation of methods that have been evolved CM PD in HV power systems. The authors concluded that the on-line PD detection would eventually become widespread, in addition to the currently applied surveys on wireless PD detection in HV equipment of power system. However, this technique provided excellent diagnostic results.

Moore, Portugues, and Glover, [46] conducted a research, which linked the smart grid company and Radio Communications Agency for the radiometry PD sources detection through a new non-contact method. The results indicated that PDs caused by electrical dielectric breakdown could be detected PD radiometry by utilising a direct sampled antenna system.

Judd et al., [89] reported that FSR measurement techniques can provide information about the location of PD, it cannot however easily quantify the apparent charge. The galvanic contact measurement technique provides information about apparent charge and may provide information about the nature of an insulation defect based on the measured PD spectrum.

Calibration capabilities of PD measurements are compared in [91] by using electrical and electromagnetic methods. The results specify that measured apparent charge provide an

indication of the actual charge of the PD source. Additionally, the authors indicate that the calibration of the UHF FSR method is not available yet, but possible, which can be done by characterization of the UHF FSR sensor using its antenna factor.

### 2.6.1 Free-space radiometric measurements system

Moore, Portugues, and Glover, [31] proposed a radiometric PD locating system use in the power substation. Preliminary results of the locator approach indicate that PD sources can localise within a few metres if the distance to the receiving antenna is less than 15m. Judd et al., [92] reported on early trials of a non-contact RF PD detection method, which has possibility use within fast switching HVDC test systems. Initial results found that remote monitoring capable of detecting and locating PD. Radiometric monitoring techniques and some research challenges, which are important for many researchers who are doing PD measurements using radiometric PD detection and locating PD, are described in [37]. Moore, Portugues and Glover, [93] demonstrated the internal PD remote detection of a HV transformer. The initial results indicate that a wideband RF receiving sensor placed approximately 10 m to 15 m from the transformer has identified the PD source, which has radiated from transformer defect. Though limited in its detection ability, the measurement technique permits low cost, and a simple and non-invasive assessment of potential insulation defects in HV equipment. Alistair, et al., [94] suggested using FSR techniques for detecting PD in HV power system which have led to important effort being concentrated in the detection of power system using FSR methods. The authors concluded that the main challenges facing FSR detection is the RF radiations interferences to measure of the severity of the PD. Portugues, Moore, and Glover, [48] use a new noninvasive method and monitor continuously based on this principle for PD monitoring of power substions. The benefit of this technique is to detect PD sources in HV equipment during normal operating condition. The results indicated that the system will be capable of locating the site of radiation in an electrical substation. It is suggested in [83] that PD sources might be detected and located using amplitude-only FSR signal. The preliminary results reported were mixed; one set of measurements suggesting greater location accuracy is possible than another set. A possible explanation, however, for the disparate location

accuracies was that one dataset may have been adversely affected by a conducting wire mesh embedded in the floor, walls and ceiling of the HV laboratory where those measurements were made. Moore, Portugues, and Glover, [95] described a method for detecting PD on overhead lines using a vehicle based RF measuring equipment. A directly sampled four antenna array measurement is made. The authors reported that this technique is suitable for estimating the faulty region and determine more accurately to the radiating component. Furthermore, they mentioned that, this remote detection is cheaper in comparison to the traditional helicopter survey method. Moore, Portugues, and Glover, [96] investigated the emission of RF emissions from HV system sources, including arcs fault, defective insulation and switchgear operations. The results indicated that spectral analysis shows that for air discharges, most of the energy is concentrated below 150 MHz. While oil and SF<sub>6</sub> discharges have a spectrum up to 800 MHz. De Souza Neto, et al., [28] suggested a self-calibrating WSN of radiometers designed to locate PD emission as a low cost method for real-time CM in the HV system. Some early progress PD WSN in the development for initially prototype is also presented. The initial results indicate that a low cost PD WSN method of the suggested type might be a significant method to locate PD source in the HV electricity substations. Zhang, et al., [97] progressed on the development of an insulation defect detection and location system using a PD WSN. De Souza Neto, et al. [98] described progress in the achievement of a PD WSN prototype. For the suggested evaluation of PD signals, numerous measurements were performed by utilising a discone wideband aerial and a commercial system based on the IEC 60270 standard. The authors concluded the suggested technique of PD detection in [98] is feasible and can be executed based on radiometric measurements. Zhang, et al., [49] reported that locating and monitoring PD in high-voltage electricity substations can be achieved by a WSN, using only the received signal strength (RSS). Given this, a plausible solution to monitor insulation integrity in electricity substations is an RSS-based PD WSN. De Souza Neto, et al., [99] proposed some early progress on PD WSN detection as a low cost alternative method for CM of real-time in HV electrical substations. The initial results indicated that a PD radiometric network of the suggested type might be achieved in the HV electrical substations with a sufficient sensor to localise PD sources. In [97] the UHF FSR location

of PD sources using a WSN is suggested for CM of HV equipment in a power system, and an ultra-wideband (UWB) printed monopole antenna is suggested for the WSN nodes.

### 2.6.2 Galvanic contact measurements system

The IEC 60270 standard [55] describes the test and measuring circuits used for PD contact measurement. It also specifies approaches for calibration. Furthermore, it provides guidance on test events and quantifies pC related to PD pulses. Lemke, [100] reviewed the existing classical capacitive PD models. It was concluded that (i) the classical model is incapable of reflecting the physics of discharges in gas-filled cavities of HV apparatus, (ii) the charge witch was caused by electrodes of the artificial PD source is the result of a dipole moment, (iii) the apparent charge is an induced charge, which is correlated with the PD severity. Boggs, and Stone, [101] compared the theoretical sensitivity of conventional PD detectors with that obtained from the UWB detection method. The result of the comparison indicates that for loss free distributed systems; the UWB system is more sensitive. Carter in [102] used radio interference voltage (RIV) methods as the standard test the PD transformer measurement . RIV methods can be used as charge indicators by making appropriate charge calibrations on the transformer under test. The results suggest that, for a given design type, RIV techniques may become less sensitive to PD severity as transformer size increases. The results also show that RIV instruments can be used with charge calibration procedures to provide a uniform measure of transformer quality. Chen, and Czaszejko, [103] investigated PD test contact circuit using small insulation samples in the laboratory. The experimental results indicated strong information conveyed in PD pulse, which reflected the properties of the electric contact circuit in which the pulse is shaped, rather than the nature of the discharge source. Judd, [104] analysed the pulses caused by contact discharges. The results showed that the pulse generator is not capable of producing repeatable pulses at high repetition rates, but it provides a robust method for creating 100ps pulses of variable amplitude. Wang, et al., [105] described an electrical contact measurements technique for detecting PD in transformers. The authors concluded that, it could be easily executed by contact measurements technique for detection and location of PD in HV transformers. Li, et al., [106], described contact measurement results

of PD under DC conditions. The results showed that discharge pulses have different shapes depending on the DC voltage and most of the energy discharge is situated below 100 MHz.

### **2.6.3 Comparison between free-space radiometric and galvanic contact measurements system**

Partial discharge measurements are compared in [107] using galvanic contact, HFCT, and FSR measurements. The results show that the HFCT measurement indicates less PD energy and, therefore, lower absolute PD intensity, than the classical galvanic measurement. FSR measurements are difficult to calibrate but qualitative agreement was found in [107], between this and the HFCT measurements indicating that FSR methods may be useful in applications where absolute calibration is not necessary. Reid, et al., [108], PD is measured concurrently using RF energy and a contact measurement method based on the IEC 60270 standard. The authors concluded that the integrated measurement technique have the capability to distinguish among discharges occurring concurrently for each of the respective samples. Cleary and Judd, [109] studied PD sources activity under 50 Hz AC HV in mineral oil, using the radiated electromagnetic energy measurement and they investigated the relationship with current signals. The authors specify that UHF signals be radiated by a diversity of dielectric defects in oil-insulated equipment. Reid, et al., [110], PD radiated energy and IEC 60270 measured apparent charge were simultaneously recorded. The results suggest that the frequency distribution of RF energy could prove useful as a means of defect identification. Kumar, et al., [111], presents numerous methods in PD measurement as a CM tool for online monitoring of HV equipment. They also present new methods used for PD analysis along with their advantages and suitability over conventional technique for appropriate condition monitoring of HV equipment. The results show that not all the approaches could detect the moisture and degradation in the oil. They also suggested that a combination of PD detection techniques is a powerful diagnostic tool. “Judd et al., [89], proposed a new integrated approach to PD monitoring using the combined and simultaneous application of UHF and IEC60270 measurements. Initial results of the combined approach show that it may be possible to differentiate between different sources of PD using apparent charge and UHF signal energy. Zhang, et al., [112],

investigated the correlation between RF measurements and the apparent charge of PD. The results show a linear association between the amplitude of the RF signal and apparent charge in a positive half cycle. Ohtsuka et al., [113], investigated the association between apparent charge and FSR signals using measurements and a Finite-difference time-domain (FDTD) simulation. It is suggested that the PD charge quantity can be corrected by using the FSR method. Reid et al., [110] calculated the energy spectrum of the RF signal, and showed that the apparent charge together with the frequency distribution of the RF signal can prove useful as an identifier of PD and a means of defect characterization. Reid et al., [114], presented phase resolved patterns of RF signals. The results showed defect detection is possible if the system is trained using both RF and contact measurement data. Reid et al., [47], recorded PD using contact and RF methods. The results indicate that the relationship between the methods creates characteristic patterns specific to defect types. Xiao, et al., [115], used RF and IEC time-domain analysis measurements to investigate the insulation integrity for six types of defects. The results were inconclusive in respect of distinguishing differing defects using time-domain analysis, but frequency-domain analysis revealed information relating to the resonances of the radiating structure, which might provide useful defect discrimination. Sarathi et al., [116], analysed UHF FSR signals caused by the movement of conducting particles subject to a HV in transformer oil. The magnitude of the UHF signal generated by a DC voltage was higher than that generated by an AC voltage. It was concluded that it was possible to classify an incipient discharge from either an AC or a DC routine substation pressure test. Sarathi et al., [117] made conventional FSR measurements of PD in gas insulated switchgear and concluded that signal bandwidth is independent of applied voltage and operating pressure” [2]. Stewart, et al., [118] display sample voids in resin that frequency content of the radiated RF signals can be used for concurrent RF and contact measurements in specifying PD generated under electrical stress. The results presented that single and multiple of the voids of various dimensions appear to generate several radiated RF frequencies bands.

#### 2.6.4 Calibration of partial discharge measurements

A calibration technique was reported in [119], to obtain the quantity of apparent discharge from the measured PD spectrum in the frequency domain. This technique is based on the calculated time domain PD current pulse signal the measured PD spectrum. Since a calibration pulse is not required with this process, it can be applied in online PD testing. The setup of a standard calibrator for measuring PD and estimating uncertainty in the measurement is described in [120]. The results showed that the standard PD calibrator increases the reliability of PD measurement and can be used as a basis for the estimation of PD uncertain. A new calibration technique was proposed in [121], for PD measurements using capacitive couplers. The results showed that an individual capacitive coupler can be precisely calibrated on-site, that it provides information about the apparent discharge values. Cavallini et al., [122], focus on the limits of PD apparent charge estimation and calibration using a unified approach. Their results indicated that applying the calibrator pulse to the terminals of the equipment induced a response which was dissimilar from a PD pulse, and leads to large errors. The correlation between UHF FSR measurement and apparent discharge was investigated in [123] by using experiment of measurement and theory analysis. The initial results showed that the optimal of the regression curve is energy of UHF FSR signal relative to square apparent discharge quantity. The applied variation of voltage was found to have no effect on the regression curve between UHF signal and square of apparent discharge quantity. Prochazka, et al., [124], deal with an impulse charge measurement in the range of pC. The resultant charge, which is generated by the calibrator, is then evaluated as numerical integration of impulse current using a digital scope. The results indicate that differences in the results can be caused by an integration error of the digital scope. It is shown that in the case of a 14-bit digitizer application and numerical calculation, better accuracy can be reached in comparison to an 8-bit digital scope. Coenen, et al., [125] deal with the PD detection UHF FSR method for calibration and verification of the sensitivity. The results indicate several conclusions: (i) UHF FSR signals multipath propagation attenuation while propagating via the active part of the internal structure of the power transformer, (ii) for propagation path, for example a fixed PD location, there is a linear correlation between the apparent charge and UHF FSR amplitude, (iii) the sensitivity

check showed that the UHF FSR method has a sensitivity of more than 100 pC, (iv) it appears unable to quantify the pC intensity of UHF FSR PD measurement on the basis of a sensitivity check according to the IEC60270 standard. Sellars, et al., [126], presented a method for simulating PD in GIS equipment. The method uses a pulse generator to inject current pulses through a suitable protrusion. Using this technique, it has been possible to investigate the relationship among the discharge event and the UHF electromagnetic signal detected by a receiving coupler. The results show that the technique has been developed to simulate a discharge event in a GIS by injecting a known current pulse into a suitable protrusion using a pulse generator. The investigation also has shown that the magnitude of the coupler signal is linearly proportional to the magnitude of the discharge pulse. Hoshino, et al., [127], investigated how the above sensitivity changes according to the radiated location of the defects inside GIS and the way of injecting the artificial pulses. Furthermore, they proposed sensitivity verification integrated with real time PD identification technique. The results indicated that the sensitivity with the UHF technique based on the apparent charge with the IEC 60 270 is different between defects. The UHF method is sensitive to the free particle on enclosure while the IEC 60 270 is unable to detect it.

### **2.6.5 Modeling of UHF PD radiation**

Partial discharge detection is measured and compared in [128] using paper resin and epoxy resin using simulation. The results showed that the epoxy resins have less strength than paper insulating material. In addition, the authors indicated that the strength of the paper resin and insulating material weakens after a long period of time. Paper resin has a high resist to stress, which could be used to reduce the maintenance cost of transformers. Rahman, et al., [129] progress on the development of a PD transformer model simulating signal propagation inside a transformer is reported. The simulation results show good agreement compared with real measurement data and therefore the transformer model can provide accurate results. Soomro, and Baharom, [130], presented a comparison between PD in paper insulation and impregnated paper in transformer by simulating a simplified model of a transformer employing CST MWS software. The simulation analysis results

specify that the paper insulating material have less sustainability and high strength to resist the electrical stresses compared to impregnated paper insulation. The propagation of PD EM wave in a distribution transformer is simulated using Finite Difference Time Domain (FDTD) technique and CST software [131]. The validation results found from FDTD technique are compared with simulation result obtained from CST software. The results indicate that for both FDTD and CST show good agreement. Karami, et al., [132], suggested a new methodology to detect a PD source in a transformer. In the suggested method, a power transformer is simulated using CST software in three-dimensions. The PD source with/without transformer oil permittivity is localized using a TDOA technique. The results indicate that the estimated PD position is better when considering transformer oil permittivity. The characteristics and radiation patterns of these travelling waves are discussed in [133]. The radiation patterns, which are created from PD signals and the high frequency PD propagation, are simulated using CST Microwave Studio. The results specify that using these simulations, they are able to demonstrate that there is a potential of detecting PD at HF spectrum even when the monitoring plant is far away from the PD source. Sinaga, et al., [134], investigated five different UHF sensors: monopole and conical; bowtie, spiral and log spiral sensors to detect PDs. They used CST software to simulate and obtain the sensor responses over the frequency range. The results showed that the conical sensor was the best choice for insertion via transformer oil drain valve and the log spiral for insertion via GIS dielectric. Man, et al., [135], presented the simulation PD in a model of switchgear and used CST software to simulate and study the relationship of transient earth voltage signal, PD pulse frequency, amplitude and transient earth voltage distribution on the switchgear surface. The simulation results show that the pulse width of transient earth voltage increases as the pulse width of PD pulse increases and the amplitude of transient earth voltage is proportional to the PD pulse amplitude. Mirzaei, et al., [136], investigated the effects of the UHF EM waves propagation in transformers using CST software. The results illustrated that the receiving antenna polarisation and PD current polarisation have a significant effect on the detected PD EM waves. Zheng, et al., [137] simulated the electromagnetic radiation spectrum from PD switchgear using the finite

element method. The simulation results indicated that location of PD in switchgear could be detected.

## 2.7 Partial Discharge Radiation

During the early 1980's, a significant amount of attention was paid to EM methods for the detection, discharge diagnostics and locations of PD [42, 138-140]. Recently, PD detection systems based on the radio frequency (RF) techniques has emerged; although, uptake has been poor, due, at least in part, to their inability to quantify the PD event. This is, partly, because the RF method captures the rate-of-change of the PD current pulse rather than its integral, which makes it difficult to quantify the absolute intensity of the PD in pC. The first RF-based PD monitoring system was developed by Westinghouse, over 40 years ago, in order to detect the presence of arcing sub-conductors in the stator windings of a large turbine generator [48]. Over the last ten years, several insightful publications have been published, proving the RF technology as a successful technique for remote detection of PD-related insulation defects [141-143].

Electromagnetic radiation is generated by a PD event. The FSR, location of PD sources using a WSN is there suggested for CM of HV equipment in substations.

In the event of any discharge electrons, initially at rest, are accelerated and decelerated. The acceleration and deceleration produce a time-varying electromagnetic field, which radiates outward from the PD location. The cause of radiation and the subsequent process are discussed below, drawing on Froula et al., 2010 as well as Longren and Savov, 2005 [144, 145]. A stationary charge has only electric field, which is radiated radially. As the charge is in motion, electric field and magnetic field are produced. The electric field at any point near the moving charge with a speed  $v$  in the  $u_r$  direction as shown in Figure 2-12, is [144]:

$$E = \frac{Q}{4\pi\epsilon_0} \frac{1}{r^2 + x^2} u_r \quad (2-9)$$

or

$$E = \frac{Q}{4\pi\epsilon_0} \frac{1}{R^2} u_r \quad (2-10)$$

where  $R^2 = r^2 + x^2$ ,  $x$  is displacement and  $r$  is the distance of the charge to the observer after moving a distance  $x$ .

The magnetic field caused by this moving particle can be calculated by using the Biot-Savart law, i.e.:

$$B = \frac{\mu_0}{4\pi} \frac{Q(v \times u_r)}{r^2 + x^2} \quad (2-11)$$

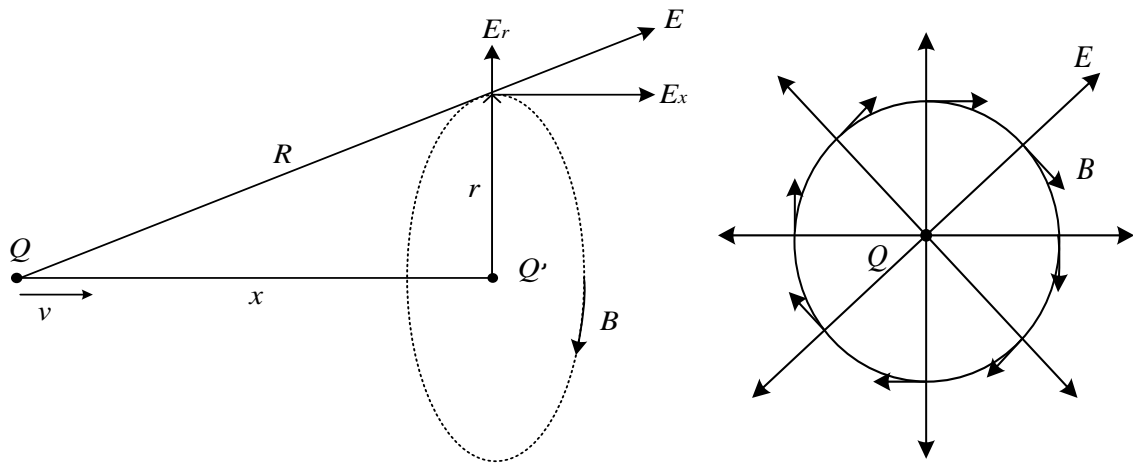


Figure 2-12 Electric and magnetic fields of a moving charge particle  $Q$ .

Assume the charge  $Q$  at point  $A$  is initially at rest then accelerated in the  $x$  direction as shown in Figure 2-13 to reach point  $B$  after which it moves with constant velocity  $v$  until it reaches point  $C$  ( $v \ll$  speed of light) [145]. The time needed during the acceleration process is  $\Delta t$  seconds. The electric field lines at any point in the  $x$  direction in the path of the moving charge are radial and must be continuous since they are produced by the same charge.

During the acceleration of the charge, the electric field lines are always updating its position. However, due to the time needed by the electric field lines to adjust, the lines will have disrupted the direction or become misaligned. This line disruption is known as a 'kink' [145]. The kinks, as shown in Figure 2-13, have both a static (Coulomb) field

component and a dynamic (transverse) field component that are perpendicular to each other. The transverse electric field causes radiation. Maximum radiation occurs along the line perpendicular to the direction of the acceleration. The radiation at point  $M$  where maximum radiation occurs is represented in Figure 2-14 as a pulse. In the direction of acceleration there is no transverse electric field component, only a static Coulomb field, thus no radiation occurs.

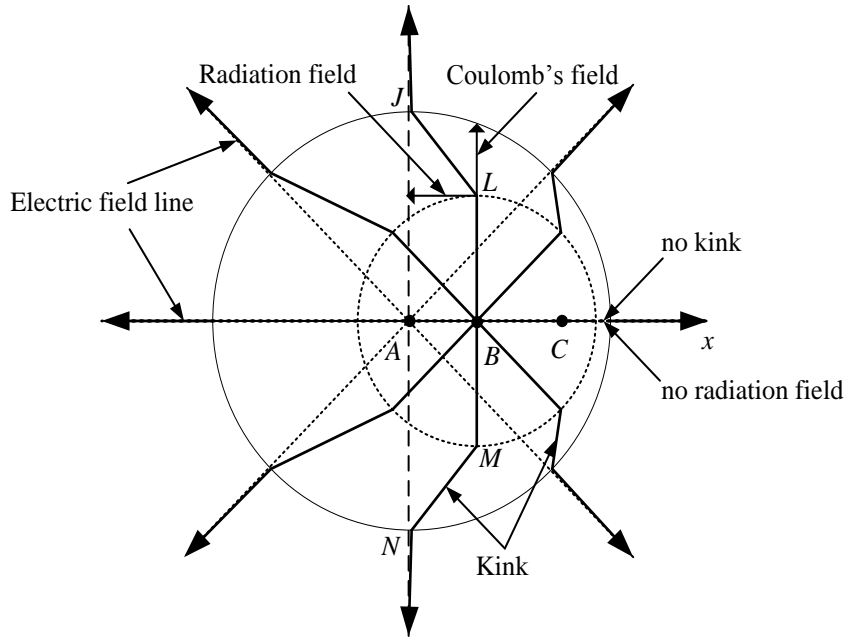


Figure 2-13 Radiation during the acceleration of charge.

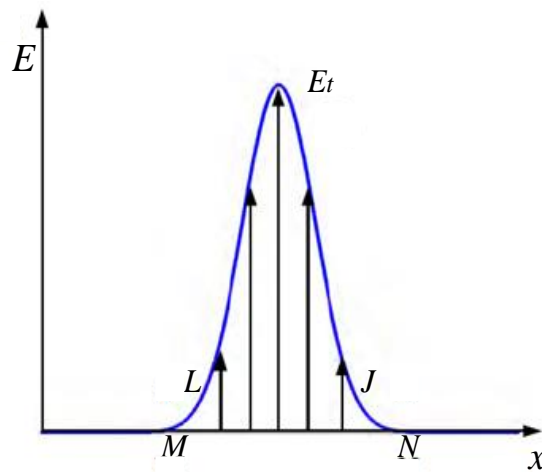


Figure 2-14 Pulse shape of the radiation at point  $M - N$  and  $L - J$ .

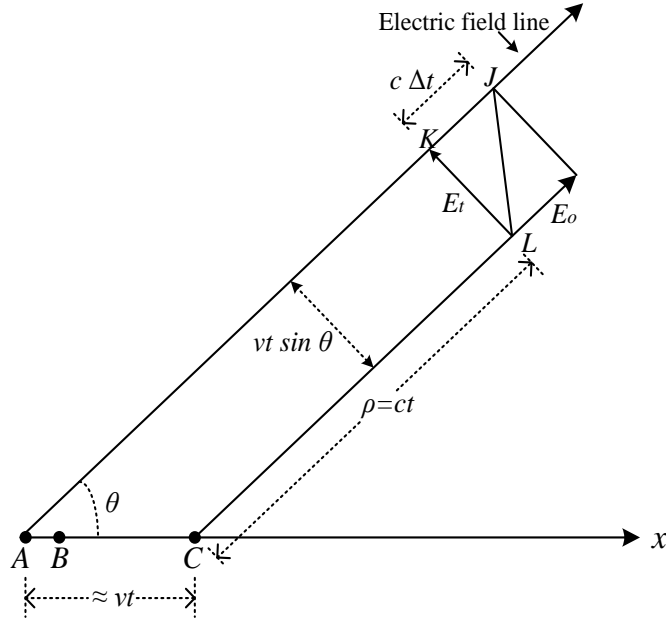


Figure 2-15 The electric field at angle  $\theta$  caused by charge  $q$  accelerated from point  $A$  to  $B$  then moving with constant speed until reaching point  $C$ .

A consider the kink at point  $L$  in Figure 2-15. The charge accelerates from stationary point  $A$  until reaching point  $B$ . The velocity at any moment during acceleration is  $v = a \Delta t$ , where  $a$  is acceleration. The charge is moves at constant velocity from  $B$  to  $C$  for  $t$  seconds. Assuming  $\Delta t \ll t$  than  $d = AB + BC \approx BC = vt$ .

The radial field  $E_0$  can be calculated using Equation 2-10:

$$E_0 = \frac{Q}{4\pi\epsilon_0} \frac{1}{R^2} = \frac{Q}{4\pi\epsilon_0} \frac{1}{(ct)^2} \quad (2-12)$$

From Figure 2-15, the transverse electric field component ( $E_t$ ) can be calculated:

$$\frac{E_0}{E_t} = \frac{JK}{KL} = \frac{JK}{AB + BC} = \frac{c \Delta t}{vt \sin\theta} \quad (2-13)$$

Solving for  $E_t$ :

$$E_t = E_0 \frac{vt \sin\theta}{c \Delta t} \quad (2-14)$$

Inserting Equation 2-12 into Equation 2-14, it becomes:

$$E_t = \frac{Q}{4\pi\epsilon_0} \frac{1}{(ct)^2} \frac{vt \sin\theta}{c \Delta t}$$

or

$$E_t = \frac{Q}{4\pi\epsilon_0} \frac{1}{c^2 t} \frac{v \sin\theta}{c \Delta t} \quad (2-15)$$

By substituting  $\mu_0 = 1/(\epsilon_0 c^2)$  and also using  $\rho = ct$  (from Figure 2-15), Equation 2-15 can be written as:

$$E_t = \frac{Q \mu_0 \sin\theta}{4\pi} \frac{v}{\rho \Delta t} \quad (2-16)$$

The factor  $v/\Delta t$  is the retarded acceleration, which is the time delay of the electric field to point  $L$  due to the time needed by the accelerating charge to move from  $C$  to  $L$ . Or, in other words, at point  $L$  the electric field of the moving charge  $Q$  is sensed at the previous time  $t$ . Simplifying Equation 2-16 by introducing the retarded acceleration  $[a]$  factor [145], the transverse electric field can be written as:

$$E_t = \frac{Q \mu_0 [a] \sin\theta}{4\pi \rho} \quad (2-17)$$

where  $[a] = a(t' = t - \rho/c)$ . For  $N$  charges:

$$E_t = \frac{NQ \mu_0 [a] \sin\theta}{4\pi \rho} \quad (2-18)$$

The radiated electromagnetic signals can then be captured and recorded using appropriate sensors and measuring systems. From Equation 2-18, the characteristics of the electromagnetic PD signal that is produced during a discharge event depends on:

- the number of charges produced during the discharge process.
- the acceleration of the charges which is determined by the surrounding electric field.
- the permeability of the medium where the PD took place (almost always the permeability of free-space).
- the location of the observer with respect to the location and velocity of accelerating charge.

## 2.8 Summary

This chapter has given a general view to help in developing the wireless PD monitoring for HV apparatuses can be used to locate PD events before failure occurs. FSR methods have features in common with other detection techniques. The FSR monitoring of PD could provide accurate prediction of insulation failure more conveniently and more cheaply than some more traditional methods. A comprehensive review of PD measurement has been presented. One of the major problems in HV power system is breakdown of insulators or degradation of insulators. Partial discharge can be detected using FSR and galvanic contact measurement techniques. Calibration of PD sources has been described and the possibility of using FSR measurements to estimate absolute intensity of PD has been demonstrated. The origin of EM radiation from PD has been described. Therefore, the next chapter will present the main PD measurement apparatus of the test facility used in this experimental study.

## CHAPTER 3

### MEASUREMENT APPARATUS

---

*This chapter will present suitable measurement technology for the radiometric measurement of PD. In this chapter also will select, design and implement an experiment to measure PD using the radiometric technique and the electrical galvanic contact method. The PD measurement-setup and describes the main PD measurement apparatus of the test facility used in this study are showed. Furthermore, floating electrode PD emulator and two types of internal PD emulators (an acrylic tube internal emulator and an epoxy dielectric internal emulator) are described. In addition, emulator structures for floating electrode PD source are explained. Partial discharge sensing antenna, HVPD pC calibrator and data capture is also described. In the next three chapters 4, 5 and 7, PD will be measured using the a radiometric and a galvanic contact measurements techniques.*

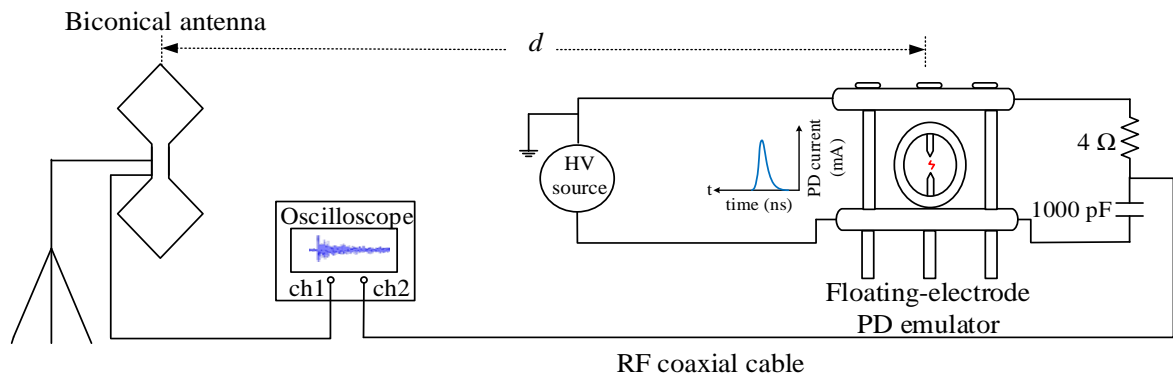
---

### 3.1 Introduction

Partial discharge measurement is an effective method to diagnose imminent failures due to insulation degradation of HV equipment. Partial discharge has traditionally been detected by contact (especially IEC 60270) and capacitive/inductive coupling techniques. The FSR detection of PD is a relatively new technique. The work to be reported describes the partial discharge measurements and calibration of PD sources required for the development of a PD WSN such that absolute partial discharge intensity (in pC) might be inferred from the radiometric measurements. The calibration of the sources suggests the possibility of using FSR measurements to estimate the absolute intensity of PD in HV insulation integrity monitoring applications [1]. This chapter will be providing the description of the measurement facility utilised by PD measurement and PD calibration apparatus.

### 3.2 Measuring Circuit

The measurement apparatus used for simultaneously obtaining galvanic contact measurements and FSR measurements for the same PD event is shown in Figure 3-1. The experiment comprises a coupling capacitor  $C_k$ , an HV power supply, a test object, a coupling device that is connected to the partial discharge detector-measuring instrument (oscilloscope) through aRF coaxial cable, and a biconical antenna. The experimental setup has used four different types of PD emulators (floating electrode PD emulator, acrylic tube PD emulator, acrylic tube PD emulator filled with transformer oil, and epoxy dielectric internal PD emulator).



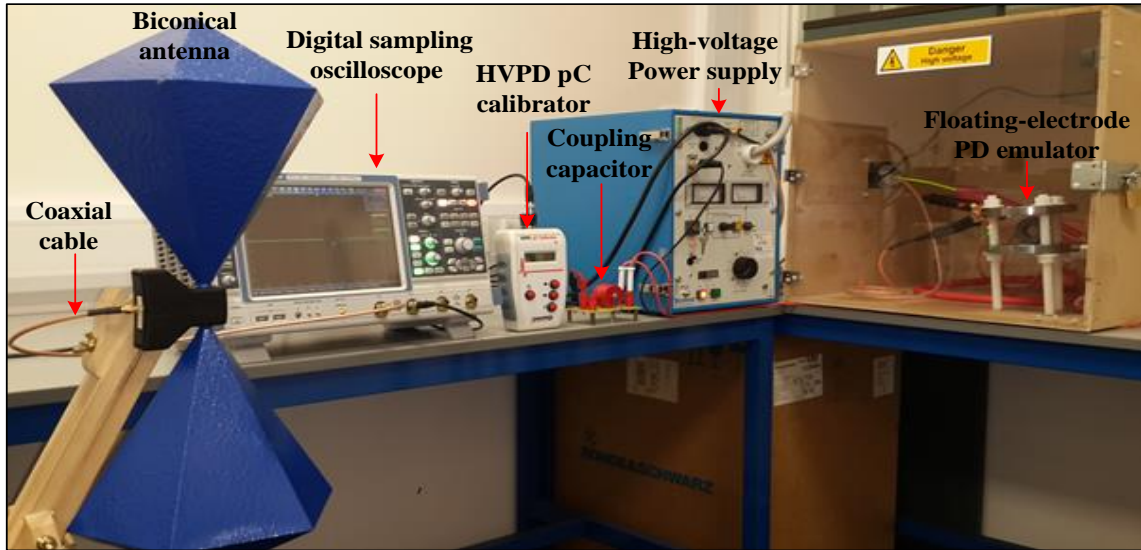


Figure 3-1 PD measurement apparatus.

Measurements of FSR and galvanic contact PD signals were taken under AC and/or DC HV with the measurement system. AC voltages were produced using a 50 Hz power supply voltage of 0 – 30 kV RMS, 1.25 kVA, while DC HV were generated using a 0 – 30 kV, 0.1 mA supply source. Partial discharge is generated by applying a HV to the artificial PD source. The radiometric measurements were made using a biconical antenna connected to the digital sampling oscilloscope (DSO) which has an analogue measurement bandwidth of 4 GHz, 20 GSa/s. The sampling rate used in this PD measurement is 10 GSa/s. The PD current signal is converted into a voltage signal across 50  $\Omega$  matching impedance and fed into a DSO. A biconical antenna was positioned at different distances from the PD source, and was vertically polarised. The voltage rating of the coupling capacitor is 40 kV in the galvanic contact measurement technique. For detecting PD, a coupling capacitor was connected in parallel with the PD emulator [1]. The coupling capacitor protects the PD detector from the high voltage and is passing only the transient PD signal.

### 3.3 Antenna

The UHF sensors used for PD detection must have broadband response [117]. The biconical antenna has been selected for the FSR measurement system. Figure 3-2 shows the wideband RF biconical antenna horizontally polarized. It is specified to respond to an

electric field in the range of 20 MHz – 1 GHz; it has an impedance of 50  $\Omega$  [146]. Figure 3-3 shows the antenna gain is around -38 dBi to -0.5 dBi and antenna factor is 17 dB/m - 34 dB/m [146]. The frequency response of the antenna in terms of antenna gain and antenna factor vs frequency as given by the antenna manufacturer.



Figure 3-2 Biconical antenna used in the FSR measurements.

The ERP was calculated assuming free-space propagation and the known antenna factor of the biconical antenna. Its dimensions are 540 mm  $\times$  225 mm  $\times$  225 mm. the biconical antenna has been vertically positioned at several distances from the PD source. As the vertical angle of the biconical geometry is enlarged, impedance becomes smaller. It becomes a dipole aerial if vertical angle reduces to zero. The UHF signals were captured and displayed in the high bandwidth DSO. Minimising any possible coupling introduced via the contacts among the oscilloscope and antenna is essential.

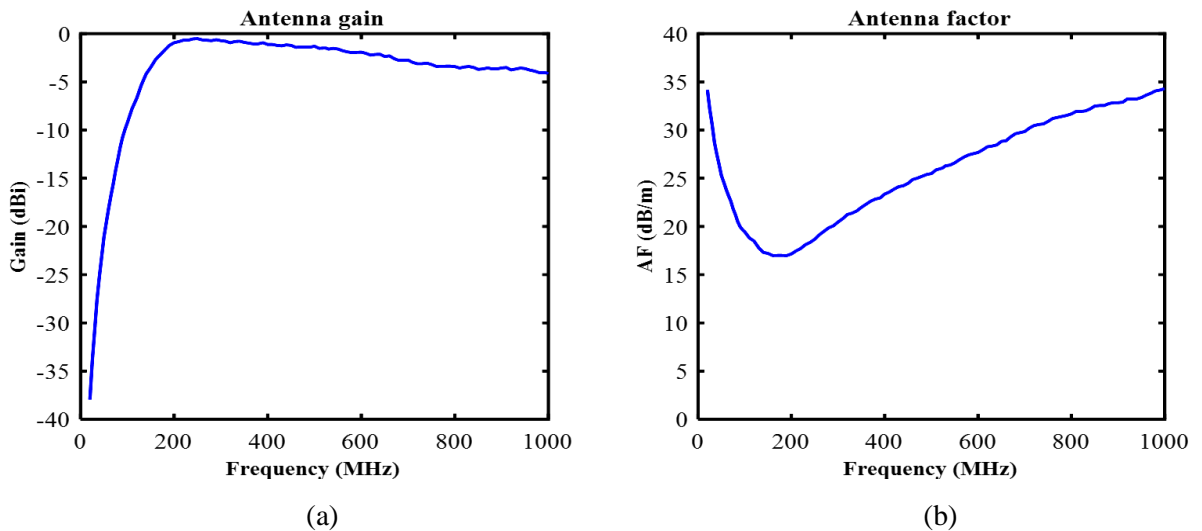


Figure 3-3 Biconical antenna (a) antenna gain (b) antenna factor.

### 3.4 Floating Electrode PD Emulator

The effect of a floating body on the breakdown voltage between an HV electrode and the earth has been a subject of study in a few previous works [147-150]. In the past, researchers have studied the effect of breakdown voltage and the time taken to breakdown with a floating electrode located approximately 1 mm away from an earthed electrode, under the application of a negative impulse voltage [148, 150, 151]. It has been found that the floating body can significantly lower the breakdown voltage, while increasing the time to breakdown. This phenomenon is further studied under positive impulse voltage applications in [152], where the reduction in the breakdown voltage was caused by a floating body situated at approximately 1/3 of the gap distance away from the earthed electrode. Later on, in [153], Philpott et al. studied the impact of floating electrode corona sources on the level of breakdown-voltage reduction.

This study, on the other hand, aims to investigate the PD phenomena created with using a floating electrode located at 0.2 to 1 mm distances from the earthed electrode, which will help further reduce the breakdown voltage [154-156]. As illustrated in Figure 3-4, a floating electrode (*FE*) is conventionally defined as an isolated metallic body, which is placed at a specific distance away from the earthed electrode. The notations used in Figure 3-5 are similar to those defined in [150, 156-158]. These notations are,

- $g_1$ : primary gap distance,
- $g_2$ : secondary gap distance,
- $A$ : complex gap,
- $E_1$ : electric field at the top of the *FE*,
- $E_2$ : electric field at the secondary gap, and
- $E_3$ : reference electric field.

In Figure 3-4, the reference electric field,  $E_3$ , deemed to be the source of PD on the *FE*, causes the *FE* to be charged, to a point where breakdown occurs in the secondary gap. In [159], it is shown that the electric field generated on the high sharp points of the *FE* surface

breakdown of the secondary gap is considered as the critical field, which eventually provides PD currents[150].

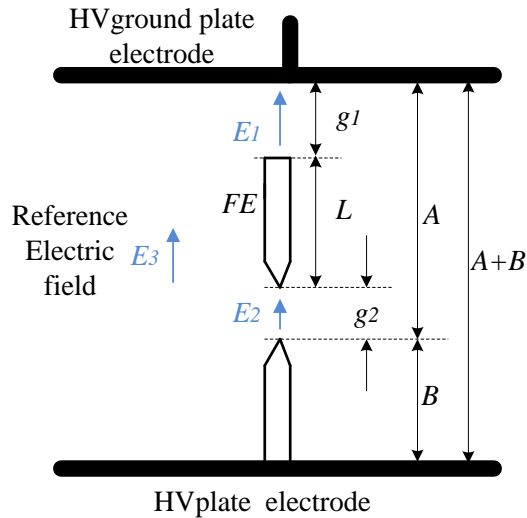


Figure 3-4 Diagram showing the gap arrangement containing a floating electrode and the electric fields.

### 3.4.1 Theory

The *FEs* are metallic objects that are disconnected or isolated from the earth potential. Under certain conditions, these objects have the capability to attract electric charge and thus, accumulate electric potential energy. In an arrangement shown in Figure 3-5, the potential level and the quantity of the potential energy that an *FE* can acquire is directly governed by its geometry, location within the gap and the voltage distribution in the gap, which can also be given as a function of the *FE*'s capacitance. Moreover, the breakdown voltage level of the *FE* largely depends on the secondary gap distance,  $g_2$ , between the *FE* and the earthed electrode [150].

In principle, when a metallic body is inserted inside a gap of length  $A$  (see Figure 3-4) and a HV impulse is applied across the gap, the *FE* distorts the electrostatic field generated within the gap. The electric field generated around the high sharp points of the *FE* will be enhanced, as the *FE*'s metallic property attracts sufficient charge to induce a voltage level higher than that of the earth's potential; although, the net charge on the *FE* will be zero. In

case the acquired voltage by the *FE* is lower than a predefined threshold voltage, no breakdown will occur.

However, in case the acquired voltage level exceeds the *FE*'s threshold limit, a discharge to earth potential will take place [156]. The discharge causes the *FE*'s potential to drop to the same level as the earth's potential. This results in a change in the net charge on the *FE*; in this case, the *FE* gains a positive charge. The acquired charge results in the weakening of the electric field strength induced in the secondary gap, while enhancing the induced electric field at the top of the *FE*. If the HV impulse applied across the gap remains constant, no further discharge will occur. Nevertheless, as the level of the HV impulse applied across the gap increases, the electric field in the secondary gap starts to increase again and once the breakdown threshold of the secondary gap has been reached, another instant of discharge to earth occur. At this stage, if the voltage remains constant, no further discharge will occur. With the HV level gradually increasing across the main gap, the floating body, inevitably, acquires a positive charge due to the accumulation of positive charge. Furthermore, the electric field at the top of the *FE* will continue to increase gradually, until a critical electric field for the initiation of corona currents has been established [150, 154].

During the activation of a particular PD source, it is possible to relate the level of potential energy absorbed by the *FE* directly to the *FE*'s capacitance and the maximum electric field level that the secondary gap can sustain. Thus, the maximum potential energy stored in the *FE* can be computed [150, 160] as:

$$E_s = \frac{CV^2}{2} \quad (3-1)$$

where  $E_s$  is the energy stored in the gap,  $C$  is the *FE*'s capacitance and  $V$  is the breakdown voltage of the secondary gap  $g_2$ . The breakdown voltage,  $V$  is given by the product of the breakdown electric field strength and the gap spacing such as,

$$V = E_2 g_2 \quad (3-2)$$

Substituting equation (3-1) into (3-2) results in an expression for the *FE*'s potential energy given as,

$$E_s = \frac{C g_2^2 E_2^2}{2} \quad (3-3)$$

Equivalently, (3-2) can be expressed in terms of the measured charge  $q$  as,

$$E_s = \frac{g_2 E_2 q}{2} \quad (3-4)$$

The floating-electrode PD emulator which is based on that described in [161] is shown in Figure 3-5. The output of the HV power source is connected to the lower electrode and the upper electrode is connected to earth. The floating electrode PD emulator contains a polythene ring that holds a metal electrode from one of the energized plates. When the electric field is sufficiently large, corona discharge originates from the floating-electrode [2].

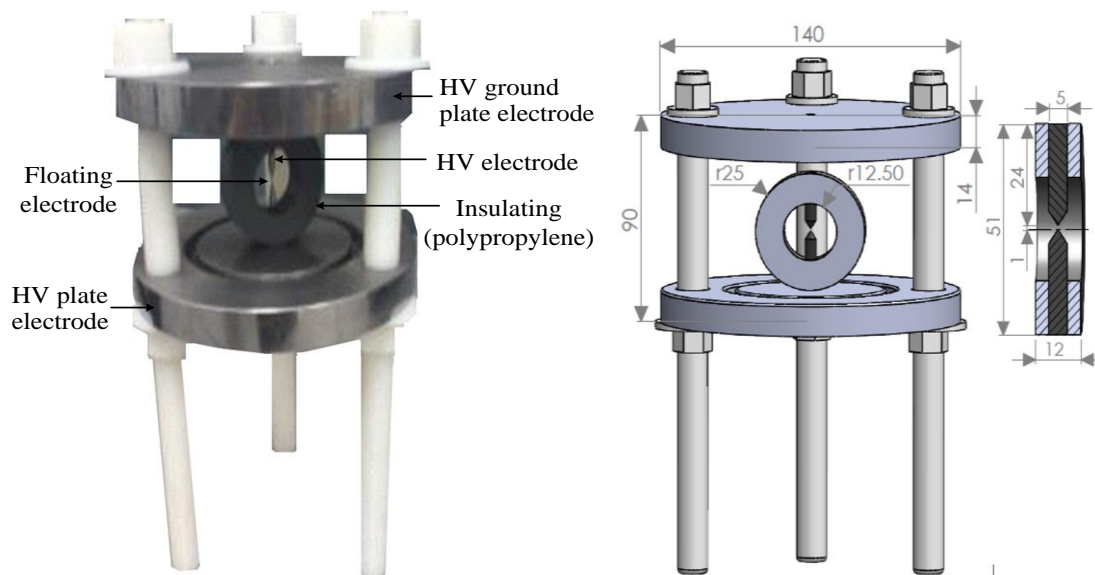


Figure 3-5 Floating – electrode PD emulator (dimensions in mm).

### 3.4.2 Equivalent circuit

The equivalent circuit of the floating electrode PD emulator and detector is shown in Figure 3-6. It is a parallel RLC circuit and ideal switch  $K$ . The PD emulator is in parallel with a coupling capacitor  $C_k$ . As shown in Figure 3-6, this combination is connected across a supply that provides the HV excitation voltage. A PD pulse in the emulator causes a high

frequency current in the loop with  $C_k$ , and into this loop is inserted a detection impedance  $Z_m$  [162].

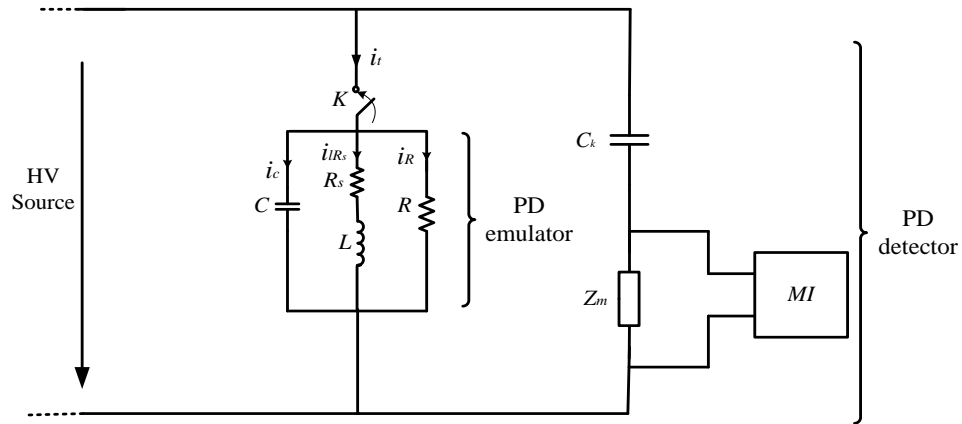


Figure 3-6 Equivalent circuit of floating electrode PD emulator and detector.

The circuit emulates PD at the closing of switch  $K$  at  $t=t_0$ . Equation 3-5 describes the resulting signal voltage across  $Z_m$ . The derivation is given in appendix A.

$$v = A \sin(\beta t) \cdot e^{-\alpha t} \quad (3-5)$$

where  $\alpha = \frac{1}{2RC}$ ,  $\beta = -4\frac{1}{LC} - \left(\frac{1}{RC}\right)^2 - 4\frac{1}{LC}$ ,  $A = L(\alpha^2 + \beta^2) i_t / \beta$ ,  $A > 0$ .

Figure 3-7 shows an example signal modelled according to equation 3-5 for a period of 1ms. The parameters are given as  $A=2$ ,  $\alpha =1000$  and  $\beta=9950$ .

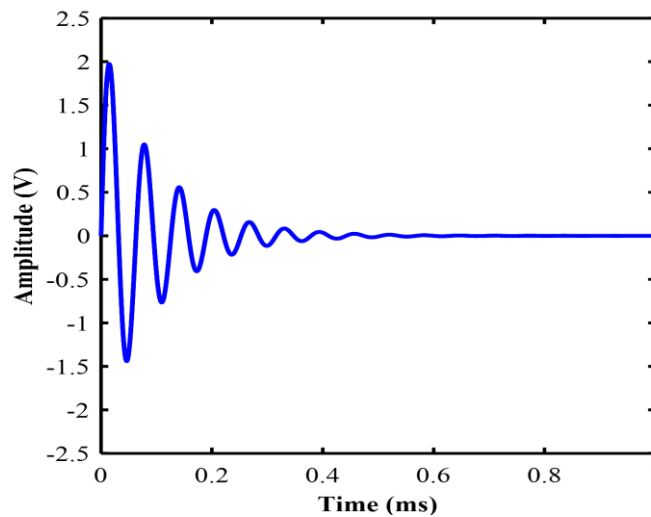


Figure 3-7 Waveform of the discharge source model.

Parameter values RL and C in the equivalent circuit can be found from the oscillation features and decay time constant of a PD event measurement.

### 3.5 An Acrylic Tube Internal PD Emulator

An acrylic tube PD source is shown in Figure 3-8. The electrodes are smaller than those in the floating electrode emulator. The insulation is perspex. The edges of the electrodes are rounded to avoid the enhanced electrical field strength, and the resulting corona, which could otherwise occur close to the sharp edge. The insulator was created by compressing three circular plates between the two electrodes to form a composite disc. The thickness of each plate is 1.5 mm. The insulation defect necessary for the occurrence of PD is realised by drilling a 1 mm hole in the middle plate. The electrodes and insulating disc are enclosed in an acrylic cylinder filled with transformer oil to avoid discharge from the disc edges [3, 99]. In addition, the space around the electrodes were filled with transformer oil to avoid surface discharges and minimize corona discharges.

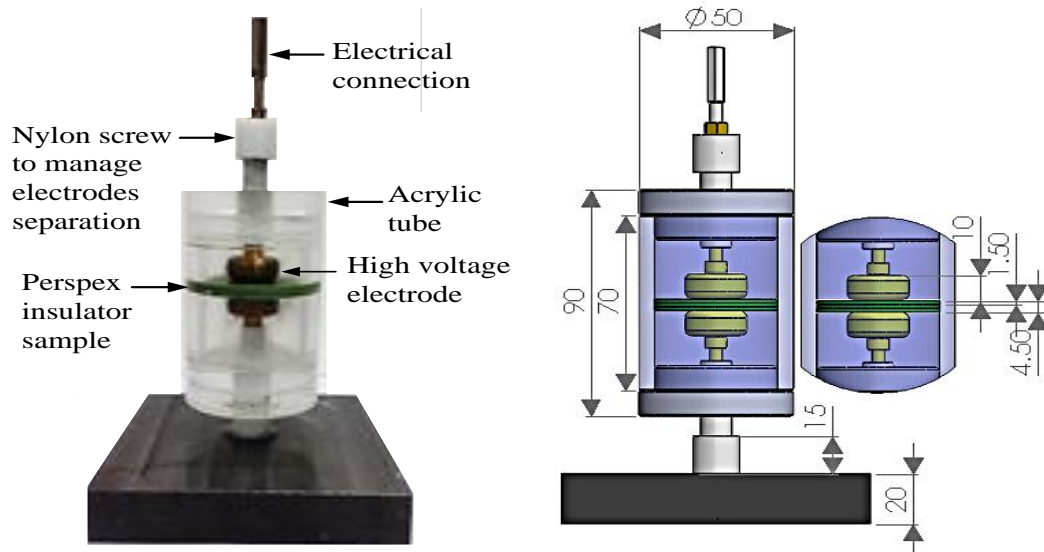


Figure 3-8 Acrylic tube internal PD emulator (dimensions in mm).

### 3.6 Epoxy Dielectric Internal PD Emulator

A second epoxy dielectric internal PD emulator is shown in Figure 3-9. The insulation comprises three epoxy glass plates. A cavity with a diameter of 1 mm was drilled in the

middle plate. The thickness of the three-plate composite is 2.4 mm. The HV electrode is made from stainless steel with a well-rounded edge to avoid surface discharge from regions of elevated field strength [3, 163].

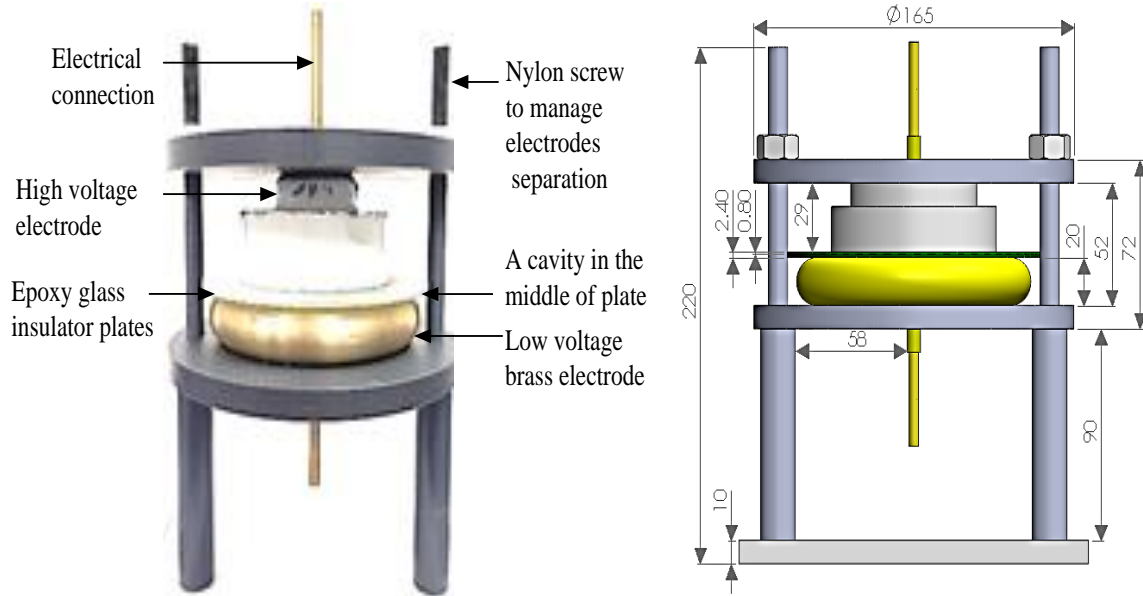


Figure 3-9 Epoxy dielectric internal PD emulator (dimensions in mm).

### 3.7 HVPD pC Calibrator

High voltage partial discharge picocoulomb (HVPD pC) calibrator is a device that injects a current pulse of determined intensity. The off-line HVPD pC calibrator is designed to provides repeatable current pulses of specified charge from 1 pC up to 100 nC and it is appropriate for PD tests according to the IEC 60270 standard [164]. The PD calibrator output has to be connected across the test object when the voltage is off. The device can be used in the laboratory and on-site test environment. With a wide range of calibration pulses, the HVPD pC calibrator can be used to test all types of HV equipment of the power substations and calculating the PD magnitude of the apparent charge [1]. HVPD calibration device has been used to assess the ERP of the emulator as a function of PD apparent charge in this research [164]. Figure 3-10 shows an off-line HVPD pC calibrator [165].

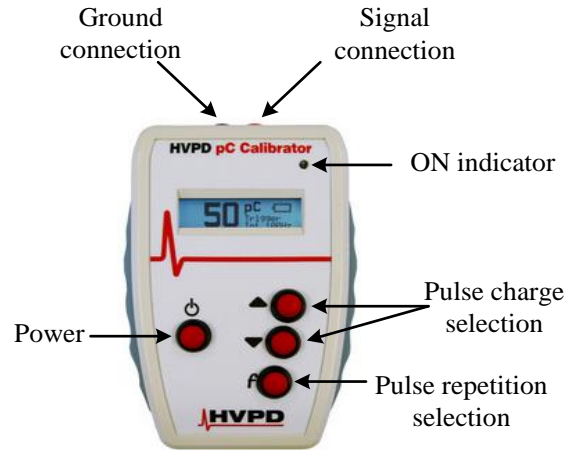


Figure 3-10 HVPD pC calibrator [165].

### 3.8 Data Capture

The digital sampling oscilloscope (DSO) has an analogue measurement bandwidth of 4 GHz, 20 GSa/s, and 4 input channels is used for capturing the time-resolved signals of the applied HV to the PD emulator and the PD activity in PD measurements. The radiometric measurements were made using a biconical antenna and galvanic contact measurement was made by a matched, low loss coaxial cable to the input channel. Simultaneous monitoring was carried out.

## CHAPTER 4

### SPECTRUM MEASUREMENTS

---

*In chapter four, the relationship between radiometric and galvanic contact measured signal using a variety of partial discharge sources will be explored. The PD is measured concurrently, using FSR technique and a galvanic contact technique based on IEC 60270 standard. The frequency spectrum is obtained by FFT analysis of time-domain pulses. The correlation of FSR and galvanic contact measurements of PD events is calculated. The frequency spectrum of radiated PD energy is compared with the spectrum measured using the galvanic contact method in order to establish the plausibility of estimating effective radiated power (ERP) as an alternative measure of absolute PD intensity to apparent charge. The PD sources used for the comparison are a floating electrode PD emulator, an acrylic tube internal PD emulator, an acrylic tube internal PD emulator filled with transformer oil, and an epoxy dielectric internal PD emulator. The cumulative energies of PD signals in both measurement techniques are also considered.*

---

## 4.1 Introduction

It is thought that the PD spectrum measured by contact and capacitive/inductive coupling methods contains diagnostic information about the PD source; whether, for example, the PD results from internal insulation voids (which may eventually lead to catastrophic failure), from floating potential conductors or from external corona (which is typically of much less concern). It is important, therefore to assess whether such diagnostic information is retained in the FSR signal.

Partial discharge is measured simultaneously, using FSR technique and galvanic contact technique based on the IEC 60270 standard. The experiment setup has been used four different types of PD emulators is shown in section 3.2. The PD sources are specially constructed: an emulator of the floating electrode and two internal PD emulator types an acrylic tube internal PD emulator (PD discharge in the air and in the transformer oil) and epoxy dielectric internal PD emulator [1]. The structure of these emulator types are presented in section 3.4, 3.5 and 3.6. The radiated signal is captured using a biconical antenna. The relative spectral densities in the frequency bands 50 MHz – 290 MHz, 290 MHz – 470 MHz and 470 MHz – 800 MHz are determined. The frequency spectrum of radiated PD signals is compared with the spectrum of signals measured using the electrical galvanic contact method. (The author regards the latter as the measurement method most likely to preserve diagnostic information). The idea is to establish the plausibility of estimating ERP as an alternative measure of absolute PD intensity to apparent charge. The PD emulators used for the comparison are the four PD emulator types. The measurements were carried out in a laboratory environment. There was no change in the environment between measurements.

## 4.2 Time Series Events

A comparison signals captured by FSR and galvanic contact measurements from the floating-electrode emulator event, the acrylic tube internal PD emulator event, the acrylic tube internal PD emulator filled with transformer oil event and finally the epoxy dielectric internal PD emulator event is shown in Figure 4-1 to 4-4. The PD signals were compared

under AC and DC voltages with the measurement system using the floating-electrode PD emulator. The PD event occurs by applying 6.2 kV DC or (15 kVrms AC voltage showed in chapter 5 section 5.2.1) to the floating-electrode emulator. The PD inception voltage usually occurs at lower voltages under DC compared to AC voltage [166]. The internal PD emulators were measured using AC voltage only. The inception AC voltages for PD are: 20 kVrms for the acrylic tube PD emulator and the same for the acrylic tube emulator filled with transformer oil, and slightly lower at 18 kVrms for the epoxy dielectric internal PD emulator.

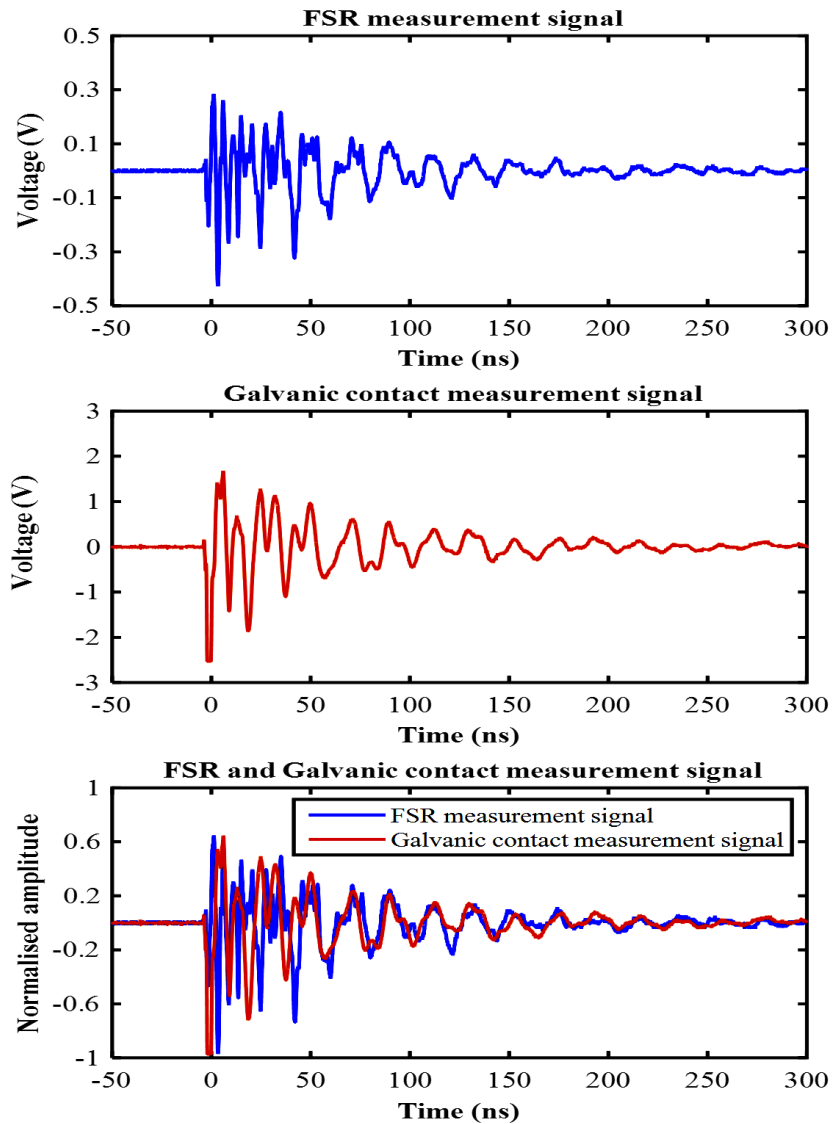


Figure 4-1 FSR and galvanic contact measurement of PD event using a floating electrode PD emulator.

FSR and galvanic contact measurements were not synchronised in time during the experiments.

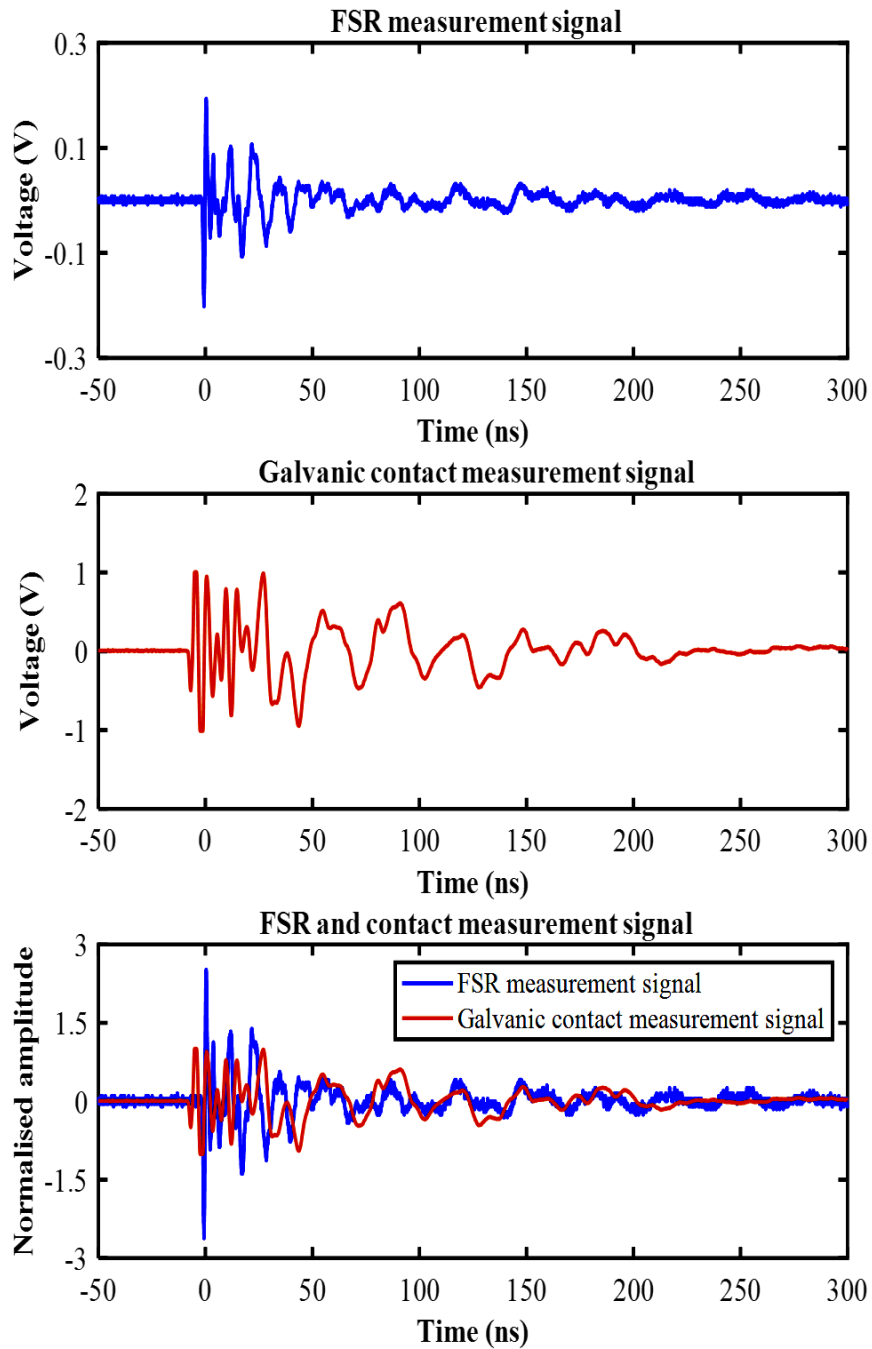


Figure 4-2 FSR and galvanic contact measurement of PD event using an acrylic tube internal PD emulator.

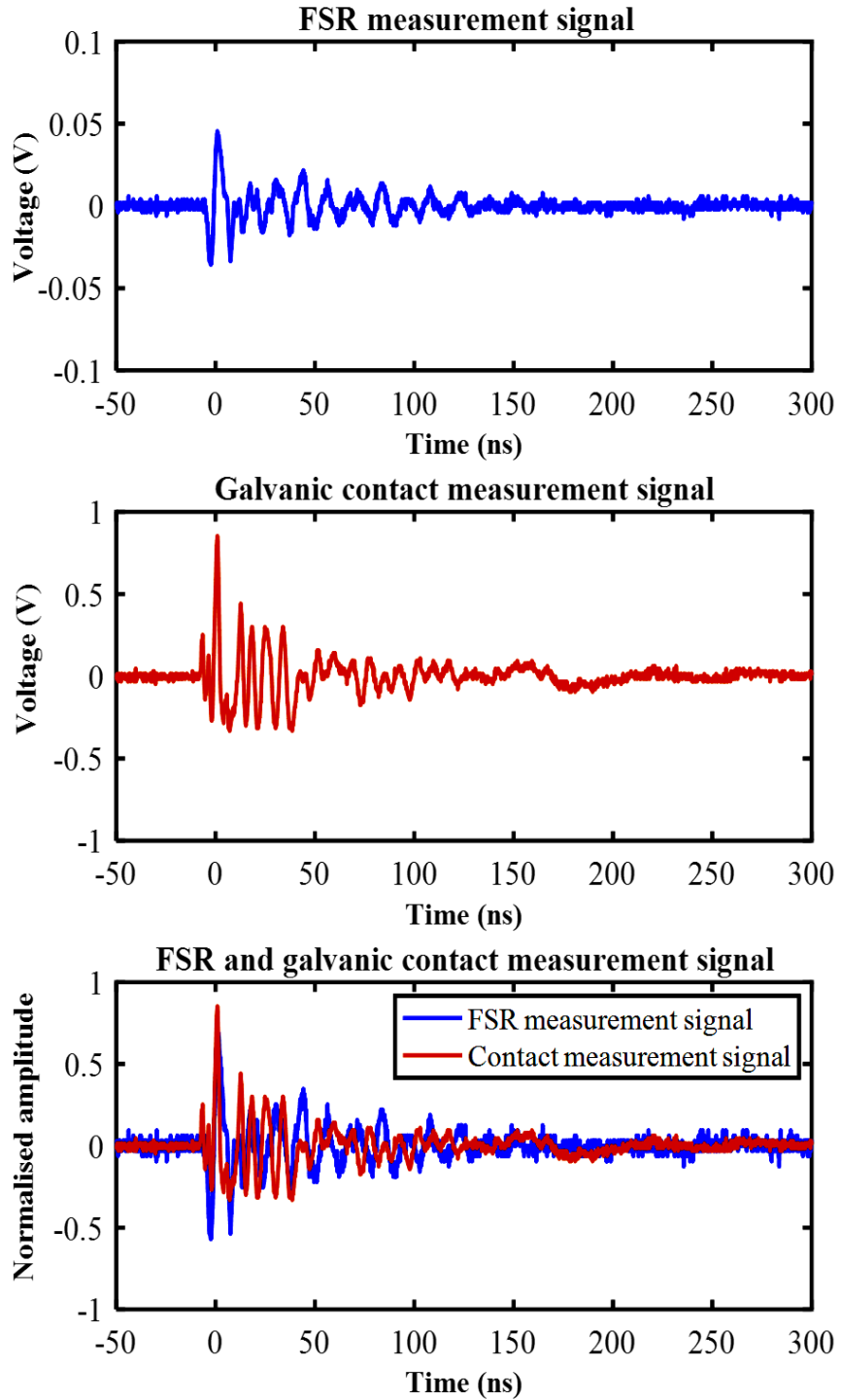


Figure 4-3 FSR and galvanic contact measurement of PD event using an acrylic tube internal PD emulator filled with transformer oil.

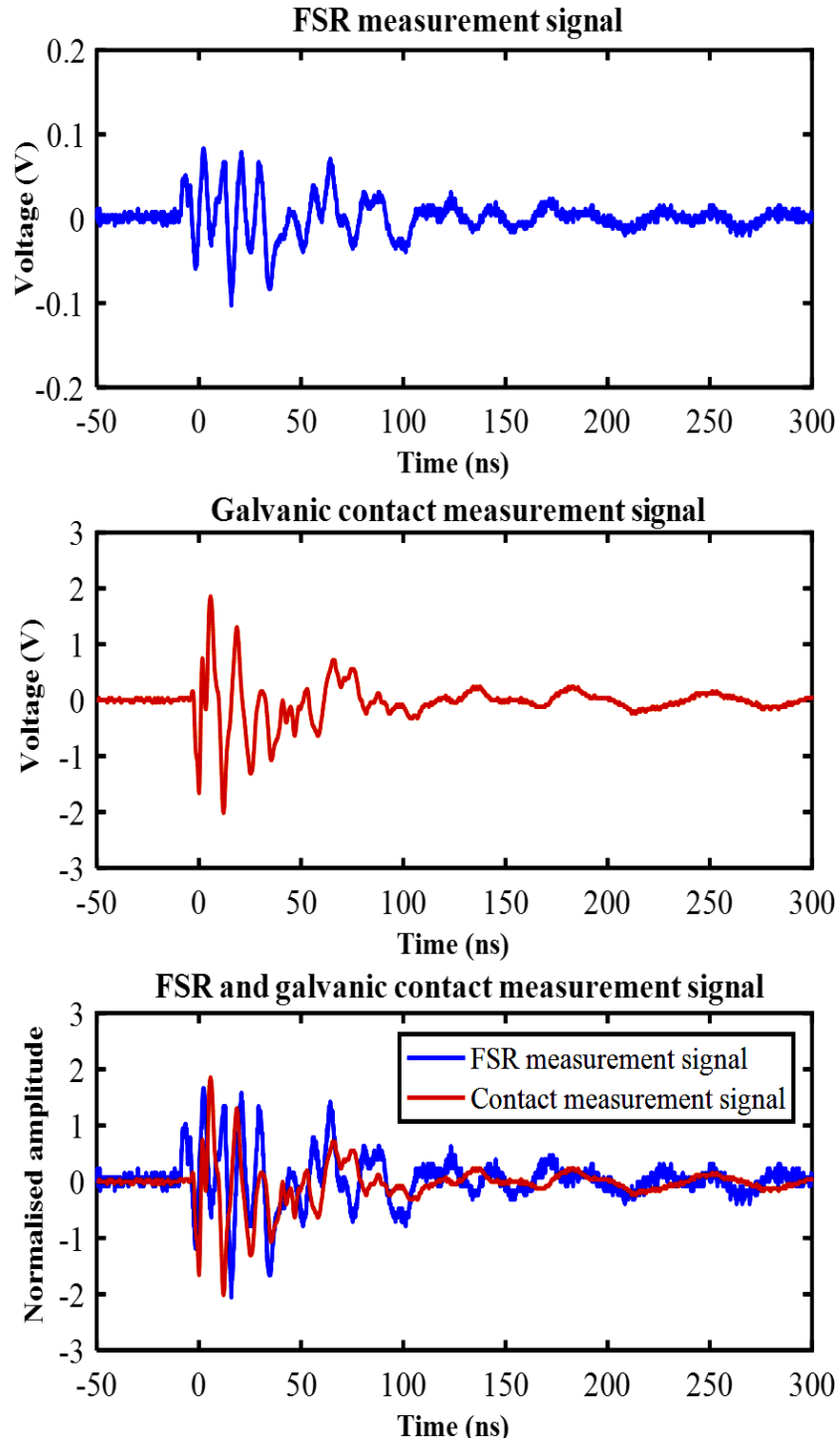


Figure 4-4 FSR and galvanic contact measurement of PD event using an epoxy dielectric internal PD emulator.

### 4.3 Correlation of FSR and Galvanic Contact Measurement of PD Events

There is an approximate similarity between the temporal decay of the two signals in the two measurements (showed in time-domain Figure 4-5), which were more similar than expected. For the FSR measurement, severe band limiting caused by the electromagnetic radiation and reception processes was expected. In contrast, the galvanic contact measurement was expected to produce less severe band limiting – this should, in principle, resulting in a less pronounced ringing. The conclusion is that band limiting is controlled by the capacitive and inductive features of PD emulators and the connecting cables, rather than the frequency response of the antenna that receives the FSR measurement. [2]. The calculated root mean squared error (RMSE) and correlation coefficient (CC) between FSR measurement signal and galvanic contact measurement signal is shown in Table 4-1. Adapted for RMSE and CC, as shown below [167]:

$$RMSE = \sqrt{\frac{1}{N} \sum_{i=1}^N |y(i) - x(i)|^2} \quad (4-1)$$

$$CC(n) = \sum_{t=0}^{N-n-1} x(i)y(i+n) \quad (4-2)$$

where  $x(i)$  and  $y(i)$  correspond to the original PD signals, and  $N$  is the length of signals.

Some weakness of this RMSE between two signals of acrylic tube internal PD emulator with oil filling and correlation coefficient of acrylic tube internal PD emulator may be due, in part, to distortion of the FSR signal caused by multipath propagation.

Table 4-1 Correlation of FSR and galvanic contact measurements signals

PD emulator	Root Mean Squared Error (V)	Correlation coefficient
Floating-electrode PD emulator	0.9147	0.8088
Acrylic tube internal PD emulator without oil filling	0.6287	0.5074
Acrylic tube internal PD emulator with oil filling	0.3236	0.5570
Epoxy dielectric internal PD emulator	0.7847	0.6689

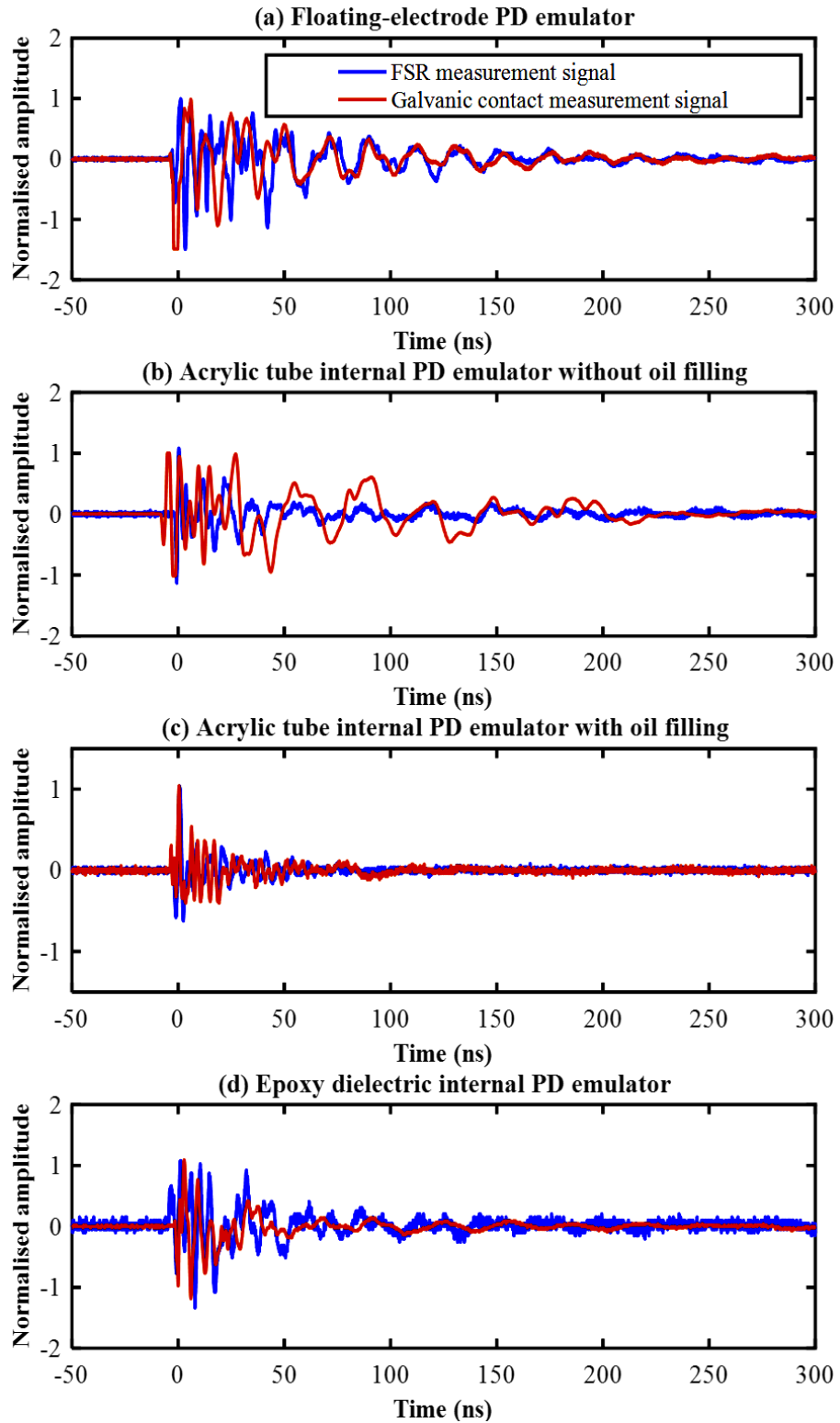


Figure 4-5 Comparison of normalized measurements of PD signals using four types of PD emulators.

#### **4.4 Frequency Spectra of FSR and Galvanic Contact Measurements**

The frequency spectra are obtained by FFT processing of the time-domain signals. An example of comparison signal between FSR and galvanic contact measurements of PD time series event and FFT oscilloscope data captured using floating electrode PD emulator is shown in appendix B.

The frequency spectra of the signals from FSR and galvanic contact measurements are compared in Figures 4-6 to 4-9 using the four types of PD emulators.

Frequency spectra show that the central frequency of the PD discharge is located in the frequency range of 50 MHz – 290 MHz with both measurement techniques. The galvanic contact signal appears to have less high-frequency contents than the FSR signal. This may be due, however, to the frequency dependence of the radiation efficiency and gain of the radiating structure resulting in suppression of low frequency radiated energy making the higher frequency energy a greater fraction of the whole. The frequency spectra of FSR and galvanic contact measurements are not identical, they have some similarities. The hypothesis is that some of the diagnostic information about PD in a galvanic contact measurement remains in the radiometric measurement. This hypothesis is currently the subject of further investigation.

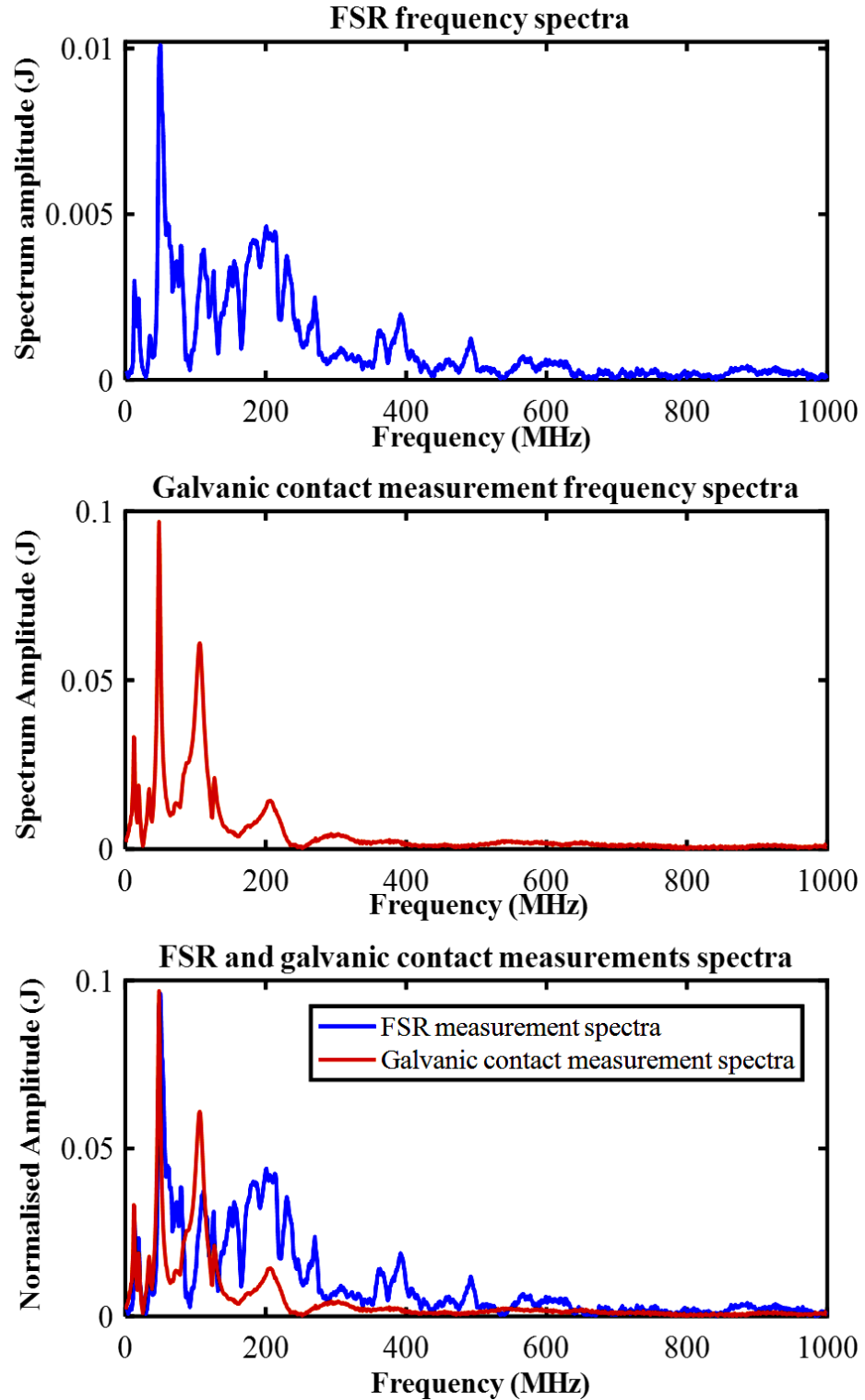


Figure 4-6 Frequency spectra of FSR and galvanic contact measurements using a floating electrode PD emulator.

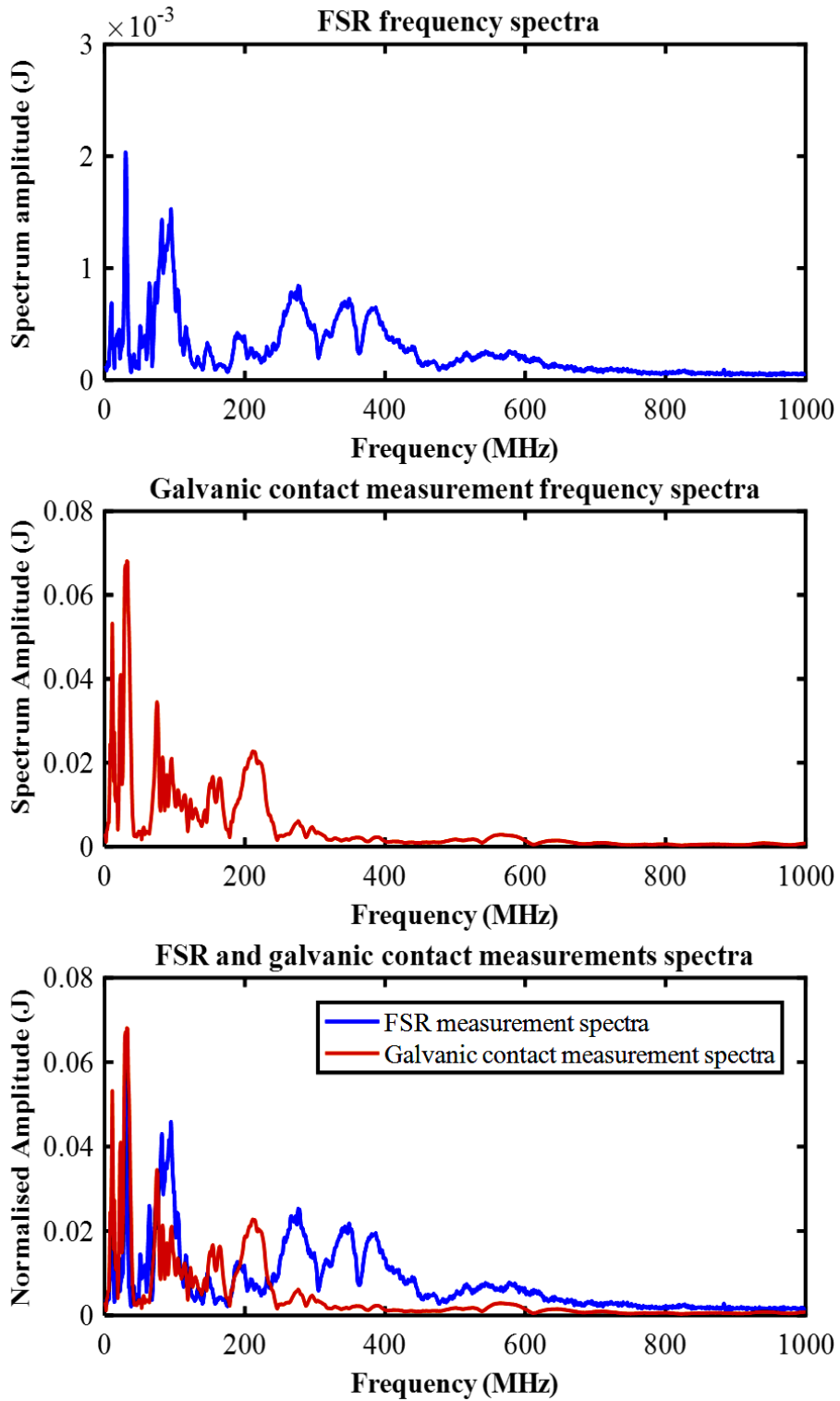


Figure 4-7 Frequency spectra of FSR and galvanic contact measurements using an acrylic tube internal PD emulator.

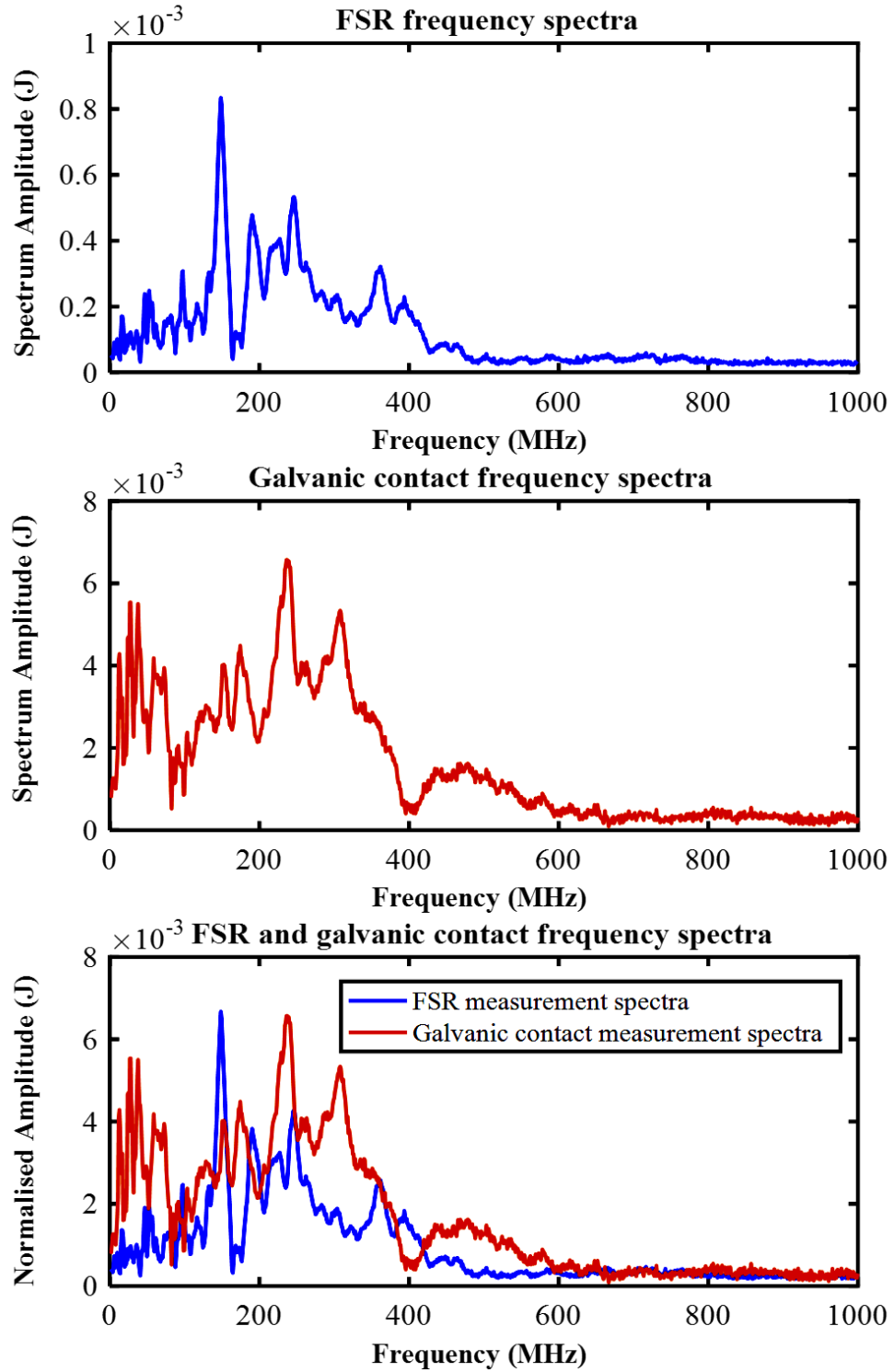


Figure 4-8 Frequency spectra of FSR and galvanic contact measurements using an acrylic tube internal PD emulator filled with transformer oil.

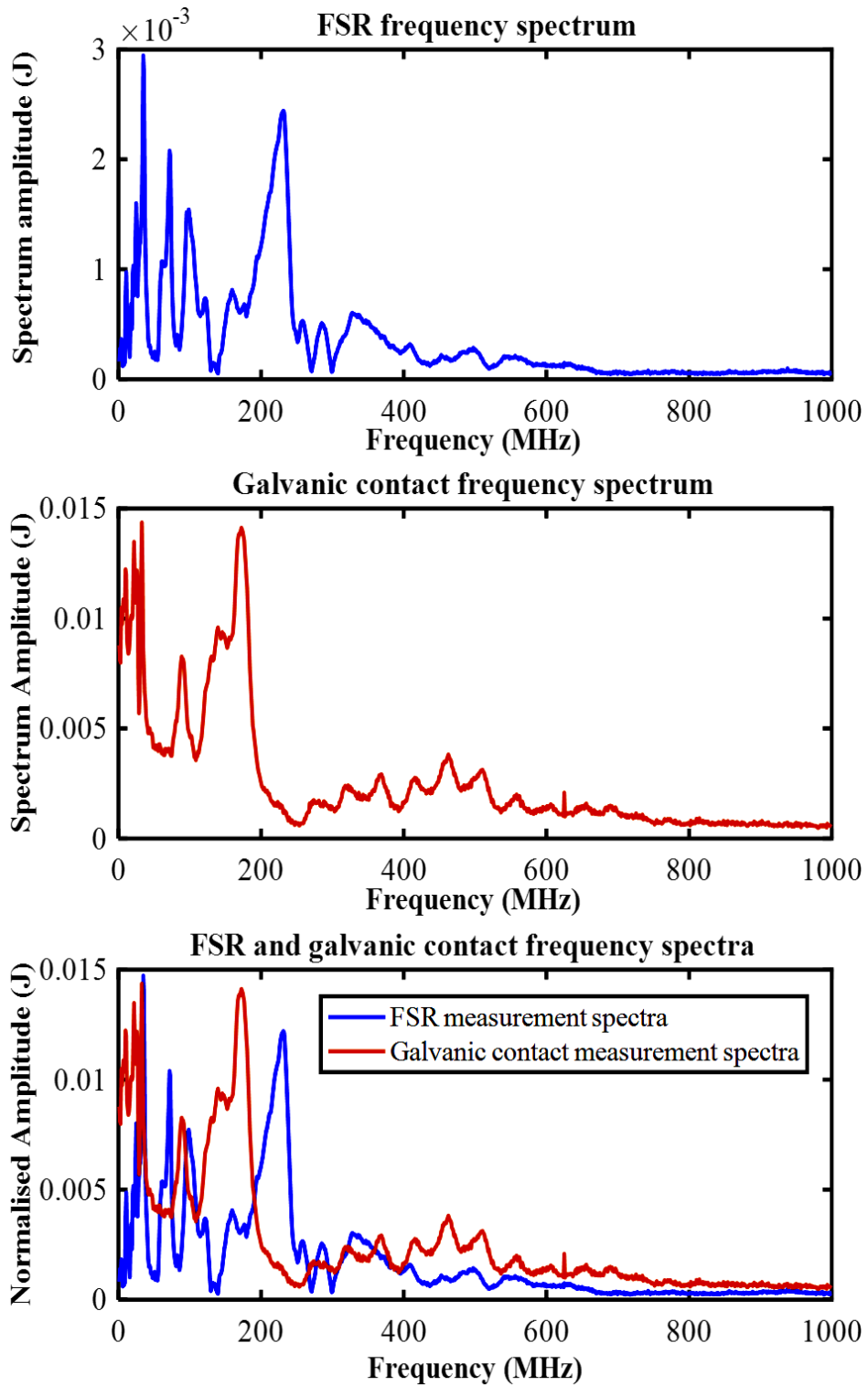


Figure 4-9 Frequency spectra of FSR and galvanic contact measurements using an epoxy dielectric internal PD emulator.

#### 4.4.1 Frequency spectrum energy analysis

The energy resides almost entirely in the band of 50 MHz to 800 MHz with a preponderance of energy below 300 MHz. The following figures depict the two measurements, in which a clear distinction is seen between the received FSR and the galvanic contact measurements. The frequency spectra were split into three bands with the energy contained within each band plotted. The frequency spectrum in the 50 MHz – 290 MHz, 290 MHz – 470 MHz and 470 MHz – 800 MHz bands is observed on a linear scale amplitude.

- **Frequency bands energy content for the FSR measurement method.**

Frequency spectra split into three bands and energy contained in the three frequency bands for the FSR measurements signal of the floating electrode PD emulator type as an example is shown in Figures 4-10 and 4-11. The frequency spectrum energy contents for bands 0 – 50 MHz and 800 MHz – 1000 MHz are also shown in Figure 4-12. The total energy distribution in the frequency spectra for four PD emulators from 0 – 1000 MHz and the percentage of energy present in the frequency bands in FSR is shown in Table 4-2.

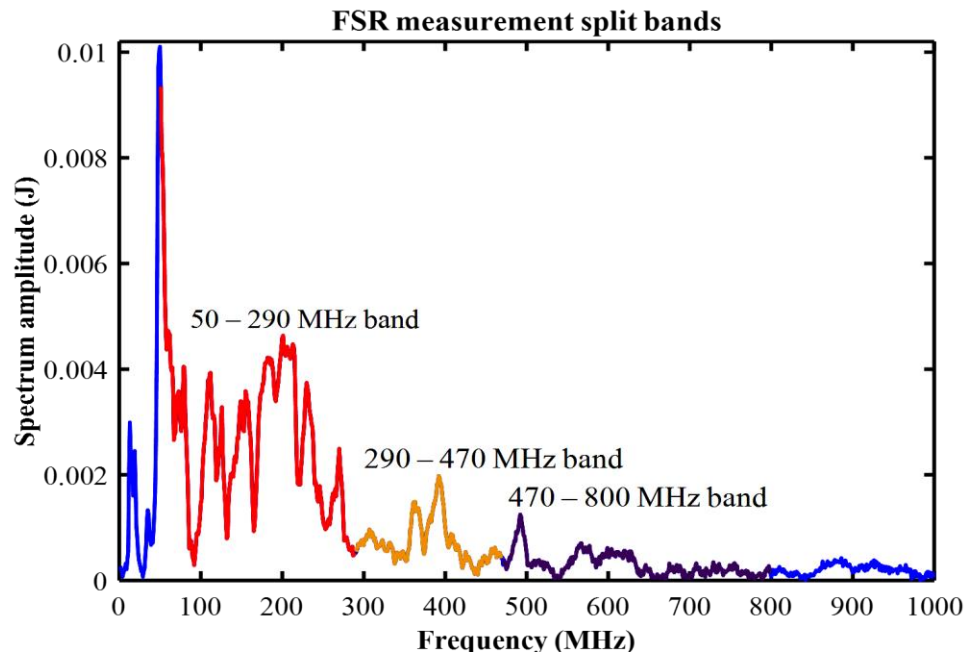


Figure 4-10 Frequency spectrum divided into bands for the FSR measurement method.

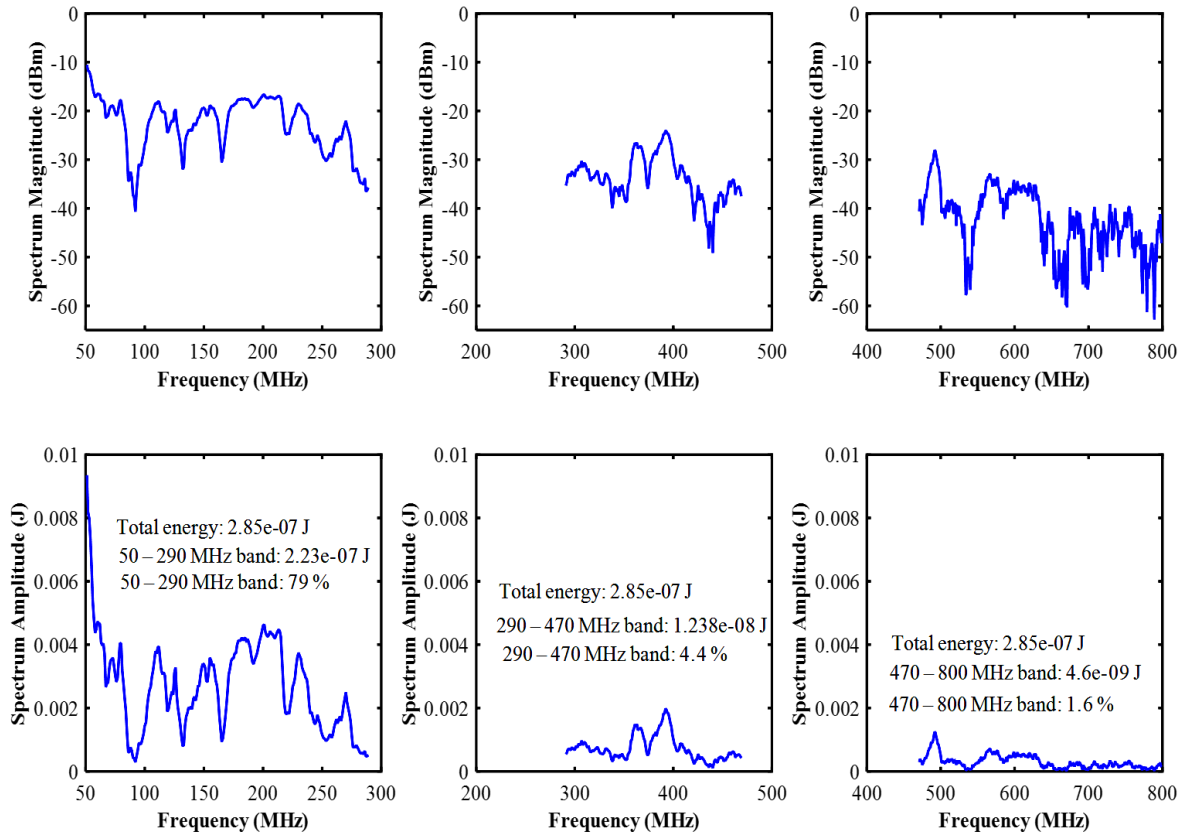


Figure 4-11 Sub-band spectra and energy proportions for FSR measurement.

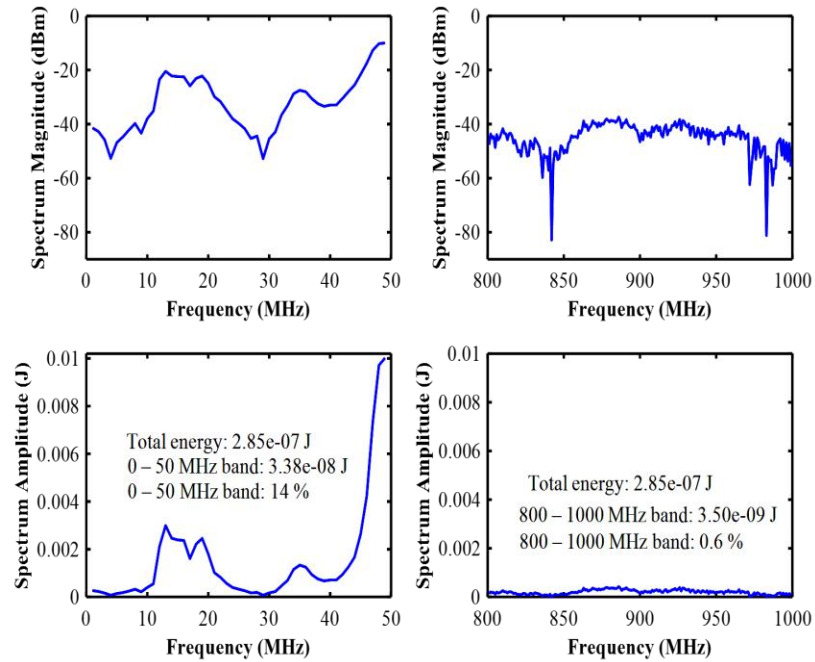


Figure 4-12 Sub-band spectra energy contained in the two frequency bands for FSR measurement.

Table 4-2 Energy of FSR measurement frequency bands for each emulator type.

Frequency spectrum ranges (MHz)	Total energy for all frequency spectrum (J)	Distribution of energy in each frequency range (J)	Percentage of energy in each frequency range %
<b>Floating electrode PD emulator</b>			
0 - 50	$2.8 \times 10^{-07}$	$3.8 \times 10^{-08}$	14.00
50 - 290		$2.23 \times 10^{-07}$	79.00
290 - 470		$1.2 \times 10^{-08}$	4.40
470 - 800		$4.6 \times 10^{-09}$	1.60
>800		$3.5 \times 10^{-09}$	0.6
<b>Acrylic cylinder internal PD emulator</b>			
0 - 50	$1.32 \times 10^{-08}$	$1.72 \times 10^{-09}$	13.00
50 - 290		$7.26 \times 10^{-09}$	54.60
290 - 470		$3.45 \times 10^{-09}$	26.05
470 - 800		$7.59 \times 10^{-10}$	5.72
>800		$1.1 \times 10^{-11}$	0.63
<b>Acrylic cylinder internal PD emulator filled with transformer oil</b>			
0 - 50	$3.04 \times 10^{-09}$	$5.95 \times 10^{-11}$	1.95
50 - 290		$2.36 \times 10^{-09}$	77.69
290 - 470		$5.47 \times 10^{-10}$	17.98
470 - 800		$5.42 \times 10^{-11}$	1.78
>800		$1.93 \times 10^{-11}$	0.4
<b>Epoxy dielectric internal PD emulator</b>			
0 - 50	$3.38 \times 10^{-08}$	$5.07 \times 10^{-09}$	14.96
50 - 290		$2.59 \times 10^{-08}$	76.69
290 - 470		$2.14 \times 10^{-09}$	6.32
470 - 800		$6.02 \times 10^{-10}$	1.77
>800		$1.00 \times 10^{-10}$	0.24

The percentage of energy in each frequency range for four PD emulator indicate that the main frequency content of the PD discharge for four types of PD emulators in the FSR measurements is situated in the range of 50 MHz – 290 MHz. For example, the total energy of floating electrode PD emulator is 79%, 54% of the total energy of an acrylic cylinder internal PD emulator, 77% of the total energy of an acrylic cylinder internal PD emulator filled with transformer oil, and 77% of the total energy of an epoxy dielectric internal PD emulator. Therefore, the floating electrode PD emulator, acrylic cylinder internal PD

emulator filled with transformer oil, and epoxy dielectric internal PD emulator present approximately the same energy for the FSR measurement with approximately 75% in the range of 50 MHz – 290 MHz than other type of acrylic cylinder internal PD emulator.

- **Frequency bands energy content for a galvanic contact measurement method.**

Example of the three frequency spectrum bands for the galvanic contact measurements of the floating electrode PD emulator type are also show in Figures 4-13 and 4-14.

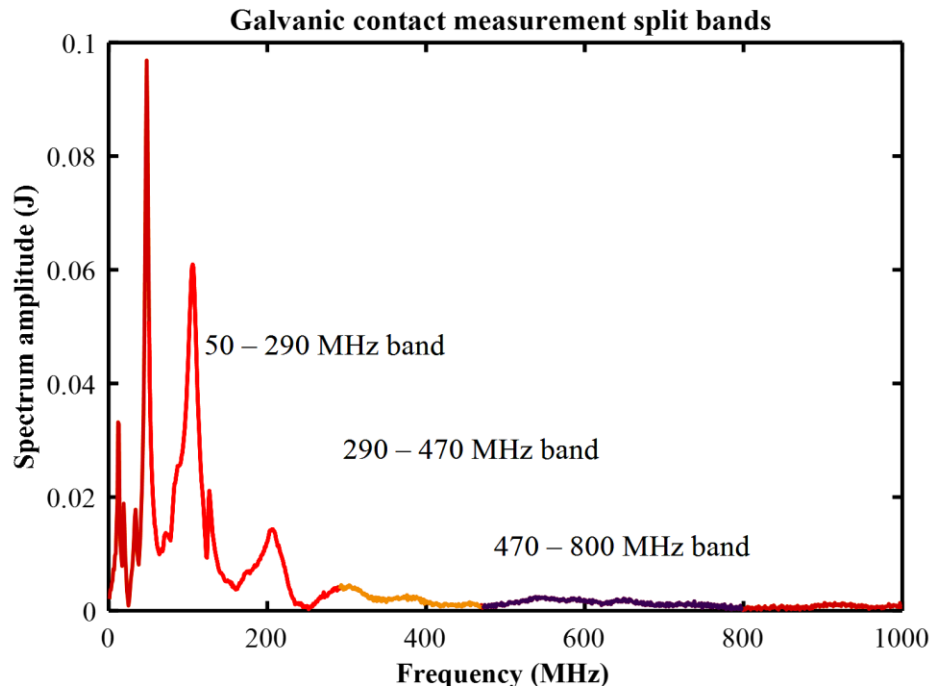


Figure 4-13 Frequency bands energy content for the galvanic contact measurement method.

The frequency spectrum energy contents for bands 0 – 50 MHz and 800 MHz – 1000 MHz is illustrated in Figure 4-15. The total energy in all bands and the percentage of energy present in the four PD emulators in galvanic contact measurements is shown in Table 4-3.

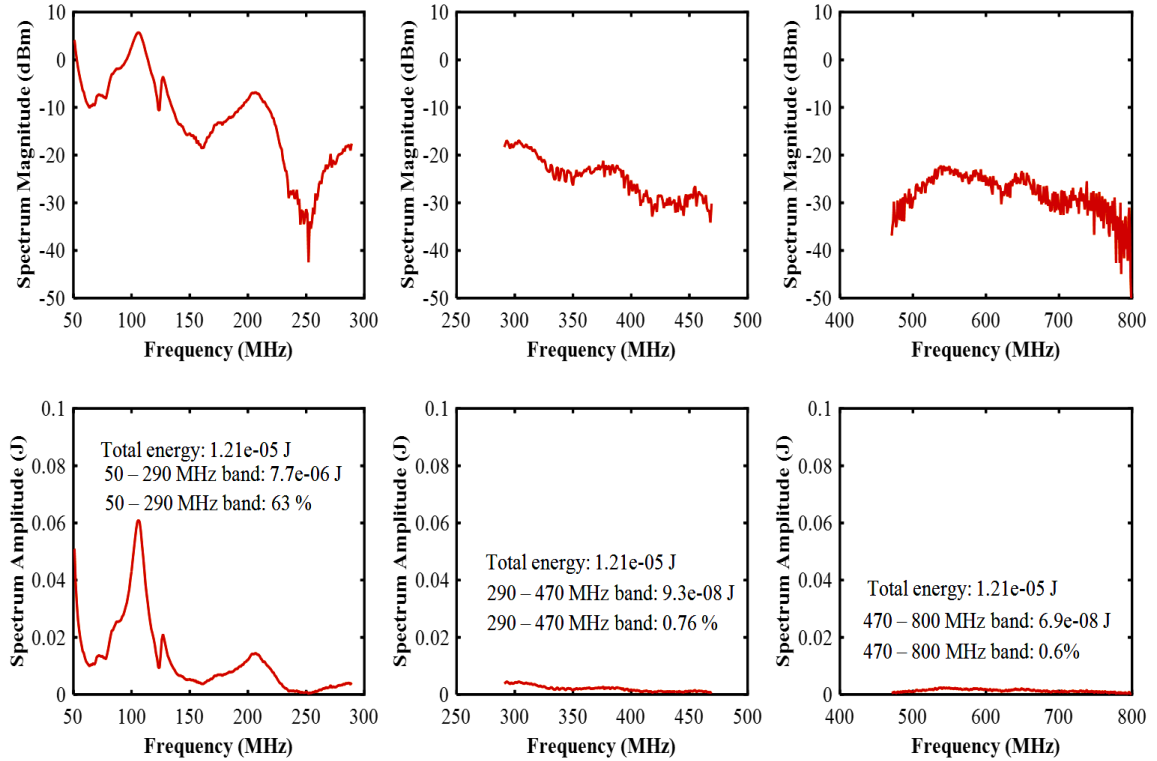


Figure 4-14 Sub-band spectra and energy proportions for the galvanic contact measurement.

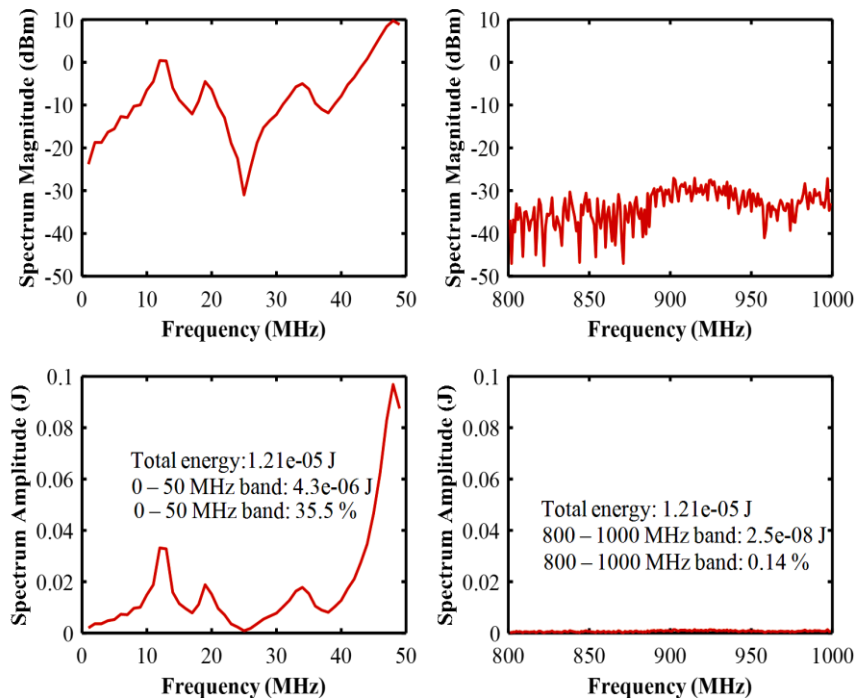


Figure 4-15 Sub-band spectra energy contained in the two frequency bands for the galvanic contact measurement method.

It is observed that most of the energy is concentrated within the initial 290 MHz band in the galvanic contact measurement method. For example, the percentage energy of floating electrode PD emulator in the 50 MHz – 290 MHz is 63%, 42% of the percentage energy of acrylic cylinder internal PD emulator, 60% of the percentage energy of an acrylic cylinder internal PD emulator filled with transformer oil, and 60% of the percentage energy of an epoxy dielectric internal PD emulator. Therefore, in galvanic contact measurement is also the floating electrode PD emulator, an acrylic cylinder internal PD emulator filled with transformer oil, and an epoxy dielectric internal PD emulator present approximately the same energy by approximately 61% than other type of an acrylic cylinder internal PD emulator.

#### 4.5 Cumulative Distribution of Energy

The time-cumulative energies of the PD pulse measurements of the floating electrode PD emulator are shown in Figures 4-16 (a) and (b). The total energy of the FSR pulse is  $2.8 \times 10^{-7} \text{J}$  and the total energy of the galvanic contact pulse is  $1.2 \times 10^{-5} \text{J}$ . The time-cumulative energy of the FSR measurement pulse has less energy than the galvanic contact measurement pulse, as expected, due to transmission losses that are normally unknown in the case of the radiometrically received PD, including the radiation efficiency of the transmitting structure and propagation losses [2].

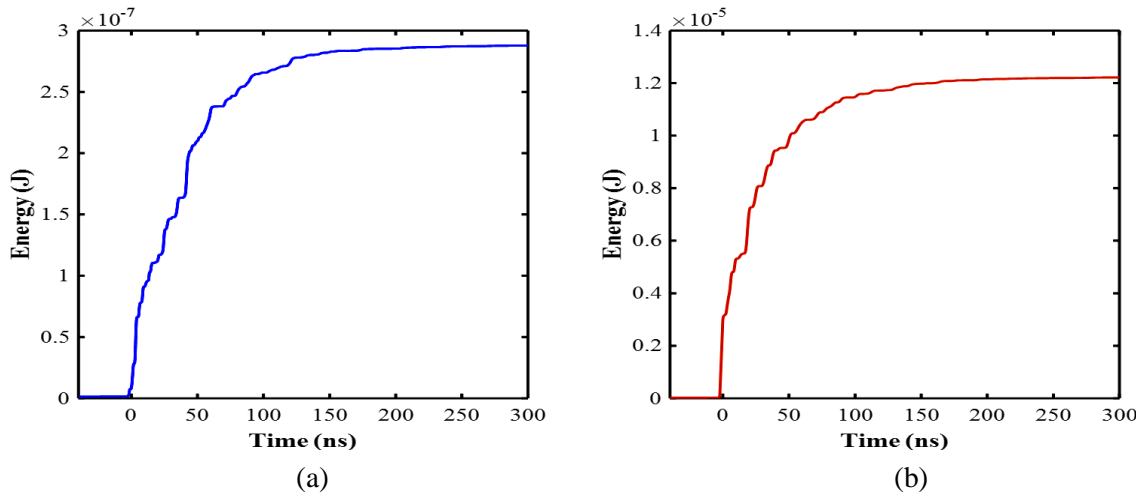


Figure 4-16 (a) Time-cumulative distribution of FSR energy. (b) Time-cumulative distribution of the galvanic contact energy.

Table 4-3 Energy of a galvanic contact measurement frequency bands for each emulator type.

Frequency spectrum ranges (MHz)	Total energy for all frequency spectrum (J)	Distribution of energy in each frequency range (J)	Percentage of energy in each frequency range %
<b>Floating electrode PD emulator</b>			
0 - 50	$1.21 \times 10^{-05}$	$4.3 \times 10^{-06}$	35.50
50 - 290		$7.7 \times 10^{-06}$	63.00
290 - 470		$9.3 \times 10^{-08}$	0.76
470 - 800		$6.9 \times 10^{-08}$	0.6
>800		$2.5 \times 10^{-08}$	0.14
<b>Acrylic cylinder internal PD emulator</b>			
0 - 50	$8.61 \times 10^{-06}$	$4.83 \times 10^{-06}$	56.16
50 - 290		$3.63 \times 10^{-06}$	42.15
290 - 470		$6.96 \times 10^{-08}$	0.80
470 - 800		$6.74 \times 10^{-08}$	0.78
>800		$1.3 \times 10^{-08}$	0.11
<b>Acrylic cylinder internal PD emulator filled with transformer oil</b>			
0 - 50	$1.38 \times 10^{-07}$	$2.04 \times 10^{-08}$	14.79
50 - 290		$8.42 \times 10^{-08}$	60.83
290 - 470		$3.16 \times 10^{-08}$	22.84
470 - 800		$1.72 \times 10^{-09}$	1.24
>800		$1.00 \times 10^{-10}$	0.3
<b>Epoxy dielectric internal PD emulator</b>			
0 - 50	$1.47 \times 10^{-06}$	$4.06 \times 10^{-07}$	27.45
50 - 290		$8.88 \times 10^{-07}$	60.07
290 - 470		$9.25 \times 10^{-08}$	6.25
470 - 800		$7.57 \times 10^{-08}$	5.11
>800		$8.00 \times 10^{-09}$	1.12

## 4.6 Summary

The measurements of PD signals and frequency spectra of FSR and galvanic contact measurements techniques are compared. The signals were analysed in the time domain and frequency domain. The correlation between FSR and galvanic contact measurements signals are calculated using root mean squared error and correlation coefficient. The results show an optical similarity in the time domain signals. Frequency spectra specify that most

of the energy in the PD radiation is content in the band 50 MHz to 800 MHz with most of the radiation energy below a frequency of 290 MHz. However, frequency spectra of FSR and galvanic contact measurements are not identical but sufficiently similar to suggest any diagnostic information residing in the galvanic contact signal is, at least partly, preserved in the FSR signal. Three measurements separate the received FSR measurements and galvanic contact measurements of PD pulses within the 50 MHz – 290 MHz, 290 MHz – 470 MHz and 470 MHz – 800 MHz frequency bands. These two measurement methods confirm that, the energy concentration of the PD signal in the frequency band of 50 MHz – 290 MHz is higher than the energy in the other frequency bands in the four types of PD emulators. The time-cumulative energy of the FSR measurements is lower than the galvanic contact measurement value, as expected, due to free-space received PD including the radiation efficiency of the transmitting structure and propagation losses. Additionally, PD FSR and galvanic contact measurements activity under AC and DC applied voltages at different distances between a PD source and a biconical antenna will be presented in chapter 7. In the next chapter, an absolute radiometric PD intensity measurement will be explored. If absolute PD measurements using FSR methods is shown to be possible, it could lead directly to more convenient and cheaper and continuous condition monitoring of HV insulation in electrical substation.

## CHAPTER 5

### **AN ABSOLUTE RADIOMETRIC PARTIAL DISCHARGE INTENSITY MEASUREMENT**

---

*A calibrate a classical PD apparent charge measurement circuit will be designed and the calculation of apparent charge from a galvanic contact measurement will be demonstrate in this chapter. A novel method of estimating absolute PD activity level from a radiometric measurement by ERP to PD intensity using a PD calibration device is presented. The addresses the calibration of four types of PD emulators required for the development of a PD WSN. Partial discharge emulators are specially constructed: an emulator of the floating-electrode type, an acrylic tube internal PD emulator, an acrylic tube internal PD emulator filled with transformer oil and an epoxy dielectric internal PD emulator.*

---

## 5.1 Introduction

The severity of a deteriorated region generating PD is indirectly correlated to the magnitude of the discharges. The deterioration in the dielectric depends on the energy dissipated in the dielectric rather than the energy dissipated in the discharge. It is difficult to identify the energy intensity from measurements made at the terminals of a HV equipment. This imposes a limitation on the effectiveness of a PD measurement method to predict the rate of degradation or the remaining plant a life [65, 168].

Free-space radiometric PD measurements can be used to locate insulation defects [31, 49]. The monitoring of the relative intensity of such PD and in particular, its time evolution has been used to predict failure of HV equipment [164]. Current pulse changes shape due to dispersion as it propagates e.g. along a cable. Area (or strength) of pulse changes much less so PD pulse strength is measured in apparent charge,  $Q$  (pC). A measurement calibration technique is proposed for the measurement of the quantity of apparent charge by injecting known short duration current pulses across the test object. This approach uses a calibrated charge injection device to excite a PD emulator. Four types of PD emulators are specially constructed: an emulator of the floating-electrode type, an acrylic tube internal PD emulator, an acrylic tube internal PD emulator filled with transformer oil and epoxy dielectric internal PD emulator, which are presented in sections 3.4, 3.5 and 3.6. The ERP from the excited emulator is measured using a biconical antenna with known antenna factor. A novel method of estimating absolute PD activity level from a radiometric measurement is by relating ERP to PD intensity using a PD calibration device [1]. The benefits if absolute PD measurements using FSR methods is shown to be possible, it could lead directly to more convenient and cheaper and continuous condition monitoring of HV insulation in electrical substation. The work to be reported describes the calibration of PD emulators required for the development of a PD WSN such that absolute PD intensity might be inferred from the radiometric measurements. Measurements have been repeated the four different PD emulators.

## 5.2 PD Calibration

PD intensity, or strength, is specified by the apparent charge transferred during a discharge event. It is typically measured in picocoulombs or nanocoulombs. Strictly, the apparent charge is that charge which, if injected into the terminals of the device under investigation, would result in the same response of the measurement instrument as the response to the PD event [51, 164]. The charge injected from the calibrator into the test circuit enables the apparent charge to be determined. The charge is given by formula 5-1 and 5-2:

$$Q = \int_0^T i(t) dt \quad (5-1)$$

where  $Q$  is charge and  $i(t)$  is current.

Conversion of a current impulse to a voltage drop in a resistor, results in the relationship:

$$Q = \frac{1}{R} \int_0^T u(t) dt \quad (5-2)$$

where  $R$  is resistor and  $u(t)$  is voltage across this resistor.

The conventional calibration procedure involves the injection of a known calibration pulse into the PD source. This means that only offline PD testing systems can be calibrated. The calibration system assumes the measured PD pulse to be linearly related to the charge value. The HVPD pC calibrator is connected to a DSO as shown in Figure 5-1.

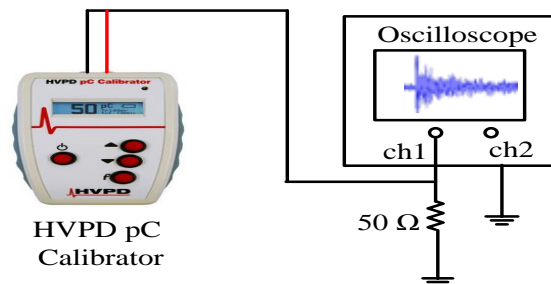


Figure 5-1 Injection of a known calibration pulse into a DSO.

The pulse that is shown in Figure 5-2 was measured using the DSO with an input impedance of 1 MΩ. Figure 5-3 is a plot of the integral of the current pulse resulting from

the range of calibration pulses as provided by the HVPD pC calibrator device as shown in Table 5-1.

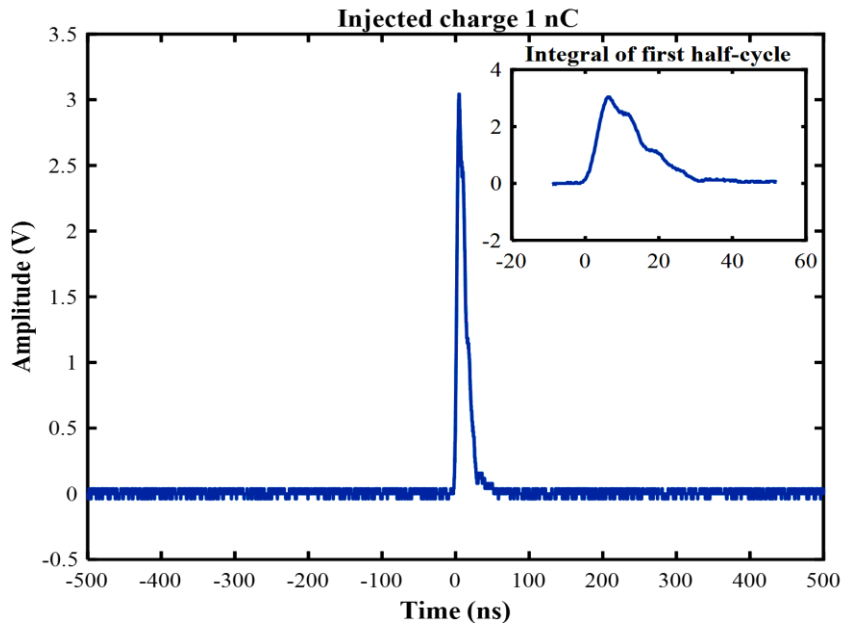


Figure 5-2 Example of current waveform for an injected charge into a DSO (1 nC.).

Table 5-1 Relationship between injected charge and calculated charge.			
Injected pulse charge	First half-cycle pulse duration (ns)	Calculated charge	Peak galvanic voltage (V)
1pC	69.0	1.5 pC	0.004
2pC	32.0	3 pC	0.011
5 pC	37.0	6.8 pC	0.023
10 pC	45.0	10.9 pC	0.037
20 pC	53.5	15 pC	0.032
50 pC	63.4	33 pC	0.09
100 pC	53.3	99.7 pC	0.32
200 pC	59.6	127 pC	0.28
500 pC	54.0	315 pC	0.9
1 nC	59.0	0.9 nC	3.04
2 nC	49.0	1 nC	2.02
5 nC	47.5	3 nC	8.5
10 nC	36.0	9.8 nC	33.2
20 nC	270.0	18.6 nC	9.8
50 nC	330.0	49 nC	26.8
100 nC	360.0	100 nC	50.2

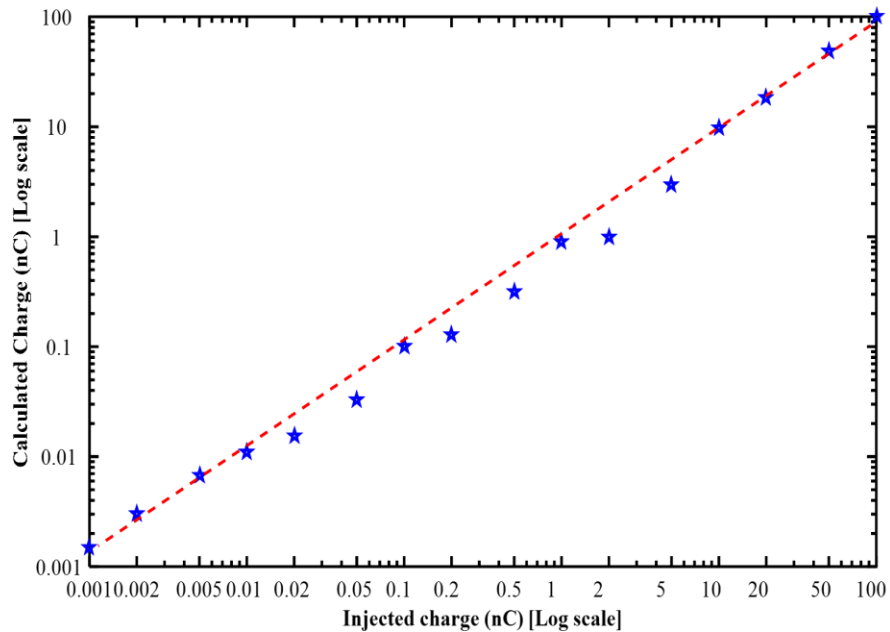


Figure 5-3 Integral of measured current pulse (calculated charge) versus calibration device injected charge.

Artificial PD sources contain electrodes connected to a HV power supply. Electrodes of different shapes have been used to produce PDs. Four different types of PD sources were created. The first type is a floating-electrode PD emulator. The second three types, of different internal discharges, are: firstly, a discharge in a void within perspex insulator sample without filling oil and secondly a discharge in a void within perspex insulator sample with filling transformer oil. The third type is an internal PD emulator within an epox glass insulator sample. The four types of artificial PD encountered in power systems were tested in the laboratory and there was no change in the environment between PD sources calibration.

### 5.2.1 Calibration of floating-electrode PD emulator

The known charge is injected into the floating-electrode PD emulator that is shown in Figure 5-4. The pulses, which are injected into the terminals of the floating-electrode PD emulator, were measured using the DSO. Figure 5-5 is a plot of the integral of the current pulse resulting from the range of calibration pulses as provided by the calibrator device.

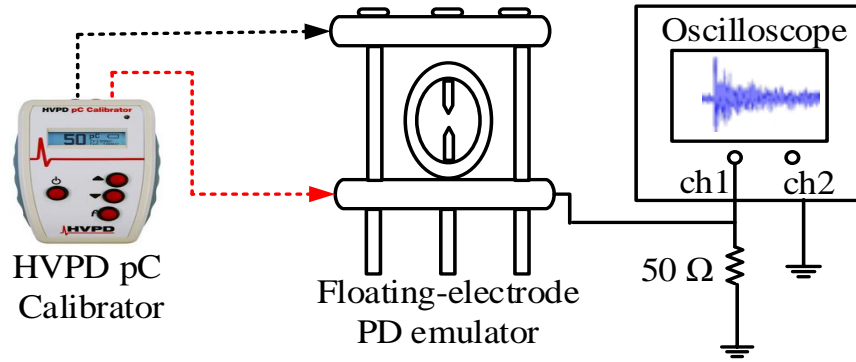


Figure 5-4 Injected charge across the terminals of floating-electrode PD source.

Table 5-2 compares injected charge, calculated charge and peak galvanic voltage of the current pulse waveform. The entries from 1 pC to 5 pC were too noisy to make reliable estimates of apparent charge.

Table 5-2 Relationship between injected charge and calculated charge of floating-electrode PD emulator.			
Injected pulse charge	First half-cycle pulse duration ((ns)	Calculated charge	Peak galvanic voltage (V)
1pC	x	x	x
2pC	x	x	x
5 pC	x	x	x
10 pC	43.0	11 pC	0.03
20 pC	52.0	15 pC	0.027
50 pC	58.0	36 pC	0.08
100 pC	45.1	107 pC	0.28
200 pC	51.6	133 pC	0.24
500 pC	47.8	344pC	0.8
1 nC	43.0	0.97 nC	2.57
2 nC	48.8	1.02 nC	1.78
5 nC	45.4	3.3 nC	7.5
10 nC	42.0	10.9 nC	28.85
20 nC	308.0	18.5 nC	9.3
50 nC	289.0	49 nC	26.0
100 nC	353.0	100 nC	50.2

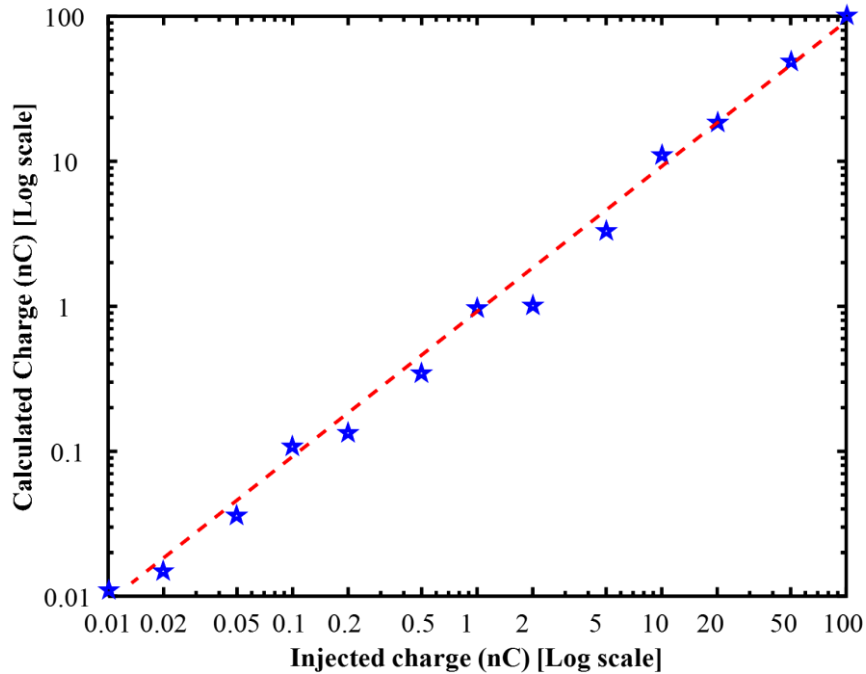


Figure 5-5 Resulting of calculated charge versus injected charge of floating-electrode PD emulator.

Classical PD measurements, as described in [55] use a galvanic connection to conduct the PD current pulse (or a voltage pulse that is proportional to the current pulse) via a cable to the measurement instrument. If the measurement is sufficiently broadband for the pulse to remain baseband in nature then it is easily, and unambiguously, integrated to find the apparent charge. If the pulse oscillates due to inductance and capacitance of the PD-source/measurement-system combination, however, then the question arises as to how best to assess the apparent charge. The integral from the start of the measured pulse to its first zero crossing has been used as a measure of apparent charge [164, 169]. This metric has been investigated here by comparing it with a variety charges injected into the emulator using the HVPC calibrator. The measurement circuit applied to the floating electrode emulator is shown in Figure 5-6. A typical observed waveform is shown in Figure 5-7.

Table 5-3 compares injected charge and charge inferred from the integral of the oscillating waveform over the first half cycle. It also shows the peak voltage of the oscillating waveform. The entries from 1 pC to 20 pC were too noisy to make reliable estimates of apparent charge. The accuracy of the first half-cycle method has been validated in practice

by comparing to the known calibrator charge value when the calibrator is connected to the measurement setup. Apparent charge is calculated from galvanic measurements using the first half-cycle integration method. The apparent charge is determined by given formula 5-1 and 5-2. The Trapezoidal numerical integration method is used as function of matlab. An example of injected 1nC into setup circuit by applying floating-electrode PD emulator is calculated. The integration time of the first half-cycle is (0 and  $4.6 \times 10^{-8}$ ), the resistor  $R$  is  $3.7 \Omega$ , and  $(V)$  is voltage across this resistor as vectors. The result of injected charge is 1.5 nC. Figure 5-8 shows the calculated (first half-cycle) charge against the charge injected by the calibrator [164].

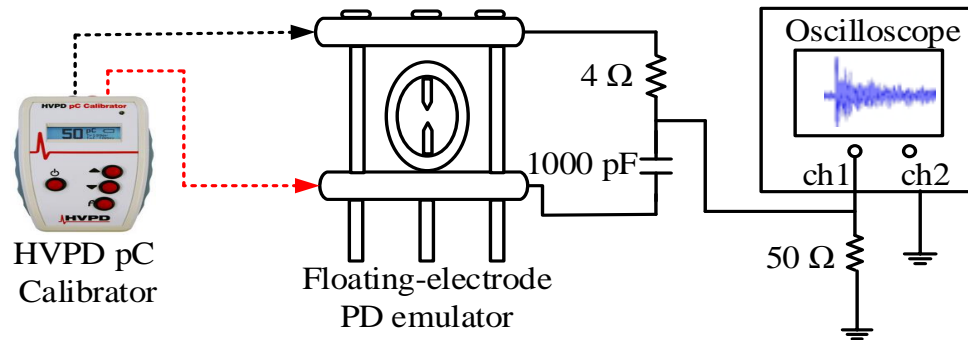


Figure 5-6 Measurement circuit for emulator calibration.

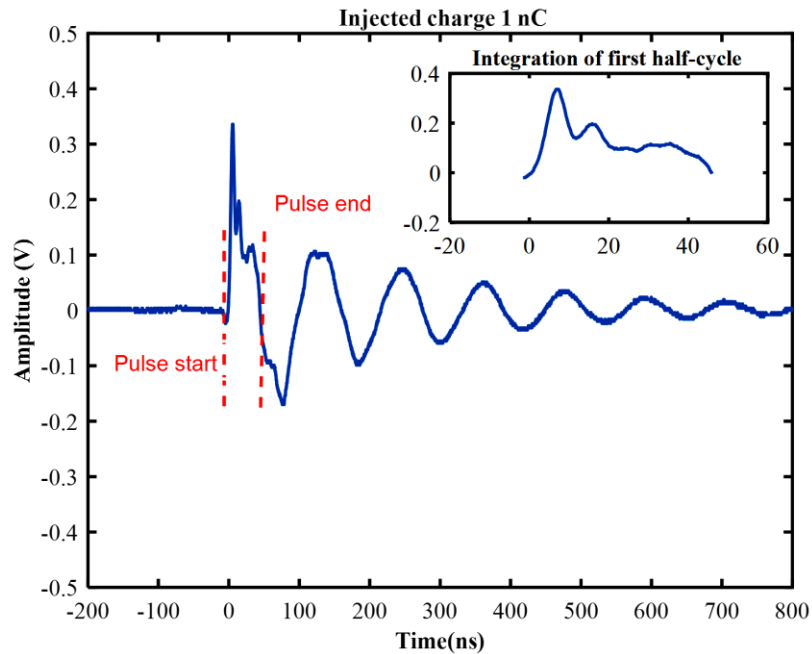


Figure 5-7 Measured waveform for an injected charge of 1 nC.

It is clear from Figure 5-8 that the first half cycle integral is linearly related to the injected charge from the calibrator. By extension, we assume that this linear relationship will hold when the charge is injected by a PD event.

Table 5-3 Relationship between injected charge and calculated charge across measured circuit.			
Injected charge	First half-cycle pulse duration (ns)	Calculated charge	Peak galvanic voltage (V)
1pc	x	x	x
2pC	x	x	x
5 pC	x	x	x
10 pC	x	x	x
20 pC	x	x	x
50 pC	48.0	50.8 pC	0.013
100 pC	47.4	119 pC	0.04
200 pC	48.4	206 pC	0.03
500 pC	45.2	544pC	0.10
1 nC	47.6	1.5 nC	0.34
2 nC	46.4	1.6 nC	0.21
5 nC	44.3	5 nC	0.88
10 nC	46.5	16 nC	3.32
20 nC	85.5	14 nC	0.96
50 nC	84.6	35 nC	2.77
100 nC	83.1	72 nC	5.77

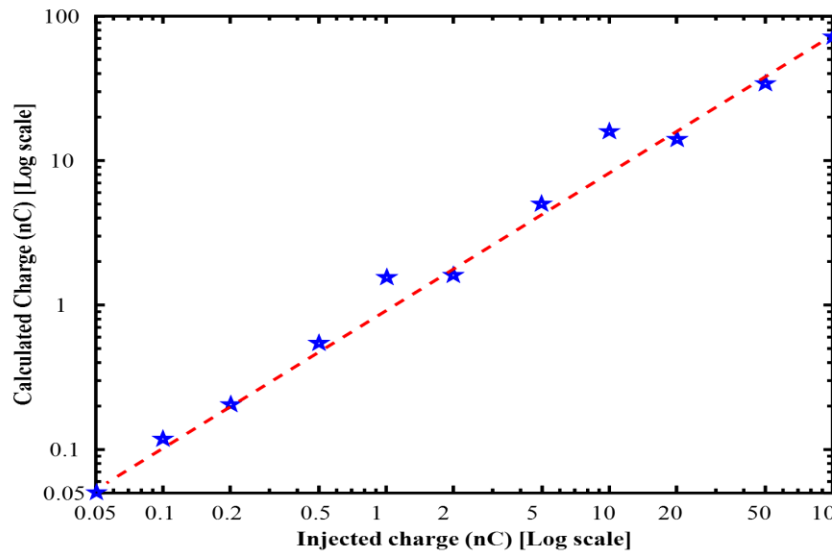


Figure 5-8 Calculate charge versus specified charge of charge injection device.

It is not obvious that the above can be easily extended to signals radiated by PD events rather than those galvanically connected to a measurement system. This is, at least in part, because the RF signal at the terminals of a receiving antenna will generally be related to a time-derivative of the PD current pulse rather than a time-integral. Furthermore, there are numerous transmission losses that are generally unknown in the case of the radiometrically received PD including the radiation efficiency of the transmitting structure and propagation losses [164].

Measurements of radiometrically, and galvanically, observed PD signals were undertaken with the measurement system shown in Figure 3-1. These measurements were made using a PD emulator and 50 Hz power supply voltage of 15 kV RMS. Figure 5-9 illustrates a galvanic contact measurement signal and galvanic contact measurement frequency spectrum.

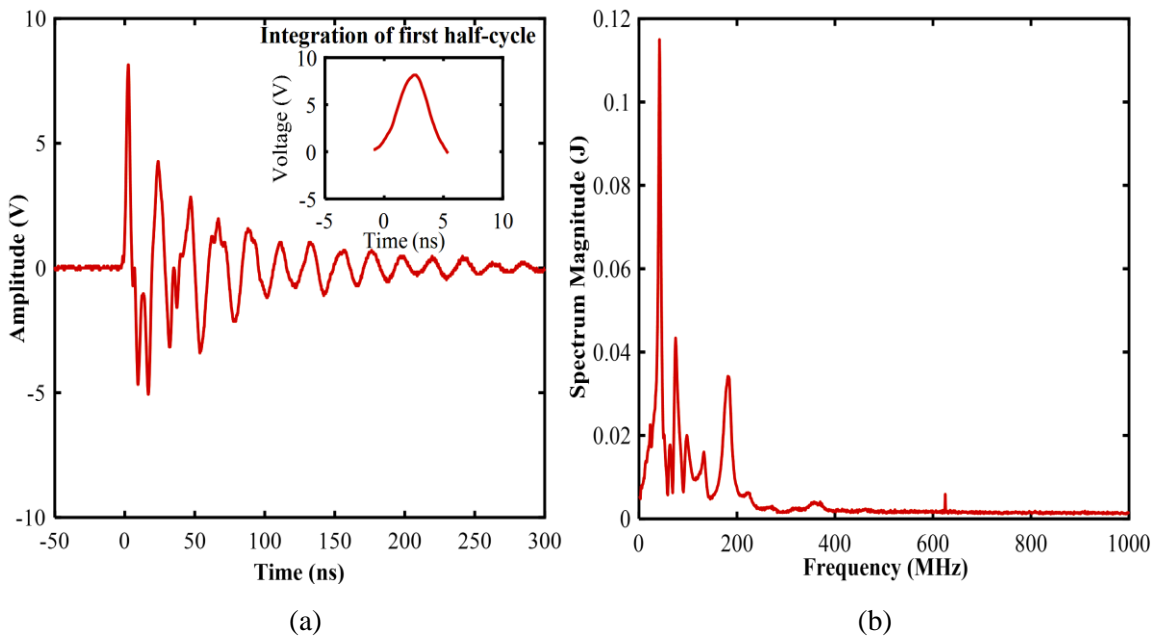


Figure 5-9 Floating-electrode PD emulator signal (a) a galvanic contact measurement pulse and (b) Frequency spectrum of galvanic contact measurement.

Figure 5-10 shows a floating-electrode PD emulator signal FSR measurement pulse. Figure 5-11 shows the average frequency spectrum of the FSR measurements. The FSR measurements were made at four distances from the PD source.

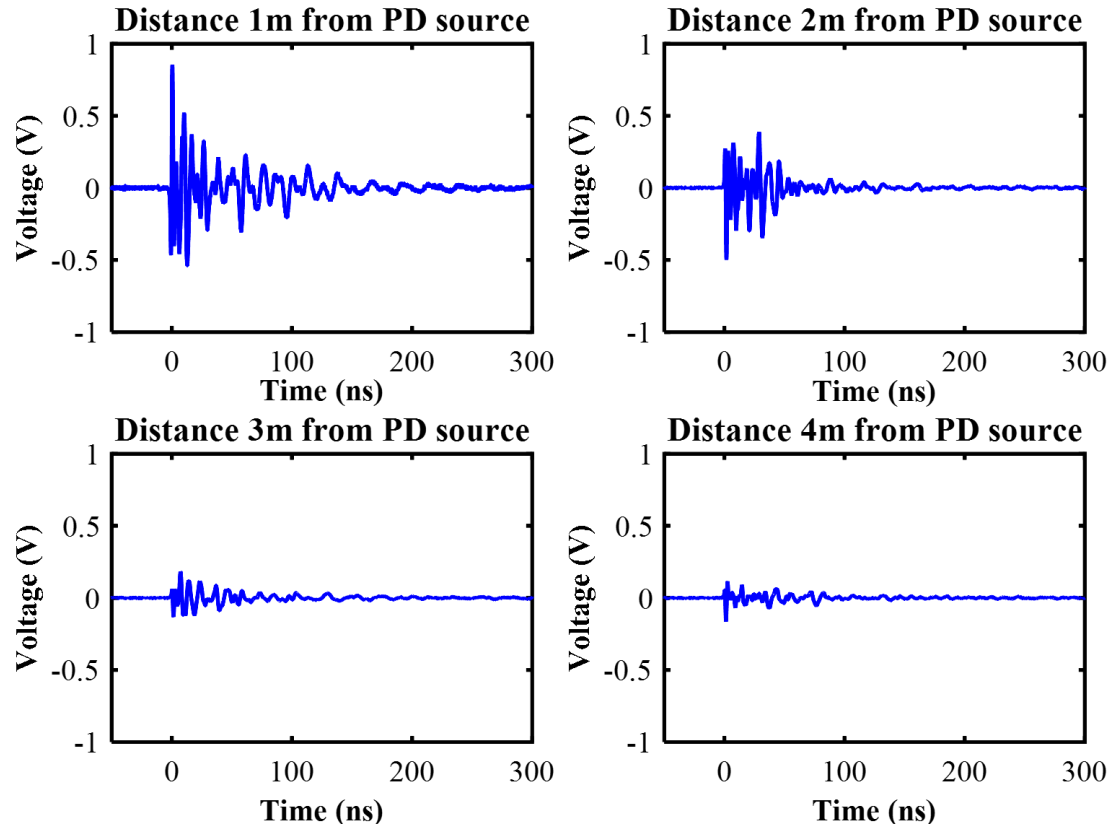


Figure 5-10 Floating-electrode PD source signal FSR measurement pulse.

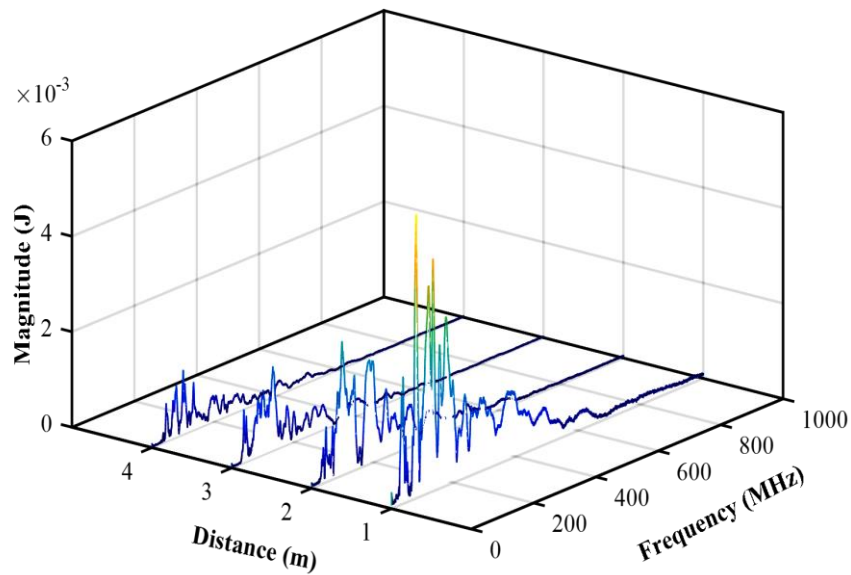


Figure 5-11 Average frequency spectrum of FSR measurements at 15 kV measurements for four locations of receiving antenna from floating-electrode PD emulator.

Table 5-4 shows the variation with distance  $d$  of the received signal peak voltage, the calculated charge (from the first half-cycle integral of the received signal) and the calculated effective radiated power (ERP) for the floating electrode PD emulator. The range of the antenna from the PD source was varied from 1 m to 4 m in steps of 1 m [164]. The ERP of the emulator is estimated from the received field strength  $E$  by using the free-space propagation formula [1, 170, 171]:

$$E(\text{dB}\mu\text{V}/\text{m}) = 107 + \text{ERP}(\text{dBm}) - 20 \log_{10}d(\text{m}) \quad (5-3)$$

where  $E$  is the electric field strength, 107 is constant number used in free-space propagation formula,  $\text{ERP}$  is the effective radiated power and  $d$  is the PD source distance from the receiving antenna.

Estimated peak ERP in dBm is calculated from FSR measurements using the free-space propagation formula for short distances together with the measured antenna factor of the receiving biconical antenna and is seen in Table 5-4. An example of calculated peak ERP at distance 1 m received signal peak voltage is 0.77 V with known antenna factor 17 dB/m is showed below:

$$\text{dB}\mu\text{V} = 20 \log \frac{\text{mV}}{1\mu\text{V}}$$

$$\text{dB}\mu\text{V} = 20 \log(0.77 \times 10^6)$$

$$\text{dB}\mu\text{V}/\text{m} = \text{dB}\mu\text{V} + \text{antenna factor}$$

$$E = 117.7 + 17 = 134.7 \text{ dB}\mu\text{V}/\text{m}$$

By using the free-space propagation formula (5-3)

$$E(\text{dB}\mu\text{V}/\text{m}) = 107 + \text{ERP}(\text{dBm}) - 20 \log_{10}d(\text{m})$$

$$134.7 = 107 + \text{ERP} - 20 \log_{10}(1)$$

$$\text{ERP} = 27.7 \text{ dBm}$$

It seems at least possible that an estimate of ERP may represent a means of inferring absolute PD intensity (i.e., apparent charge) from a remote radiometric measurement such as those described in [49]. Apparent charge is estimated from the galvanic contact

measurement method, while the FSR method is used for the estimation of the ERP of the PD source.

Table 5-4 Concurrent measurements of FSR and galvanic measurements using the floating-electrode PD emulator.

Power supply voltage (kV)	Galvanic measurement	—	Galvanic mean peak voltage (V)	Galvanic mean peak voltage (dB $\mu$ V)	Galvanic measurement standard deviation (V)	First half-cycle duration (ns)	Calculated charge (nC)
		—	6.57	136.3	2.29	6.9	5.3
15	FSR measurement	Antenna - emulator range (m)	FSR mean peak voltage (V)	FSR mean peak voltage (dB $\mu$ V)	Peak electric field strength (dB $\mu$ V/m)	Peak ERP (dBm)	Standard deviation (V)
		1	0.77	117.7	134.7	27.7	0.30
		2	0.35	110.8	127.9	26.8	0.09
		3	0.179	105.05	122.05	24.5	0.06
		4	0.129	102.2	119.2	24.2	0.03

Figure 5-12 displays the measured FSR peak voltage, the calculated field strength and the calculated ERP plotted versus distance  $d$ . In this experiment, the apparent peak ERP varies from 27.7 dBm at a range of 1 m to 24.2 dBm at a range of 4 m. An example for 12 locations of antenna distance from PD source is shown in appendix C. The approximate value of ERP for the floating electrode PD emulator is in the range of 25-27 dBm, however it is safer to assume a ‘far-field’ value of around 25 dBm. The variation observed in Figure 5-12 are due to near field and/or multipath effects. In principle, the ERP in Figure 5-12 (c) should be independent of distance. If it were independent of distance then, in a radiometric PD location system such as those described in [20, 49] there seems to be the possibility of inferring an absolute PD intensity (in terms of apparent charge) from a remote radiometric estimate of ERP [164].

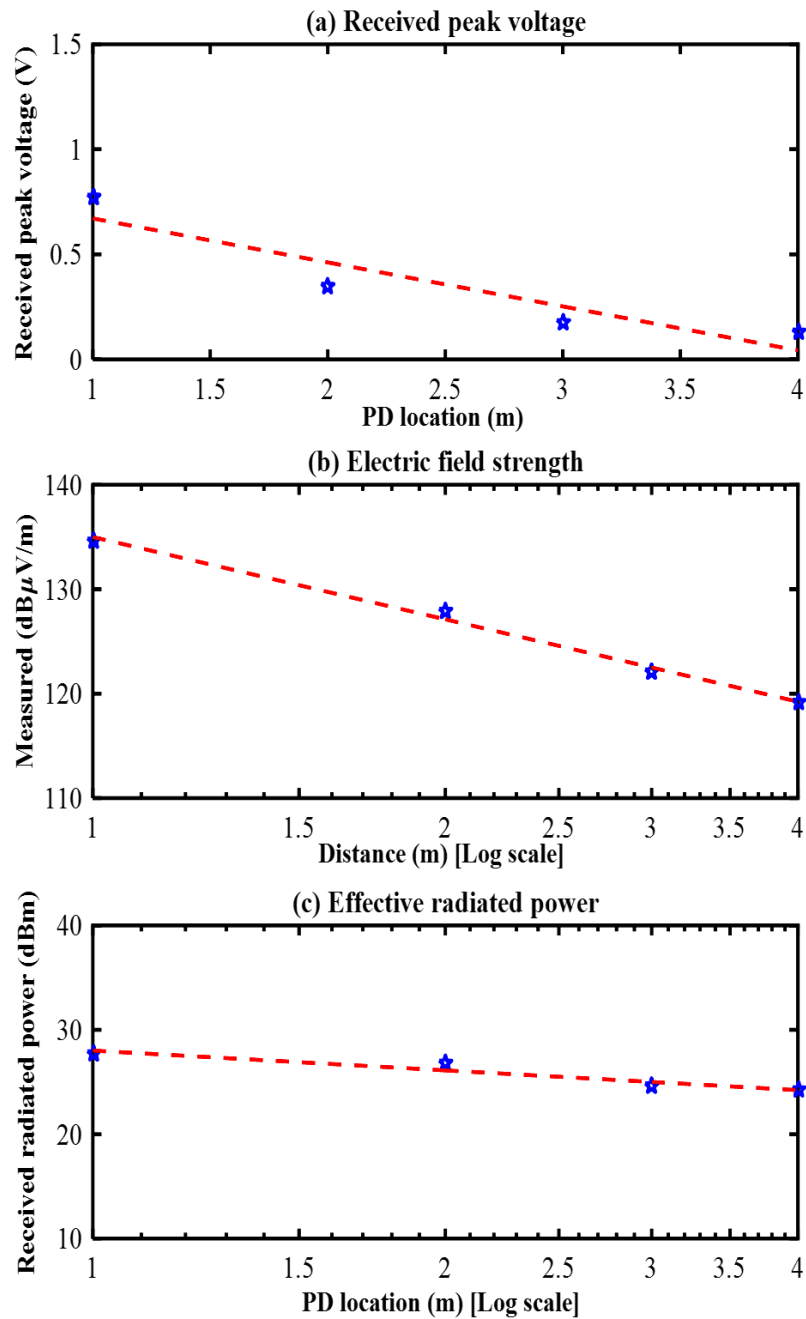


Figure 5-12 (a) Received peak voltage, (b) Electric field strength and (c) ERP as a function of (floating-electrode PD emulator) – antenna distance from emulator.

### 5.2.2 Calibration an acrylic tube internal PD emulator

Figure 5-13 setup was used for calibrating an acrylic tube internal PD source with transformer oil filling and without oil filling. A charge injection device injected a charge

into the terminals of the acrylic tube internal PD source. The pulses were measured using a DSO with an input impedance of 1 M $\Omega$ . Figure 5-14 shows graph of calculated charge versus injected charge of acrylic tube internal PD emulator.

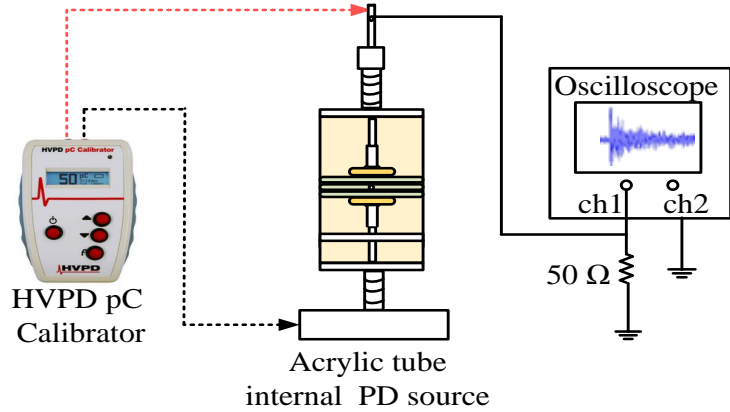


Figure 5-13 Injected charge across the terminals of an acrylic tube internal PD emulator.

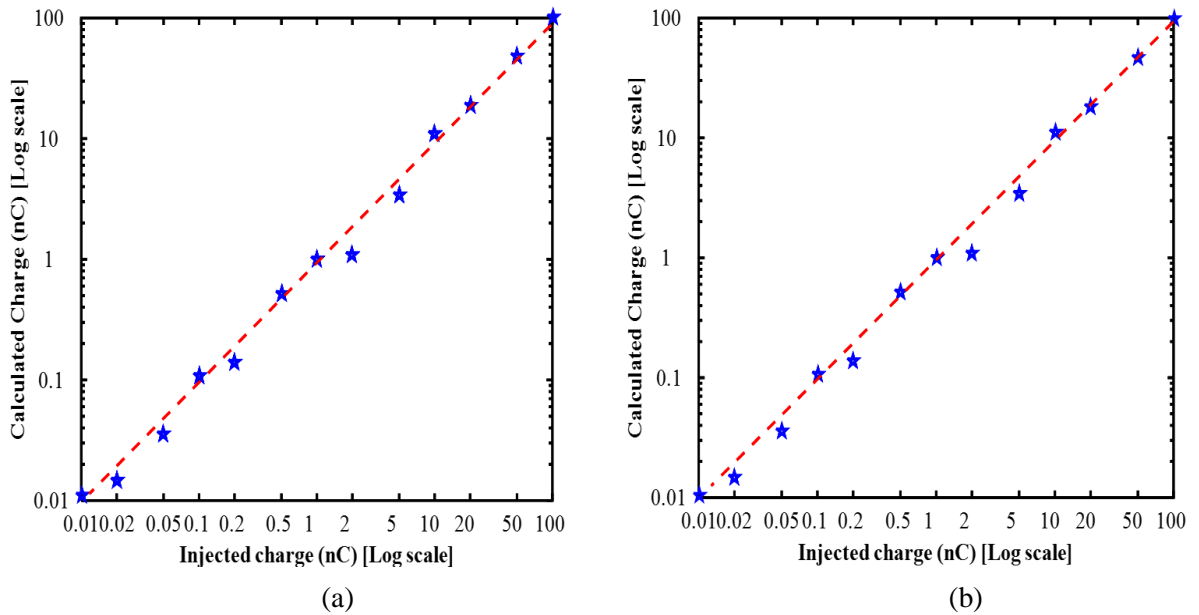


Figure 5-14 Graph of calculated charge versus injected charge of an acrylic tube internal PD emulator (a) without oil filling and (b) with oil filling.

Table 5-5 compares the injected charge and the charge inferred from the integral of the oscillating waveform over the first half cycle. However, it was difficult to distinguish the signals recorded which came from the 1 pC to 5 pC discharges or even from background

noise in order to make reliable estimates of apparent charge in both cases. The first half – cycle duration of 20 nC, 50 nC and 100 nC becomes larger due to a larger duration of the injected pulses from the calibration device. The peak galvanic voltage increases with increases the injected charge value which is injected from the calibration device. It is clear from Figure 5-14 that the calculated charge from the integration of the current pulse is linearly related to the true injected charge from the calibrator for both cases.

Table 5-5 Relationship between injected charge and calculated charge across the terminals of an acrylic tube internal PD emulator.						
Injected charge	Acrylic tube internal PD source without oil filling			Acrylic tube internal PD source with oil filling		
	First half-cycle duration (ns)	Calculated charge	Peak galvanic voltage (V)	First half-cycle duration (ns)	Calculated charge	Peak galvanic voltage (V)
10 pC	50.0	10.9 pC	0.024	49.0	10.5 pC	0.026
20 pC	51.6	15 pC	0.022	51.0	14.6 pC	0.022
50 pC	52.7	36 pC	0.064	52.7	35.6 pC	0.066
100 pC	47.8	108 pC	0.22	47.8	108 pC	0.23
200 pC	53.0	139 pC	0.22	55.0	138 pC	0.21
500 pC	46.4	520pC	0.71	51.48	518pC	0.69
1 nC	47.0	1 nC	2.2	47.0	1 nC	2.2
2 nC	54.7	1.1 nC	1.66	53.7	1.1 nC	1.66
5 nC	50.3	3.4 nC	6.8	50.0	3.4 nC	6.6
10 nC	46.7	11 nC	25.3	46.0	11 nC	25.3
20 nC	292.0	19nC	9.8	292.0	18.3nC	9.17
50 nC	282.0	48nC	25.3	282.0	46.6nC	24.9
100 nC	300.0	100 nC	53.0	302.0	98.5 nC	52.0

The experimental measurement circuit calibration of acrylic tube internal PD source with oil filling and without oil filling is shown in Figure 5-15. The integral from the start of the measured pulse to its first zero crossing has been used as a measure of apparent charge.

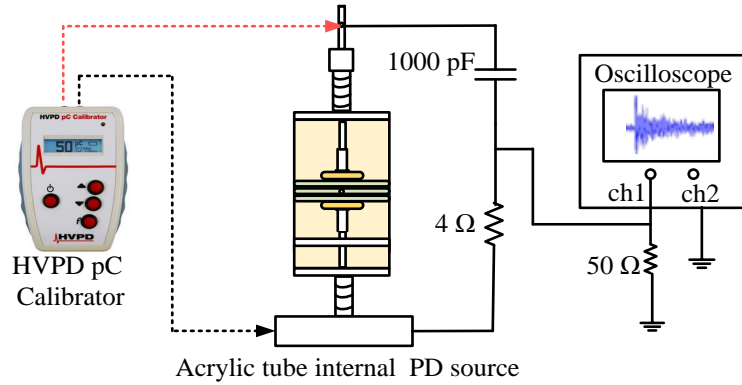


Figure 5-15 Experimental measurement circuit calibration of acrylic tube internal PD emulator.

The relationship between injected charge and calculated charge is shown in Table 5-6. The entries from 1 pC to 20 pC were too noisy to estimates of apparent charge. Figure 5 -16 is good evidence that the first half-cycle integral provides a useful estimate of injected charge showed in both cases. By extension we assume that the linear relationship will hold for the apparent charge.

Table 5-6 Relationship between injected charge and calculated charge across the terminals of a measurement circuit with an acrylic tube internal PD emulator.						
Injected charge	Acrylic tube internal PD source without oil filling			Acrylic tube internal PD source with oil filling		
	First half-cycle duration (ns)	Calculated charge	Peak galvanic voltage (V)	First half-cycle duration (ns)	Calculated charge	Peak galvanic voltage (V)
50 pC	38.5	37.3 pC	0.01	32.6	44 pC	0.01
100 pC	38.8	119 pC	0.04	23.7	117 pC	0.05
200 pC	42.3	178 pC	0.03	40.9	181 pC	0.03
500 pC	39.1	502pC	0.12	36.0	511pC	0.13
1 nC	32.6	1.3 nC	0.39	32.1	1.4 nC	0.44
2 nC	43.8	1.56 nC	0.23	44.0	1.75 nC	0.28
5 nC	42.7	5.1 nC	1.05	41.7	5.1 nC	1.17
10 nC	40.9	16 nC	3.83	24.0	12 nC	4.19
20 nC	83.0	14 nC	1.06	83.0	13.5 nC	1.12
50 nC	79.8	35 nC	2.76	79.7	32 nC	2.92
100 nC	81.0	72 nC	6.0	81.2	69 nC	6.40

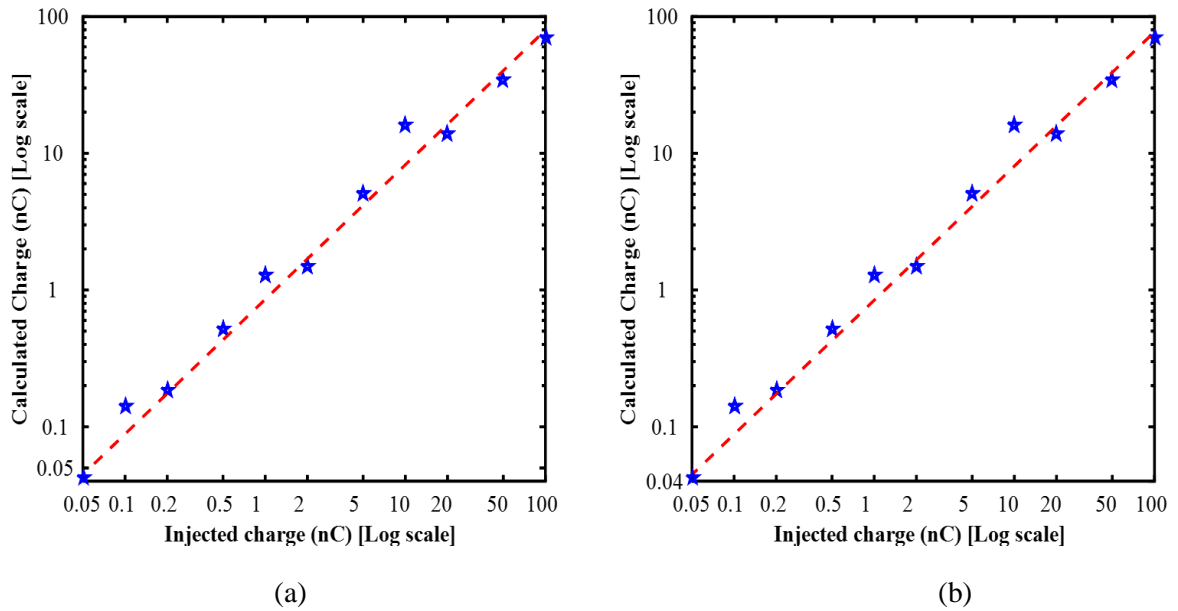


Figure 5-16 Graph of calculated charge versus injected charge of acrylic tube internal PD emulator (a) without oil filling and (b) with oil filling.

The apparatus used to simultaneously capture FSR PD measurements and galvanic contact measurements using an acrylic tube internal PD emulator are shown in Figure 5-17.

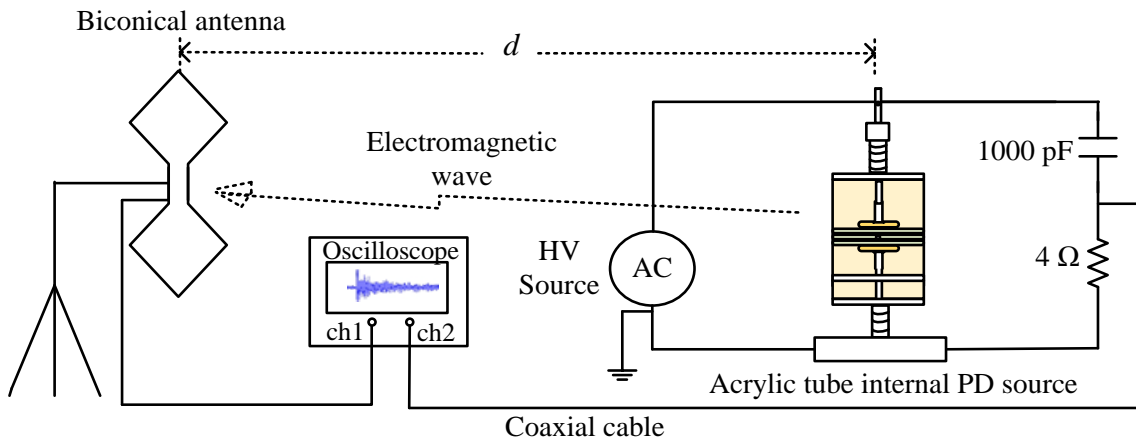


Figure 5-17 Measurement apparatus using an acrylic tube internal PD emulator.

The measurements were made using an acrylic tube internal PD emulator and a 50 Hz power supply voltage of 20 kV RMS. The FSR measurements were made at four distances from the acrylic tube internal PD emulator and receiving antenna. In this experiment, two cases of measurement are used (without transformer oil filling and with oil filling). The permittivity is ( $\epsilon_r$ , air = 1,  $\epsilon_r$ , oil  $\approx$  2.3). Free space radiometric and galvanic contact

measurement results without oil filling will present first [1]. Figure 5-18 shows an FSR measurement pulse and Figure 5-19 illustrates the average frequency spectrum.

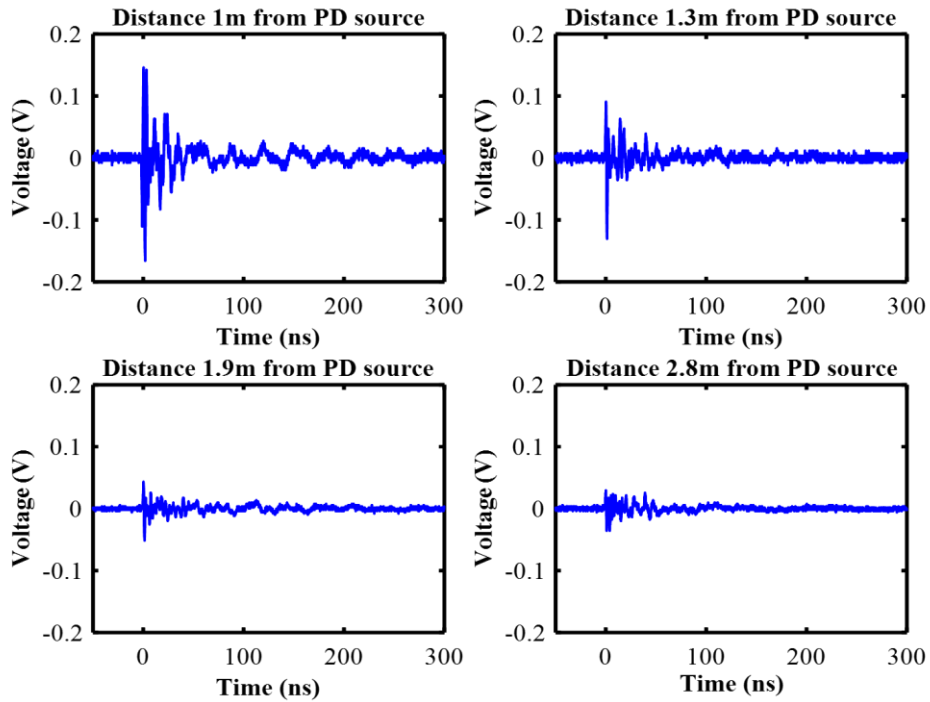


Figure 5-18 An acrylic tube internal PD emulator without oil filling FSR measurement pulse.

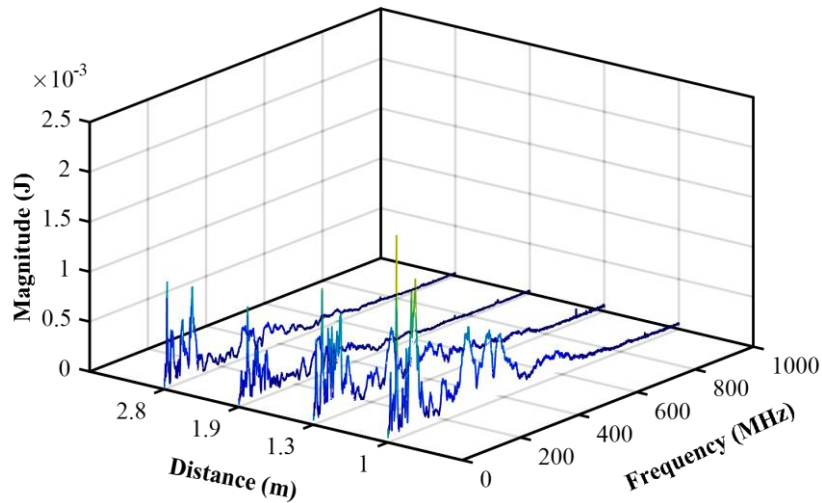


Figure 5-19 Averaged frequency spectra of FSR measurements at 20 kV for four locations of the receiving antenna from an acrylic tube internal PD emulator without oil filling.

Figure 5-20 shows the galvanic contact measurement signal and frequency spectrum of acrylic tube internal PD emulator without oil filling. Spectral analysis in FSR and galvanic

contact measurements shows that for air discharges, most of the energy is present between 50 MHz – 290 MHz.

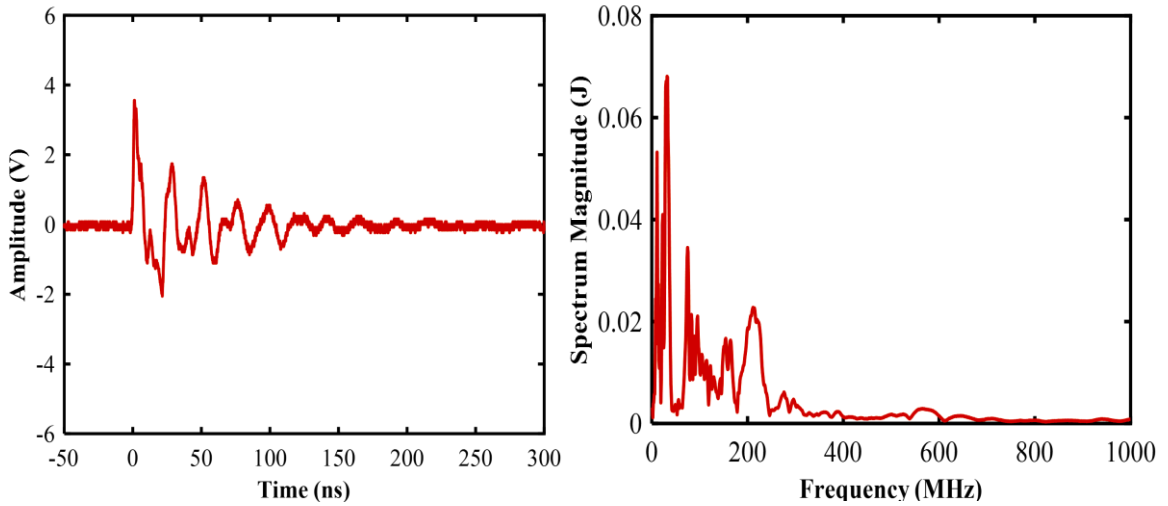


Figure 5-20 A galvanic contact measurement signal and average frequency spectrum of an acrylic tube internal PD emulator without oil filling.

Free space radiometric and galvanic contact measurement results of acrylic tube internal PD emulator with oil filling are presented. The PD event and frequency spectra of galvanic contact measurements are shown in Figures 5-21.

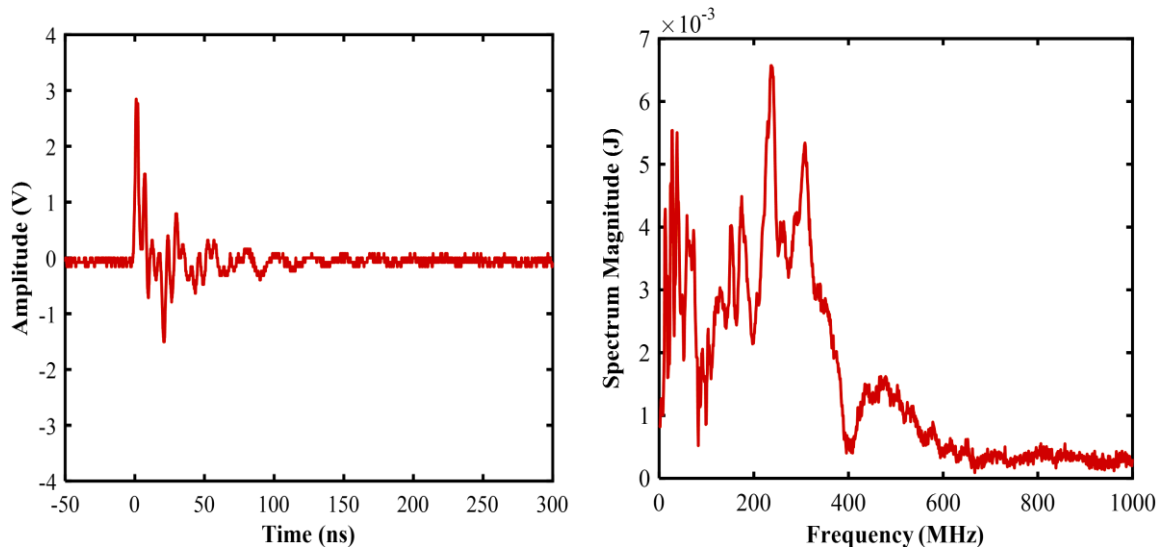


Figure 5-21 A galvanic contact measurement signal and frequency spectrum of acrylic tube internal PD emulator with oil filling.

Figures 5-22 and 5-23 show FSR measurements for PD time domain signals and the average frequency spectra. Free space radiometric and galvanic contact spectra analysis shows that for oil discharges, most of the energy is located between 50 MHz – 300 MHz.

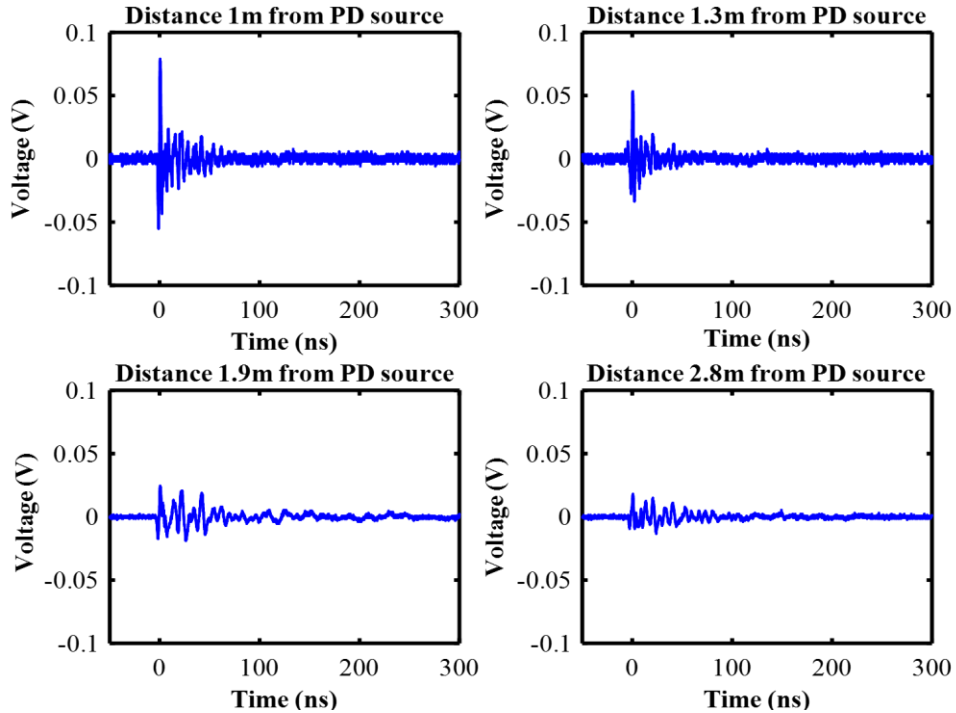


Figure 5-22 FSR measurement pulse of an acrylic tube internal PD emulator with oil filling.

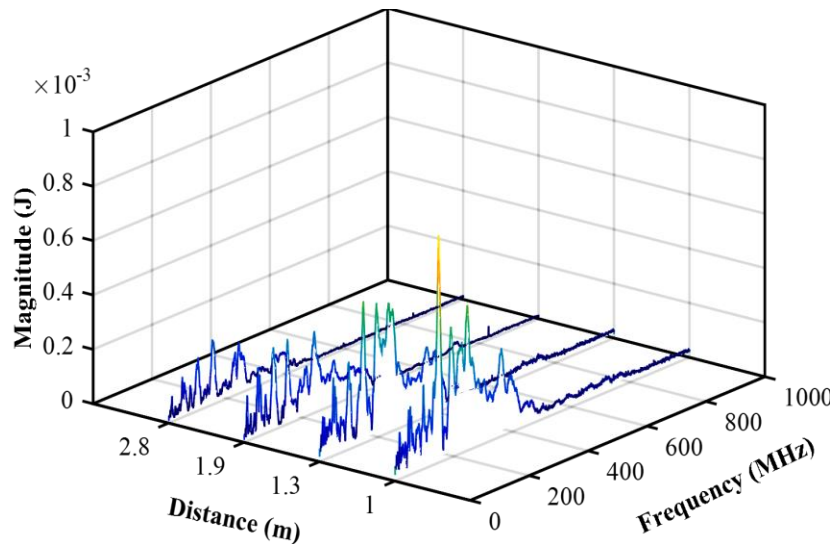


Figure 5-23 Averaged frequency spectra of FSR measurements at 20 kV for four locations of the receiving antenna from an acrylic tube internal PD emulator with oil filling.

Table 5-7 shows the variation with distance of the received mean peak voltage amplitude, calculated charge and calculated ERP for the FSR measurements for both cases. The range of the antenna from the acrylic tube internal PD source was varied from 1 m to 2.8 m. It is apparent that the peak ERP varies from 12.9 dBm to 12 dBm for an emulator without oil filling and from 7.7 dBm to 4.9 dBm for an emulator with oil filling. The average peak ERP is approximately 12 dBm in the case of without oil filling and 7 dBm in the case of oil filling.

Table 5-7 Concurrent measurements of FSR and galvanic measurements using the acrylic tube internal PD emulator with and without oil filling.

AC High voltage source (kV)	Galvanic contact measurement	—	Galvanic mean peak voltage (V)	Galvanic mean peak voltage (dB $\mu$ V)	Galvanic measurement standard deviation (V)	First half-cycle duration (ns)	Calculated charge (nC)	
		Without oil filling						
		—	3.91	131.8	1.98	10.4	3.8	
		Oil filling						
		—	2.76	128.8	1.28	4.7	2.1	
20	FSR measurement	Antenna - emulator range (m)	FSR mean peak voltage (V)	FSR mean peak voltage (dB $\mu$ V)	Peak electric field strength (dB $\mu$ V/m)	Peak ERP (dBm)	Standard deviation (V)	
		Without oil filling						
		1	0.14	102.9	119.9	12.9	0.06	
		1.30	0.09	99.08	116.08	11.3	0.03	
		1.90	0.04	93.06	110.06	8.63	0.01	
		2.80	0.04	93.06	110.06	12.00	0.01	
		Oil filling						
		1	0.07	97.7	114.7	7.7	0.02	
		1.30	0.06	95.5	112.5	9.0	0.03	
		1.90	0.03	89.5	106.5	5.1	0.01	
2.80	0.02	86.0	103.0	4.9	0.01			

The variations observed in Figures 5-24 and 5-25 are due to near field or multipath effects. The Figures show received peak voltage, electric field strength and ERP as a function of distance from the emulator.

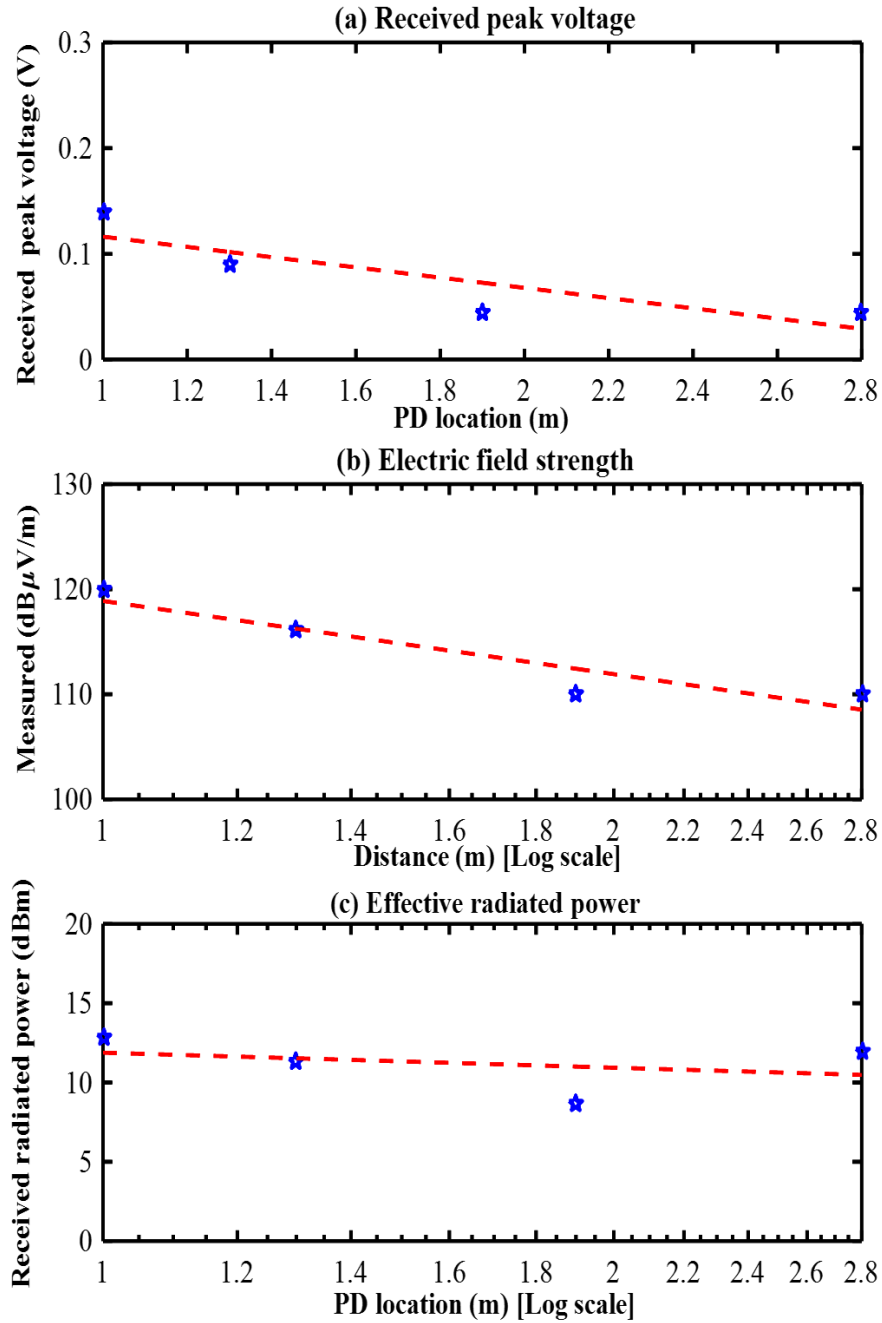


Figure 5-24 (a) Received peak voltage, (b) Electric field strength and (c) ERP as a function of (emulator without oil filling) – antenna distance from emulator .

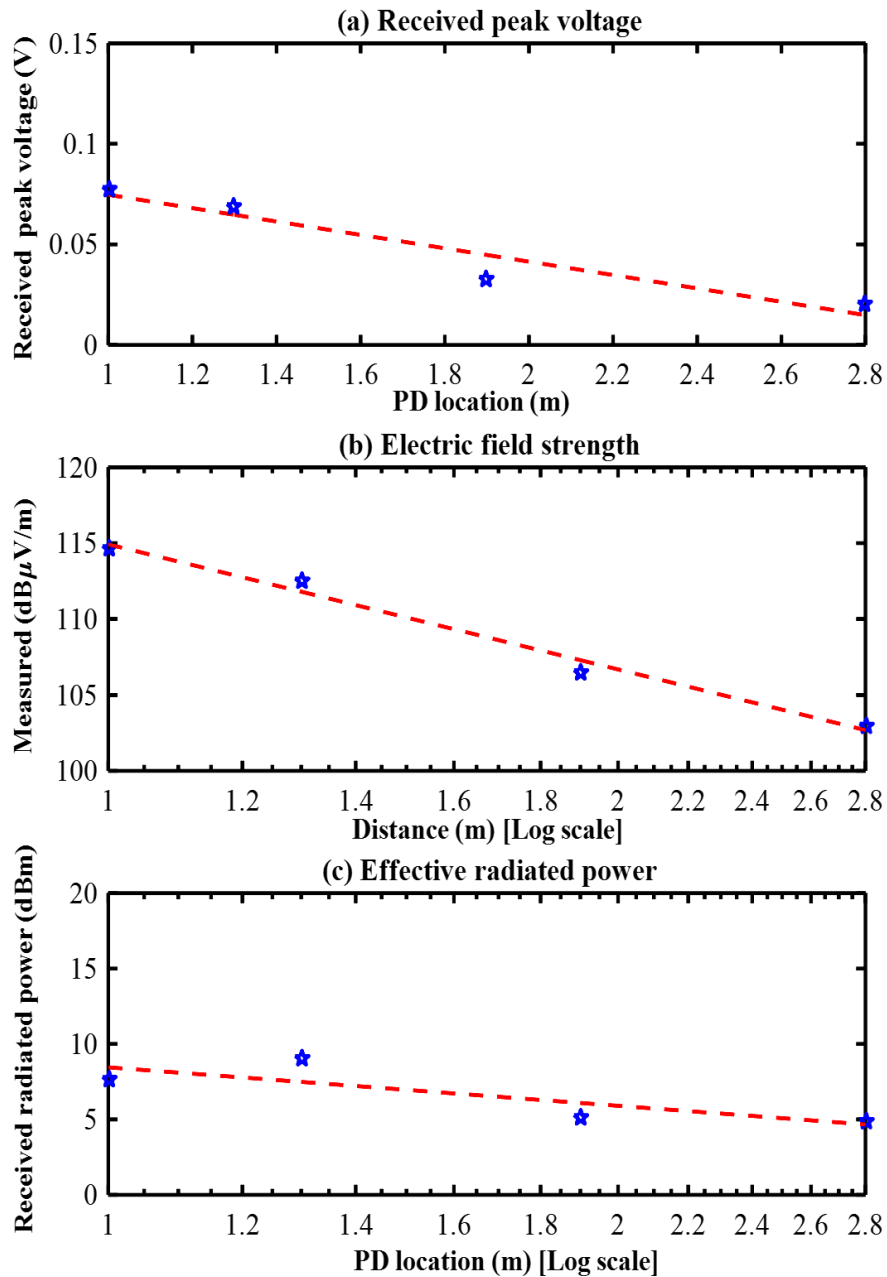


Figure 5-25 (a) Received peak voltage, (b) Electric field strength and (c) ERP as a function of (emulator with oil filling) – antenna distance from emulator.

### 5.2.3 Calibration an epoxy dielectric internal PD emulator

The charge injection device that is injecting into the terminals of an epoxy dielectric internal PD emulator is shown in Figure 5-26. Figure 6-27 shows the calculated charge from the integration of the current pulse versus injected charge.

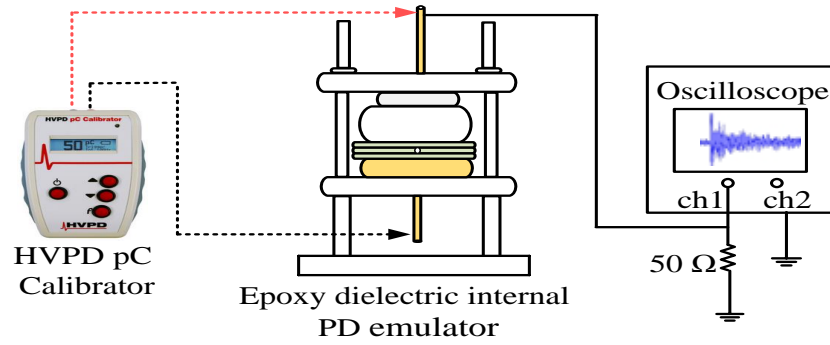


Figure 5-26 Injected charge across the terminals of an epoxy dielectric internal PD emulator.

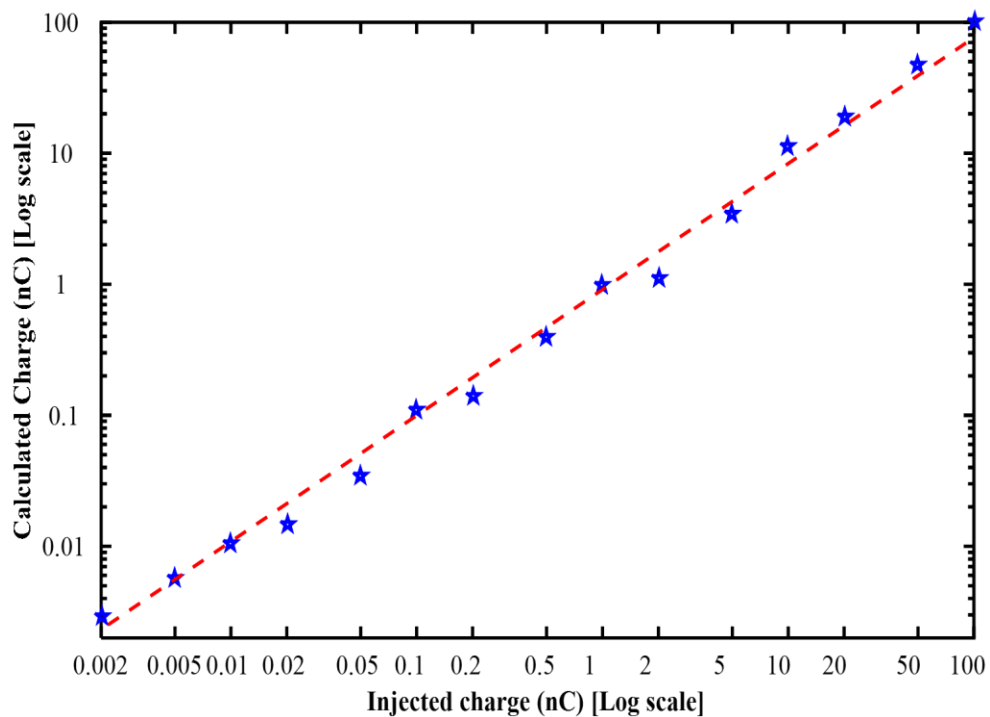


Figure 5-27 Calculated charge versus injected charge.

Table 5-8 compares injected charge, charge inferred from the integral of the first half cycle and the peak galvanic voltage. It was difficult to estimate the apparent charge from the 1 pC discharge because of background noise. The first half-cycle pulse duration from 2 pC to 10 nC is approximately 60 ns. The first half-cycle duration of 20 nC, 50 nC and 100 nC is around 280 ns due to a larger duration of the injected pulse from the calibration device as mentioned in the last section.

Table 5-8 Relationship between injected charge and calculated charge across the terminals of an epoxy dielectric internal PD emulator.			
Injected charge	First half-cycle pulse duration (ns)	Calculated charge	Peak galvanic voltage (V)
2 pC	56.2	2.9 pC	0.005
5 pC	64.8	5.7 pC	0.012
10 pC	60.0	10 pC	0.021
20 pC	62.8	15 pC	0.026
50 pC	61.9	35 pC	0.07
100 pC	56.0	111 pC	0.245
200 pC	62.8	140 pC	0.249
500 pC	56.0	390 pC	0.82
1 nC	54.6	1 nC	2.45
2 nC	66.0	1.1 nC	1.89
5 nC	56.5	3.5 nC	7.9
10 nC	55.0	11 nC	28.4
20 nC	282.0	19 nC	9.17
50 nC	280.0	48 nC	24.5
100 nC	272.0	100 nC	52.0

The experimental measurement circuit for the calibration of an epoxy dielectric internal PD emulator is shown in Figure 5-28.

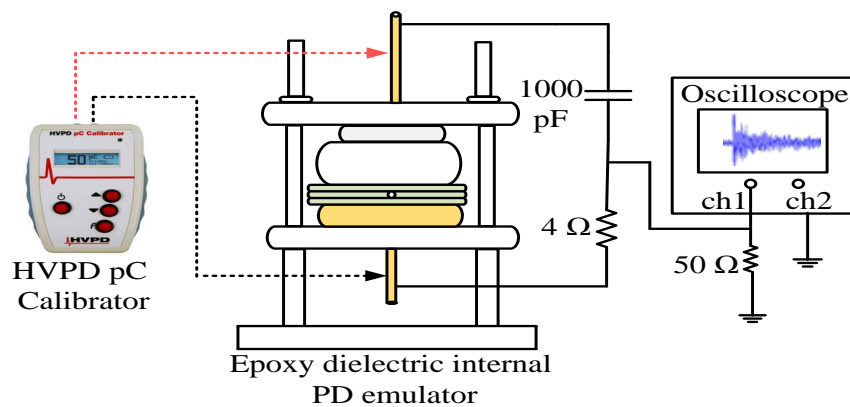


Figure 5-28 Measurement circuit for the calibration of an epoxy dielectric internal PD emulator.

The relationship between the injected charge and the calculated charge is shown in Table 5-9. The entries from 1 pC to 5 pC were too noisy and thus they omitted. The duration of

the first half-cycle shows some variations. The relation between calculated charge and injected charge is linear as shown in Figure 5 -29.

Table 5-9 Relationship between injected charge and calculated charge for an epoxy dielectric internal PD emulator.			
Injected charge	First half-cycle pulse duration (ns)	Calculated charge	Peak galvanic voltage (V)
10 pC	15.2	8.9 pC	0.004
20 pC	31.0	19.7 pC	0.005
50 pC	46.5	43 pC	0.012
100 pC	24.6	109 pC	0.043
200 pC	46.5	176 pC	0.037
500 pC	43.0	503 pC	0.128
1 nC	21.0	1.1 nC	0.42
2 nC	56.0	1.7 nC	0.30
5 nC	47.2	5 nC	1.22
10 nC	17.35	11 nC	4.40
20 nC	86.5	14 nC	1.08
50 nC	82.1	33 nC	3.00
100 nC	83.0	70 nC	6.70

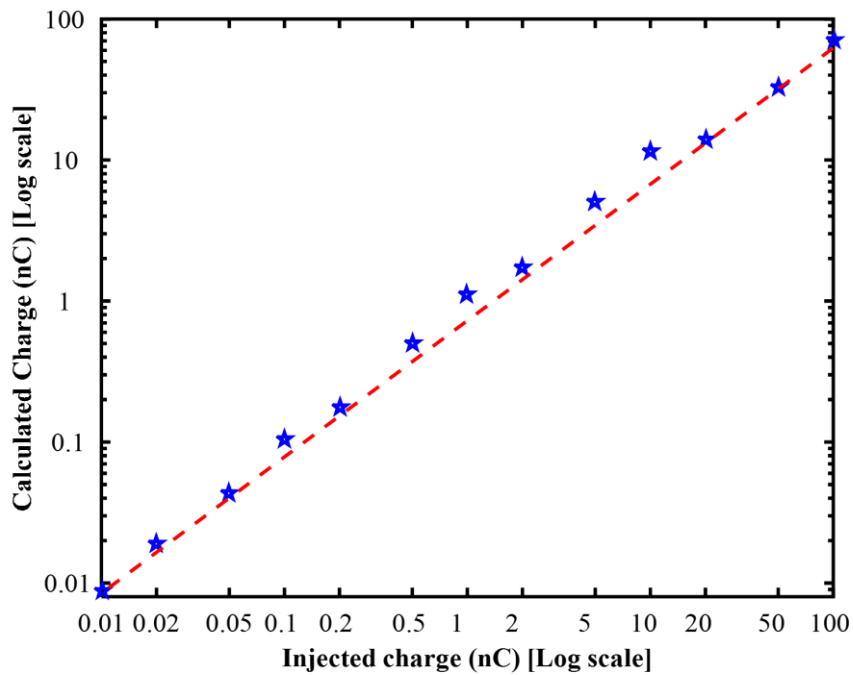


Figure 5-29 Calculated charge versus specified charge from the charge injection device.

Partial discharge is measured simultaneously using FSR and a galvanic contact measurements technique by using the measurement system shown in Figure 5-30. The measurements were made using an epoxy dielectric internal PD emulator and a 50 Hz power supply voltage of 18 kV RMS. The FSR measurements were made at four distances from the epoxy dielectric internal PD emulator.

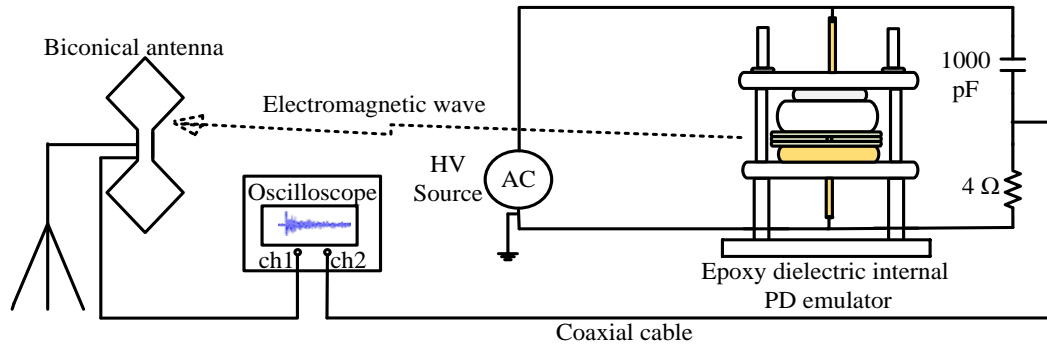


Figure 5-30 Measurement system using an epoxy dielectric internal PD emulator.

Figure 5-31 shows the galvanic contact measurement signal and frequency spectra. Figure 5-32 shows the FSR measurement signal and Figure 5-33 shows the averaged frequency spectra.

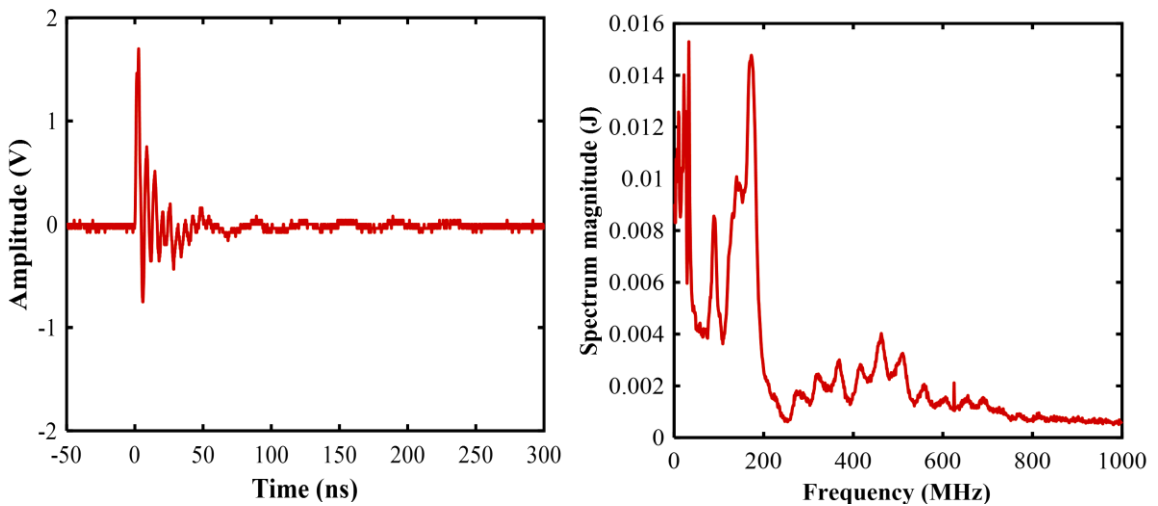


Figure 5-31 Epoxy dielectric internal PD emulator (a) Galvanic contact measurement pulse (b) Frequency spectra.

The frequency spectrum is concentrated around 50 MHz that is also the resonant frequency. The spread of the spectrum is increased and there are additional peaks at 80 MHz, 110

MHz and 200 MHz. The overall magnitude of the harmonic components is reduced above 300 MHz. It can therefore be inferred that the FSR radiation signal contains information relating to the effect of the shape of the internal PD emulator and a cavity between the epoxy glass insulator samples, which have created new resonances.

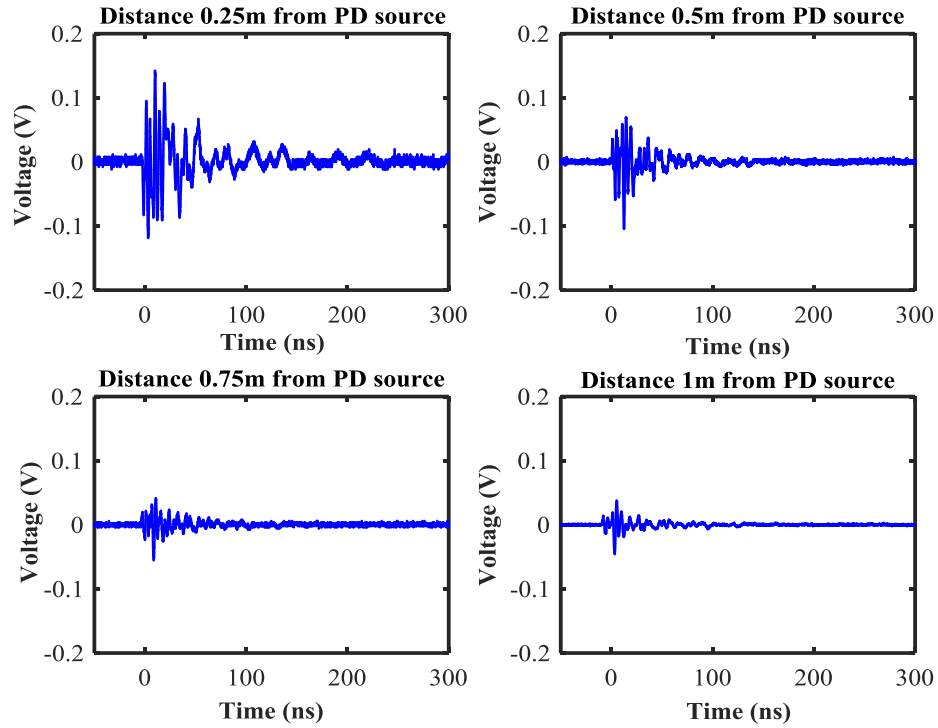


Figure 5-32 FSR measured pulse from an epoxy dielectric internal PD emulator.

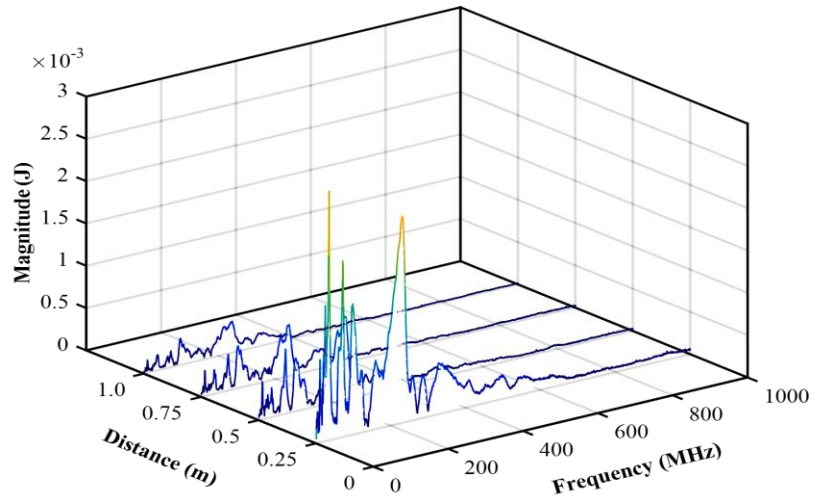


Figure 5-33 Averaged frequency spectra of FSR measurement at 18 kV for four locations of the receiving antenna from of an epoxy dielectric internal PD emulator.

Table 5-10 shows the variation with distance of the received peak voltage, received field strength, apparent ERP, and calculated charge. On FSR measurements, the range of the antenna from the epoxy dielectric internal PD emulator was varied from 0.25 m to 1 m. Peak ERP varies from 1.73 dBm to 1.15 dBm for a PD emulator a range of 0.25 m to a range of 1m. The average peak ERP is about 1.4 dBm. Figure 5-34 show received peak voltage, electric field strength and peak ERP as a function of PD source distance from the receiving antenna.

Table 5-10 Simultaneous measurements of FSR and galvanic pulses using the epoxy dielectric internal PD emulator.

AC High voltage source (kV)	Galvanic measurement	–	Galvanic mean peak voltage (V)	Galvanic mean peak voltage (dB $\mu$ V)	Galvanic measurement standard deviation (V)	First half-cycle duration (ns)	Calculated charge (nC)
			–	1.66	124.4	0.82	4.8
18	FSR measurement	Antenna emulator range (m)	FSR mean peak voltage (V)	FSR mean peak voltage (dB $\mu$ V)	Peak electric field strength (dB $\mu$ V/m)	Peak ERP (dBm)	Standard deviation (V)
		0.25	0.153	103.7	120.7	1.73	0.060
		0.50	0.076	97.7	114.7	1.70	0.029
		0.75	0.048	93.6	110.6	1.17	0.018
		1.00	0.036	91.1	108.1	1.15	0.016

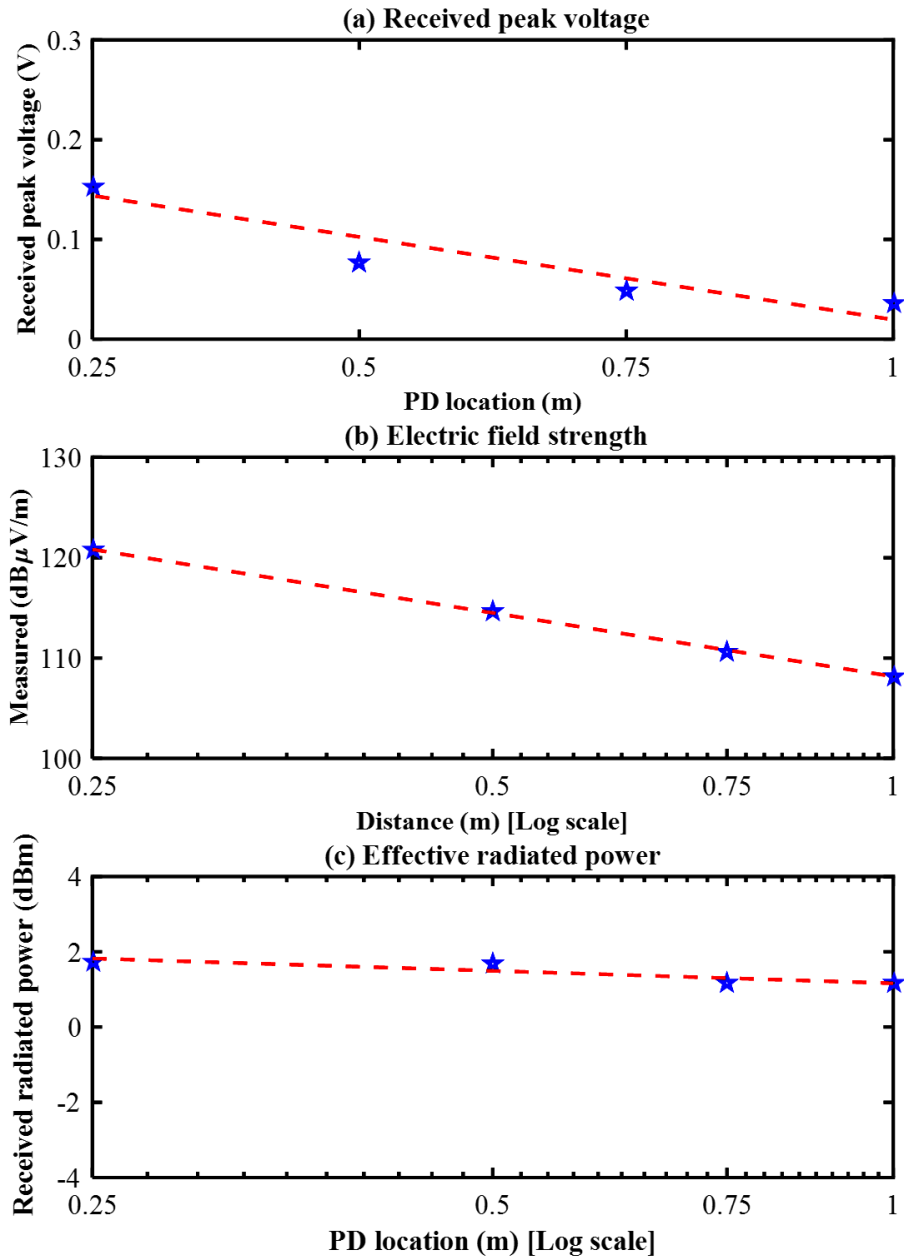


Figure 5-34 (a) Received peak voltage, (b) Electric field strength and (c) ERP as a function of epoxy dielectric internal PD emulator – antenna range.

#### 5.2.4 Relationship between calculated charge and effective radiated power for different PD emulators

The relationship between estimated apparent charge and estimated ERP for different PD emulator types is presented in Table 5-11. It is seen that the radiated power of the floating

electrode PD emulator is far greater than the radiated power of other types of emulators, and this by at least 13 dB [1]. On the other hand, the epoxy dielectric internal PD emulator is radiating the least power. Finally, Figure 5-35 shows ERP in dBm versus apparent charge in nC, in an almost linear relationship, and suggests that estimation of absolute PD intensity originating from HV insulation defects might be possible using an FSR measurement alone.

Table 5-11 Relationship between calculated charge and peak effective radiated power of PD emulators.

PD emulator	Floating-electrode PD source	Acrylic tube internal PD source without oil filling	Acrylic tube internal PD source with oil filling	Epoxy dielectric internal PD emulator
Calculated charge (nC)	5.3	3.8	2.1	0.9
Average peak ERP (dBm)	25	12	7	1.4

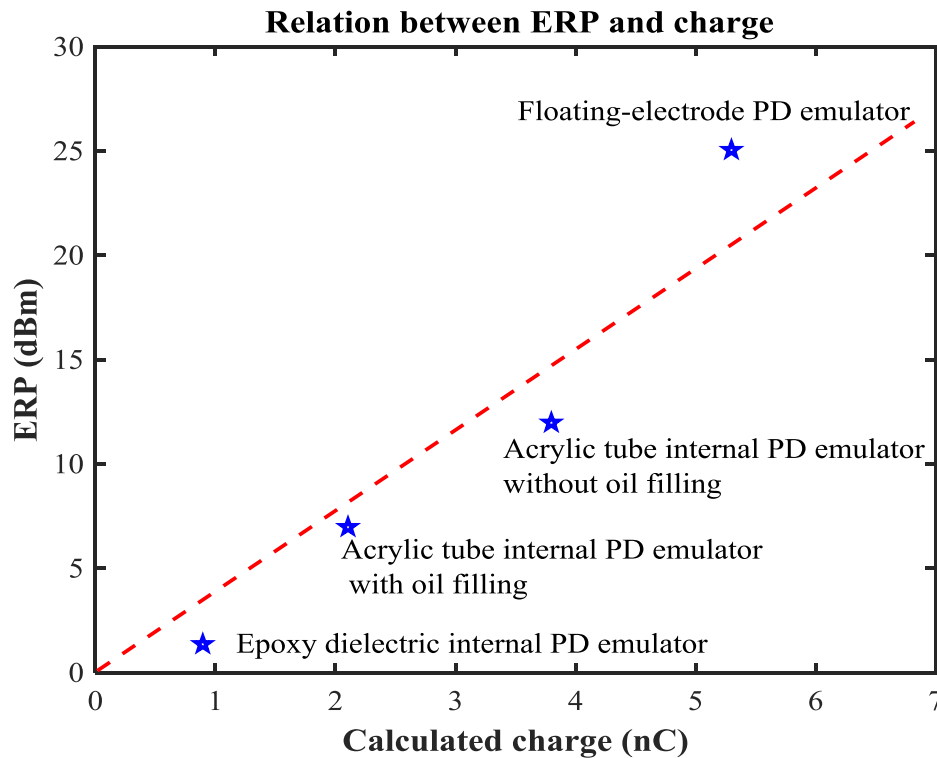


Figure 5-35 Determined ERP for different types of PD sources versus calculated charge.

### 5.3 Summary

Partial discharge signals were captured using FSR measurements and galvanic contact measurements techniques. The calibration pulse emulates a PD event of a particular (known) intensity. The charge is calculated by integrating the first half-cycle of the PD emulator current (measured charge). Calculated charge, peak voltage radiated amplitude and ERP of FSR measurement against the location of the PD emulator are compared for the calibration of FSR signals [1]. Absolute PD intensity (in pC) from a remote FSR measurement was traditionally thought to be impractical. If PD intensity can be reliably related to PD ERP, however, then there is the possibility of inferring PD intensity and the charge from a measurement of ERP using a radiometric system that locates the PD sources. Several issues remain to be investigated before such an absolute radiometric estimate of PD intensity can be realised. The most important of these is the anisotropy of the PD radiation and the error in the inferred PD intensity, which this introduces in practice. (It is thought that, in practice, the gain of the PD radiating structure will be modest). In addition, inferred ERP in the work above has some modest dependence on range. It is possible that this apparent variation is due to the propagation environment in which the measurements were carried out (an indoor laboratory) and the fact that the measurements were not carried out unambiguously in the far field. It is felt that the results reported here are sufficiently encouraging, however, to pursue this work further [164]. In the next chapter, the simulation models, which are used in chapter 4 and 5 for the calibration of radiometric measurements, will be validated by measuring the radiated fields, comparing them with the fields predicted from simulation. The validated simulations will be used to investigate the relationship between FSR PD measurements and absolute PD intensity.

## CHAPTER 6

### **VALIDATION OF PARTIAL DISCHARGE EMULATORS SIMULATION USING FREE-SPACE RADIOMETRIC MEASUREMENTS**

---

*This chapter presents the simulation and measurement of PD emulator sources, which are a floating electrode PD emulator type and two internal PD emulators. The PD emulators have been implemented in order to model the propagation of the electromagnetic (EM) wave due to PD in electrical substations. The emulators have been simulated using the CST Microwave Studio. The intention is to use the simulated emulators to establish a relationship between radiated PD signals and PD intensity as defined by apparent charge transfer. There is a sufficient agreement between simulations and measurements to suggest that simulations could be used to investigate the relationship between PD intensity and the field strength of radiated signals [3].*

---

## 6.1 Introduction

Partial discharge is often a precursor event to HV equipment failure. PD diagnosis is an established means of verifying insulation condition. Any method to locate PD sources and assess their intensity would be a significant tool for the early detection of faulty HV equipment. Sensors positioned near the HV equipment can detect electromagnetic waves radiated from the PD. The majority of energy in radiated PD signals lies in the VHF and UHF bands. The radiation of EM waves created by PD in HV apparatus therefore facilitates compromised insulation diagnosis and location [49, 172]. The use of radiated PD signals is referred to as a FSR method of PD detection and source location [3, 20, 21, 31, 97]. The design, validation and calibration of a FSR PD sensor network requires emulated PD sources, i.e. devices that radiate PD-like signals at stable, known, and levels of intensity. If FSR measurements are to be used to infer the absolute intensity (in pC) of PD processes, then simulations in which both absolute PD intensity and radiated signal field strength can be simultaneously calculated will be enormously helpful. This models three PD sources and shows that they can be simulated successfully, thus allowing future investigation of the radiated field strength versus absolute PD intensity relationship [3]. Validation of the simulations requires measurement of FSR PD signals from real PD sources (referred to here as PD emulators). Three PD emulators have been constructed to model the propagation of the EM wave due to PD in electrical substations. An emulator of the floating-electrode type, an acrylic tube internal PD emulator and an epoxy dielectric internal PD emulator are depicted in Figure 6-1. The CST Microwave Studio (CST MWS), which can simulate transient electromagnetic fields using time-domain solver method, has been used to model these emulators [3, 133]. CST MWS is an effective transient EM wave simulation technique is easy to realize and has extensive applicability [173]. The parameters are calculated using analytical calculations based on the geometrical dimensions using available mathematics package. The geometrical dimensions and state of the material of the three PD emulators shown in chapter three in sections 3.4, 3.5 and 3.6. The gap length between electrodes of floating-electrode PD emulator is 0.6 mm. An example of finding unknown parameters of capacitor and inductance of floating electrode PD emulator is given in appendix D.

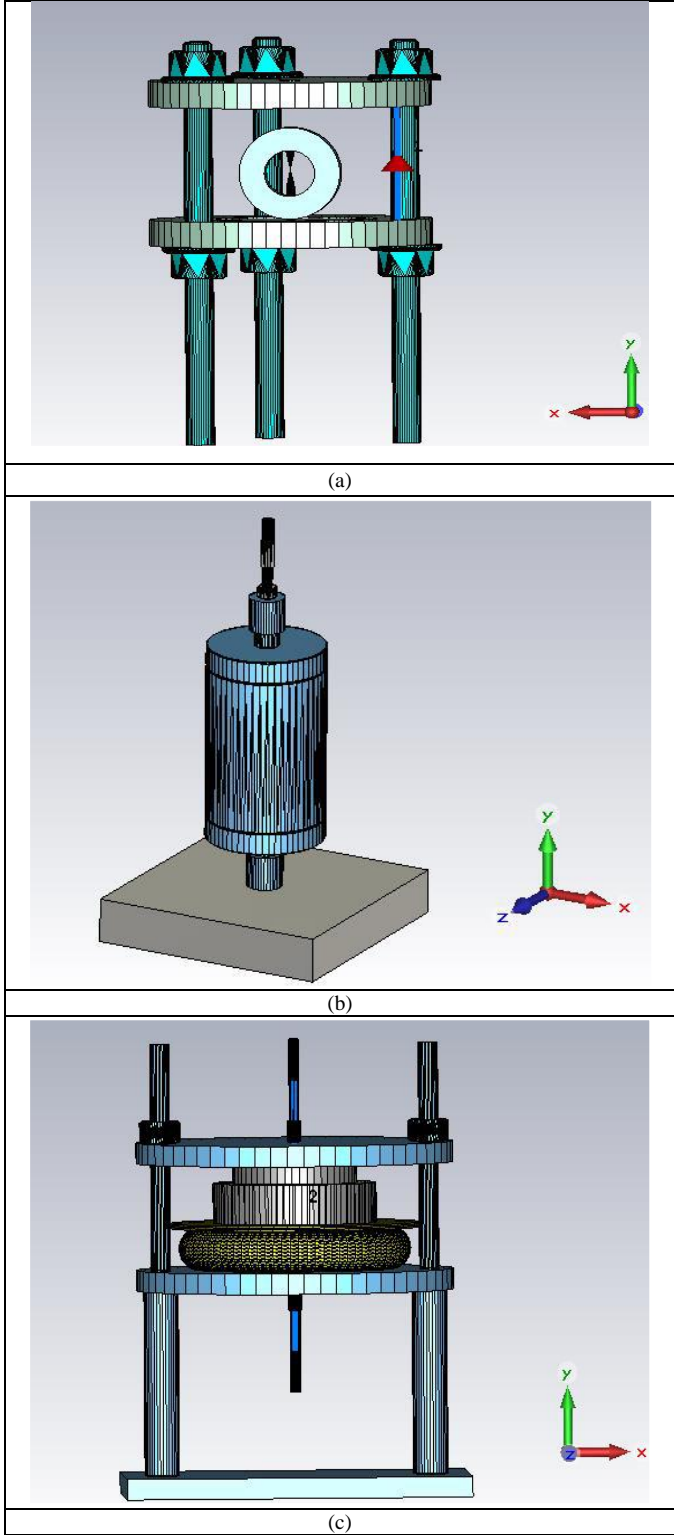


Figure 6-1 PD emulator types: (a) floating-electrode (b) acrylic tube internal and (c) epoxy dielectric internal.

To measure PD from the different emulators, an example of setup shown in Figure 6-2 is used. More information about PD measurement can be found in [1, 3, 164, 174].

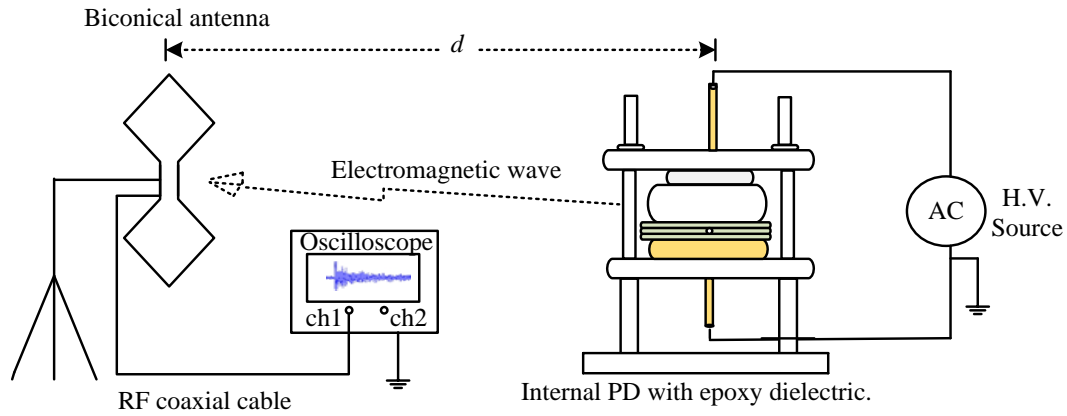


Figure 6-2 PD measurement circuit with an epoxy dielectric internal PD emulator.

Partial discharge is created by applying an HV 50 Hz AC signal to three PD emulators. Measurements were performed using voltages of 15 kV RMS for a floating-electrode PD emulator, 20 kV RMS for an acrylic tube internal PD emulator and 18 kV RMS for an internal epoxy dielectric PD emulator. The FSR measurements were made using a biconical antenna connected to a 20 GSa/s DSO with an analog-bandwidth of 4 GHz. The biconical antenna (shown in Figure 3-2) was placed at a distance of 2 m from the PD emulator and was vertically polarised [3]. More information about three PD emulators, which generated PD, can be found in chapter three, sections 3.4, 3.5, and 3.6.

## 6.2 FSR PD Measurements and Simulations

Measurements were made of the radiated PD signals from all three emulators. In each case, the antenna was located 2 m from the emulator. The received signals are shown in Figure 6-3 [3].

A Gaussian current signal with a frequency spectrum in the VHF-UHF band has been used as excitation in the simulated PD sources as shown in Figure 6-4. The Gaussian pulse is excitation pulse used in CST MWS. The PD current pulses were modelled using a Gaussian equation as follows [132, 173]:

$$i(t) = I_0 e^{\left(\frac{-(t-t_0)^2}{2\sigma^2}\right)} \quad (6-1)$$

where  $I_0$  is the peak current,  $\sigma$  characterizes the pulse width and  $t_0$  is the time when the pulse peaks.

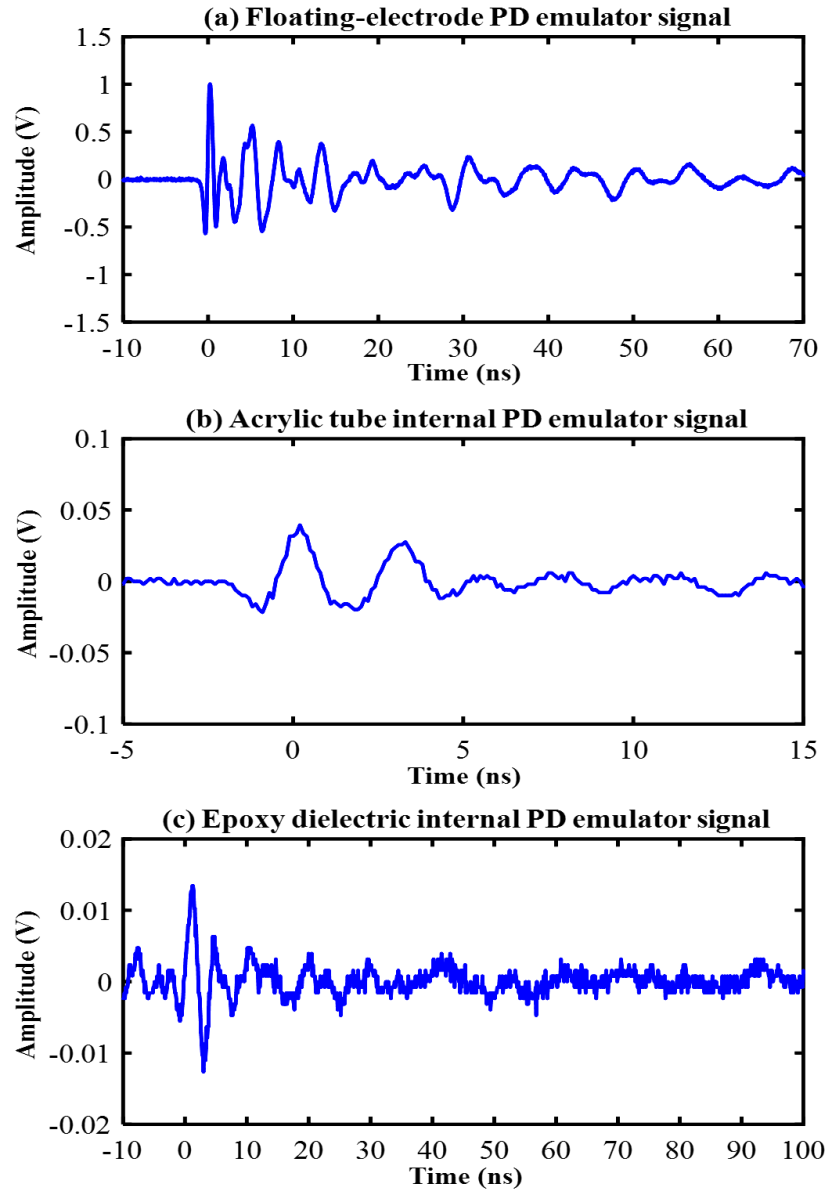


Figure 6-3 PD FSR measurement signal (a) floating-electrode (b) acrylic tube internal and (c) epoxy dielectric internal.

The charge contained within the pulse (at least approximately equal to the apparent charge of the PD intensity) is:

$$q = I_0 \sigma \sqrt{2\pi}$$

(6-2)

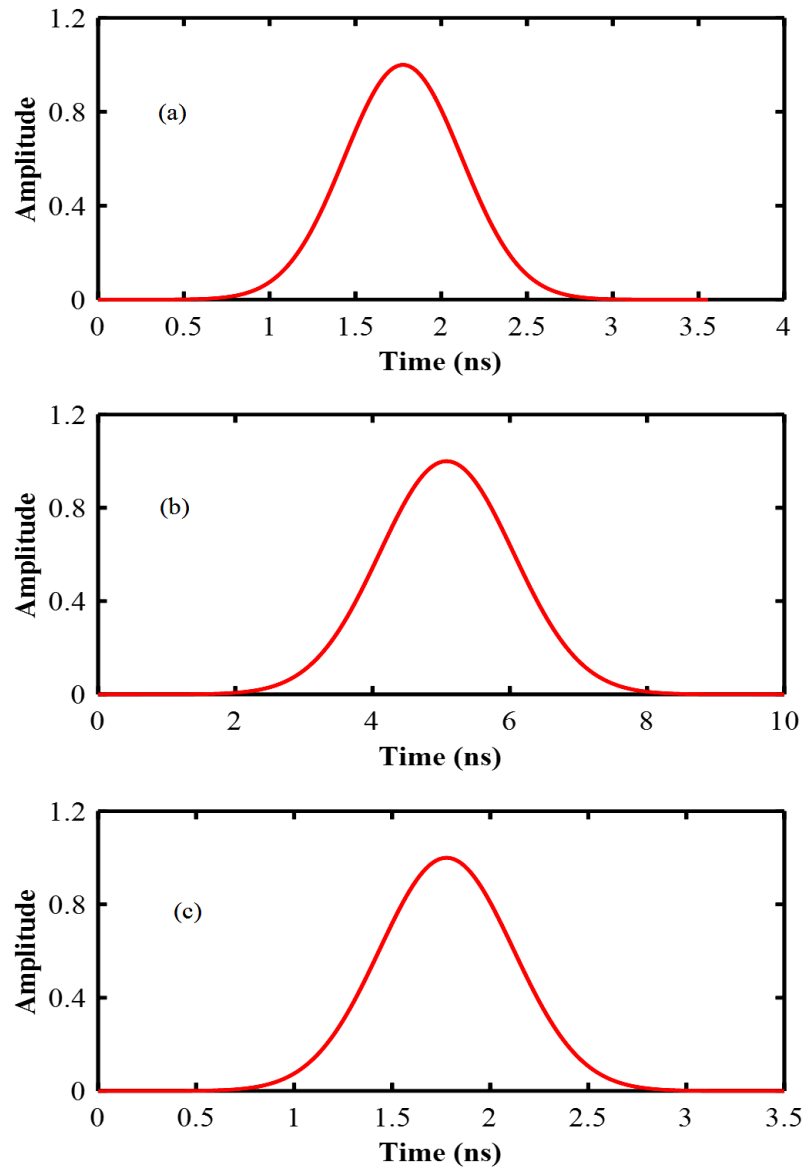


Figure 6-4 Excitation current signal (a) floating-electrode (b) Acrylic tube internal and (c) Epoxy dielectric internal.

The electromagnetic wave propagation from the PD emulators model is simulated and recorded at a certain probe position. The radiated electric fields predicted by simulation at a distance of 2 m for each of the emulators in response to the current pulse excitation are illustrated in Figure 6-5. The simulation is implemented by using CST MWS time-domain

solver. The duration time of the first half cycle of the transient is measured and with approximately 5 ns for the floating-electrode PD emulator, 2.5 ns for the acrylic tube internal PD emulator, and 5 ns for the epoxy internal PD emulator.

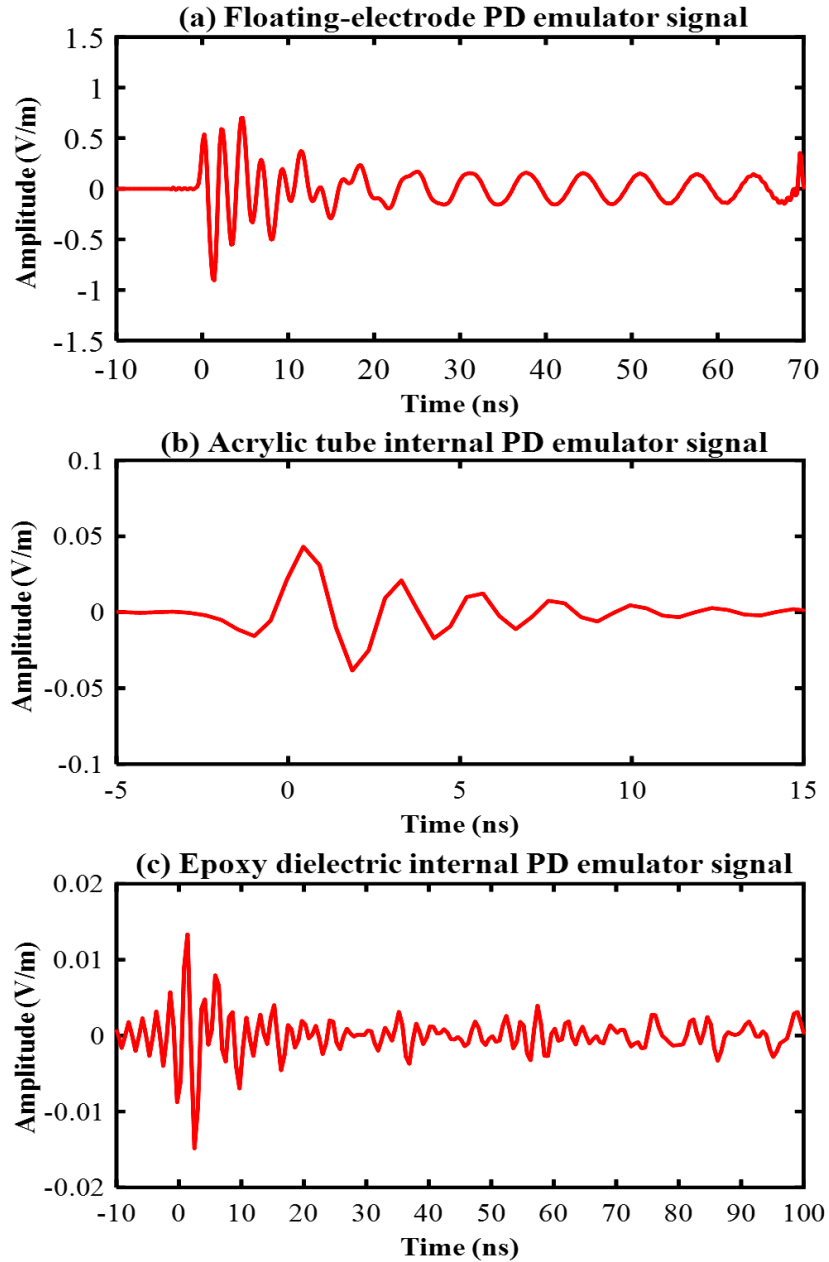


Figure 6-5 Simulated PD electrical fields (a) floating-electrode (b) Acrylic tube internal and (c) Epoxy dielectric internal.

The comparison between simulated and measured fields is exhibited in Figure 6-6. It seems that the simulated fields extracted from CST MWS are in good agreement with the measured ones for all the PD emulators. Table 6-1 shows such comparison. The following evaluation metrics are computed using RMSE and correlation coefficient. This gives confidence in the simulations, which may, therefore, be used to calculate absolute PD intensity (in pC) and relate this to radiated signal field strength at a particular distance from the PD source [3].

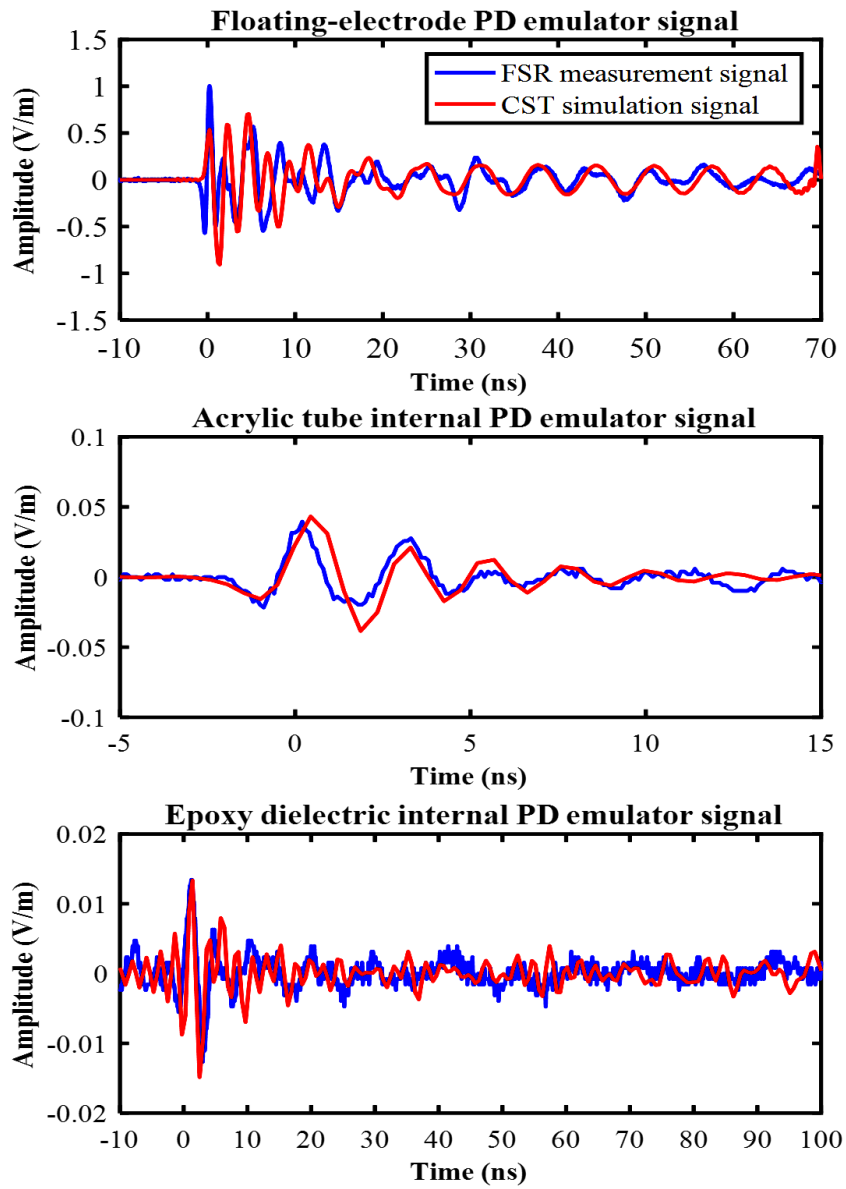


Figure 6-6 Comparison of measured and simulated PD electrical field amplitudes.

Table 6-1 Correlation of measured PD signal and simulated signal

PD emulator	Root Mean Squared Error (V)	Correlation coefficient
Floating-electrode PD emulator	0.5685	0.9273
Acrylic tube internal PD emulator	0.5286	0.8681
Epoxy dielectric internal PD emulator	0.4109	0.7097

Figures 6-7 and 6-8 show an example of the simulated transient behavior of the signals which are decaying with time from the emulators. The Figures display little variation in terms of oscillation however, they are different in terms of amplitude when distance is larger.

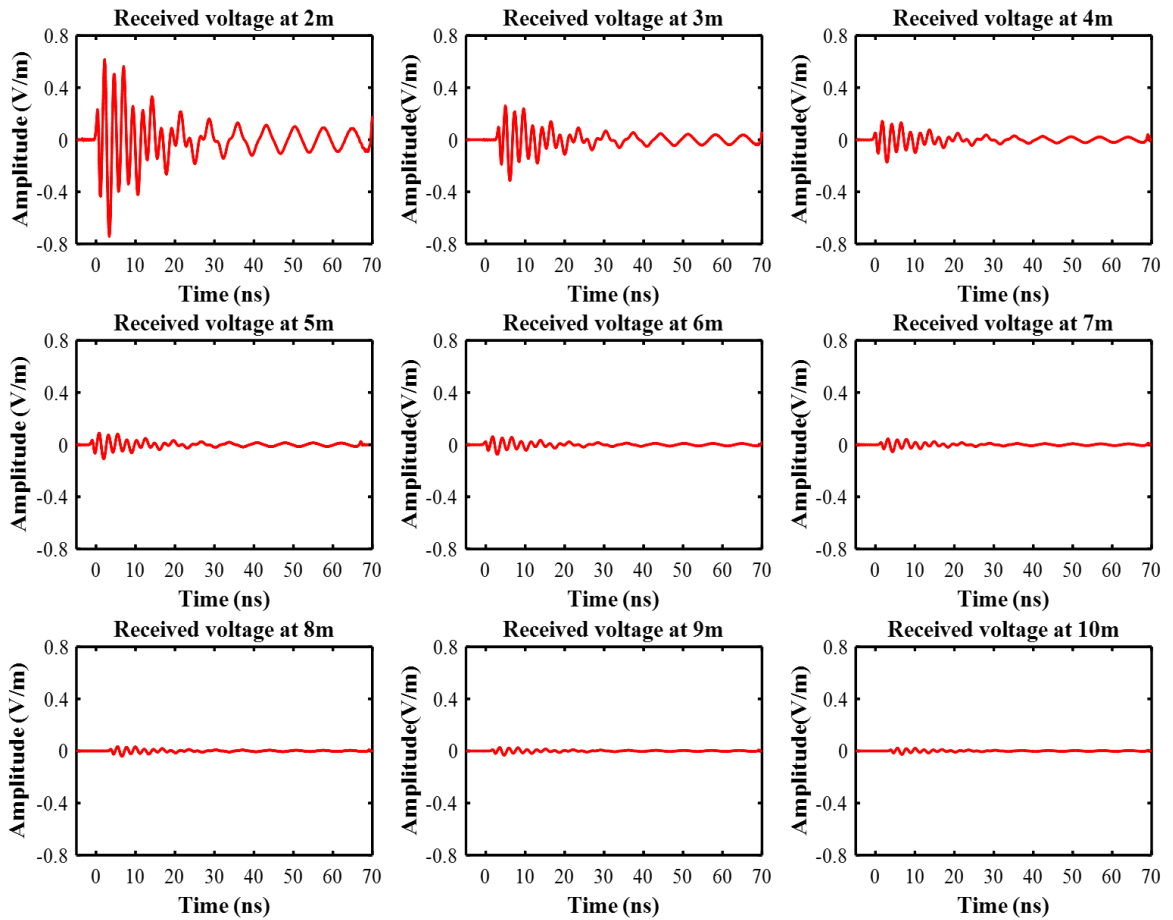


Figure 6-7 Simulated transient behavior of the signals propagating of different distances from the floating electrode PD emulator model.

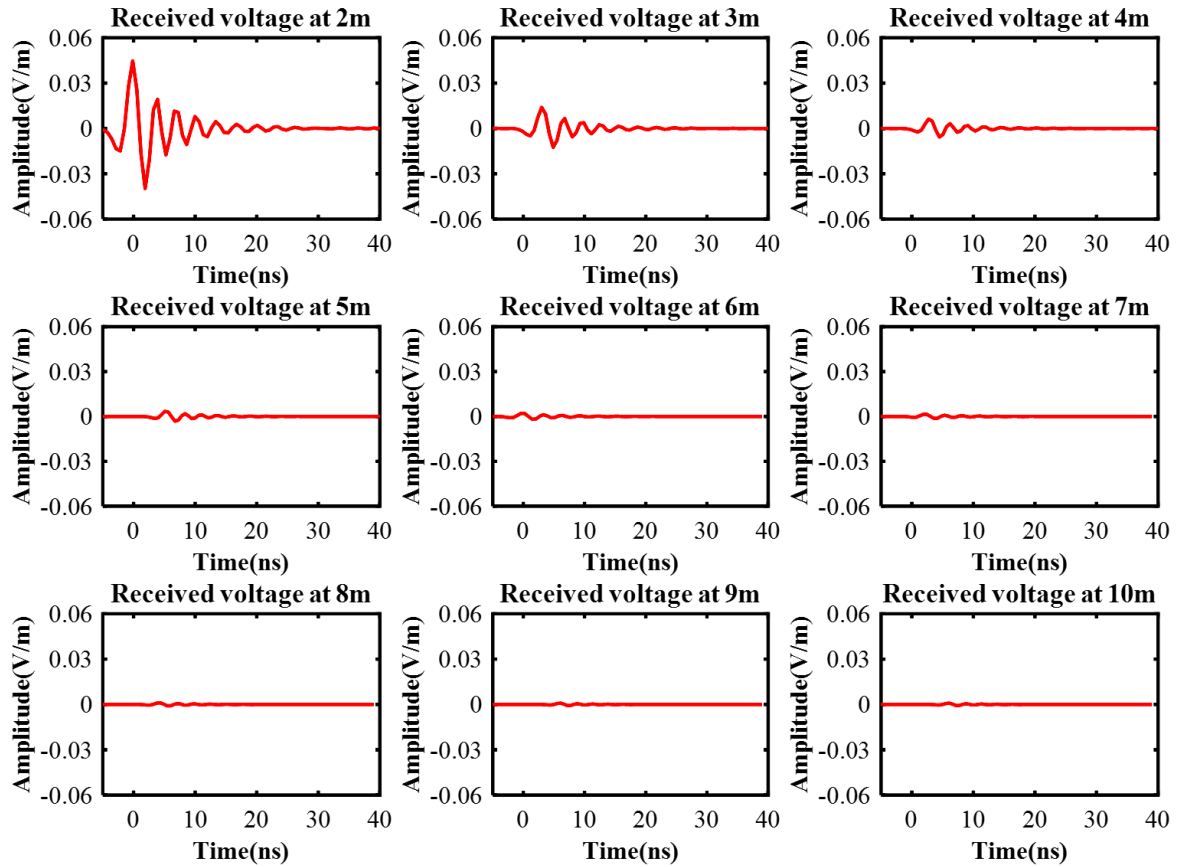


Figure 6-8 Simulated transient behavior of the signals propagating of different distances from an acrylic tube internal PD model.

### 6.3 Summary

Three different PD emulators have been constructed and the radiated fields from each due to a given excitation derived by simulation. The PD intensity corresponding to the excitation is easily calculated allowing this to be related to radiated PD field strength. The simulations have been validated by using RMSE and correlation coefficient between the measuring the radiated fields signals, comparing them with the fields predicted from simulation signals and showing the agreement to be good. The validated simulations will be used to investigate the relationship between FSR PD measurements and absolute PD intensity. If such a relationship can be, even approximately, established then the utility of FSR PD measurement and locations systems for the condition monitoring of insulation integrity in high voltage plant will be greatly enhanced [3].

## CHAPTER 7

### **PARTIAL DISCHARGE ACTIVITY UNDER AC AND DC VOLTAGES**

---

*The work reported in this chapter presents the PD measurement activity. The PD FSR and galvanic contact measurements activity under AC and DC applied voltages at different distances between a PD source and a biconical antenna are presented. Partial discharge source i.e. an emulator of the floating-electrode is specially constructed. The relationship between gap length and peak voltage amplitude of FSR and galvanic contact measurements is investigated. FSR outdoor measurements have been performed with variable distance of receiving antenna from the floating electrode PD emulator.*

---

## 7.1 Introduction

Measurements of FSR and galvanic contact, PD signals were taken under AC and/or DC voltages with the measurement system using the floating-electrode PD emulator and shown in Figure 3-1. AC voltages were engendered using a 50 Hz power supply voltage of 0 – 50 kV RMS. DC voltages were created using a 0 – 30 kV, 0.1mA HV supply source.

When AC and/or DC high voltages were applied, three PD measurement waveforms of FSR signals were recorded as illustrated in Table 7-1. The distance between the floating-electrode PD emulator and the biconical antenna was 1 m, 2 m, and 4 m. The peak voltage of the FSR pulse signal against the applied voltage was measured. The radiated signal amplitude is decreasing by increasing the distance between the PD emulator and the biconical antenna, due to radiation losses [1].

Table 7-1 Peak voltage of FSR pulse amplitude under AC and DC applied voltage at different distances between PD source and the biconical receiving antenna.

PD distance (m)	DC High voltage (kV)	DC Peak voltage of FSR pulse (V)	DC Peak voltage of FSR pulse (dB $\mu$ V)	Peak electric field strength (dB $\mu$ V/m)	Peak effective radiated power (dBm)
1	15.5	0.50	114	131.0	27.5
2		0.39	111.8	128.8	27.8
4		0.20	106.02	123.02	22.02
PD distance (m)	AC High voltage (kV)	AC Peak voltage of FSR pulse (V)	AC Peak voltage of FSR pulse (dB $\mu$ V)	Peak electric field strength (dB $\mu$ V/m)	Peak effective radiated power (dBm)
1	15	0.77	117.7	134.7	27.7
2		0.27	108.6	125.6	24.6
4		0.19	105.6	122.6	21.6

### 7.1 Influence of Emulator Geometry on PD Intensity under AC Applied Voltages

The measurement system shown in Figure 3-1 is used in this section to investigate, how the relationship between FSR measurement signal and galvanic contact measurement

signal changes with changing applied AC high voltage and gap length between the floating electrodes of the PD emulator.

### 7.1.1 FSR measurement

The strength of PD events was measured by using the FSR measurement technique. The relationship between gap lengths of floating electrodes of PD emulator and the peak voltage amplitude of FSR measurement changes is investigated. The strength of several PD events was measured and their average (is shown in Table 7-2) when the applied HV is 12 kV, 15 kV, 16.5 kV, and 18 kV. The mean peak voltage amplitude and standard deviation are calculated from 15 measurements for each case. The ERP of the PD source emulator is estimated from received electric field strength according to the free space propagation formula (5-3) and the known antenna factor of the biconical antenna [1].

The gap length between the floating electrodes of the PD emulator was varied from 0.2 mm to 1mm in steps of 0.2 mm. Feeler gauge were used to measure the gap between the electrodes. The variation of the applied HV value has no impact on the peak voltage amplitude of the FSR measurement. However, the peak voltage amplitude of FSR measurement is decreasing due to an increase in the electrode gap of the PD emulator.

The time series events of the PD signal for each case of applied voltage are shown in Figure 7-1. The peak voltage amplitude for all cases is shown in Table 7-2, for example, in the gap distance of 0.2 mm for all cases of applied voltage was approximately 0.45 V, 0.39 V for the gap of 0.4 mm, 0.37 V for the gap of 0.6 mm, 0.28 V for the gap of 0.8 mm, and finally 0.13 V for the gap of 1mm.

Therefore, the peak voltage amplitude of the FSR measurement is decreasing due to an increase of the electrode gap length. This is because when electrons move in the electrode gap, the magnitude of the PD signal due to the motion of free electrons increases with a decrease in the electrode gap. Figure 7-2 shows the peak voltage amplitude of the FSR measurement for each gap as a function of applied voltage. The variation of the applied HV value has a minor impact on the peak voltage amplitude of FSR measurements.

Table 7-2 Peak voltage amplitude of FSR measurements depending on gap length between floating electrodes of PD emulator under AC applied voltage.

Power source (kV) AC	PD source distance (m)	Gap length between floating electrodes of PD emulator (mm)	Mean peak voltage amplitude of FSR measurement (V)	Peak voltage of FSR pulse (dB $\mu$ V)	Electric field strength (dB $\mu$ V/m)	Effective radiated power (dBm)	Standard deviation (V)
12	2	0.2	0.49	113.8	130.8	29.8	0.02
		0.4	0.39	111.8	128.8	27.8	0.07
		0.6	0.35	110.9	127.9	26.9	0.07
		0.8	0.26	108.2	125.3	24.2	0.08
		1.0	0.06	95.6	112.5	11.6	0.04
15		0.2	0.46	113.3	130.3	29.3	0.06
		0.4	0.43	112.7	129.7	28.7	0.08
		0.6	0.38	111.6	128.6	27.6	0.03
		0.8	0.28	108.9	125.9	24.9	0.08
		1.0	0.10	100.0	117.0	16.0	0.05
16.5		0.2	0.45	113.0	130.0	29.0	0.05
		0.4	0.36	111.0	128.0	27.0	0.09
		0.6	0.38	111.6	128.6	27.6	0.01
		0.8	0.24	107.6	124.6	23.6	0.08
		1.0	0.16	104.0	121.0	20.1	0.05
18		0.2	0.43	112.7	129.7	28.7	0.06
		0.4	0.38	111.6	128.6	27.6	0.07
		0.6	0.39	111.8	128.8	27.8	0.03
		0.8	0.36	111.0	128.0	27.0	0.06
		1.0	0.19	105.6	122.6	21.6	0.04

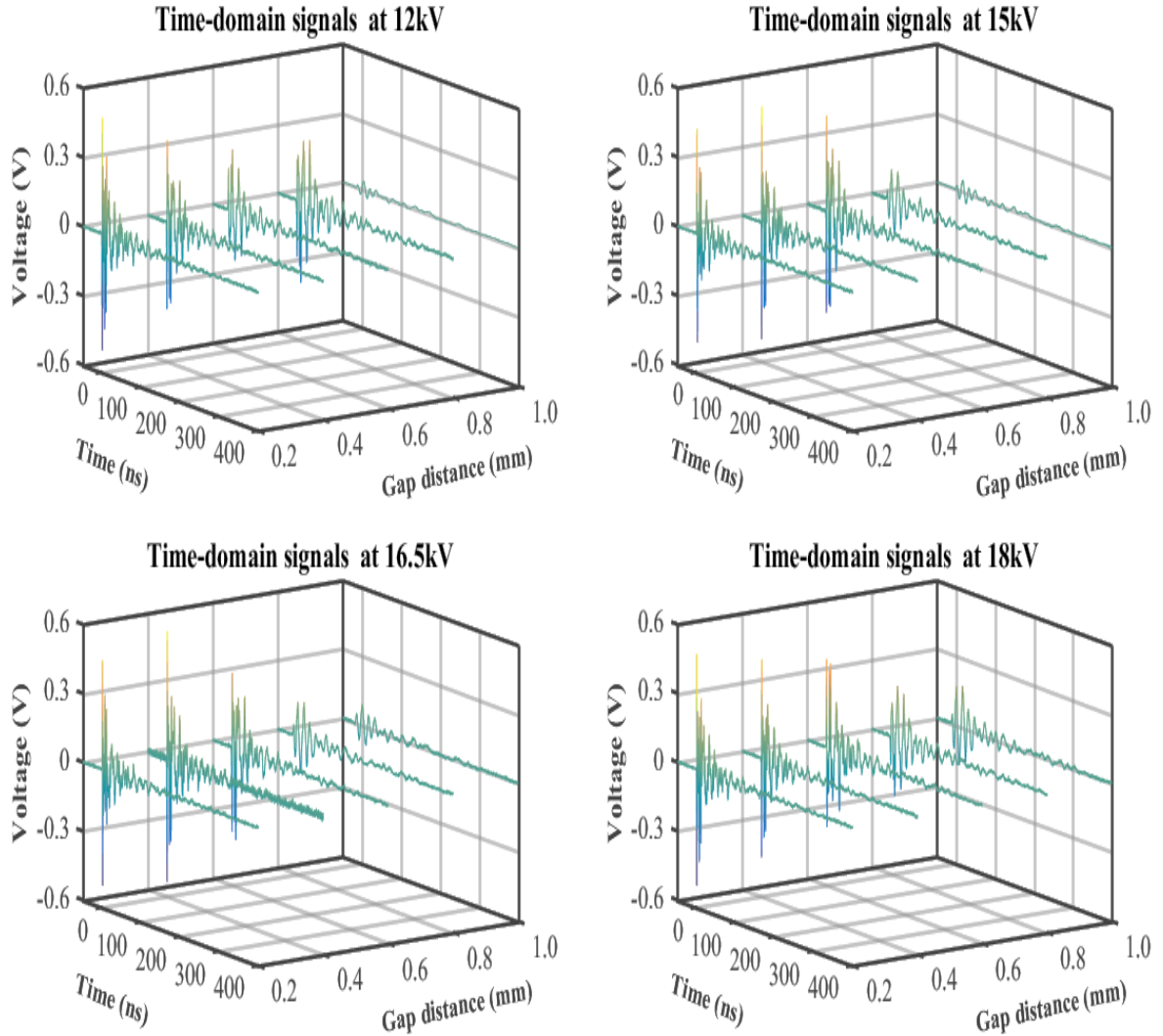


Figure 7-1 Time series events of FSR PD signal for various gaps.

The mean average spectra of FSR measurements for each gap length between electrodes of the floating electrode PD emulator are shown in Figure 7-3. The dominant frequency content of the UHF signal radiated by the PD lies in the range of 50 MHz – 800 MHz. The peak amplitude of the spectrum has small dependence on the HV power supply values.

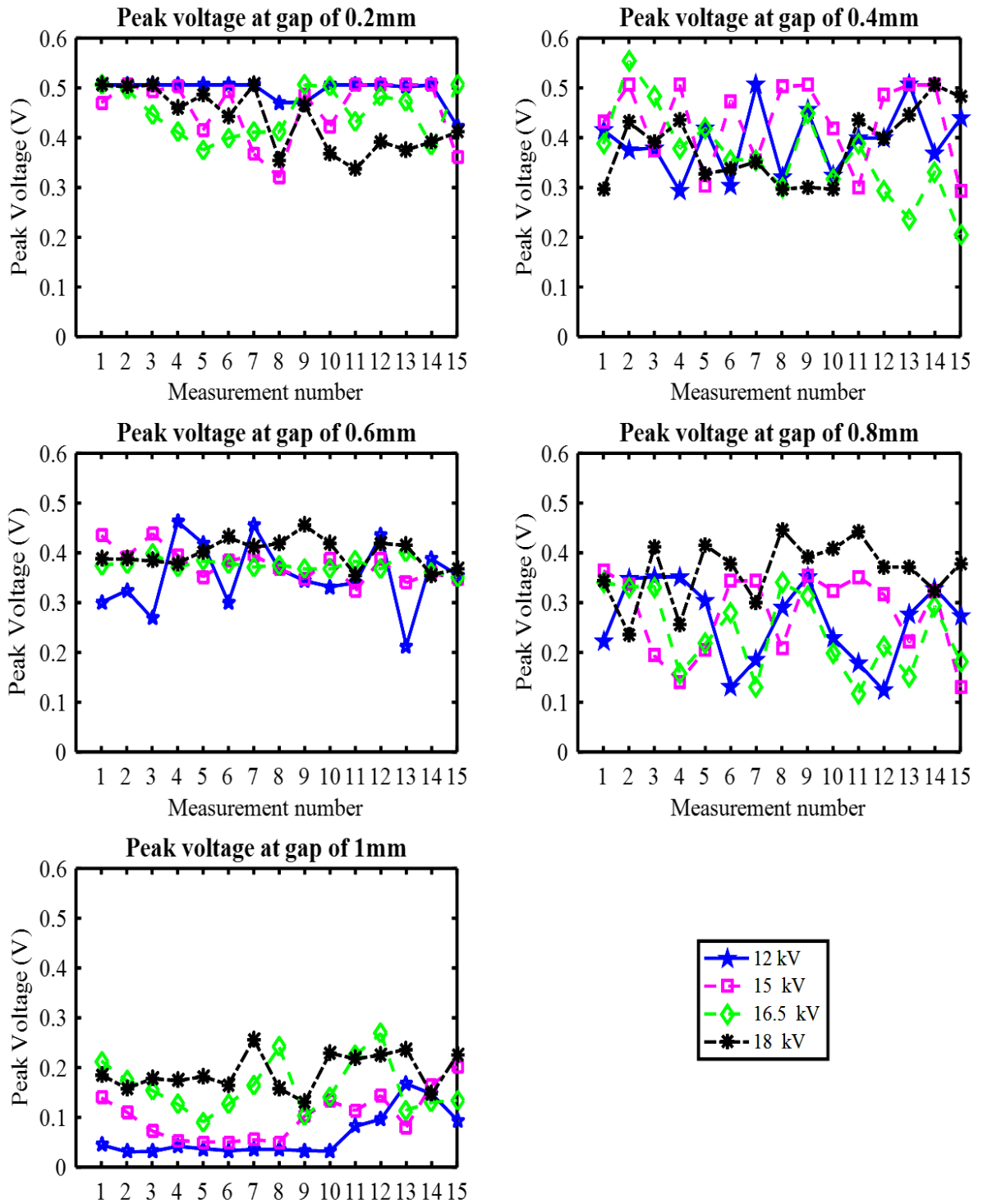


Figure 7-2 Peak voltage amplitude of FSR measurements for each gap as a function of the applied HV value.

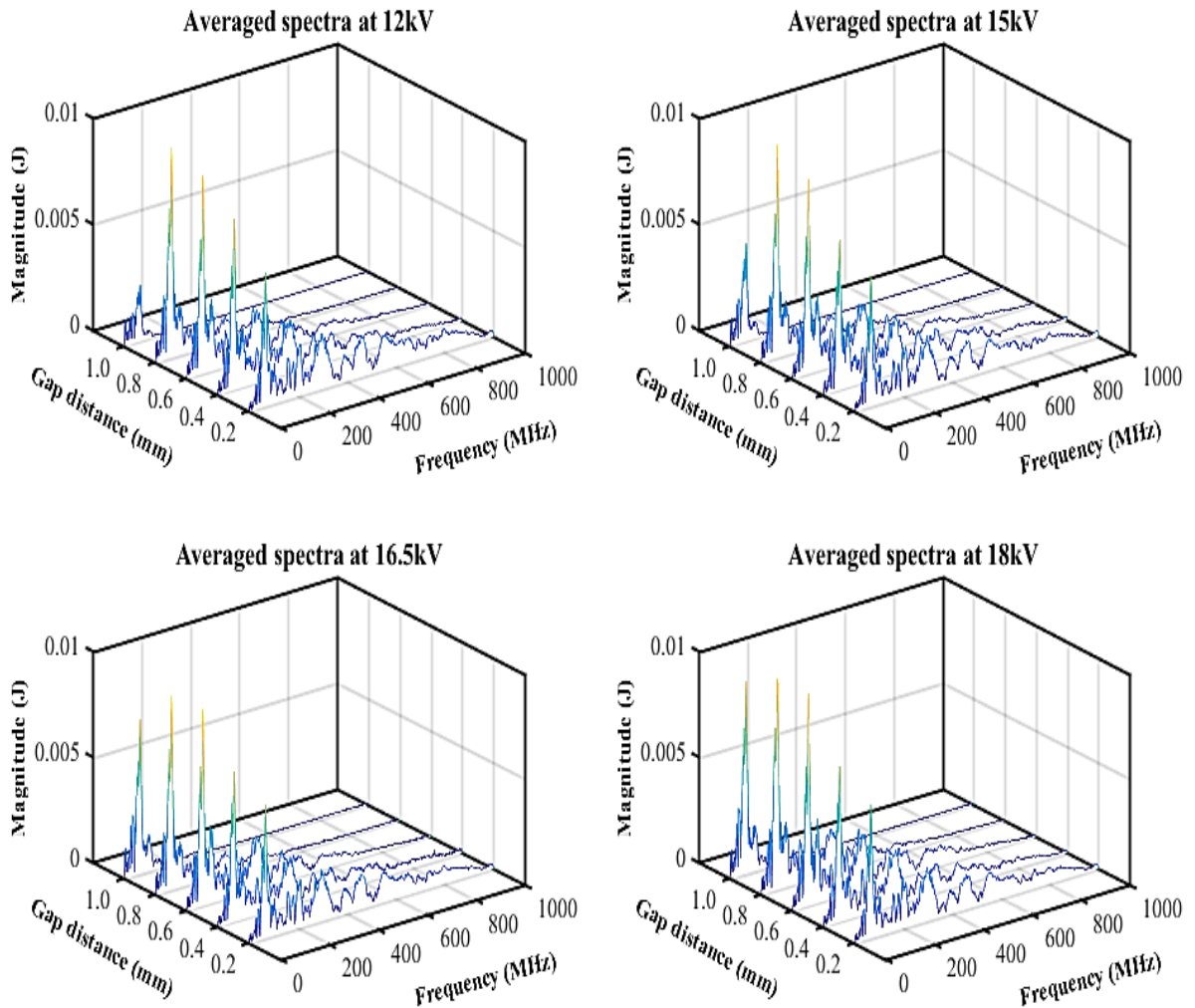


Figure 7-3 Mean average spectra of FSR measurements as a function of the inter-electrode gap length between electrodes of PD emulator with different applied voltage.

### 7.1.2 Galvanic contact measurements

The galvanic contact measurement signal with applied voltages and gap lengths is shown in Figure 7-4. The peak amplitude voltage of galvanic contact measurements under AC applied voltage (12 kV, 15 kV, 16.5 kV, and 18 kV) is illustrated in Figure 7-5. Table 7-3 demonstrated the peak received voltage amplitude and the calculated charge of a galvanic contact measurement. The measured charge was calculated by integration of the first half cycle of the PD signal pulse. The range of the gap between electrodes of the PD emulator varied from 0.2 mm to 1 mm in steps of 0.2 mm.

The peak voltage amplitude when the gap gets smaller and larger changes randomly for example when 0.2 mm and 1 mm. The variation of the applied HV has a relatively small impact on the peak voltage amplitude of the galvanic contact measurement signal.

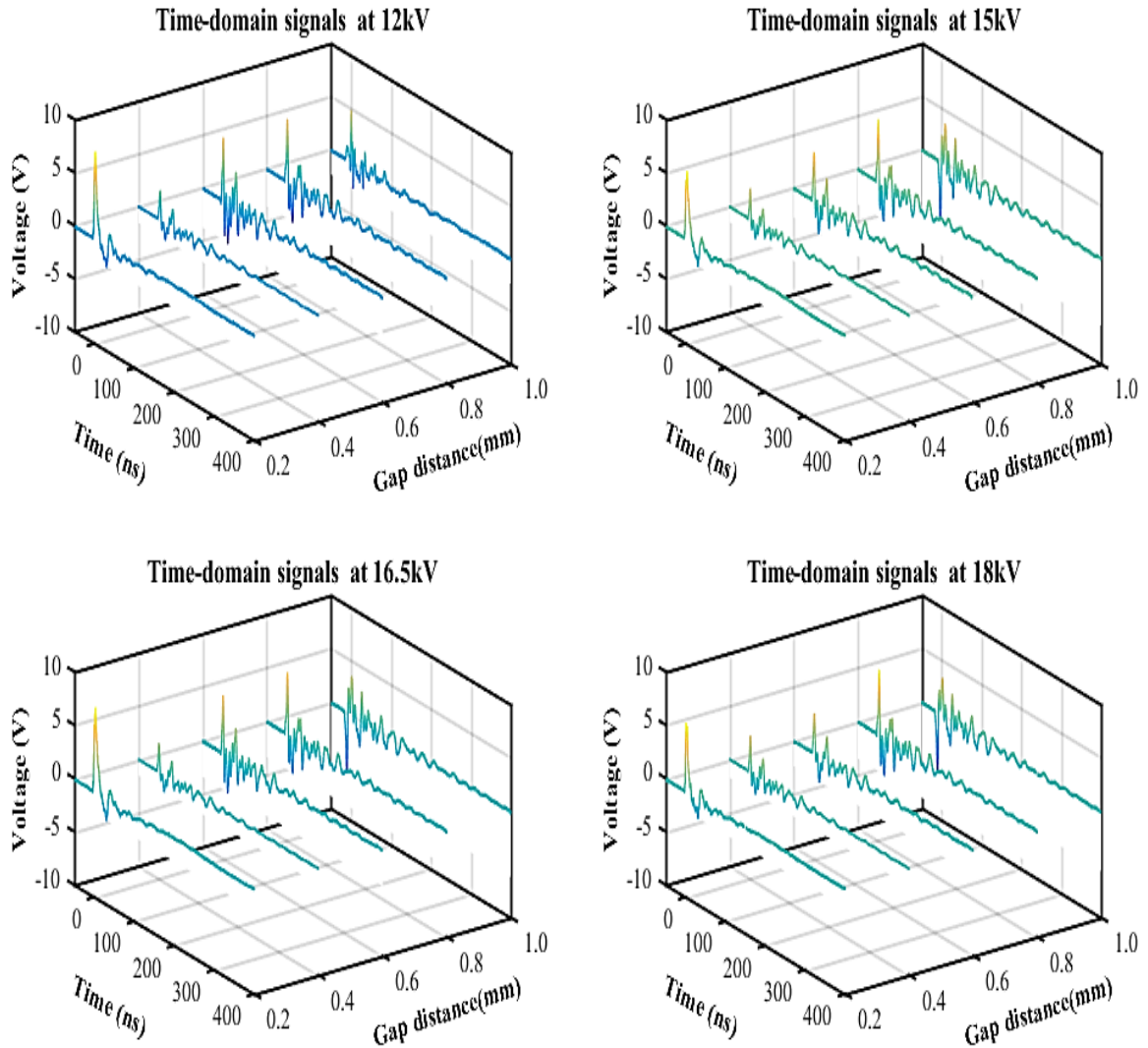


Figure 7-4 Time series events of galvanic contact measurement PD signal.

Figure 7-6 shows the mean average spectra of galvanic contact measurements for various inter-electrode gap lengths. Frequency spectra demonstrate that the PD discharge main frequency content is located in the frequency range of 50 MHz – 290 MHz. The peak amplitude spectra of the galvanic contact measurements are relatively in sensitive to the applied voltage.

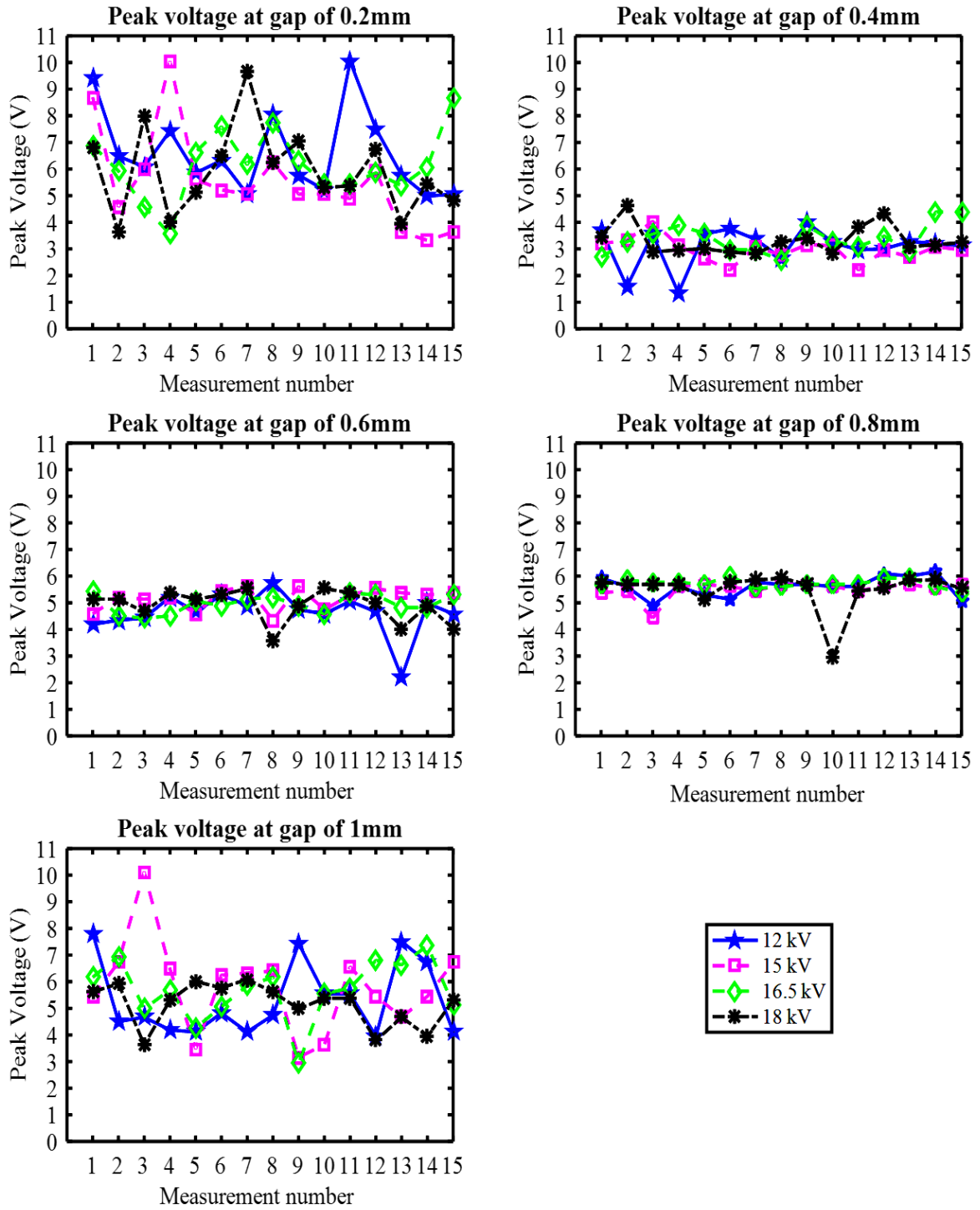


Figure 7-5 Peak voltage amplitude of galvanic contact measurements for each gap.

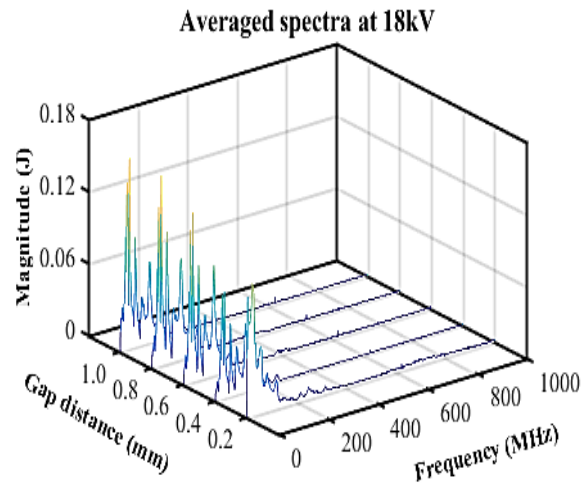
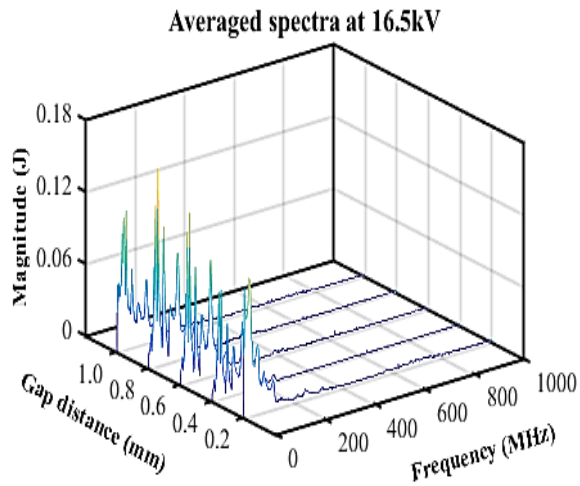
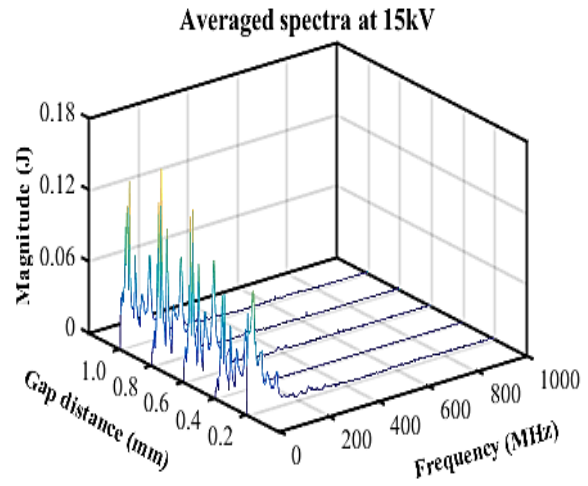
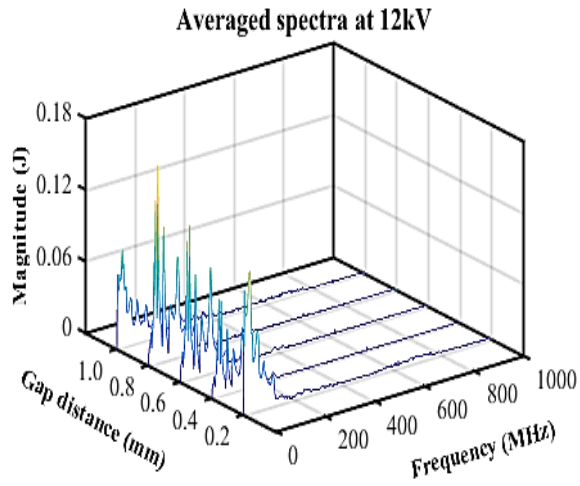


Figure 7-6 Mean average spectra of a galvanic contact measurements for various gap distances and different applied voltages.

Table 7-3 Peak voltage of a galvanic contact measurement depending on inter-electrode gap length.

Power source (kV)	Gap length between floating electrodes of PD emulator (mm)	Mean Peak voltage amplitude of galvanic contact measurement (V)	Peak voltage of contact measurement (dB $\mu$ V)	Standard deviation (V)	Integration time (ns)	Measured charge (nC)
12	0.2	6.60	136.3	1.58	15.0	15.0
	0.4	3.08	129.7	0.75	7.3	3.6
	0.6	4.64	133.3	0.79	7.6	4.3
	0.8	5.61	134.9	0.37	8.6	6.1
	1.0	5.31	134.4	1.38	7.1	4.8
15	0.2	5.53	134.8	1.80	17.0	14
	0.4	2.97	129.4	0.45	7.5	3.2
	0.6	5.15	134.2	0.40	7.4	4.6
	0.8	5.50	134.8	0.32	8.6	5.9
	1.0	5.79	135.2	1.70	8.6	6.7
16.5	0.2	6.15	135.2	1.27	16.3	13.5
	0.4	3.39	130.6	0.56	9.0	3.00
	0.6	4.95	133.9	0.34	7.2	4.5
	0.8	5.72	135.1	0.16	8.5	6.1
	1.0	5.68	135.0	1.13	10.7	6.3
18	0.2	5.90	135.4	1.62	18.0	16.5
	0.4	3.31	130.4	0.55	7.7	3.5
	0.6	4.90	133.8	0.59	7.5	4.8
	0.8	5.49	134.8	0.74	8.6	5.9
	1.0	5.15	134.3	0.80	10.7	6.7

### 7.1.3 Influence of gap length between the HV ground plate electrode and the floating electrode

An experimental setup was devised (showed in Figure 3-1 and Figure 3-5) in order to investigate the influence of gap length between the HV ground plate electrode and the floating electrode for PD measurement. The peak voltage of FSR measurement that is observed relatively increases with a decrease in the gap length between the HV ground

plate electrode and the floating electrode when applied voltage 15 kV as shown in Figures 7-7 and 7-8.

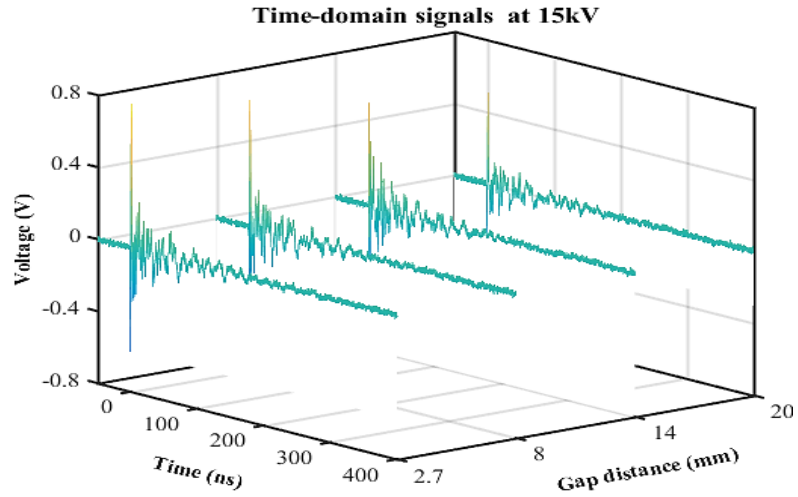


Figure 7-7 Voltage amplitude of FSR measurements signal under AC applied voltage.

Table 7-4 shows the gap length and the mean peak voltage amplitude of the FSR measurement. The physical explanation is that aPD signal is radiated due to the accumulation of anions between the HV ground plate electrode and the floating electrode that is very similar to the electron movement between the two main electrodes.

Table 7-4 Peak voltage of FSR measurement depending on inter-electrode gap length.

AC power source (kV)	PD source distance (m)	Gap length between floating electrodes of PD emulator (mm)	Gap length between ground top PD emulator and insulting (mm)	Mean peak voltage amplitude of FSR measurement (V)	Peak voltage of FSR pulse (dB $\mu$ V)	Electric field strength (dB $\mu$ V/m)	Effective radiated power (dBm)	Standard deviation (V)
15	2	0.4	2.7	0.72	117.1	134.1	33.1	0.16
			8.0	0.67	116.5	133.5	32.5	0.07
			14	0.68	116.6	133.6	32.6	0.13
			20	0.55	114.8	131.8	30.8	0.12

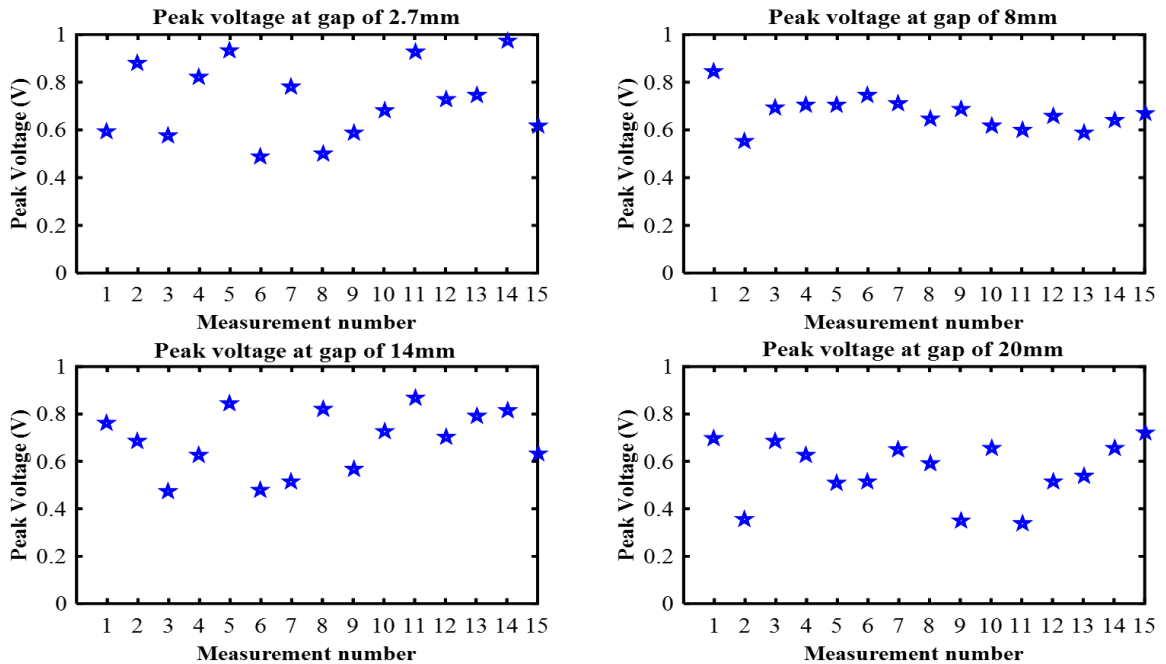


Figure 7-8 Peak voltage amplitude of FSR measurements for various gap lengths.

The measured UHF signal demonstrates that the PD discharge central frequency is located in the frequency range of 50 MHz – 800 MHz. In addition, when the ground plate electrode is sitting on a polypropylene insulation away from the axis of the electrode, the signal produced is similar to that created by corona discharge. Figure 7-9 shows the mean average spectrum of FSR measurements for each case of gap length between the ground top of the floating electrode and the insulation.

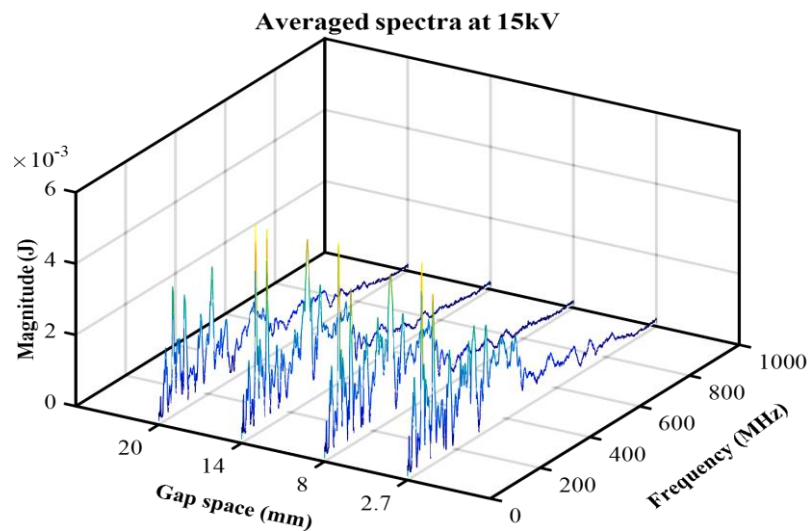
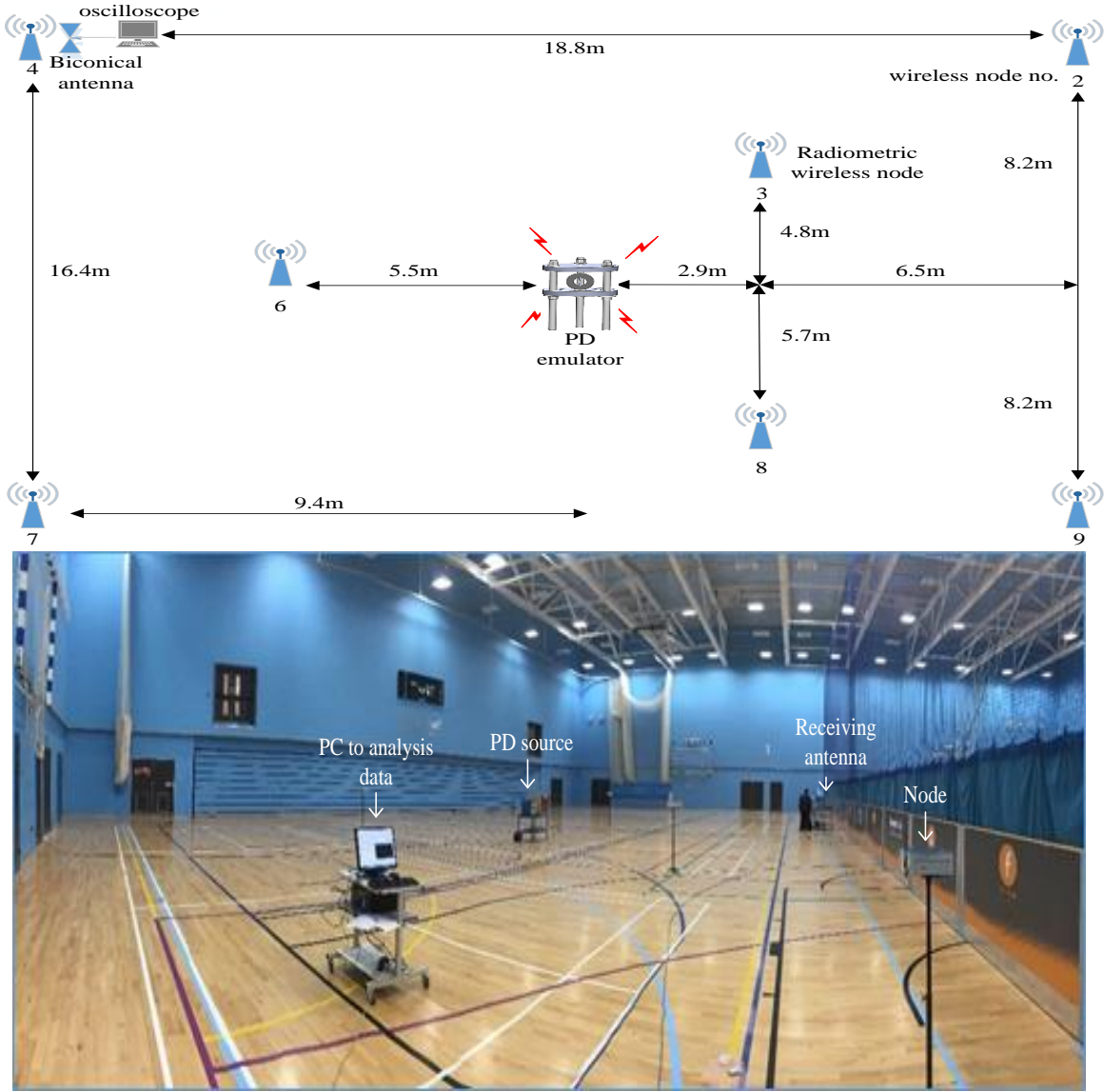


Figure 7-9 Mean averaged spectra of FSR measurements.

## 7.2 FSR Measurement at Different Locations of Receiving Antenna

Free space radiometric PD measurements have been performed outdoors. The excitation applied to the floating electrode PD source is AC and the radiated signal is captured using a wideband biconical antenna. Measurement space plan and measurement space for different locations of PD source to receiving antenna is shown in Figure 7-10. The distance between the PD emulator and the biconical antenna was 12.5 m, 5.6 m, 12.5 m, 5.5 m, 12.5 m, 6.4 m and 12.5 m. When 20 kV AC voltage was applied to the PD emulator a PD was generated.



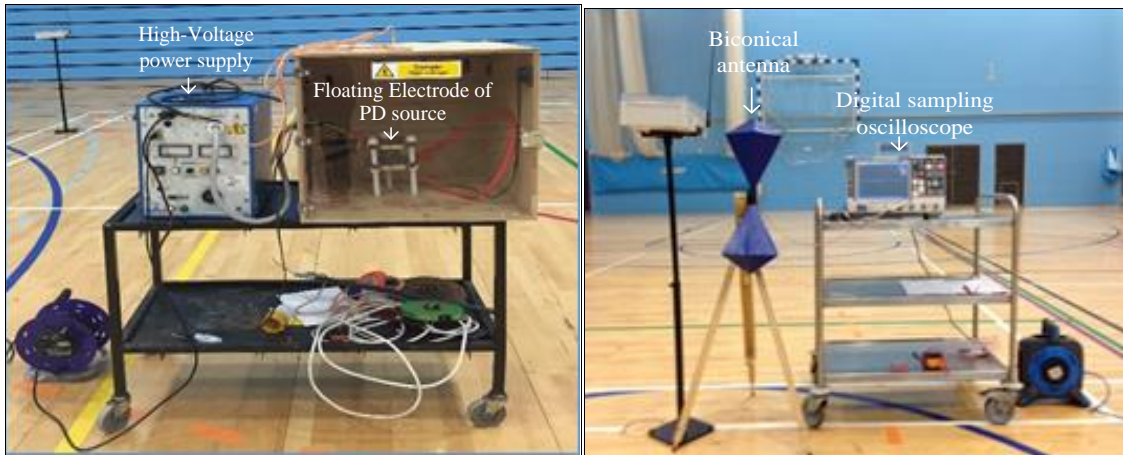


Figure 7-10 Measurement space plan and measurement space.

Example FSR signals at different distances of receiving antenna is shown in Figure 7-11. The mean peak voltage amplitude of receiving antenna and calculated ERP is illustrated in Table 7-5. The radiated signal amplitude is decreasing with increasing distance between the PD source and the biconical antenna, due to radiation losses [1].

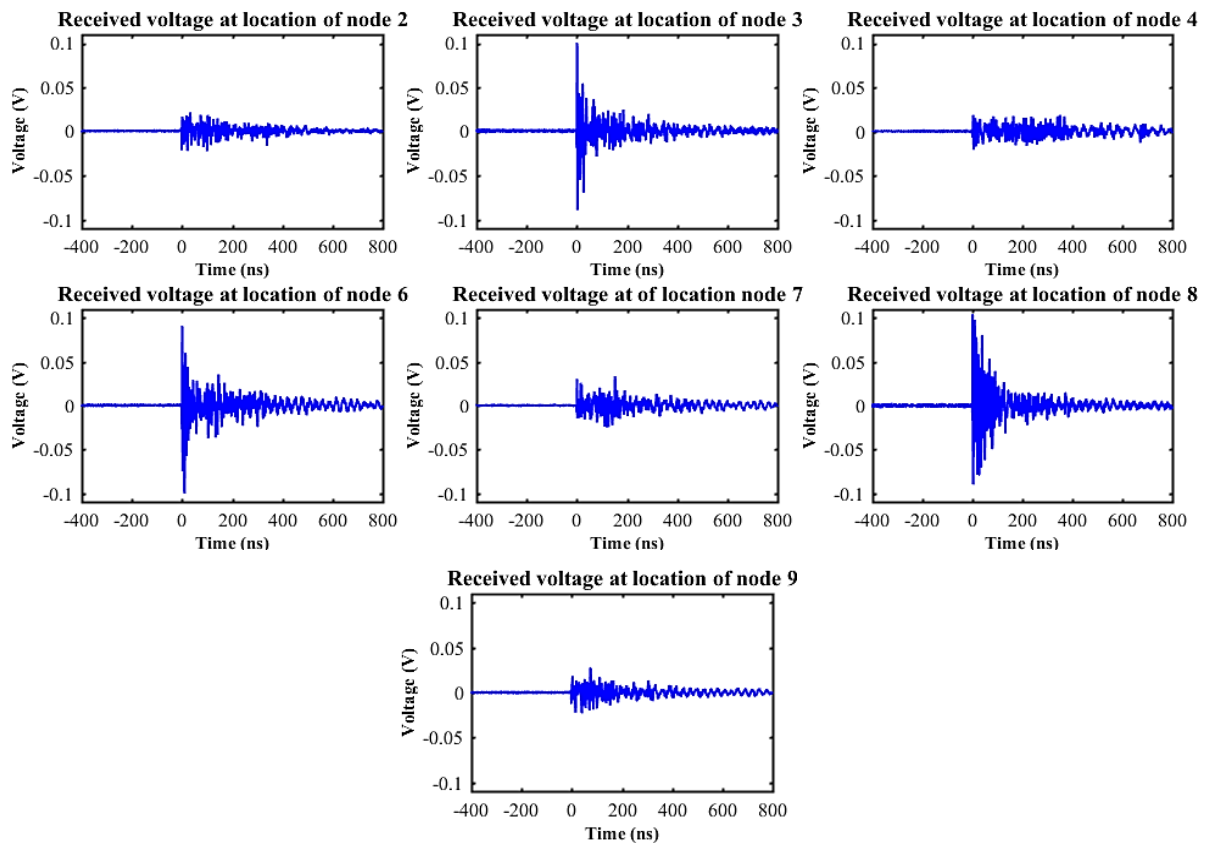


Figure 7-11 FSR measurements at different locations from the receiving antenna.

Figure 7-12 shows the mean averaged spectra at different distances from the receiving antenna. The majority of the energy of the PD discharge is located in the frequency range of 50 MHz – 300 MHz. Figure 7-13 shows the received peak voltage, electric field strength and ERP as a function of PD source.

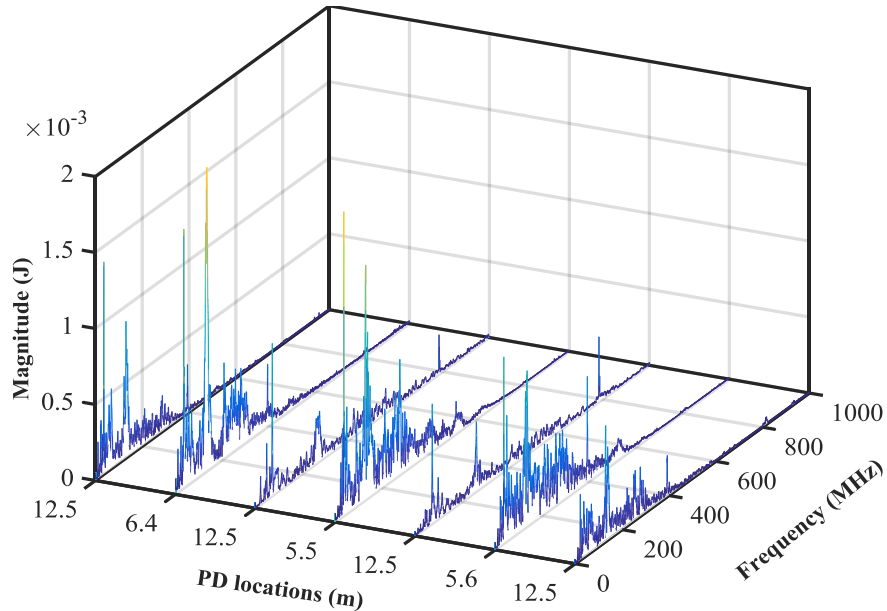


Figure 7-12 Mean averaged spectra at different distances from the receiving antenna.

Table 7-5 Received peak voltage at various distances.

Power supply voltage (kV)		Received voltage at location of node	Antenna - emulator range (m)	FSR mean peak voltage (V)	FSR mean peak voltage (dB $\mu$ V)	Peak electric field strength (dB $\mu$ V/m)	Peak ERP (dBm)	Standard deviation (V)
20	FSR measurement	2	12.5	0.02	87.60	104.60	19.54	0.002
		3	5.6	0.08	98.98	115.98	23.94	0.01
		4	12.5	0.02	86.02	104.60	19.54	0.003
		6	5.5	0.09	99.55	116.55	24.35	0.01
		7	12.5	0.03	89.82	106.82	21.76	0.003
		8	6.4	0.08	98.38	115.38	24.50	0.02
		9	12.5	0.03	89.82	106.82	21.76	0.005

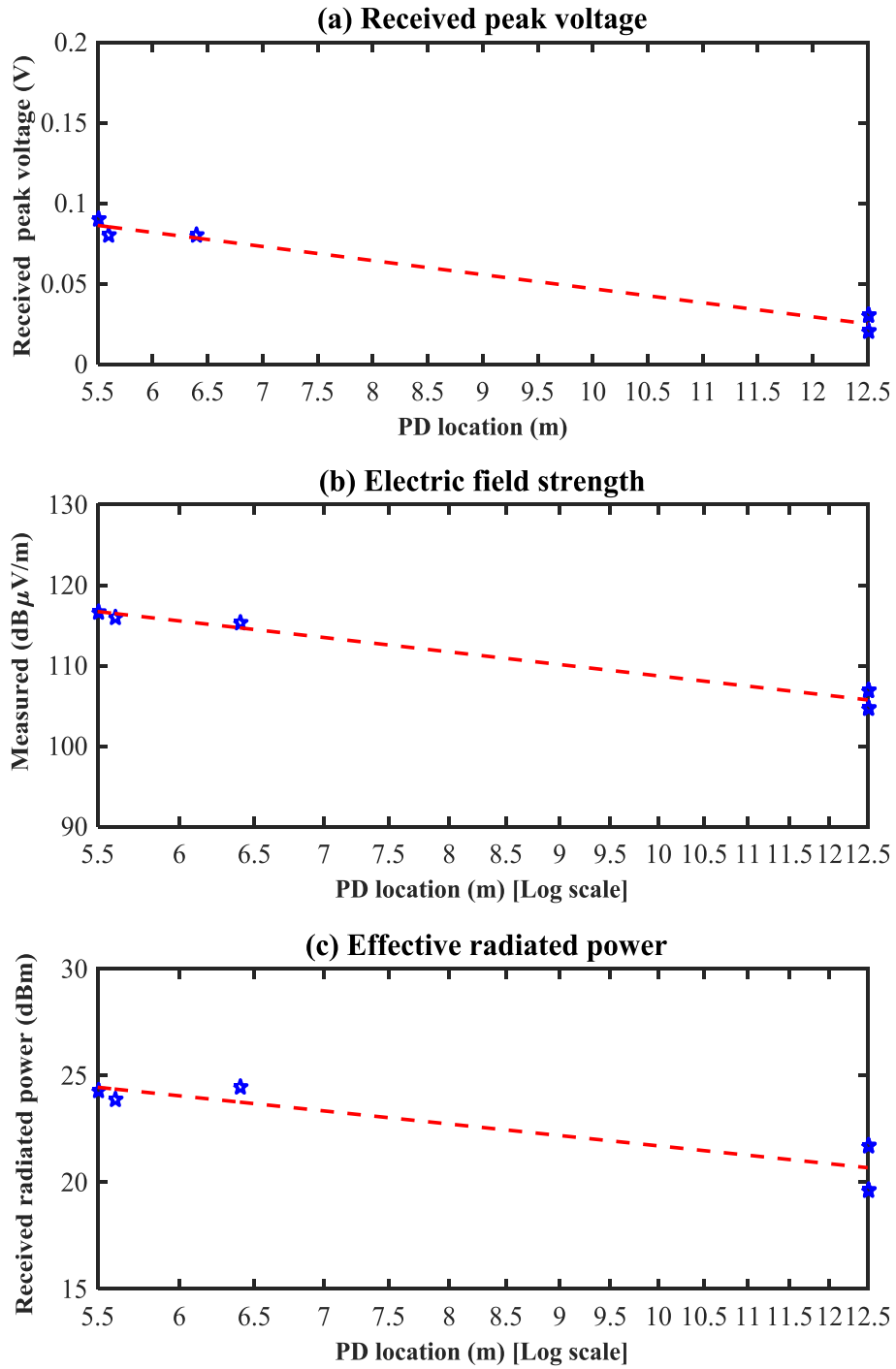


Figure 7-13 (a) Received peak voltage (b) Electric field strength and (c) ERP as a function of PD source – antenna distance from emulator.

### 7.3 Influence of Emulator Geometry on PD Intensity for various DC Applied High Voltages

The measurement system shown in Figure 3-1 is used to investigate the relationship between FSR measurement signal and galvanic contact measurement signal changes with applied DC voltages and gap length between the floating electrodes of the PD emulator. Table 7-6 illustrates the received peak voltage amplitude, electric field strength and calculated charge of the galvanic contact measurement. It also shows the peak voltage, electric field strength and calculated ERP of FSR measurement for 5.5 kV, 6.2 kV, 7.2 kV, 8.2 kV and 8.9 kV using the DC power supply. The range of the gap between electrodes was varied from 0.2 mm to 1mm in steps of 0.2 mm.

Table 7-6 Peak voltage amplitude of galvanic contact measurement and FSR depending on inter-electrode gap length for DC applied voltage.

Power source (kV)	Gap length between floating electrodes of PD emulator (mm)	Peak voltage amplitude of galvanic contact measurement (V)	Peak voltage of galvanic contact measurement (dB $\mu$ V)	Integration time (ns)	Calculated charge (nC)	PD source distance (m)	Peak voltage amplitude of FSR measurement (V)	Peak voltage of FSR pulse (dB $\mu$ V)	Electric field strength (dB $\mu$ V/m)	ERP (dBm)
5.5	0.20	4.58	133.3	23.0	4.2	2	0.37	111.4	128.4	24.9
	0.4	5.05	134.1	27.0	4.9		0.57	115	132.0	28.5
	0.6	3.08	129.8	35.7	3.5		0.25	107.9	124.9	21.4
	0.8	3.47	130.8	28.3	3.7		0.26	108.3	125.3	21.8
	1.0	3.2	130.1	42.0	3.9		0.26	108.3	125.3	21.8
6.2	0.2	5.05	134.1	28.0	4.5		0.50	114	131	27.5
	0.4	5.05	134.1	29.7	4.9		0.49	113.8	130.8	27.3
	0.6	2.4	127.6	51.0	3.4		0.21	106.4	123.4	19.9
	0.8	3.63	131.2	37.5	4.1		0.25	107.9	124.9	21.4
	1.0	3.6	131.1	43.0	4.1		0.19	105.6	122.6	19.1
7.2	0.2	5.05	134.1	24.0	4.7		0.8	118.1	135.1	31.6
	0.4	4.7	133.4	35.0	4.0		0.46	113.3	130.3	26.8
	0.6	3.12	129.8	55.0	4.5		0.22	106.8	123.8	20.3
	0.8	3.16	129.9	37.5	3.3		0.23	107.2	124.2	20.7
	1.0	2.56	128.2	42.5	4.1		0.19	105.6	122.6	19.1
8.2	0.2	5.05	134.1	36.7	4.5		0.46	113.3	130.3	26.8
	0.4	5.05	134.1	27.0	4.4		0.48	113.6	130.6	27.1
	0.6	5.05	134.1	38.0	4.9		0.49	113.8	130.8	27.3
	0.8	4.22	132.5	54.0	4.9		0.32	110.1	127.1	23.6
	1.0	4.42	132.9	29.0	4.5		0.40	112.04	129.04	25.54
8.9	0.2	4.66	133.4	45.0	5.1		0.44	112.9	129.9	26.4
	0.4	5.05	134.1	32.0	4.7		0.56	114.9	131.9	28.4
	0.6	5.05	134.1	38.0	4.8		0.27	108.6	125.6	22.1
	0.8	4.70	133.4	45.0	5.0		0.33	110.4	127.4	23.9
	1.0	5.05	134.1	41.0	4.6		0.45	113.06	130.06	26.56

Figure 7-14 shows that the FSR signal is relatively decreasing by increasing the gap length between the floating electrodes of the PD source. However, some FSR measurements signals are affected due to radiated electromagnetic signal, which radiated from HV equipment and HV power supply. The variation of applied voltage has a relatively small influence on the received peak voltage amplitude of the galvanic contact measurement.

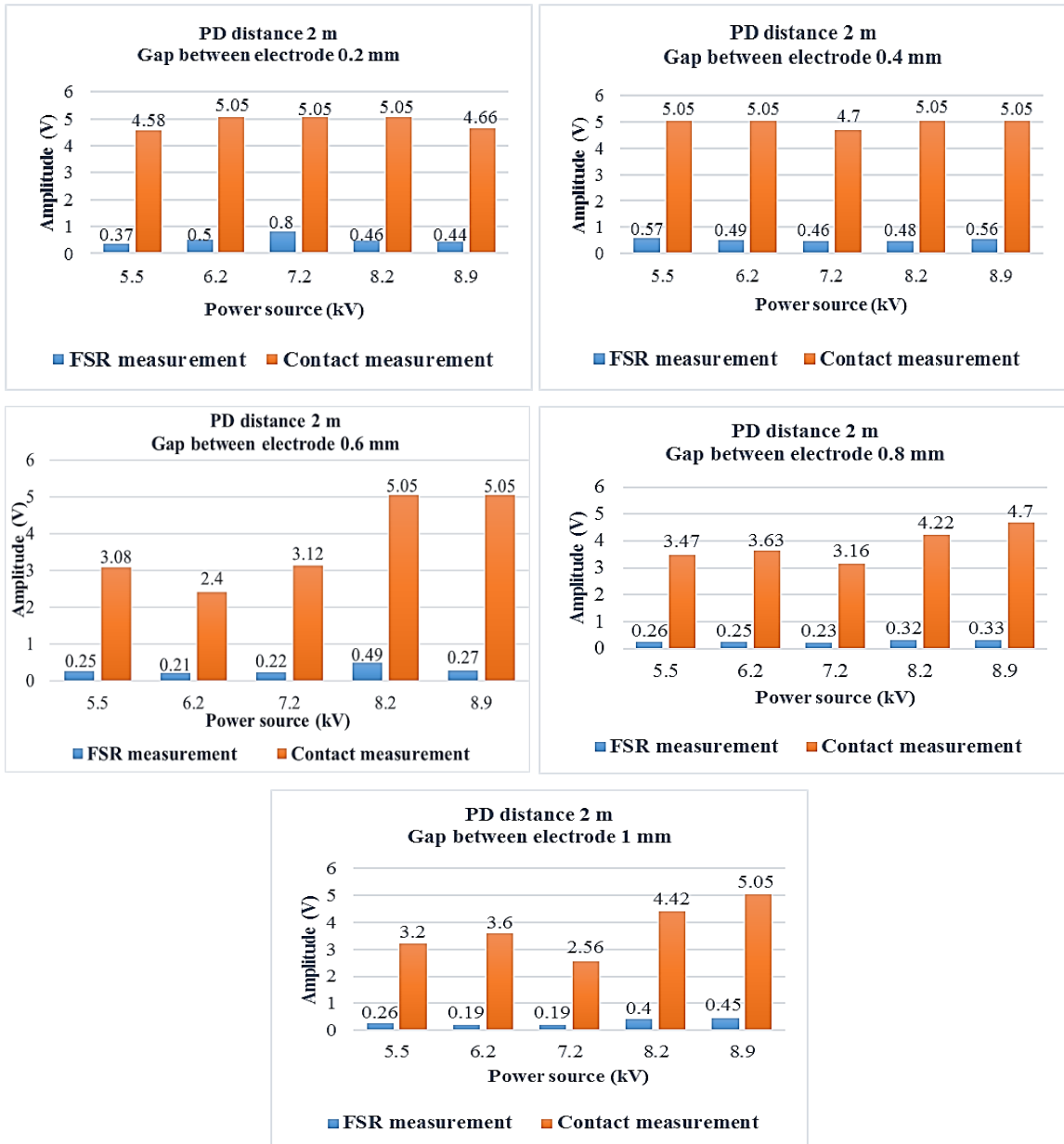


Figure 7-14 Relationship between FSR and galvanic contact measurement signals under DC applied voltage for each inter-electrode of gap length.

## 7.4 Summary

The PD FSR and galvanic contact measurements activity under AC and DC applied voltages at different distances between PD source and biconical antenna have been investigated. It is found that the variation of HV power supply has a relatively small impact on the received peak voltage amplitude of FSR and galvanic contact measurements signal. The received peak voltage amplitude of FSR measurement has decreased by increasing the distance between the floating electrode PD source and the receiving biconical antenna due to transmission losses [2] that are normally unknown in the case of the radiometrically received PD including the radiation efficiency of the transmitting structure and propagation losses. Moreover, it has been investigated that when the gap distance gets larger, the receiving peak voltage amplitude gets smaller. This is because the PD of floating electrode PD source gap is limited in small range.

## CHAPTER 8

### **CONCLUSIONS AND FUTURE WORK**

---

*This chapter presents and summarises the key conclusions arising from this research. Finally, recommendations are made for future research.*

---

## 8.1 Conclusions

The PD associated with HV equipment and HV power systems has been studied. The main PD types are divided into three types based on the place of occurrence and the discharge properties. These types are: internal discharges (that include electrical treeing), surface discharges, and corona discharges. Internal discharges are especially damaging. Electromagnetic, UHF, acoustic and ultrasonic, optical, chemical, light and ultraviolet, and thermal detection techniques have been suggested for localisation and detection of PD in HV equipment in electrical substations. The electrical methods used include near-field coupling and galvanic contact. These methods have the advantages that they can measure absolute PD intensity in terms of apparent charge transfer. IEC 60270 is the most reliable (galvanic contact) method for measuring apparent charge. Therefore, the PD electrical detection technique measures a quantity of the apparent charge using a conventional PD measuring circuit.

An overview of PD theory and PD measurements have been presented. Partial discharge occurring in air, voids and/or voids within transformer oil are short; a few nanoseconds or less in duration.

The IEC 60270 apparent charge measurement circuit is typically used for practical off-line acceptance test and commissioning measurements. In the IEC 60270 measurement a coupling capacitor protects the PD detector from the high voltage passing only the transient PD signal. A calibration process is needed to measure specific charge correct. The IEC 60270 measurement attempts infers charge from the integral of the PD current. Until now it has been believed that absolute measurement of partial discharge intensity using radiometric method is not possible. In this thesis it is demonstrated that such measurement is possible and the first ever such absolute measurements are presented. It has been shown that an FSR measurement can provide useful information about absolute PD intensity.

Partial discharge has been measured concurrently using FSR and galvanic contact techniques for four PD emulators. The PD signals have been analysed in both time-domain and frequency-domain. The correlation between FSR and galvanic contact measurements

signals have been calculated using root mean squared error and correlation coefficient. A comparison between two methods show greater similarity than might be expected. It appears that the signal characteristics in both cases are dominated by the lossy equivalent (resonant) circuit of the radiating structure. Normalised frequency spectra obtained by FFT analysis of the time domain pulses indicate that the principle frequency content in the band 50 MHz to 800 MHz with most of the radiation energy lies in the range of 50 MHz – 290 MHz [2]. The FSR and galvanic contact measurements are not identical but do have some similarities. The galvanic contact signal has less high-frequency content than the FSR signal. This may be due to the frequency dependence of the radiation efficiency and gain of the radiating structure or from the lower sensitivity of the receiving antenna at lower frequencies resulting in suppression of low or frequency radiated energy. Care must be exercised in the interpretation of these results therefore. It is seen that the radiated power of the floating electrode PD emulator is far greater than the radiated power of other three internal types of emulators, and this by at least 13 dB. On the other hand, the epoxy dielectric internal PD emulator is radiating the least power. Free-space radiometry and galvanic contact measurement techniques confirm that, the energy of the PD signal in the frequency band 50 MHz – 290 MHz is higher than in the other frequency bands.

A calibration pulse from a commercial calibrator emulates a PD event of known intensity. The apparent charge can be estimated by integrating the first half-cycle of the PD source time-series current. Estimated charge, peak received voltage, radiated electric field amplitude, and effective radiated power of FSR measurements against range to the PD emulator have been obtained. The ERP was calculated assuming free space propagation and the known antenna factor. Effective radiated power (which should, naturally, be independent of range) is determined and related to the estimated charge of four different PD sources [1]. The measurement of absolute PD intensity from a remote FSR measurement has traditionally thought to be impractical (if not impossible). If PD intensity can be reliably related to PD ERP, however, then there is the possibility of inferring PD intensity from a measurement of ERP using a radiometric system that also locates the PD source. Several issues remain to be investigated before such an absolute radiometric estimate of PD intensity can be realised. Important of these is the anisotropy of the PD

radiation and the error in inferred PD intensity, which this introduces in practice. (It is thought that, in practice, the gain of the PD radiating structure will be modest.) The inferred ERP this work has some modest dependence on range. It is possible this apparent variation is due to the propagation environment in which the measurements were carried out (an indoor laboratory) and the fact that the measurements were not carried out unambiguously in the far field. It is felt that the results reported here are sufficiently encouraging, however, to pursue this work further [164].

Three different PD emulators have been modelled and the radiated fields from each due to a given excitation derived by CST simulation. The PD intensity corresponding to the excitation has been calculated allowing this to be related to radiate PD field strength. The simulations have been validated by using RMSE and correlation coefficient between the measuring the radiated fields signals, comparing them with the fields predicted from simulation signals and showing the agreement to be good. measuring the radiated fields, comparing them with the fields predicted from simulation. Agreement is good. The validated simulations are used to investigate the relationship between FSR PD measurements and absolute PD intensity. If the relationship can be (even approximately) established then the utility of FSR PD measurement and locations systems for the condition monitoring of insulation integrity in high voltage plant will be greatly enhanced [3].

## 8.2 Recommendations for Future Work

- Recommendation one

Field tests are required to demonstrate the accuracy with which absolute PD source intensity (in pC) can be estimated from a radiometric measurement. A high accuracy radiometric measurement system requires optimizations and improvements that could be specified by operating the system under real conditions.

- Recommendation two

Development of location algorithms based on multiple spatial measurements of absolute PD intensity.

- Recommendation three

Wireless Sensor Networks (WSN) should be developed to monitor free space radiometric PD signals in high voltage systems.

## REFERENCES

- [1] A. Jaber, P. Lazaridis, B. Saeed, Y. Zhang, U. Khan, D. Upton, *et al.*, "Comparative study of Partial Discharge emulators for the calibration of Free-Space radiometric measurements," in *Automation and Computing (ICAC), 2016 22nd International Conference on*, 2016, pp. 313-316.
- [2] A. Jaber, P. Lazaridis, Y. Zhang, D. Upton, H. Ahmed, U. Khan, *et al.*, "Comparison of contact measurement and free-space radiation measurement of partial discharge signals," in *Automation and Computing (ICAC), 2015 21st International Conference on*, 2015, pp. 1-4.
- [3] A. Jaber, P. Lazaridis, B. Saeed, Y. Zhang, U. Khan, D. Upton, *et al.*, "Validation of partial discharge emulator simulations using free-space radiometric measurements," in *Students on Applied Engineering (ISCAE), International Conference for*, 2016, pp. 475-478.
- [4] Y. Han and Y. Song, "Condition monitoring techniques for electrical equipment-a literature survey," *IEEE Transactions on Power delivery*, vol. 18, pp. 4-13, 2003.
- [5] B. Sarkar, C. Koley, N. Roy, and P. Kumbhakar, "Low cost RF sensor for partial discharge detection of high voltage apparatus," in *Condition Assessment Techniques in Electrical Systems (CATCON), 2013 IEEE 1st International Conference on*, 2013, pp. 259-264.
- [6] P. J. Tavner and J. Penman, *Condition monitoring of electrical machines* vol. 1: Research Studies Pre, 1987.
- [7] O. Thorsen and M. Dalva, "Methods of condition monitoring and fault diagnosis for induction motors," *European transactions on electrical power*, vol. 8, pp. 383-395, 1998.
- [8] C. Bengtsson, "Status and trends in transformer monitoring," *IEEE Transactions on Power delivery*, vol. 11, pp. 1379-1384, 1996.
- [9] H. T. Grimmelius, P. P. Meiler, H. L. Maas, B. Bonnier, J. S. Grevink, and R. F. van Kuilenburg, "Three state-of-the-art methods for condition monitoring," *IEEE Transactions on Industrial Electronics*, vol. 46, pp. 407-416, 1999.

- [10] D. A. Genutis, "Using Partial Discharge Surveys to Increase Electrical Reliability," presented at the Annual Technical Conference Communications and Metering-NETA WORLD, USA, 2002.
- [11] D. A. Genutis, "Partial Discharge Testing of Rotating Apparatus," presented at the Neta World, 2008.
- [12] D. A. Genutis, "Partial Discharge Monitoring of Medium-Voltage Switchgear," presented at the Neta World, 2010.
- [13] J. M. A. S. Grubic, B. Lu, and T. G. Habetler, "A survey on testing and monitoring methods for stator insulation systems of low-voltage induction machines focusing on turn insulation problems," *Industrial Electronics, IEEE Transactions*, vol. 55, pp. 4127-4136, 2008.
- [14] D. A. Genutis, "On-Line Shielded Cable Partial Discharge Locating — An Overview," presented at the Neta World, 2006.
- [15] B. E. A. G. Stone, I. Culbert, H. Dhirani, "Electrical Insulation for Rotating Machines," presented at the IEEE Press, 2004.
- [16] M. Aruna, V. Pattanshetti, K. N. Ravi, and N. Vasudev, "Insulation System in Energy Sector: The Benefits of Polymer Composites," *44 INDIAN JOURNAL OF APPLIED RESEARCH*, vol. 1, 2011.
- [17] D. A. Genutis, "Electrical Equipment Condition Assessment Using On-Line Solid Insulation Sampling," presented at the NETA WORLD Spring, 2006.
- [18] C. Walton and R. Mackinlay, "PD monitoring-a critical tool for condition-based assessments," *Transmission and Distribution World*, vol. 55, pp. 38-46, 2003.
- [19] L. Renforth, C. Smith, and C. Armstrong, "Effective asset management for life extension of HV Plant," in *High voltage plant life extension. Conference*, 2000, pp. 212-219.
- [20] J. M. Neto, Y. Zhang, A. Jaber, M. Zhu, M. Judd, R. Atkinson, *et al.*, "Radiometric location of partial discharge sources for the future smart grid," in *General Assembly and Scientific Symposium (URSI GASS), 2014 XXXIth URSI*, 2014, pp. 1-4.

- [21] E. Iliana, J. Philip, and A. Ian, "RF-Based Partial Discharge Early Warning System for Air-Insulated Substation," *IEEE Transactions on Power Delivery*, vol. 24, pp. 20-29, 2009.
- [22] A. Haddad and D. F. Warne, *Advances in high voltage engineering* vol. 40: IET, 2004.
- [23] Y. Tian, P. Lewin, and A. Davies, "Comparison of on-line partial discharge detection methods for HV cable joints," *IEEE Transactions on Dielectrics and Electrical Insulation*, vol. 9, pp. 604-615, 2002.
- [24] X. Wang, B. Li, H. T. Roman, O. L. Russo, K. Chin, and K. R. Farmer, "Acousto-optical PD detection for transformers," *IEEE transactions on power delivery*, vol. 21, pp. 1068-1073, 2006.
- [25] L. Wang, N. Fang, C. Wu, H. Qin, and Z. Huang, "A fiber optic PD sensor using a balanced Sagnac interferometer and an EDFA-Based DOP Tunable fiber ring laser," *Sensors*, vol. 14, pp. 8398-8422, 2014.
- [26] J. Posada-Roman, J. A. Garcia-Souto, and J. Rubio-Serrano, "Fiber optic sensor for acoustic detection of partial discharges in oil-paper insulated electrical systems," *Sensors*, vol. 12, pp. 4793-4802, 2012.
- [27] M. Yaacob, M. A. Alsaedi, J. Rashed, A. Dakhil, and S. Atyah, "Review on partial discharge detection techniques related to high voltage power equipment using different sensors," *Photonic Sensors*, vol. 4, pp. 325-337, 2014.
- [28] J. M. R. de Souza Neto, J. S. da Rocha Neto, L. Chang, K. Atkinson, K. Sasloglou, and I. Glover, "A self-calibrating partial discharge WSN for condition monitoring in the future smart grid," 2012.
- [29] I. S. IEC, "60270, High Voltage Test Techniques–Partial Discharge Measurements," *International Electrotechnical Commission*, 2000.
- [30] M. D. Judd, G. P. Cleary, and C. J. Bennoch, "Applying UHF Partial Discharge Detection to Power Transformers," *IEEE Power Engineering Review*, vol. 22, pp. 57-59, 2002.

- [31] P. J. Moore, I. E. Portugues, and I. A. Glover, "Radiometric location of partial discharge sources on energized high-Voltage plant," *IEEE Transactions on Power Delivery*, vol. 20, pp. 2264-2272, 2005.
- [32] F. Álvarez, F. Garnacho, J. Ortego, and M. Á. Sánchez-Urán, "Application of HFCT and UHF sensors in on-line partial discharge measurements for insulation diagnosis of high voltage equipment," *Sensors*, vol. 15, pp. 7360-7387, 2015.
- [33] A. Rodrigo, P. Llovera, V. Fuster, and A. Quijano, "Influence of high frequency current transformers bandwidth on charge evaluation in partial discharge measurements," *IEEE Transactions on Dielectrics and Electrical Insulation*, vol. 18, pp. 1798-1802, 2011.
- [34] A. Rodrigo, P. Llovera, V. Fuster, and A. Quijano, "Study of partial discharge charge evaluation and the associated uncertainty by means of high frequency current transformers," *IEEE Transactions on Dielectrics and Electrical Insulation*, vol. 19, pp. 434-442, 2012.
- [35] L. Renforth, R. Armstrong, D. Clark, S. Goodfellow, and P. S. Hamer, "A new technique for the remote partial discharge monitoring of the stator insulation of high-voltage motors located in "Ex"(hazardous) locations," in *Petroleum and Chemical Industry Technical Conference (PCIC), 2012 Record of Conference Papers Industry Applications Society 59th Annual IEEE*, 2012, pp. 1-10.
- [36] X. Song, C. Zhou, and D. M. Hepburn, "An algorithm for indentifying the arrival time of PD pulses for PD source location," in *2008 Annual Report Conference on Electrical Insulation and Dielectric Phenomena*, 2008, pp. 379-382.
- [37] M. D. Judd, "Radiometric partial discharge detection," in *Condition Monitoring and Diagnosis, 2008. CMD 2008. International Conference on*, 2008, pp. 1025-1030.
- [38] M. D. Judd, Y. Li, and I. B. B. Hunter, "Partial discharge monitoring for power transformer using UHF sensors. Part 2: field experience," *IEEE Electrical Insulation Magazine*, vol. 21, pp. 5-13, 2005.

- [39] S. Boggs, "Electromagnetic techniques for fault and partial discharge location in gas-insulated cables and substations," *IEEE Transactions on Power Apparatus and Systems*, vol. 7, pp. 1935-1941, 1982.
- [40] B. Hampton and R. Meats, "Diagnostic measurements at UHF in gas insulated substations," in *IEE Proceedings C-Generation, Transmission and Distribution*, 1988, pp. 137-145.
- [41] J. Pearson, B. Hampton, and A. Sellars, "A continuous UHF monitor for gas-insulated substations," *IEEE transactions on electrical insulation*, vol. 26, pp. 469-478, 1991.
- [42] J. S. Pearson, O. Farish, B. F. Hampton, M. D. Judd, D. Templeton, B. W. Pryor, *et al.*, "Partial discharge diagnostics for gas insulated substations," *IEEE Transactions on Dielectrics and Electrical Insulation*, vol. 2, pp. 893-905, 1995.
- [43] W. Rutgers and Y. Fu, "UHF PD-Detection in a power transformer," in *10th International Symposium on High Voltage Engineering*, 1997, pp. 219-222.
- [44] M. Judd, O. Farish, J. Pearson, T. Breckenridge, and B. Pryor, "Power transformer monitoring using UHF sensors: installation and testing," in *Electrical Insulation, 2000. Conference Record of the 2000 IEEE International Symposium on*, 2000, pp. 373-376.
- [45] M. Judd, G. Cleary, C. Bennoch, J. Pearson, and T. Breckenridge, "Power transformer monitoring using UHF sensors: site trials," in *Electrical Insulation, 2002. Conference Record of the 2002 IEEE International Symposium on*, 2002, pp. 145-149.
- [46] P. J. Moore, I. Portugues, and I. A. Glover, "A nonintrusive partial discharge measurement system based on RF technology," in *Power Engineering Society General Meeting, 2003, IEEE*, 2003, pp. 1-633 Vol. 2.
- [47] A. Reid, M. D. Judd, R. A. Fouracre, B. Stewart, and D. Hepburn, "Simultaneous measurement of partial discharges using IEC60270 and radio-frequency techniques," *Dielectrics and Electrical Insulation, IEEE Transactions on*, vol. 18, pp. 444-455, 2011.

- [48] I. E. Portugues, P. J. Moore, I. A. Glover, C. Johnstone, R. H. McKosky, M. B. Goff, *et al.*, "RF-based partial discharge early warning system for air-insulated substations," *IEEE Transactions on Power Delivery*, vol. 24, pp. 20-29, 2009.
- [49] Y. Zhang, D. Upton, A. Jaber, H. Ahmed, B. Saeed, P. Mather, *et al.*, "Radiometric wireless sensor network monitoring of partial discharge sources in electrical substations," *International Journal of Distributed Sensor Networks*, vol. 2015, p. 179, 2015.
- [50] A. Reid, M. Judd, B. Stewart, D. Hepburn, and R. Fouracre, "Identification of multiple defects in solid insulation using combined RF and IEC60270 measurement," in *Solid Dielectrics, 2007. ICSD'07. IEEE International Conference on*, 2007, pp. 585-588.
- [51] E. Lemke, S. Berlijn, E. Gulski, M. Muhr, E. Pultrum, T. Strehl, *et al.*, "Guide for partial discharge measurements in compliance to IEC 60270," *CIGRE Technical Bochure*, vol. 366, 2008.
- [52] K. C. Kao, *Dielectric phenomena in solids*: Academic press, 2004.
- [53] J. Kuffel and P. Kuffel, *High voltage engineering fundamentals*: Newnes, 2000.
- [54] M. S. Naidu and V. Kamaraju, *High voltage engineering*: Tata McGraw-Hill Education, 2013.
- [55] I. E. Commission, *High-voltage Test Techniques: Partial Discharge Measurements*: International Electrotechnical Commission, 2000.
- [56] I. Standard, "High-voltage test techniques: partial discharge measurements," *IEC-60270*, 2000.
- [57] A. Ovsyannikov and S. Korobeynikov, "'Apparent' and true charges of partial discharges," in *Dielectrics (ICD), 2016 IEEE International Conference on*, 2016, pp. 485-488.
- [58] M. G. Danikas, "The definitions used for partial discharge phenomena," *IEEE transactions on electrical insulation*, vol. 28, pp. 1075-1081, 1993.
- [59] S. A. Boggs, "Partial discharge: overview and signal generation," *IEEE Electrical Insulation Magazine*, vol. 6, pp. 33-39, 1990.

- [60] C. Min-Yen, L. Chang-Hsing, H. Chih-Hsien, and Y. Shih-Shong, "The application of on-line PDM on in-service MV cable terminations," in *Condition Monitoring and Diagnosis, 2008. CMD 2008. International Conference on*, 2008, pp. 1171-1174.
- [61] A. M. b. Ishak, "Calibration and design of UHF partial discharge sensors using finite-difference time-domain modelling," University of Strathclyde, 2013.
- [62] F. Kreuger, E. Gulski, and A. Krivda, "Classification of partial discharges," *IEEE Transactions on Electrical Insulation*, 28 (6)[see also *IEEE Transactions on Dielectrics and Electrical Insulation*], 1993.
- [63] R. Energy. (2016). *Partial Discharge Service PDS*. Available: <http://isolatedphasebus.com/Partial-Discharge-Service>
- [64] J. He, J. Braun, J. Densley, N. Fujimoto, and H. Sedding, "Partial discharge characteristics of electrical trees in polymeric cable insulation," in *Electrical Insulation and Dielectric Phenomena, 1994., IEEE 1994 Annual Report., Conference on*, 1994, pp. 91-96.
- [65] O. Bergius, "Implementation of On-line Partial Discharge Measurements in Medium Voltage Cable Network," 2012.
- [66] J. Densley, T. Kalicki, and Z. Nodolny, "Characteristics of PD pulses in electrical trees and interfaces in extruded cables," *IEEE Transactions on Dielectrics and Electrical Insulation*, vol. 8, pp. 48-57, 2001.
- [67] G. J. Paoletti and A. Golubev, "Partial discharge theory and technologies related to medium-voltage electrical equipment," *Industry Applications, IEEE Transactions on*, vol. 37, pp. 90-103, 2001.
- [68] R. J. Van Brunt, "Physics and chemistry of partial discharge and corona. Recent advances and future challenges," *Dielectrics and Electrical Insulation, IEEE Transactions on*, vol. 1, pp. 761-784, 1994.
- [69] C. D. E. i. E. T. Lines, "Corona Discharge Effect," 2016.
- [70] G. C. Lichtenberg, "Novi Commentarii Societatis Regiae Scientiarum Gottingensis," vol. 8, 1777.

- [71] M. Muhr, T. Strehl, E. Gulski, K. Feser, E. Gockenbach, W. Hauschild, *et al.*, "Sensors and sensing used for non-conventional PD detection," *Proceedings of the CIGRE session paper D*, vol. 1, p. 102, 2006.
- [72] A. K. Lazarevich, "Partial discharge detection and localization in high voltage transformers using an optical acoustic sensor," 2003.
- [73] X. Song, C. Zhou, and D. M. Hepburn, "An algorithm for indentifying the arrival time of PD Pulses for PD source location," in *Electrical Insulation and Dielectric Phenomena, 2008. CEIDP 2008. Annual Report Conference on*, 2008, pp. 379-382.
- [74] HVPD. (20.10). *HVPD TEV Sensor*. Available: [www.hvpd.co.uk](http://www.hvpd.co.uk)
- [75] M. Judd and O. Farish, "High bandwidth measurement of partial discharge current pulses," in *Electrical Insulation, 1998. Conference Record of the 1998 IEEE International Symposium on*, 1998, pp. 436-439.
- [76] M. D. Judd, L. Yang, and I. B. Hunter, "Partial discharge monitoring of power transformers using UHF sensors. Part I: sensors and signal interpretation," *Electrical Insulation Magazine, IEEE*, vol. 21, pp. 5-14, 2005.
- [77] C. Sung In, "On-line PD (partial discharge) Monitoring of power system components," 2011.
- [78] M. Muhr, T. Strehl, E. Gulski, K. Feser, E. Gockenbach, W. Hauschild, *et al.*, "Sensors and sensing used for non-conventional PD detection," *CIGRE, Paris*, pp. 1-7, 2006.
- [79] J. Ramírez-Niño and A. Pascacio, "Acoustic measuring of partial discharge in power transformers," *Measurement Science and Technology*, vol. 20, p. 115108, 2009.
- [80] I. Kemp, "Partial discharge plant-monitoring technology: present and future developments," *IEE Proceedings-Science, Measurement and Technology*, vol. 142, pp. 4-10, 1995.
- [81] S. C. Oliveira and E. Fontana, "Optical detection of partial discharges on insulator strings of high-voltage transmission lines," *Instrumentation and Measurement, IEEE Transactions on*, vol. 58, pp. 2328-2334, 2009.

- [82] R. Meggs and K. Daffey, "Partial Discharge Monitoring in Marine HV Systems," ed: IMAREST, 2011.
- [83] M. Muhr and R. Schwarz, "Experience with optical partial discharge detection," *Materials Science-Poland*, vol. 27, pp. 1139-1142, 2009.
- [84] J. S. N'cho, I. Fofana, Y. Hadjadj, and A. Beroual, "Review of Physicochemical-Based Diagnostic Techniques for Assessing Insulation Condition in Aged Transformers," *Energies*, vol. 9, p. 367, 2016.
- [85] B. H. Ward, "A survey of new techniques in insulation monitoring of power transformers," *IEEE Electrical Insulation Magazine*, vol. 17, pp. 16-23, 2001.
- [86] J. M. Braun and F. Y. Chu, "Novel Low-Cost SF6 Arcing Byproduct Detectors for Field Use in Gas-Insulated Switchgear," *IEEE Transactions on Power Delivery*, vol. 1, pp. 81-86, 1986.
- [87] M. Duval and J. Dukarm, "Improving the reliability of transformer gas-in-oil diagnosis," *IEEE Electrical Insulation Magazine*, vol. 21, pp. 21-27, 2005.
- [88] D. A. Genutis, "On-Line Partial Discharge Testing Applications — An Overview," presented at the No-Outage Inspection Corner, 2009.
- [89] M. D. Judd, A. J. Reid, L. Yang, B. G. Stewart, and R. A. Fouracre, "A new integrated diagnostic partial discharge monitoring strategy for HV plant items: combining UHF couplers and the IEC60270 standard," in *Electricity Distribution, 2005. CIRED 2005. 18th International Conference and Exhibition on*, 2005, pp. 1-4.
- [90] G. J. Paoletti and A. Golubev, "Partial discharge theory and technologies related to medium-voltage electrical equipment," *IEEE Transactions on Industry Applications*, vol. 37, pp. 90-103, 2001.
- [91] M. Siegel and S. Tenbohlen, "Comparison between Electrical and UHF PD Measurement concerning Calibration and Sensitivity for Power Transformers," *differences*, vol. 6, p. 7, 2014.
- [92] M. D. Judd, S. D. J. McArthur, A. J. Reid, V. M. Catterson, Y. Li, B. Jacobson, *et al.*, "Investigation of radiometric partial discharge detection for use in switched

- HVDC testing," in *2006 IEEE Power Engineering Society General Meeting*, 2006, p. 7 pp.
- [93] P. J. Moore, I. E. Portugues, and I. A. Glover, "Partial discharge investigation of a power transformer using wireless wideband radio-frequency measurements," *IEEE Transactions on Power Delivery*, vol. 21, pp. 528-530, 2006.
- [94] J. R. Alistair, D. J. Martin, G. S. Brian, and A. F. Richard, "Partial discharge current pulses in SF 6 and the effect of superposition of their radiometric measurement," *Journal of Physics D: Applied Physics*, vol. 39, p. 4167, 2006.
- [95] P. Moore, I. Portugues, and I. Glover, "Remote diagnosis of overhead line insulation defects," in *Power Engineering Society General Meeting, 2004. IEEE, 2004*, pp. 1831-1835.
- [96] I. Portuguds, P. J. Moore, and I. Glover, "Characterisation of radio frequency interference from high voltage electricity supply equipment," in *Antennas and Propagation, 2003.(ICAP 2003). Twelfth International Conference on (Conf. Publ. No. 491)*, 2003, pp. 820-823.
- [97] Y. Zhang, J. Neto, D. Upton, A. Jaber, U. Khan, B. Saeed, *et al.*, "Radiometer monitoring system for partial discharge detection in substation," in *Radio Science Conference (URSI AT-RASC), 2015 1st URSI Atlantic*, 2015, pp. 1-1.
- [98] J. de Souza Neto, J. da Rocha Neto, E. C. Macedo, I. A. Glover, and M. Judd, "An envelope detector as a trading cost technique for radiometric partial discharge detection," in *Instrumentation and Measurement Technology Conference (I2MTC) Proceedings, 2014 IEEE International*, 2014, pp. 1584-1589.
- [99] J. de Souza Neto, E. de Macedo, J. da Rocha Neto, E. Da Costa, S. Bhatti, and I. Glover, "Partial Discharge Location using Unsynchronized Radiometer Network for Condition Monitoring in HV Substations-A Proposed Approach," in *Journal of Physics: Conference Series*, 2012, p. 012053.
- [100] E. Lemke, "A critical review of partial-discharge models," *IEEE Electrical Insulation Magazine*, vol. 28, pp. 11-16, 2012.
- [101] S. Boggs and G. Stone, "Fundamental limitations in the measurement of corona and partial discharge," *IEEE Transactions on Electrical Insulation*, pp. 143-150, 1982.

- [102] W. Carter, "Practical Aspects of Apparent Charge Partial Discharge Measurements," *IEEE Transactions on Power Apparatus and Systems*, pp. 1985-1989, 1982.
- [103] S. Chen and T. Czaszejko, "Partial discharge test circuit as a spark-gap transmitter," *IEEE Electrical Insulation Magazine*, vol. 3, pp. 36-44, 2011.
- [104] M. Judd, "Contact discharges as a source of sub-nanosecond high voltage pulses," *Journal of Physics D: Applied Physics*, vol. 34, p. 2883, 2001.
- [105] Z. Wang, S. Hettiwatte, and P. Crossley, "A measurements-based discharge location algorithm for plain disc winding power transformers," *Dielectrics and Electrical Insulation, IEEE Transactions on*, vol. 12, pp. 416-422, 2005.
- [106] X. Li, G. Wu, X. Zhang, and S. Bian, "Partial discharge pulse shape detection and analysis under DC condition," in *Electrical Insulation Conference and Electrical Manufacturing Expo, 2007*, 2007, pp. 48-51.
- [107] E. C. de Macedo, J. de Souza Neto, J. Moises, M. Villanueva, E. C. Guedes, R. C. S. Freire, *et al.*, "Partial discharge estimation based on radiometric and classical measurements," in *Instrumentation and Measurement Technology Conference (I2MTC), 2012 IEEE International*, 2012, pp. 807-811.
- [108] A. J. Reid, M. D. Judd, R. A. Fouracre, B. G. Stewart, and D. M. Hepburn, "Identification of simultaneously active partial discharge sources using combined radio frequency and IEC60270 measurement," *IET Science, Measurement & Technology*, vol. 5, pp. 102-108, 2011.
- [109] G. P. Cleary and M. D. Judd, "UHF and current pulse measurements of partial discharge activity in mineral oil," *IEE Proceedings - Science, Measurement and Technology*, vol. 153, pp. 47-54, 2006.
- [110] A. Reid, M. Judd, B. Stewart, and R. Fouracre, "Frequency distribution of RF energy from PD sources and its application in combined RF and IEC60270 measurements," in *Electrical Insulation and Dielectric Phenomena, 2006 IEEE Conference on*, 2006, pp. 640-643.
- [111] A. S. Kumar, R. P. Gupta, K. Udayakumar, and A. Venkatasami, "Online partial discharge detection and location techniques for condition monitoring of power

- transformers: A review," in *Condition Monitoring and Diagnosis, 2008. CMD 2008. International Conference on*, 2008, pp. 927-931.
- [112] X. Zhang, J. Tang, and Y. Xie, "Investigation of the relationship between PD measured with RF techniques and apparent charge quantity of metal protrusion in air," in *High Voltage Engineering and Application (ICHVE), 2010 International Conference on*, 2010, pp. 286-289.
- [113] S. Ohtsuka, T. Teshima, S. Matsumoto, and M. Hikita, "Relationship between PD-induced electromagnetic wave measured with UHF method and charge quantity obtained by PD current waveform in model GIS," in *Electrical Insulation and Dielectric Phenomena, 2006 IEEE Conference on*, 2006, pp. 615-618.
- [114] A. Reid, M. Judd, B. Stewart, and R. Fouracre, "Comparing IEC60270 and RF partial discharge patterns," in *Condition Monitoring and Diagnosis, 2008. CMD 2008. International Conference on*, 2008, pp. 89-92.
- [115] S. Xiao, P. Moore, and M. Judd, "Investigating the assessment of insulation integrity using radiometric partial discharge measurement," in *Sustainable Power Generation and Supply, 2009. SUPERGEN'09. International Conference on*, 2009, pp. 1-7.
- [116] R. Sarathi, A. Reid, and M. D. Judd, "Partial discharge study in transformer oil due to particle movement under DC voltage using the UHF technique," *Electric Power Systems Research*, vol. 78, pp. 1819-1825, 2008.
- [117] R. Sarathi and R. Umamaheswari, "Understanding the partial discharge activity generated due to particle movement in a composite insulation under AC voltages," *International Journal of Electrical Power & Energy Systems*, vol. 48, pp. 1-9, 2013.
- [118] B. G. Steward, A. J. Reid, M. D. Judd, and R. A. Fouracre, "UHF and IEC60270 correlation analysis of radiated frequency band measurements on resin insulation void samples," in *2007 Electrical Insulation Conference and Electrical Manufacturing Expo*, 2007, pp. 138-141.
- [119] J. Guo and O. Morel, "Partial Discharge calibration using frequency domain measurement in power cables," in *2014 IEEE Conference on Electrical Insulation and Dielectric Phenomena (CEIDP)*, 2014, pp. 200-203.

- [120] K.-H. Kim, S.-H. Yi, H.-J. Lee, and D.-S. Kang, "Setup of standard PD calibrator and its uncertainties," *Journal of Electrical Engineering and Technology*, vol. 6, pp. 677-683, 2011.
- [121] L. Zhong, G. Chen, and Y. Xu, "A novel calibration method for PD measurements in power cables and joints using capacitive couplers," *Measurement Science and Technology*, vol. 15, p. 1892, 2004.
- [122] A. Cavallini, G. C. Montanari, and M. Tozzi, "PD apparent charge estimation and calibration: A critical review," *IEEE Transactions on Dielectrics and Electrical Insulation*, vol. 17, pp. 198-205, 2010.
- [123] X.-x. Zhang, J.-z. Tang, J. Tang, Y. Chen, and Y.-b. Xie, "Relationship between UHF PD detection and apparent charge quantity of metal protrusion in air," *Przegląd Elektrotechniczny*, vol. 88, pp. 266-270, 2012.
- [124] R. Prochazka, K. Draxler, J. Hlavacek, and V. Kvasnicka, "Verification of partial discharge calibrators," in *Applied Electronics (AE), 2013 International Conference on*, 2013, pp. 1-3.
- [125] S. Coenen, S. Tenbohlen, S. Markalous, and T. Strehl, "Sensitivity of UHF PD measurements in power transformers," *IEEE Transactions on Dielectrics and Electrical Insulation*, vol. 15, pp. 1553-1558, 2008.
- [126] A. Sellars, S. MacGregor, and O. Farish, "Calibrating the UHF technique of partial discharge detection using a PD simulator," *IEEE transactions on dielectrics and electrical insulation*, vol. 2, pp. 46-53, 1995.
- [127] T. Hoshino, S. Maruyama, K. Nojima, and M. Hanai, "A unique sensitivity verification combined with real-time partial-discharge identification method," *IEEE transactions on power delivery*, vol. 20, pp. 1890-1896, 2005.
- [128] I. A. Soomro and M. N. Ramdon, "Study on different techniques of partial discharge (PD) detection in power transformers winding: Simulation between paper and EPOXY resin using UHF method," *International Journal of Conceptions on Electrical and Electronics Engineering*, vol. 2, April 2014.
- [129] M. S. A. Rahman, P. Rapisarda, and P. L. Lewin, "Partial discharge propagation inside a high voltage transformer winding: Comparison of measurement and

- simulation," in *Electrical Insulation and Dielectric Phenomena (CEIDP), 2012 Annual Report Conference on*, 2012, pp. 56-59.
- [130] I. A. Soomro and M. N. R. Baharom, "Comparison between partial discharge in paper and impregnated paper insulators used in power transformer winding based on ultra-high frequency (UHF) detection method," 2013.
- [131] M. Zanjani, A. Akbari, N. Shirdel, E. Gockenbach, and H. Borsi, "Investigating partial discharge UHF electromagnetic waves propagation in transformers using FDTD technique and 3D simulation," pp. 497-500.
- [132] H. Karami, G. B. Gharehpetian, and M. S. A. Hejazi, "Oil Permittivity Effect on PD Source Allocation Through Three-dimensional Simulation," presented at the International Power System Conference, Tehran- Iran, Nov 2013.
- [133] S. Fernando, W. Rowe, and K. Wong, "Partial discharge detection using antenna like activity of overhead distribution cables," in *Universities Power Engineering Conference (AUPEC), 2010 20th Australasian*, 2010, pp. 1-5.
- [134] H. Sinaga, B. Phung, and T. Blackburn, "Design of ultra high frequency sensors for detection of partial discharges," in *Proc. Int. Symp. High Voltage Engineering, Cape Town, South Africa*, 2009, pp. 892-896.
- [135] Y.-Y. Man, C. Zhang, X.-G. Xi, M.-L. Wu, Y.-W. Dong, Z. Sun, *et al.*, "Simulation Analysis of Transient Earth Voltages Aroused by Partial Discharge in Switchgear," *Research Journal of Applied Sciences, Engineering and Technology*, vol. 7, pp. 97-104, 2014.
- [136] H. R. Mirzaei, A. Akbari, M. Zanjani, E. Gockenbach, and H. Borsi, "Investigating the partial discharge electromagnetic wave propagation in power transformers considering active part characteristics," in *Condition Monitoring and Diagnosis (CMD), 2012 International Conference on*, 2012, pp. 442-445.
- [137] B. Zheng, A. Bojovschi, and X. Chen, "Electromagnetic radiation spectrum from partial discharge in air-insulated medium voltage switchgear," in *Power Engineering and Automation Conference (PEAM), 2012 IEEE*, 2012, pp. 1-4.

- [138] S. A. Boggs, "Electromagnetic Techniques for Fault and Partial Discharge Location in Gas-Insulated Cables and Substations," *IEEE Transactions on Power Apparatus and Systems*, vol. PAS-101, pp. 1935-1941, 1982.
- [139] B. F. Hampton and R. J. Meats, "Diagnostic measurements at UHF in gas insulated substations," *IEE Proceedings C - Generation, Transmission and Distribution*, vol. 135, pp. 137-145, 1988.
- [140] J. S. Pearson, B. F. Hampton, and A. G. Sellars, "A continuous UHF monitor for gas-insulated substations," *IEEE Transactions on Electrical Insulation*, vol. 26, pp. 469-478, 1991.
- [141] A. Tungkanawanich, E. Y. Hamid, Z. I. Kawasaki, and K. Matsuura, "Analysis of VHF-wideband electromagnetic noises from partial discharge using discrete wavelet transform," in *Power Engineering Society Winter Meeting, 2001. IEEE*, 2001, pp. 263-268 vol.1.
- [142] A. Tungkanawanich, Z.-I. Kawasaki, J. Abe, and K. Matsuura, "Location of partial discharge source on distribution line by measuring emitted pulse-train electromagnetic waves," in *Power Engineering Society Winter Meeting, 2000. IEEE*, 2000, pp. 2453-2458.
- [143] M. Hikita, H. Yamashita, T. Hoshino, T. Kato, N. Hayakawa, T. Ueda, *et al.*, "Electromagnetic noise spectrum caused by partial discharge in air at high voltage substations," *IEEE transactions on power delivery*, vol. 13, pp. 434-439, 1998.
- [144] D. H. Froula, S. H. Glenzer, N. C. Luhmann, and J. S. Jr., *Plasma Scattering of Electromagnetic Radiation*, 2nd ed. SCITECH Publishing, 2001.
- [145] K. Lonngren and S. Savov, *Fundamentals of Electromagnetics with MATLAB*, 1st ed. SciTech Publishing, 2005.
- [146] A. AG. (2014). *Biconical EMC broadband antennas - BicoLOG Series*. Available: [http://www.aaronia.com/Datasheets/Antennas/EMCMeasurement\\_Antenna\\_BicoLOG-Series.pdf](http://www.aaronia.com/Datasheets/Antennas/EMCMeasurement_Antenna_BicoLOG-Series.pdf)
- [147] M. Abdel-Salam, *High-Voltage Engineering: Theory and Practice, Revised and Expanded*: CRC Press, 2000.

- [148] A. Pillai and R. Hackam, "Electric field and potential distributions for unequal spheres using symmetric and asymmetric applied voltages," *IEEE Transactions on Electrical Insulation*, pp. 477-484, 1983.
- [149] N. Kishore, G. S. Punekar, and H. Shastry, "Sparkover in sphere gaps with alternating voltages and perturbed electric fields," in *Electrical Insulation and Dielectric Phenomena, 2009. CEIDP'09. IEEE Conference on*, 2009, pp. 634-637.
- [150] F. Roman, V. Cooray, and V. Scuka, "Corona from floating electrodes," *Journal of electrostatics*, vol. 37, pp. 67-78, 1996.
- [151] P. B. Sankar, "Measurement of air breakdown voltage and electric field using standad sphere gap method," National Institute of Technology, Rourkela, 2011.
- [152] S. C. CIGRE, "Strength of external insulation during live line maintenance and repair work with special reference to transient overvoltages,," presented at the Fonseca, Garbagnati, Hutzler, Zheng-Jianchao. Electra N. 129, Task Force 07.02 of Study Committee 33: Britten, March 1990.
- [153] P. L. J. Phillipott, E.L. White, H.M. Ryan et al., "Lightning strike point location studies on scale models," presented at the Lightning and static electricity, Conference Paper, Royal Aeronautical Society., Culham, 1975.
- [154] F. Roman, V. Cooray, and V. Scuka, "Corona from floating electrodes," *Journal of Electrostatics*, vol. 37, pp. 67-78, 1996.
- [155] F. Román, E. Lötberg, R. Högberg, and V. Scuka, "Electrical characteristics of insulated metallic bodies in a lightning breakdown field," in *22nd International Conference on Lightning Protection (ICLP), Budapest, Hungary*, 1994.
- [156] F. Roman, V. Cooray, and V. Scuka, "The principle of operation of a simple electrostatic field measuring device based on the properties of floating electrodes," *Journal of electrostatics*, vol. 40, pp. 483-488, 1997.
- [157] F. J. Roman, "Electrostatic field measuring device based on properties of floating electrodes for detecting whether lightning is imminent," ed: Google Patents, 1999.
- [158] F. Román, "The influence of a floating electrode on the breakdown voltage of a complex gap," 1995.

- [159] N. Mora, F. Vega, F. Román, N. Peña, and F. Rachidi, "Corona Charged subnanosecond impulse generator," in *20th International Zurich Symposium on Electromagnetic Compatibility*, 2008.
- [160] A. Reid, "A new approach to partial discharge measurements for testing electrical insulation systems," University of Strathclyde, 2007.
- [161] B. Hampton, "UHF diagnostics for gas insulated substations," in *High Voltage Engineering, 1999. Eleventh International Symposium on (Conf. Publ. No. 467)*, 1999, pp. 6-16.
- [162] Z. De-wen, C. Jian, and D. Jia-feng, "Study on equivalent circuit model of partial discharge in power transformers," in *Mechatronic Science, Electric Engineering and Computer (MEC), 2011 International Conference on*, 2011, pp. 12-15.
- [163] M. G. Niasar, N. Taylor, P. Janus, X. Wang, H. Edin, and R. Kiiza, "Partial discharges in a cavity embedded in oil-impregnated paper: effect of electrical and thermal aging," *Dielectrics and Electrical Insulation, IEEE Transactions on*, vol. 22, pp. 1071-1079, 2015.
- [164] A. Jaber, P. Lazaridis, Y. Zhang, B. Saeed, U. Khan, D. Upton, *et al.*, "Assessment of absolute partial discharge intensity from a free-space radiometric measurement," in *URSI Asia-Pacific Radio Science Conference (URSI AP-RASC)*, 2016, pp. 1011-1014.
- [165] HVPD. (2015). *PD Calibrator*. Available: <http://www.hvpd.co.uk/>
- [166] R. Sarathi, A. Reid, and M. Judd, "Partial discharge study in transformer oil due to particle movement under DC voltage using the UHF technique," *Electric Power Systems Research*, vol. 78, pp. 1819-1825, 2008.
- [167] R. Hussein, K. B. Shaban, and A. H. El-Hag, "Histogram-based thresholding in discrete wavelet transform for partial discharge signal denoising," in *Communications, Signal Processing, and their Applications (ICCSPA), 2015 International Conference on*, 2015, pp. 1-5.
- [168] C. Laurent and C. Mayoux, "Partial discharge. XI. Limitations to PD as a diagnostic for deterioration and remaining life," *Electrical Insulation Magazine, IEEE*, vol. 8, pp. 14-17, 1992.

- [169] "Introduction to Partial Discharge (PD)," presented at the HV PD company, UK, 2015.
- [170] C. Haslett, *Essentials of Radio Wave Propagation*. United Kingdom: Cambridge University Press, 2008.
- [171] M. Hata, "Empirical formula for propagation loss in land mobile radio services," *IEEE transactions on Vehicular Technology*, vol. 29, pp. 317-325, 1980.
- [172] Y. Zhang, D. Upton, A. Jaber, H. Ahmed, U. Khan, B. Saeed, *et al.*, "Multiple Source Localization for Partial Discharge Monitoring in Electrical Substation," *sign*, vol. 10, p. 6, 2015.
- [173] M. Zanjani, A. Akbari, N. Shirdel, E. Gockenbach, and H. Borsi, "Investigating partial discharge UHF electromagnetic waves propagation in transformers using FDTD technique and 3D simulation," in *Condition Monitoring and Diagnosis (CMD), 2012 International Conference on*, 2012, pp. 497-500.
- [174] A. Jaber, P. Lazaridis, Y. Zhang, B. Saeed, U. Khan, D. Upton, *et al.*, "Frequency Spectrum Analysis of Radiated Partial Discharge Signals," presented at the IET EUROEM 2016 conference (European Electromagnetics Symposium), London, UK, 2016.

## APPENDICES

### Appendix A

- Equivalent circuit of the floating electrode PD emulator

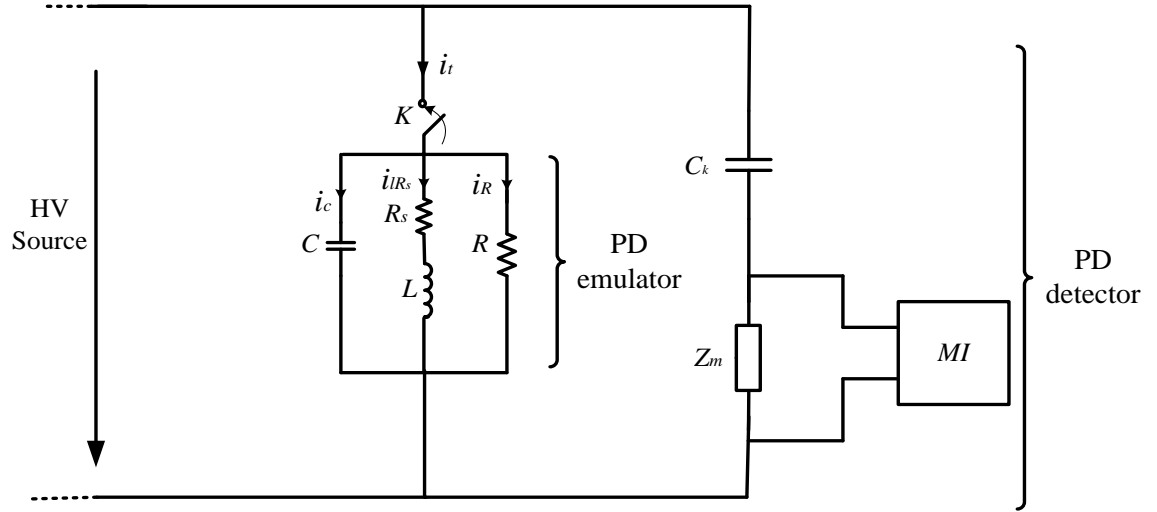


Figure A-1 Equivalent circuit of floating electrode PD emulator and detector.

Referring to Kirchhoff's Current Law (KCL),  $i_t$  is equal to :

$$i_t = i_R + i_{L,R_s} + i_C \quad (A - 1)$$

Where:  $v(0) = V_0$  and  $i(0) = I_0$ ,  $i_{L,R_s} = I_0 + \frac{1}{LR_s} \int_{-\infty}^0 v_L(t) dt$ . According to eq. (A - 1), in terms of V, the voltage across all components:

$$C \frac{dv(t)}{dt} + \frac{v_R}{R} + [I_0 + \frac{1}{LR_s} \int_0^t v_L(t) dt] = i_t(t) \quad (A - 2)$$

Let the  $i_{L,R_s}$  current is the unknown variable, where  $i_{L,R_s} = I_0 + \frac{1}{LR_s}$  eq. (A - 2) .is rewritten as follows:

$$CLR_s \frac{d^2 i_{L,R_s}(t)}{dt^2} + \frac{LR_s}{R} \frac{di_{L,R_s}(t)}{dt} + i_{L,R_s} = i_t(t) \quad (A - 3)$$

For the homogeneous, equation

$$CLR_s \frac{d^2 i_{L,R_s}(t)}{dt^2} + \frac{LR_s}{R} \frac{di_{L,R_s}(t)}{dt} + i_{L,R_s} = 0 \quad (\text{A} - 4)$$

Equation (A – 4) represents a second order ordinary (homogeneous) linear differential equation with constant coefficients. The circuit elements specify the value of the coefficients.

It is well known that the solutions of such equations consist of exponential functions.

Assume the solution is  $i_{L,R_s}(t) = Ae^{-st}$  the resulting characteristic polynomial equation therefore is:

$$s^2 + \frac{1}{RC}s + \frac{1}{LC} = 0 \quad (\text{A} - 5)$$

The coefficients of the eq (A – 5) are  $a = 1$ ,  $b = \frac{1}{RC}$  and  $c = \frac{1}{R_s LC}$ .

If  $b^2 - 4ac = 0$  then, there will be only one repeated root and  $s = \frac{-b}{2a}$ . Applying this

condition on the characteristic equations (A – 5) yields:  $(\frac{1}{RC})^2 - 4\frac{1}{R_s LC} = 0$ , provides the

characteristic solution of eq (A – 4) is  $s_1 = s_2 = \frac{-1}{2RC}$ . For simplification and convenience,

let  $s = \frac{-1}{2RC}$ ; therefore, the general solution of eq (A – 4) is:

$$i_{L,R_s} = (A_1 + A_2 t)e^{-st} \quad (\text{A} - 6)$$

so the general solution of eq. (A – 3) is:

$$i_{L,R_s} = i_t + (A_1 + A_2 t)e^{-st} \quad (\text{A} - 7)$$

Initially, the voltage of capacitor is zero, and the current flowing over the inductor is zero, namely  $i_{LR_1} = (0 -) = 0$ ,  $v_C = (0 -) = 0$ , then get:

$$\begin{cases} i_t + A_1 = 0 \\ -sA_1 + A_2 = 0 \end{cases} \quad (\text{A} - 8)$$

so,

$$i_{L,R_s} = i_t - i_t e^{-st} - s i_t t e^{-st} \quad (\text{A} - 9)$$

Consequently, the voltage function is:

$$v = s^2 i_t t e^{-st} \quad (\text{A} - 10)$$

where  $s$  and  $i_t$  are positive. eq. (A – 10) is a single index attenuation function.

If  $(\frac{1}{RC})^2 - 4\frac{1}{LC} \neq 0$  supposing  $s_1$  and  $s_2$  of the characteristic equation. Then get the general solution of eq. (A – 4):

$$i_{L,R_s} = A_1 e^{s_1 t} + A_2 e^{s_2 t} \quad (\text{A} - 11)$$

where

$$s_{1,2} = -\frac{1}{2RC} \mp \sqrt{\left(\frac{1}{2RC}\right)^2 - \left(\frac{1}{LC}\right)} \quad (\text{A} - 12)$$

so, the solution of Eq. (A – 13) is:

$$i_{L,R_s} = i_t + A_1 e^{s_1 t} + A_2 e^{s_2 t} \quad (\text{A} - 13)$$

The initial condition  $i_{L,R_s} = (0^-) = 0$ ,  $v_C = (0^-) = 0$ , obtain:

$$\begin{cases} i_t + A_1 + A_2 = 0 \\ A_1 s_1 + A_2 s_2 = 0 \end{cases} \quad (\text{A} - 14)$$

The solutions of equation (A – 14) are:

$$\begin{cases} A_1 = \frac{s_2 i_t}{s_2 - s_1} \\ A_2 = \frac{s_1 i_t}{s_2 - s_1} \end{cases} \quad (\text{A} - 15)$$

and because  $v = v_L = L \frac{di_L}{dt}$  get voltage function:

$$v = L s_1 A_1 e^{s_1 t} + L s_2 A_2 e^{s_2 t} \quad (\text{A} - 16)$$

From eq. (A – 15) and (A – 16), obtain:

$$v = \frac{L s_1 s_2 i_t}{s_1 - s_2} e^{s_1 t} - e^{s_2 t} \quad (\text{A} - 17)$$

If  $\left(\frac{1}{2RC}\right)^2 - 4\frac{1}{LC} > 0$   $s_1$  and  $s_2$  are real number  $<$  than Zero, and  $|s_1| \geq |s_2|$  then  $Ls_1 s_2 i_t / s_1 - s_2$  then conclude:

$$v = A(e^{-\alpha_1 t} - e^{-\alpha_2 t}) \quad (\text{A} - 18)$$

where  $\alpha_1$  ,  $\alpha_2$  ,  $A$  are positive and the expression is a double exponential attenuation function.

If  $\left(\frac{1}{2RC}\right)^2 - 4\frac{1}{LC} < 0$  ,  $s_1$  and  $s_2$  are conjugate . Supposing that  $s_1 = a + j\beta$  ,  $s_2 = a - j\beta$  in which  $\alpha$  and  $\beta$  are real number.

so the voltage function can be simplified as:

$$v = A \sin(\beta t) \cdot e^{-\alpha t} \quad (\text{A} - 19)$$

where  $\alpha = \frac{1}{2RC}$  ,  $\beta = -4\frac{1}{LC} - \left(\frac{1}{RC}\right)^2 - 4\frac{1}{LC}$  ,  $A = L (\alpha^2 + \beta^2)^{i_t} / \beta$  ,  $A > 0$ .

## Appendix B

- Compare between FSR and galvanic contact measurements of PD time series event oscilloscope data capture using floating electrode PD emulator.

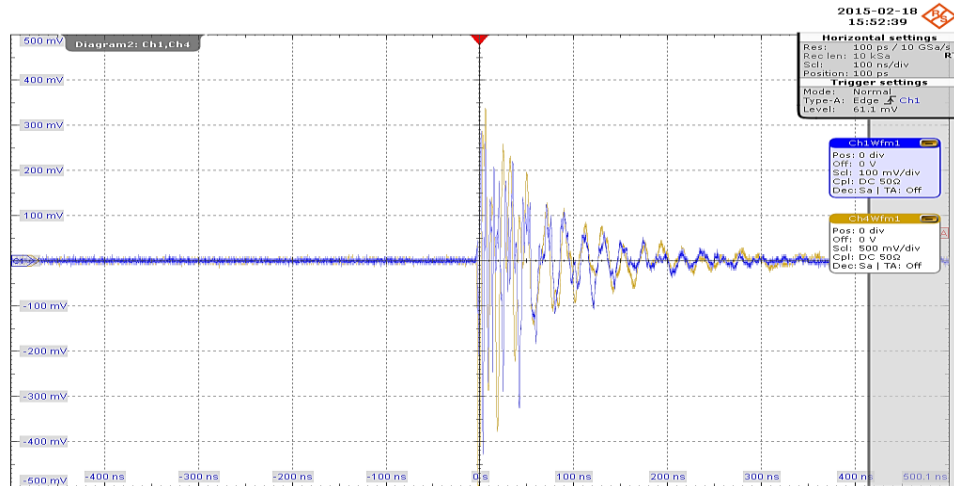


Figure B-1 Comparing FSR and galvanic contact signal for the same PD event.

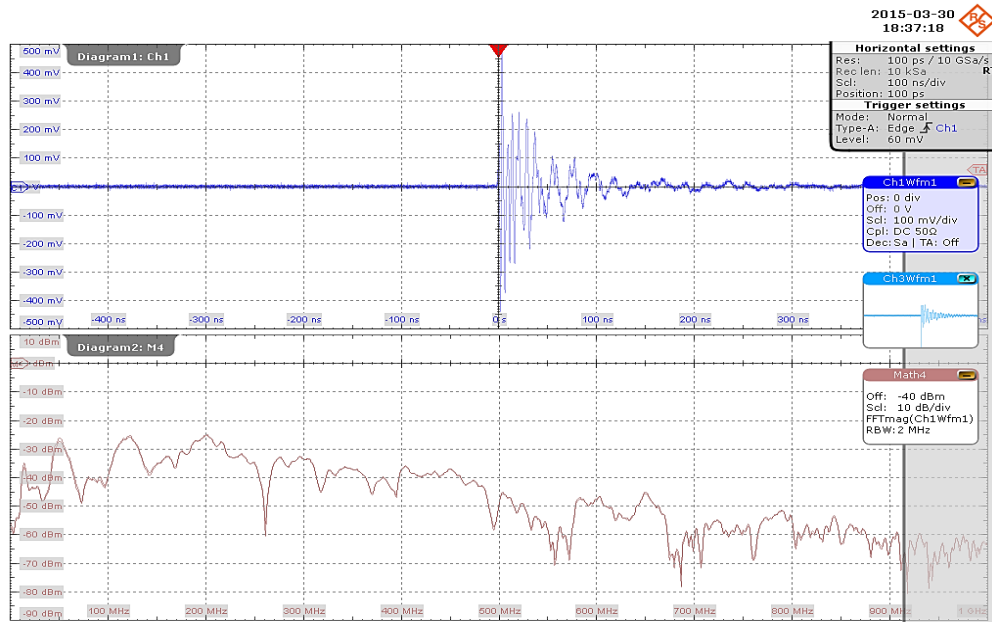


Figure B-2 FSR measurements of PD time series event and FFT oscilloscope data capture.

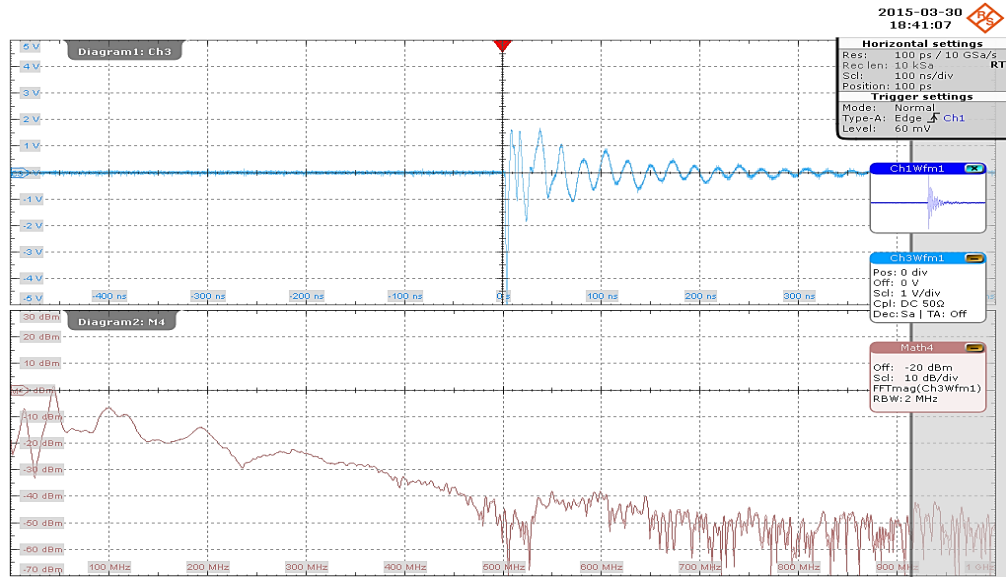


Figure B-3 Galvanic contact measurements of PD time series event and FFT oscilloscope data capture.

## Appendix C

Example of the variation with distance of received peak voltage, received field-strength and apparent effective radiated power using floating electrode PD emulator for 12 locations antenna distance from PD emulator.

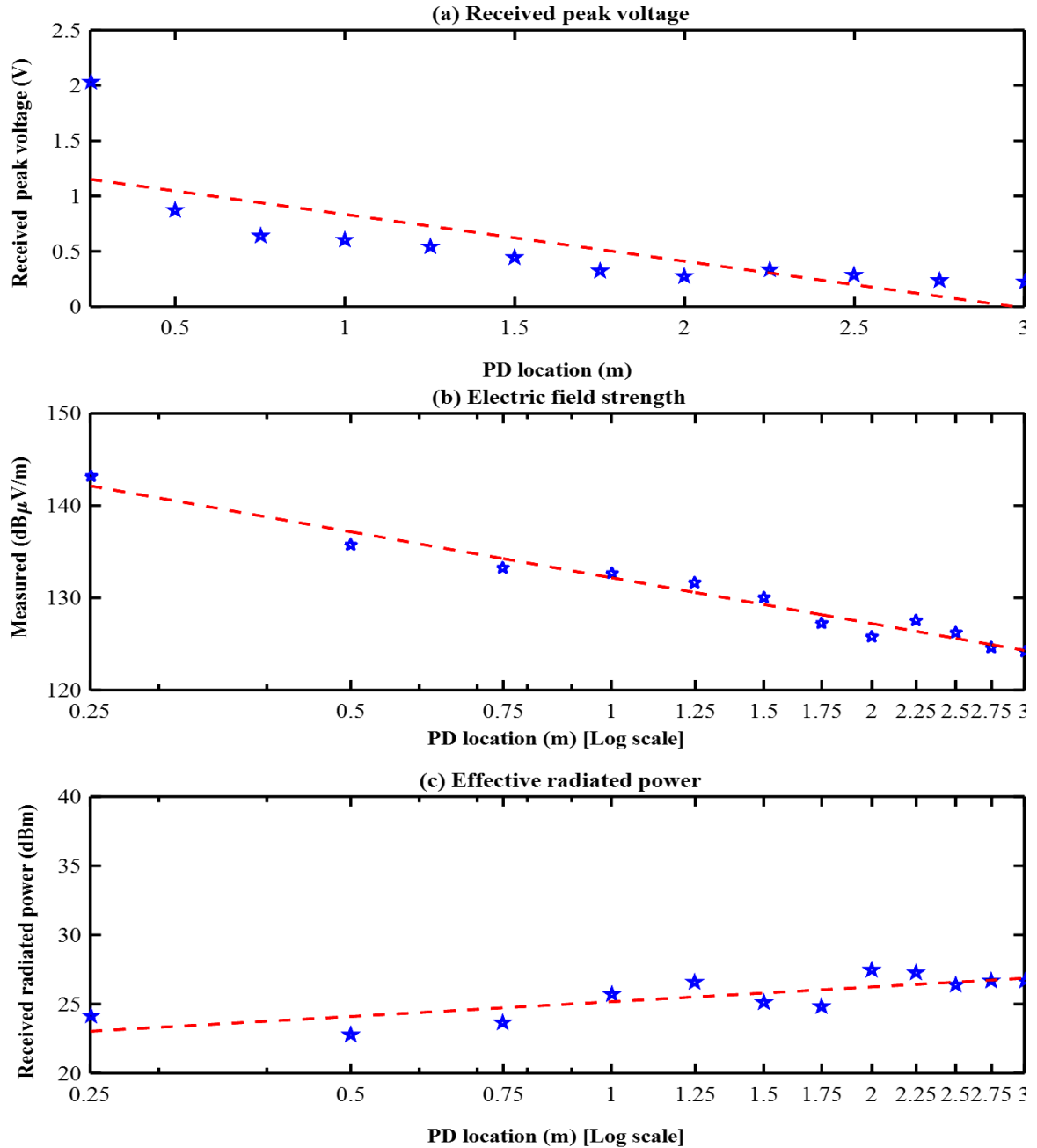


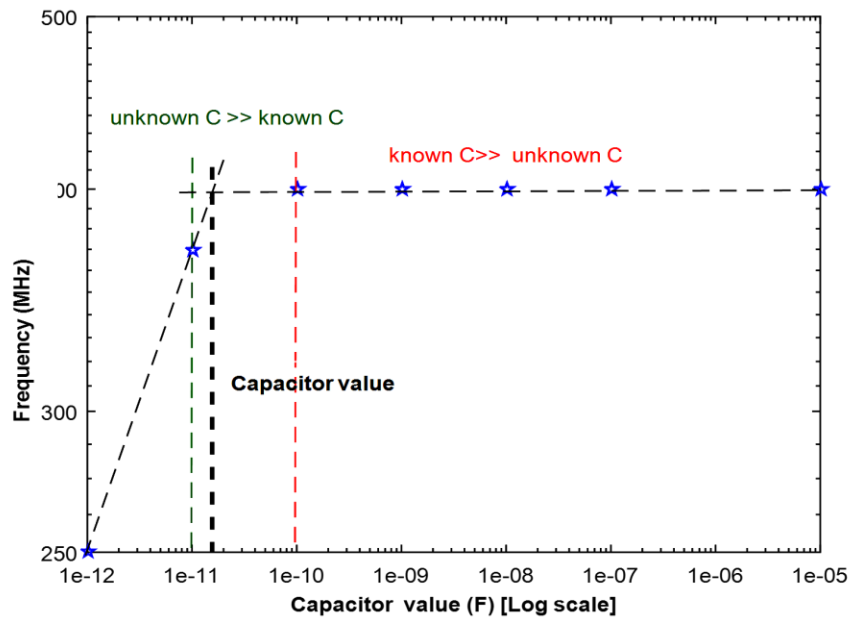
Figure C-1 (a) Received peak voltage, (b) Electric field strength and (c) ERP as a function of (floating-electrode PD emulator) – 12 location antenna distance from emulator.

## Appendix D

- Finding unknown parameters of capacitor and inductance of floating electrode PD emulator

The known capacitance is connected in parallel with equivalent circuit of floating electrode PD emulator.

Capacitor value (F)	Time of the first half-cycle of the PD model (ns)	Calculated frequency (MHz)
$1 \times 10^{-5}$	2.5	400
$1 \times 10^{-7}$	2.5	400
$1 \times 10^{-8}$	2.5	400
$1 \times 10^{-9}$	2.5	400
$1 \times 10^{-10}$	2.5	400
$1 \times 10^{-11}$	2.7	370
$1 \times 10^{-12}$	4	250



Unknown capacitor is  $1.6 \times 10^{-11} \Rightarrow 16 \text{ pF}$

Known capacitor is  $1 \times 10^{-11} \Rightarrow 10 \text{ pF}$

Total capacitors is 26 pF

$$f_o = \frac{1}{2\pi\sqrt{LC}} = 370 \text{ MHz}$$

$L=7\text{nH}$